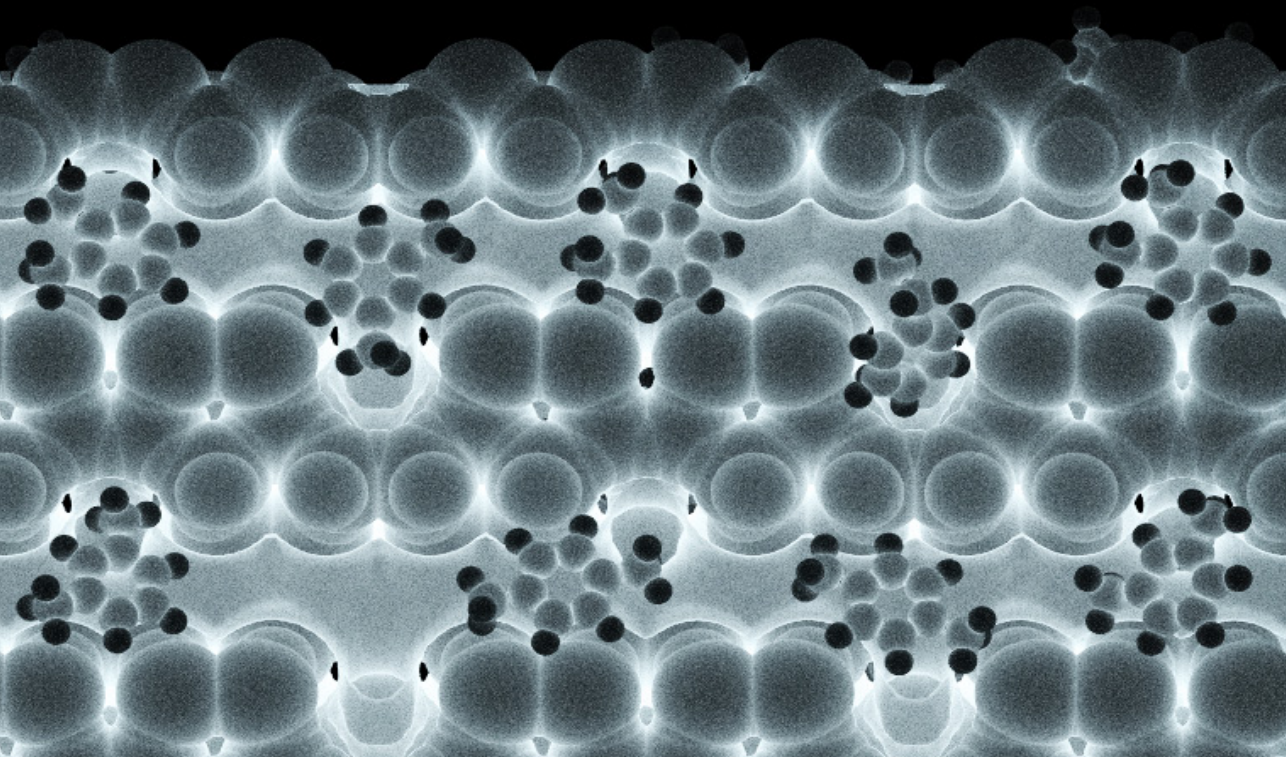


# ADSORPTION AND SEPARATION OF C<sub>8</sub> AROMATIC HYDROCARBONS IN ZEOLITES

Sebastián Caro Ortiz





**ADSORPTION AND SEPARATION OF  
C<sub>8</sub> AROMATIC HYDROCARBONS IN ZEOLITES**



# **ADSORPTION AND SEPARATION OF C<sub>8</sub> AROMATIC HYDROCARBONS IN ZEOLITES**

## **Proefschrift**

ter verkrijging van de graad van doctor  
aan de Technische Universiteit Delft,  
op gezag van de Rector Magnificus Prof.dr.ir. T.H.J.J. van der Hagen,  
voorzitter van het College voor Promoties,  
in het openbaar te verdedigen op  
vrijdag 9 april 2021 om 15:00 uur

door

## **Sebastián Andrés CARO ORTIZ**

Magíster en Ciencias de la Ingeniería Mecánica  
Universidad Técnica Federico Santa María, Chili  
geboren te Iquique, Chili.

Dit proefschrift is goedgekeurd door de promotoren

Prof.dr.ir. T.J.H. Vlugt

Dr. D. Dubbeldam

Samenstelling promotiecommissie bestaat uit:

Rector Magnificus, voorzitter

Prof.dr.ir. T.J.H. Vlugt Technische Universiteit Delft, promotor

Dr. D. Dubbeldam Universiteit van Amsterdam, promotor

Onafhankelijke leden:

Prof.dr. J.I. Siepmann University of Minnesota, USA

Prof.dr. C.E. Wilmer University of Pittsburgh, USA

Dr. E. Zuidema Shell Global Solutions International B.V.

Prof.dr. E.A. Pidko Technische Universiteit Delft

Prof.dr.ir. W. de Jong Technische Universiteit Delft



The research reported in this thesis was carried out at the Process & Energy Department, Faculty of Mechanical, Maritime and Materials Engineering, Delft University of Technology. This project was sponsored by Shell Global Solutions International B.V. This work was sponsored by NWO Exacte Wetenschappelijk (Physical Sciences) for the use of supercomputer facilities, with financial support from the Nederlandse Organisatie voor Wetenschappelijk Onderzoek (Netherlands Organization for Scientific Research, NWO).

*Keywords:* Zeolites, Aromatics, Hydrocarbons, Adsorption, Diffusion, Separation, Molecular Simulation

*Printed by:* Ridderprint | [www.ridderprint.nl](http://www.ridderprint.nl)

*Front & Back:* Cover design by S. Caro Ortiz. C<sub>8</sub> aromatics in MFI-type zeolite. Design inspired by X-ray images of the human body.

Copyright © 2021 by S. Caro Ortiz

ISBN 978-94-6366-384-7

An electronic version of this dissertation is available at  
<http://repository.tudelft.nl/>.

*«Llore si le parece  
yo x mi parte  
me muero de risa».*

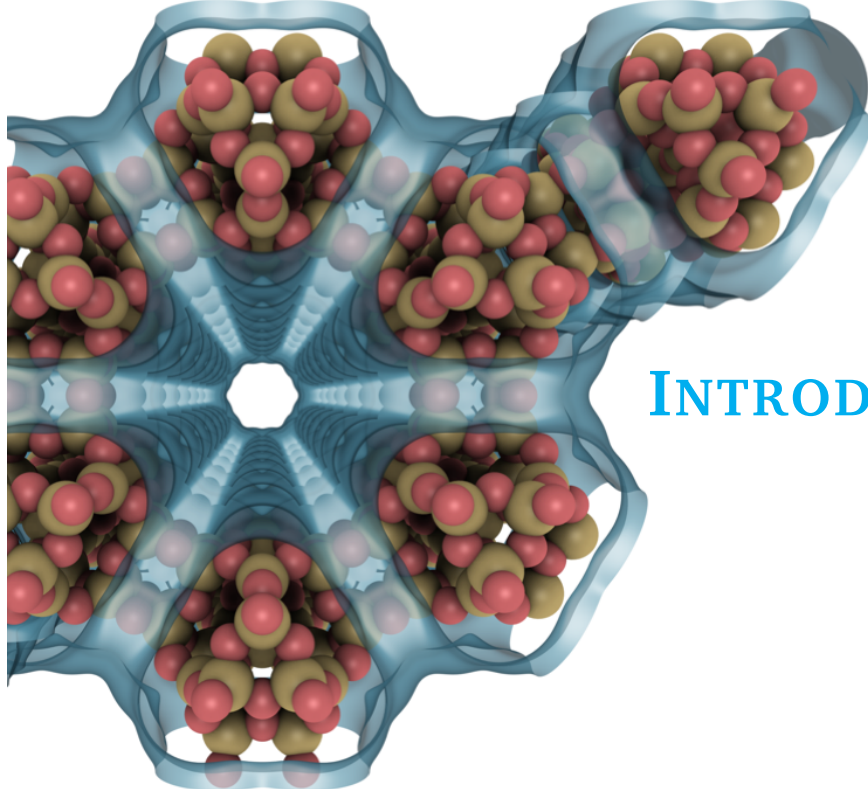
Nicanor Parra



# CONTENTS

<b>1</b>	<b>Introduction</b>	<b>1</b>
1.1	Zeolites in industrial catalysis of aromatics . . . . .	1
1.2	Molecular simulation of zeolite adsorption . . . . .	5
1.3	Outline of this thesis . . . . .	8
<b>2</b>	<b>Vapor-liquid equilibria of xylene mixtures</b>	<b>11</b>
2.1	Introduction . . . . .	12
2.2	Methods . . . . .	13
2.3	Results and discussion . . . . .	15
2.3.1	Vapor-liquid equilibria of pure xylenes . . . . .	15
2.3.2	Vapor-liquid equilibria of binary mixtures . . . . .	20
2.4	Conclusions . . . . .	25
<b>3</b>	<b>Effects of models for framework flexibility on the adsorption of aromatics in MFI-type zeolites</b>	<b>27</b>
3.1	Introduction . . . . .	28
3.2	Methods . . . . .	30
3.3	Results and discussion . . . . .	34
3.3.1	Force field induced effects in MFI-type zeolites . . . . .	34
3.3.2	Adsorption of n-heptane in MFI-type zeolite . . . . .	42
3.3.3	Adsorption of ethylbenzene in MFI-type zeolite . . . . .	43
3.3.4	Adsorption of xylene isomers in MFI-type zeolite . . . . .	47
3.3.5	Discussion . . . . .	51
3.4	Conclusions . . . . .	52
<b>4</b>	<b>Influence of framework flexibility on the adsorption and diffusion of aromatics in MFI-type zeolites</b>	<b>55</b>
4.1	Introduction . . . . .	56
4.2	Methods . . . . .	59
4.3	Results and discussion . . . . .	61
4.3.1	Henry coefficients of xylenes in MFI-type zeolite . . . . .	61
4.3.2	Framework flexibility in MFI-type zeolite . . . . .	61
4.3.3	'Flexible snapshot' method for adsorption in MFI-type zeolite . . . . .	63
4.3.4	Adsorption of aromatics in MFI-type zeolite . . . . .	65
4.3.5	Diffusion of aromatics in MFI-type zeolite . . . . .	67
4.4	Conclusions . . . . .	70

<b>5 Competitive adsorption of xylenes at chemical equilibrium in zeolites</b>	<b>71</b>
5.1 Introduction . . . . .	72
5.2 Methods . . . . .	75
5.3 Results and discussion . . . . .	79
5.3.1 Properties of mixture of xylenes . . . . .	79
5.3.2 Zeolite structures . . . . .	81
5.3.3 Adsorption of xylenes in zeolites . . . . .	83
5.4 Conclusions . . . . .	105
<b>6 Conclusions</b>	<b>107</b>
<b>Appendix</b>	<b>111</b>
A.1 Force field parameters and initial conditions . . . . .	111
A.2 Partition functions of xylenes from thermodynamic tables . . . . .	116
A.3 Multiple linear regression for computing thermodynamic properties of adsorption . . . . .	118
A.4 Fugacity coefficient from chemical potentials . . . . .	118
<b>References</b>	<b>121</b>
<b>Summary</b>	<b>151</b>
<b>Samenvatting</b>	<b>153</b>
<b>Acknowledgements</b>	<b>155</b>
<b>Curriculum Vitæ</b>	<b>157</b>
<b>List of Publications</b>	<b>159</b>



# 1

## INTRODUCTION

### 1.1. ZEOLITES IN INDUSTRIAL CATALYSIS OF AROMATICS

Separation processes are essential for the chemical and petrochemical industry [1]. In these processes, physical, chemical, or electrical forces are used to separate components of a mixture [2]. Processes commonly used for separation of molecules use ca. 10–15% of the world's energy consumption [3, 4]. Separation technologies can improve the energy efficiency, increase the efficiency of the use of raw materials, and reduce the residuals from the separation process [2]. The separation of hydrocarbons is considered -with the separation of greenhouse gases from dilute emissions and uranium from seawater- as one of the “seven chemical separation processes to change the world” [5].

Common separation of hydrocarbons is performed using fractional distillation [6]. In this process, the separation is based on the boiling points of the different components of the hydrocarbon mixture [7]. Fractional distillation is considered to be the main crude oil separation process, as it performs the initial rough separation of different fuels [8]. Typical products of the fractional distillation of crude oil are: light gases (butane/propane), gasoline, kerosene, diesel, and light/heavy fuel oils [9]. Producing these account for ca. 1/3 of the total primary energy consumption

1

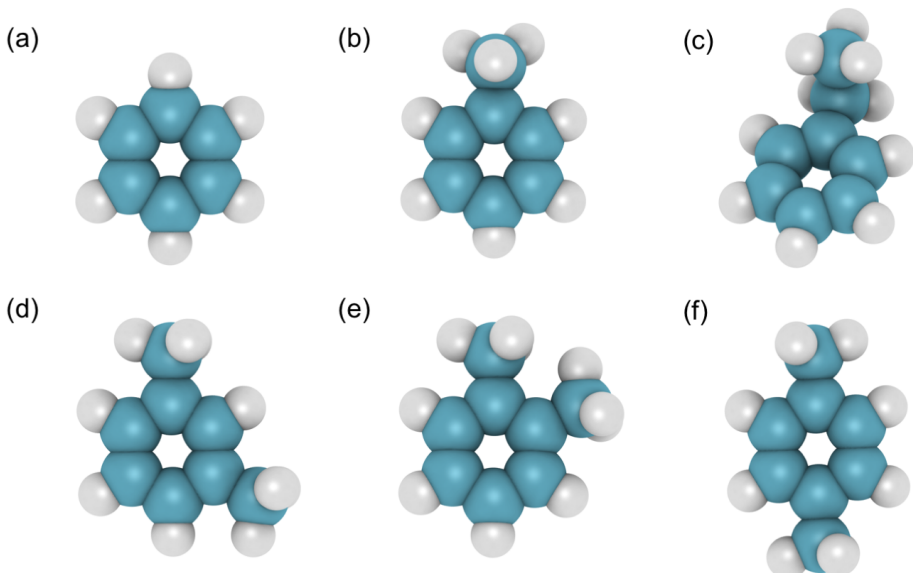


Figure 1.1: BTEX aromatic compounds. Carbon atoms are shown in blue. Hydrogen atoms are shown in white. (a) Benzene, (b) toluene, (c) ethylbenzene, (d) *m*-xylene, (e) *o*-xylene, and (f) *p*-xylene. Molecules visualized with iRASPA. [22]

of the world [10]. At the top end of the gasoline distillation range, there is usually a surplus called naphtha [11]. This is used as feedstock for petrochemical plants. Naphtha contains two main types of hydrocarbons: aliphatic and aromatic [12]. The aliphatic group is composed by paraffinic hydrocarbons and cycloparaffins [13]. The aromatic group is mainly composed by alkyl-substituted benzenes [13].

Aromatics are important building blocks for the production of fine chemicals, polymers, and fuels [14, 15]. The aromatic hydrocarbons of commercial interest for the petrochemical industry include benzene, toluene, and mixed xylenes [16, 17]. This group of aromatics is often referred to as BTX, or BTEX if ethylbenzene is included. The BTEX compounds are shown in Fig. 1.1. The International Energy Agency [18] reported that the production of primary chemicals, specifically ammonia, methanol, ethylene, propylene, and BTX consumes 2/3 of the total energy consumption of the chemical sector. It is expected that the demand of such primary chemicals increases 41% by 2040 [19]. Traditionally, mixed BTX are obtained by catalytic cracking and catalytic reforming processes of naphtha [20]. After cracking and reforming of naphtha, the BTX mixture is separated using distillation to produce benzene, toluene, and mixed xylenes [21].

Benzene is mostly used for the production of ethylbenzene and cumene [23]. These are raw materials for the production of styrene [24], phenol [25], and long-chain alkylbenzenes [26]. Such products are used as feedstocks in the manufacture of surfactants [27]. Toluene is commonly added to gasoline as an octane booster

[28]. Most of the toluene that is not used for fuel purposes is converted into benzene and xylenes or used for solvents [29, 30]. Xylenes are components of solvents, cleaning agents, paint thinners, varnish, and corrosion preventives [31, 32]. A mixture of xylenes at thermodynamic equilibrium typically contains 53% *m*-xylene, 24% *o*-xylene, and 23% *p*-xylene [33]. From the xylene isomers, *p*-xylene has the highest economic value [34, 35]. It is a core raw material for manufacturing polyethylene terephthalate [36, 37], commonly known as PET. This is typically used for packaging [38, 39], containers for liquids and food [40–42], clothes [43], textiles [44], engineering resins [45], and medical protection equipment [46, 47]. Recently, the production of PET fiber overtook cotton as the largest-volume fiber produced globally [48]. *o*-Xylene is used for the production of phthalic anhydride [49–51], which is mostly used as a plasticizer for the production of polyvinyl chloride (PVC) [52]. The end uses of PVC include pipes, fittings, window and door frames, clothing, car seat covers, inflatable structures, toys, etc. [53–57] *m*-Xylene -the main component of the mixture of xylenes- has a limited end use and is preferably isomerized into *p*-xylene or *o*-xylene [58, 59]. The different practical applications and economic value of xylene isomers make the separation of the isomers from the mixture a relevant industrial process [60, 61]. Separation of xylenes is a major challenge [62–64]. The separation of C<sub>8</sub> aromatics is one of the most classical separation problems in the petrochemical industry [65]. The separation using distillation is a very difficult process due to the similar boiling points of xylene isomers [66, 67]. Crystallization processes can be used for separation, as *p*-xylene has a higher melting point than the other isomers [68]. However, cooling the mixture down to the appropriate crystallization temperature is very energy demanding [69].

The efficient use of the energy resources of the world has become an issue urgent to address [70]. Efforts to develop and improve technologies to transform hydrocarbons efficiently are important [71]. Sholl and Lively [5] have underlined that improvements to the separation processes of benzene and C<sub>8</sub> aromatics would greatly benefit the world. Separation using adsorption in porous materials is an attractive alternative to distillation for the separation of chemicals [72]. Adsorption in a porous material is a process in which molecules are accumulated at a surface in the pores of the material [73]. The use of solid adsorbents for separation yields higher separation efficiencies and lower energy consumption than traditional separation processes [74–76]. Minceva and Rodrigues [77] reported that about 40% and 60% of the worldwide supply of pure *p*-xylene is produced by crystallization and adsorption technologies, respectively. The selective adsorption of one specie over another is the base of the separation of molecules using porous materials [78, 79]. The separation of xylenes in porous materials can be achieved by the adsorption in zeolites (such as FAU-type [77, 80–89]) and metal-organic frameworks [90–93]. Current research efforts are focused on advances of new membranes and sorbents that decrease the energy consumption of such xylene isomer separation [5]. However, this is not a straightforward task as *p*-xylene is less than 1 Å smaller than *o*-xylene [94]. This makes the separation of xylenes in porous materials a particularly difficult endeavor.

1

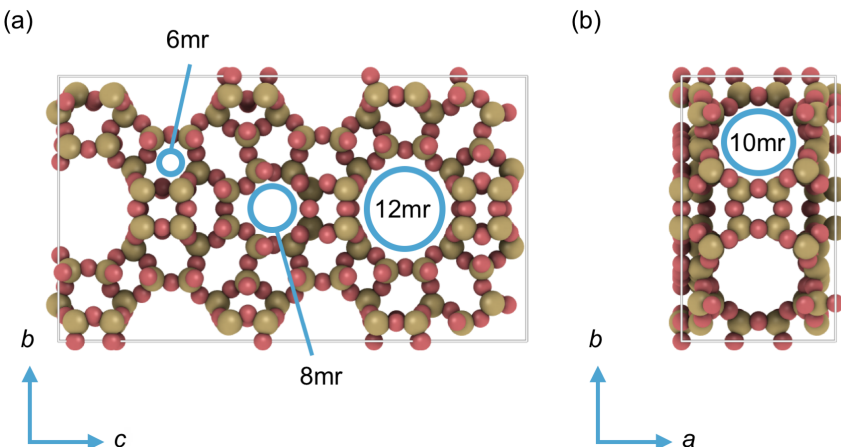


Figure 1.2: UOV-type zeolite structure [123]. Silicon and oxygen atoms are shown in yellow and red, respectively. The blue rings indicate some of the 6-, 8-, 10, and 12-membered rings (mr) of the zeolite framework. The zeolite rings are circuits of alternating Si (or Al) and O atoms [122]. In this zeolite type, the 8-, 10- and 12-mr form interconnected 8-, 10- and 12-mr channels, respectively.

Zeolites have been widely used in many processes for the transformation of hydrocarbons [95–97]. These materials are considered the most important heterogeneous catalyst in the petrochemical industry [98, 99]. Other uses of zeolites range from water cleaning materials [100–102], builder for laundry powders [103], odor control agents [104], to the capture of radioactive particles [105], and several other applications [106–115].

Zeolites have a porous structure with well defined pores and channel systems [116]. These systems offer large void volumes that are able to host a wide variety of molecules while maintaining mechanical stability [117, 118]. Zeolites are based on  $\text{TO}_4$  tetrahedra (T represents either Si or Al atoms) [119]. Several  $\text{TO}_4$  tetrahedra form crystalline structures with defined void spaces that shape cavities and interconnecting channels [120]. Zeolites have different channel sizes [121]. These are characterized by rings of connected T and O atoms [122]. Fig. 1.2 shows the UOV-type zeolite structure with highlighted 6-, 8-, 10-, and 12-membered rings that evince the different sizes of the rings.

Each zeolite structure has particular physical and chemical properties. Practically, there is no limit to the number of hypothetical zeolite structures [124–126]. However, there are currently only 253 different zeolite types [123] that have been discovered in nature or synthesized in the lab [127]. These are assigned a three-letter code (e.g., UOV). Nearly twenty types are used in industry [128]. Five of these are significantly produced as commercial catalysts [129]. These are the so-called 'big five' [107] zeolite types and are shown in Fig. 1.3.

Many industrial molecule separation applications strongly rely on the selective hosting capabilities of zeolites [130–135]. For example, xylene molecules diffusing along the zeolite pores can undergo isomerization, disproportionation and

transalkylation reactions [136–139]. Before molecules can be transformed inside a zeolite, the molecules have to be adsorbed and then diffuse to the active sites [140, 141]. After transformation, the reaction products have to diffuse and desorb from the zeolite [142]. Thus, knowledge of the adsorption and diffusion behavior of hydrocarbons in the pores of zeolites is important for the understanding of the catalytic activity of the zeolite [130, 143–149].

## 1.2. MOLECULAR SIMULATION OF ZEOLITE ADSORPTION

The experimental study of adsorption of aromatics in zeolites has many challenges [150], specially at high pressures and temperatures [151, 152]. There are many practical difficulties for obtaining reliable experimental adsorption data. Such difficulties are related to large error propagation [153], leaking at high pressures [150], the determination of the void volume of the porous material, and the description of real gas behavior at high pressures [154, 155]. The adsorbed loadings are usually determined by weight changes of the porous material or by volume/pressure differences in the fluid phase [156]. This implies that when considering the adsorption of a multi-component mixture, determining the composition of the adsorbed mixture is not as straightforward as when a pure component is adsorbed [150, 157, 158]. The prediction of the adsorption equilibrium of multiple components is one of the most challenging problems in adsorption [159–161]. Experimental studies of adsorption of a multi-component mixture are time consuming, as only a single particular pressure point can be measured per experiment [162]. Also, the zeolite samples must be synthesized [163, 164]. The zeolite synthesis can be complex, expensive, time consuming, and require careful adjustment of synthesis conditions [165–169]. This can be unpractical for screening purposes [170].

As most of the activity occurs inside the pores of the material, it is very difficult to carry out experiments that yield information at the molecular level [144]. Simulations can provide detailed insight on the molecular scale that are not easily accessible from experimental methods [171, 172]. Molecular simulations are an extensively used tool to predict the thermodynamic properties of a wide diversity of systems [173]. Thermodynamic properties of pure components and mixtures can be computed for large ranges of conditions, even when experiments can be challenging, expensive, or dangerous [173]. The accurate description and characterization of the thermodynamic properties of the aromatics -such as the vapor-liquid equilibrium (VLE), adsorption equilibrium, and diffusion rate of molecules- is critical for the design of proper techniques, equipment, and processes for efficient separation [174–178].

The thermodynamic properties of hydrocarbons in zeolites have been considerably studied and predicted using molecular simulations [179–188]. These simulation techniques have also been applied to study other nanoporous materials [189–196]. Monte Carlo (MC) simulations in the grand-canonical ensemble can be used to compute sorbate loadings in a zeolite for different temperatures and pressures [197–199]. Several studies where MC is used to study adsorption of aromatics in zeolites can be found in literature [135, 200–210].

Many key process properties can be predicted using molecular simulations. For

1

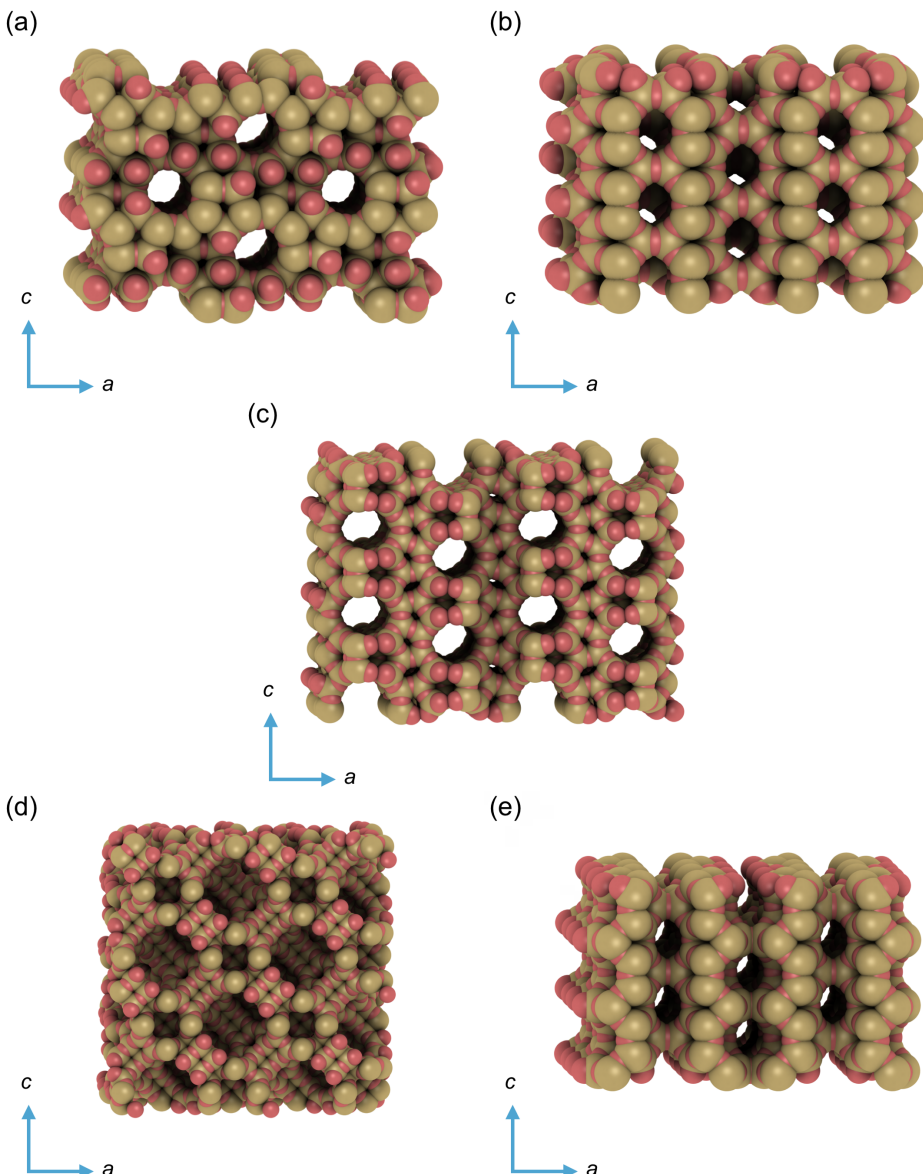


Figure 1.3: Framework structures of the so-called 'big five' zeolite types. These zeolite types are frequently used as commercial catalysts for industrial purposes [129]. Silicon and oxygen atoms are shown in yellow and red, respectively. (a) MFI-type zeolite, (b) MOR-type zeolite, (c) BEA-type zeolite, (d) FAU-type zeolite, and (e) FER-type zeolite. The maximum diameter of a sphere that can fit in these zeolite types are: 6.36, 6.7, 6.68, 11.24, and 6.31 Å, respectively [123]. MFI- and FER-type zeolites contain 10-membered ring (mr) channels. BEA- and MOR-type zeolites contain 12-mr channels. FAU-type zeolites contain 12-mr cages.

example, the heat of adsorption, Henry coefficient, diffusion coefficients, saturation capacities, adsorption selectivities, and adsorption isotherms [144, 211]. The heat of adsorption is a reference for the energy demand of the adsorption/desorption of the species involved in the separation process [212, 213]. The diffusion coefficient is related to the residence time of the hydrocarbons in the zeolite [214, 215]. Adsorption loadings provide information regarding the occupancy of the void volumes of the zeolite for a given pressure and temperature [73]. These properties can be compared to empirical data or used for screening materials that may have been overlooked for separation applications.

Computer simulations of the adsorption of hydrocarbons in zeolites are typically performed using rigid zeolite frameworks [186, 197, 216]. However, molecular simulation studies have reported that the computed loadings can be sensitive to small differences in the atom positions of the zeolite, especially for aromatics [217]. This suggests that interactions that include framework flexibility and polarizability may be required to simulate systems where molecules fit tightly in the pores of zeolites [217, 218]. Only a limited amount of studies have approached the simulations of adsorption using a flexible zeolite framework [216, 219–223]. However, none of these studies have addressed the effect of framework flexibility on the adsorption of aromatics in zeolites [204].

Molecular Dynamics studies have shown that accounting for framework flexibility considerably affects the diffusion coefficient of aromatics in zeolites [137]. It has been reported that framework flexibility changes the diffusivity of benzene in zeolites by orders of magnitude [224, 225]. If the diffusion coefficient of a molecule in a zeolite framework is sufficiently high, Molecular Dynamic simulations can be directly used [144]. Processes such as the separation of aromatic mixtures in zeolites, show self-diffusion coefficients lower than  $10^{-12} \text{ m}^2\text{s}^{-1}$  [226]. As such, the diffusion behavior may occur outside the time scales accessible to Molecular Dynamics simulations [227]. The free energy landscape of molecules within the pores of a zeolite indicates the mobility of the molecules inside the zeolite and can be used in a more quantitative investigation of product shape selectivity of zeolite catalysts [228]. Low diffusion coefficients are observed when the molecules are trapped in low free energy sites in the zeolite framework, and sporadically hop from one low energy site to another [144]. Transition state theory (TST) methods can be used to estimate the diffusion coefficients in porous materials at slow diffusion time scales [229, 230], using the free energy landscape [231]. Such methods have been used for the estimation of diffusion coefficients of aromatics in MFI-type zeolites [224, 225, 232–234].

Industrial separation and catalytic processing of aromatics considers adsorption in a zeolite from a stream of mixed aromatics [235]. In practice, most C<sub>8</sub> processing technologies have considered adsorption from a vapor phase. More recently, there has been interest in adsorption from a liquid phase [236]. Considering adsorption from a liquid phase leads to an efficient use of all the pore volume of the zeolite. Liquid phase adsorption is preferred due to its operational, maintenance and environmental advantages over other processing technologies [237]. Comprehensive knowledge regarding the effect of the selective mechanisms for the adsorption of hy-

drocarbons in zeolites at high loadings and reaction conditions is of great interest for the petrochemical industry [238]. Industrial applications deal with adsorption from a mixture of hydrocarbons at chemical equilibrium. However, not much is known about the chemical equilibrium of the adsorbed molecules at reaction conditions. Most studies of adsorption of aromatics in zeolites, either experimental or computational [202], have focused on adsorption of pure components from the vapor phase. Experimentally, it is very difficult to determine the adsorption equilibrium at saturation conditions [159, 160]. In molecular simulations, very difficult insertion and deletion of molecules make simulations extremely inefficient [239]. However, advanced biasing techniques -such as Continuous Fractional Component (CFCMC) [240–242] or Configurational-Bias (CBMC) [243, 244]- can be used nowadays in Monte Carlo simulations to overcome this issue.

In this thesis, the following issues are addressed: (1) the choice of force fields for the appropriate computation of thermodynamic properties of aromatic molecules; (2) the sensitivity of adsorption and diffusion of aromatic molecules to zeolite framework flexibility; (3) the effect of the zeolite topology on the chemical equilibrium of xylenes at reaction conditions.

### 1.3. OUTLINE OF THIS THESIS

In this thesis, the separation of aromatics hydrocarbons in zeolites is studied using classical molecular simulations. The different chapters address different aspects that influence the separation of aromatics in zeolites. Such aspects provide physical insight for the improvement of the models that are used for molecular simulations of aromatics in zeolites, as well as guidelines for the design and improvement of separation processes that use molecular sieves. Important research questions that will be addressed here are: (1) how does framework flexibility influence adsorption and diffusion of C<sub>8</sub> aromatics in zeolites?; (2) what is the role of the pore topology?; for the separation and catalytic conversion of xylenes, (3) how does the type of framework influence the product distribution of xylene isomers?; (4) are there any possible zeolite structures that may have been overlooked for the processing of aromatics?. This may ultimately lead to improvements in processes for aromatic industrial separation and catalytic transformations.

The intermolecular interactions between aromatic molecules are studied in chapter 2. The vapor-liquid equilibria (VLE) of xylenes as pure components and binary mixtures is computed by Monte Carlo simulations using different force fields. A common practice in the development of the potentials for aromatics is to fit the interaction parameters to reproduce the VLE of the pure component [245–248], or by *ab initio* quantum mechanical calculations [249–251]. Several force field for xylene interactions have been reported in literature [248, 251–255]. Each of these force fields offer particular features and characteristics (i.e. electrostatic interactions, united/all-atom approach, etc.). The effects of these characteristics on the accurate prediction of the VLE of pure components and binary mixtures of xylenes are assessed.

The zeolite intra-framework interactions and the interaction of the framework with guest aromatic molecules is studied in chapters 3 and 4. The effects of the

use of force fields for framework flexibility in the adsorption of aromatics in zeolites is examined in chapter 3. Adsorption loadings in MFI-type zeolites are computed by Monte Carlo simulations in the grand-canonical ensemble. MFI-type zeolite is chosen as a study case as it shows potential for the separation of aromatic hydrocarbons due to its average pore size between 6 and 7 Å [256]. It is shown that force fields for framework flexibility inherently produce changes of the zeolite structure, and hence the adsorption isotherms are changed. These changes are due to the intra-framework interactions of the force fields and not to the presence of guest molecules. The influence of framework flexibility on the adsorption and diffusion of aromatics in zeolites is studied in chapter 4. Adsorption loadings and self-diffusion coefficients of aromatics in an MFI-type zeolite are computed by Monte Carlo simulations in the grand-canonical ensemble and using TST, respectively. It is shown that for very flexible zeolite frameworks, loadings up to two times larger than in a rigid zeolite framework are obtained at a given pressure. It is also shown that framework flexibility changes the diffusion of aromatics in a zeolite channel by many orders of magnitude compared to a rigid zeolite framework.

The interactions of aromatic molecules inside different zeolite types are studied in chapter 5. The competitive adsorption of xylenes in zeolites is studied. Computations of adsorption of pure xylenes and a mixture of xylenes at chemical equilibrium in several zeolite types are performed by Monte Carlo simulations in the grand-canonical ensemble. Adsorption from both vapor and liquid phases are considered. The different mechanisms that drive adsorption in each zeolite type are studied. Chapter 5 provides insight on how the zeolite framework can influence the competitive adsorption and selectivity of xylenes at reaction conditions. Different selectivities are observed when a vapor phase is adsorbed compared to the adsorption from a liquid phase. This insight has a direct impact on the design criteria for future applications of zeolites in industry.

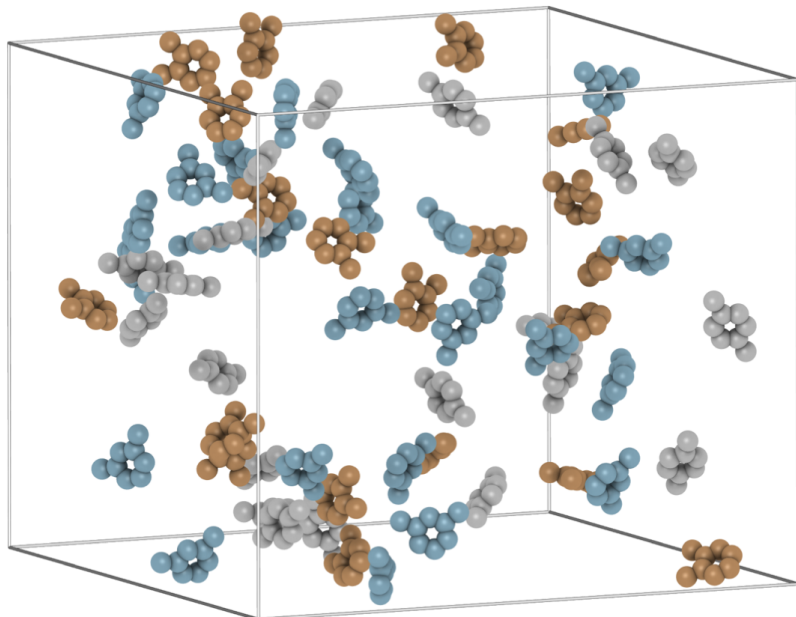


# 2

## VAPOR-LIQUID EQUILIBRIA OF XYLENE MIXTURES

This chapter is based on the article:

S. Caro-Ortiz, R. Hens, E. Zuidema, M. Rigutto, D. Dubbeldam, T. J. H. Vlugt,  
*Molecular simulation of the vapor-liquid equilibria of xylene mixtures: Force field performance, and Wolf vs. Ewald for electrostatic interactions*, *Fluid Phase Equilibr.* **485**, 239 (2019) [257, 258].



## 2.1. INTRODUCTION

The accurate description and characterization of the thermodynamic properties - such as the vapor-liquid equilibrium (VLE)- is critical for the design of proper techniques, equipment, and processes for an efficient separation [174]. Experimental VLE measurements for xylene mixtures are scarce and only a handful of studies provide data for pure components and binary mixtures of xylenes. For pure component, VLE curves are reported by Smith and Srivastava [259]. For binary mixtures, Rodrigues et al. [260] presented coexistence curves for the *p*-xylene/*m*-xylene, *p*-xylene/*o*-xylene and *m*-xylene/*o*-xylene systems at 100.65 kPa. The *p*-xylene/*m*-xylene binary system is described by Kato et al. [261] at atmospheric pressure. Data for 5, 20, 40 and 101.325 kPa is reported by Onken and Arlt [262]. Llopis and Monton [263, 264] reported data for *p*-xylene/*o*-xylene and *m*-xylene/*o*-xylene systems at 6.66 and 26.66 kPa, Parvez et al. [265] characterized the *p*-xylene/*o*-xylene coexistence curves at 81.3 kPa. The coexistence of *o*-xylene-*m*-xylene at 298.15K is described by Wichterle et al. [266]. Such studies report that binary mixtures of xylenes have small differences from an ideal mixture [260–263, 265].

Molecular simulations are an extensively used tool to predict the thermodynamic properties of a wide variety of systems [173]. Fluid phase properties of pure components and mixtures can be computed for large ranges of conditions, even when experiments can be challenging, expensive or dangerous [173]. The Monte Carlo (MC) method in the Gibbs ensemble [267] has been widely used to compute VLE [199, 268–273]. The choice of a force field that accurately describes the interaction potential between atoms and molecules is a crucial factor. The Gibbs ensemble considers two simulation boxes to simulate the properties of coexisting phases avoiding the vapor-liquid interface [268]. Fig. 2.1 shows the vapor and liquid phases of a xylene mixture in two separate simulation boxes of an *NPT*-Gibbs ensemble MC simulation. Molecular simulations of VLE are typically performed employing force fields that model the interactions with Lennard-Jones potentials (LJ) or a combination of LJ and electrostatic interactions. In the case of aromatic compounds, a common practice in the development of the potentials is to fit the interaction parameters to reproduce the VLE of the pure component [245–248], or by ab initio quantum mechanical calculations [249–251]. Several force field for xylene interactions have been reported in literature [248, 251–255], some of which are briefly described in the next section for further use.

The electrostatic interactions are generally represented by charged interaction sites. The Ewald summation method [274] has been extensively used to account these interactions in periodic systems [275]. The electrostatic energy is calculated in two parts by dividing the potential in a short-range contribution computed in real space, and a long-range contribution calculated involving a Fourier transform of the charge density [173]. The long-range contribution constitutes the main disadvantage of the method, it is computationally expensive. Several alternative methods have been developed such as the particle-particle and particle-mesh algorithm [276], the reaction field method [277], the fast multipole algorithm [278], and the Wolf method [279]. These methods are reviewed in depth by Cisneros et al. [280]. From these methods, the Wolf method has been effectively applied to a wide variety

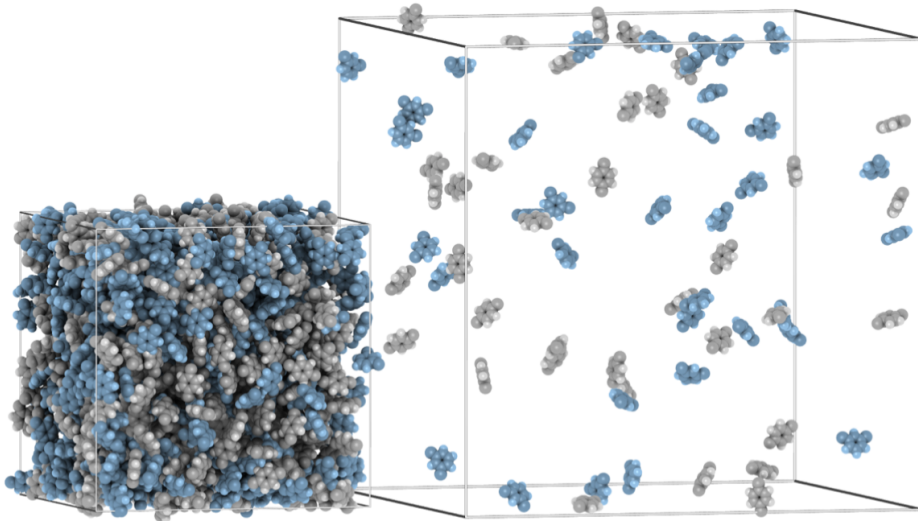


Figure 2.1: Schematic representation of the *NPT*-Gibbs Ensemble MC simulation of the *p*-xylene/*m*-xylene binary mixture. *m*-Xylene and *p*-xylene are shown in blue and grey, respectively. The two simulation boxes represent the liquid (left) and vapor (right) phases. Molecules visualized with iRASPA [22].

of systems [281–288] and has gained attention due to its efficiency compared to the Ewald method as the Fourier part is not often needed in dense systems. For the Wolf method, all interactions are pairwise and the computationally expensive Fourier transform of the charge density is not needed [289]. As this method is based on the screening of charges -which depends on density of the system-, the cut-off radius ( $R_c$ ) and the damping factor ( $\alpha$ ) have to be determined for each system with the procedures described by Hens and Vlugt [290], and Waibel and Gross [291].

This chapter explores how the VLE of pure components and binary mixtures of xylenes can be predicted using molecular simulations and how well the Wolf method can be applied. The simulation details such as the input and force fields are summarized in Section 2.2. The simulation results of VLE for pure components and binary mixtures are analyzed in Section 2.3. The concluding remarks about force field performance and the use of the Wolf method are discussed in Section 2.4.

## 2.2. METHODS

The Monte Carlo technique in the Gibbs Ensemble [267] is used for the simulations. The calculations for the VLE of pure components are performed using the Gibbs ensemble at constant total volume (*NVT*). The isothermal-isobaric version of the Gibbs ensemble (*NPT*) is used for the binary mixture VLE calculations. The total system contains 1000 molecules and the interactions between different atom types

are calculated using Lorentz-Berthelot mixing rules [292]. The LJ interactions are truncated at 14 Å and analytic tail corrections are applied [292]. The Continuous Fractional Component MC (CFCMC) method in the Gibbs ensemble developed by Poursaeidesfahani et al. [240, 242, 293, 294] is used. The Gibbs ensemble is expanded with one extra molecule -the fractional molecule- per molecule type. The fractional molecules have negligible effect on the thermodynamic properties [293]. The interactions of the fractional molecule are scaled in range 0 to 1 (0 for no interactions with surrounding molecules and 1 for full interactions with surrounding molecules) described by the so-called  $\lambda$  parameter. The trial moves in each MC cycle are selected at random within the following fixed probabilities: 33% translations, 33% rotations, 17% changes of the value of  $\lambda$ , 8% identity changes of the fractional molecule -where the fractional molecule turns into a whole one, while a molecule in the other simulation box turns into a fractional molecule-, 8% swap trial moves -the fractional molecule is transferred from one simulation box to the other-, and 1% volume changes. All simulations are performed using the Brick-CFCMC software [295]. The number of steps per MC cycle is equal to the total number of molecules in the system, with a minimum of 20. Each simulation starts with 5000 MC cycles to initialize the system by only allowing rotation and translation trial moves. After that, a stage of 40000 MC cycles equilibrates the system and all types of trial moves are allowed. In this stage, the Wang-Landau algorithm [296] is used to construct a weight function that flattens the probability distribution of  $\lambda$ , so that all values of the  $\lambda$  parameter have the same probability, and that the fractional molecule is equally likely to be found in one of the simulation boxes. The chemical potential is calculated from the probability distribution of  $\lambda$  using the procedure described by Poursaeidesfahani et al. [240]. The initialization stage is followed by a production run of 100000 MC cycles. The reported errors account for the 95% confidence interval calculated by dividing the production run into five sections.

Each simulation starts with a different initial composition (i.e. different number of molecules in each simulation box) which is based on the experimental data available for each system. For pure components, the number of molecules and simulation box sizes can be found in the table A.7 of the Appendix A.1. For binary mixtures, the initial composition can be obtained with the procedure described by Ramdin et al. [268] when experiments are not available. The *p*-xylene/*o*-xylene binary mixtures at 6.66 kPa and 81.3 kPa are simulated. The initial guess for the side length of the cubic boxes are 60 Å for the liquid phase box and 145 Å for the vapor phase box. Initially, 920 and 80 molecules are assigned to the liquid and vapor boxes, respectively. The guess for the initial phase compositions of each box are chosen to match the experimental phase compositions [263, 265].

Four different force fields that model the interactions between xylene isomers are used, each one having a particular approach to describe electrostatic interactions. All molecules are defined as rigid and the bond lengths and angles between pseudo-atoms are according to the original references [245, 248, 252, 253]. The force field parameters are listed in table A.1 of Appendix A.1. Schematic representations of *m*-xylene for the force fields considered in this work are shown in Fig. 2.2. The force fields considered in this work are the following:

1. Transferable Potential for Phase Equilibria - United Atom (TraPPE-UA) [252], a widely used force field that is designed to reproduce the VLE of alkylbenzenes as single components. The united atom approach is conveniently used by merging a carbon atom and its bonded hydrogen atoms into a single uncharged interaction site representing each  $\text{CH}_x$  group in the aromatic species.

2. A modification of the TraPPE-UA force field to include an all-atom approach and charges in the aromatic ring, here called TraPPE-UA-EH. This force field uses the united atom approach from TraPPE-UA [252] to represent the methyl groups, while the bonded carbon and hydrogen atoms from the aromatic ring are individually represented in single interaction centers with charges of  $-0.95\text{e}$  and  $+0.95\text{e}$ , respectively [245].

3. Optimized Potential for Liquid Simulations (OPLS) [253, 297], a widely applied force field that represents the aromatic ring with an all atom approach and the methyl group as a carbon centered atom [298]. Each atom has electrostatic charges.

4. Anisotropic United Atom (AUA) [248, 299]. This force field presents a united atom approach, having uncharged single interaction centers for the  $\text{CH}_x$  groups and positioning the atom in the direction of the center of mass of the atom group, displacing it from the carbon atom position, unlike the other force fields. One of its main features is the representation of the  $\pi$ -cloud in the aromatic ring. One positive partial charge ( $+8.13\text{e}$ ) in the center of the ring, and two negative partial charges ( $-4.065\text{e}$ ) located at  $0.4 \text{ \AA}$  above and below the plane of the aromatic ring are introduced. The negative charges are displaced from the center of the ring to reproduce the experimental dipole moment of the molecule.

The Ewald summation parameters are chosen such that a relative precision of  $10^{-6}$  is achieved [173]. The Wolf summation parameters are chosen according to the procedure described by Hens and Vlugt [290]. By taking into account the experimental data as a starting point, a short simulation in the *NVT* ensemble is performed. The chosen density is close to the equilibrium coexistence density. The chosen temperature is above the critical temperature. The system sizes are equal to the initial guess of the simulation box sizes for the binary mixture calculations in the Gibbs ensemble. From this configuration, the electrostatic energy is calculated for several cut-off radii ( $R_c$ ) and damping factors ( $\alpha$ ). This energy can be compared to a reference calculated with the Ewald method for the same system configuration. Following this procedure, it is determined that an optimum parameter set for the vapor phase is:  $R_c=85 \text{ \AA}$ ,  $\alpha=0.04 \text{ \AA}^{-1}$ ; and for the liquid phase:  $R_c=16 \text{ \AA}$ ,  $\alpha=0.17 \text{ \AA}^{-1}$ .

## 2.3. RESULTS AND DISCUSSION

### 2.3.1. VAPOR-LIQUID EQUILIBRIA OF PURE XYLEMES

The VLE of pure components are calculated with *NVT*-Gibbs ensemble Monte Carlo simulations using the CFCMC method [240]. Simulations are performed for each isomer using the Ewald and the Wolf methods. The densities for *m*-xylene are shown in Fig. 2.3. The calculated coexistence densities for the three isomers with the statistical uncertainties are listed in the Supporting Information of Ref. [257]. The

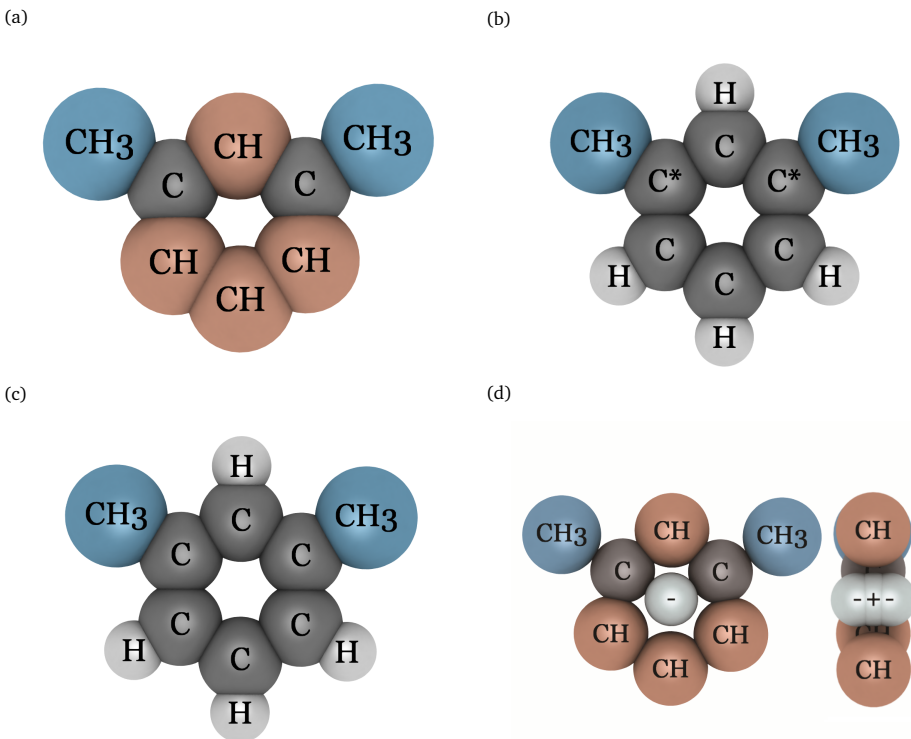


Figure 2.2: Schematic representation of *m*-xylene for the (a) TraPPE-UA [252], (b) TraPPE-UA-EH [245, 252], (c) OPLS [253, 297], and (d) AUA [248, 299] force fields. Pseudo-atom labels use the notation of table A.1 of Appendix A.1. Lennard-Jones parameters and partial charges of these force fields are listed in table A.1 of Appendix A.1.

differences of the use of the Wolf and Ewald methods for *p*-xylene and *o*-xylene computed VLEs are qualitatively the same as for *m*-xylene. The computed VLEs for the TraPPE-UA-EH and AUA show excellent agreement between the Ewald and Wolf methods. The differences in the calculated densities are lower than 1% of the densities and lower than the statistical error of the simulation. The vapor-liquid coexistence densities calculated with the OPLS force field show agreement within the statistical error. The calculated vapor phase densities are underestimated at temperatures between 500 and 550 K using the Wolf method. At high temperatures, the size of the vapor phase simulation box and the number of molecules are different than the values used to determine the optimal damping factor  $\alpha$  and cut-off radius ( $R_c$ ). This suggests that the vapor density of the system is more sensitive to the choice of the Wolf parameters for the OPLS force field than for the other force fields. The chemical potentials as a function of temperature for the two phases of *m*-xylene using the Wolf method are shown in Fig. 2.4. The differences in the chemical potential between the phases are within the statistical error. Chemical

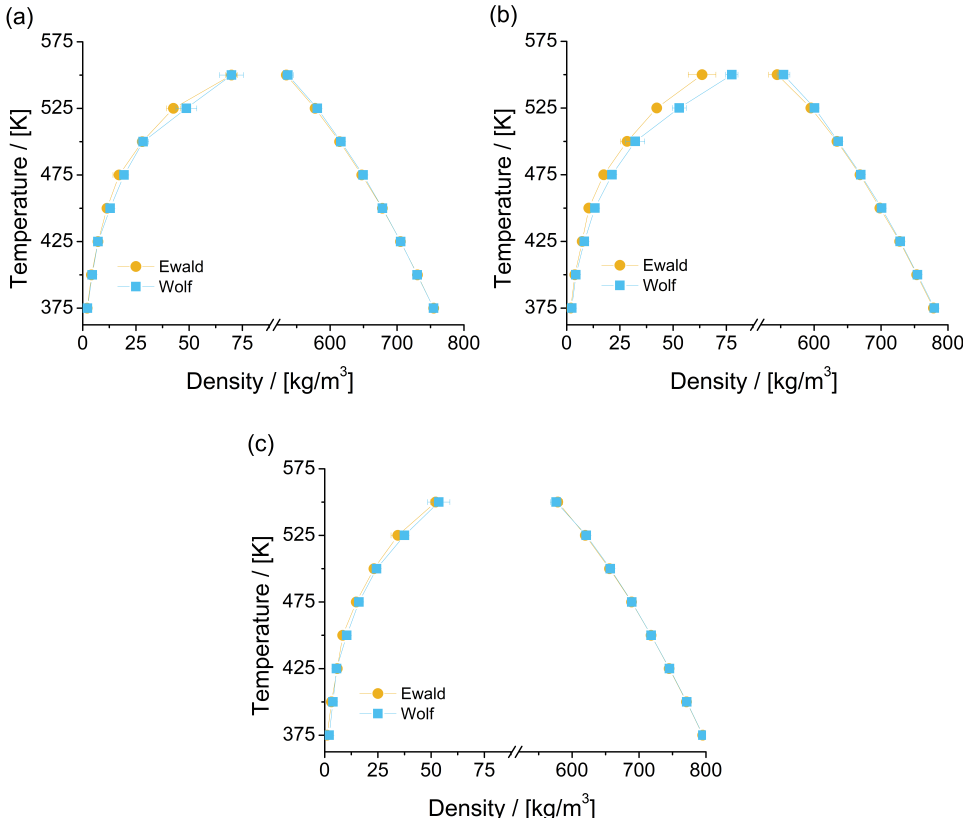


Figure 2.3: Vapor-liquid equilibria of *m*-xylene for different force fields using the Ewald (orange symbol) and the Wolf (blue symbol) methods. (a) TraPPE-UA-EH [245, 252], (b) OPLS [253], (c) AUA [248].

equilibrium between the vapor and liquid phases is observed as the same chemical potential is calculated for both phases.

The vapor-liquid coexistence curves of *m*-xylene, *o*-xylene, and *p*-xylene calculated using the Ewald method are shown in Fig. 2.5 for each force field. Clear differences can be observed in Fig. 2.5 for the density calculations with the experimental data. For *m*-xylene, the TraPPE-UA and the AUA force field predict liquid densities that deviate up to 3% from the experimental data, while TraPPE-UA-EH and OPLS force fields show significantly higher differences. The experimental liquid densities of *p*-xylene are well predicted by TraPPE-UA, TraPPE-UA-EH and AUA, as the difference with the computed density is below the statistical error. The OPLS force field shows slightly higher differences of up to 4% at 550 K. The use of the TraPPE-UA force field yields the best prediction of the experimental density of *o*-xylene. The differences are of the order of two times the statistical uncertainty for the considered temperature range, followed by AUA, with three times the statistical error.

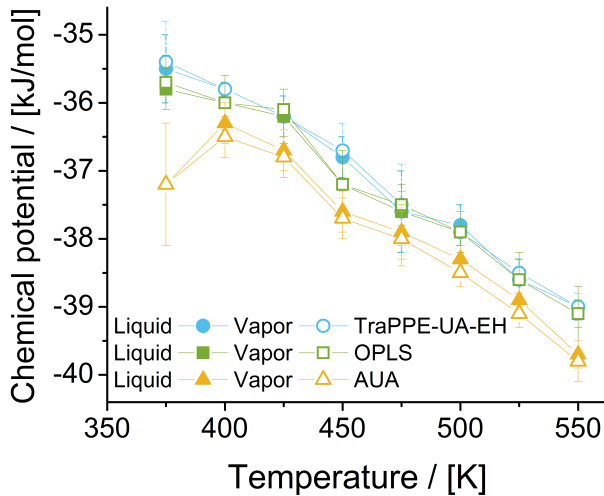


Figure 2.4: Chemical potential (ideal gas as reference state [300]) of *m*-xylene at VLE coexistence as a function of temperature using the Wolf method for each force field. Closed and open symbols represent the liquid and vapor phases, respectively.

Significantly larger differences than in the liquid phase can be observed in the vapor phase for the simulations and the experimental data. The calculated vapor densities are in agreement with the experiments at low temperatures (i.e. < 450 K), and the differences arise at higher temperatures. The vapor densities obtained with the TraPPE-UA and AUA force fields closely follow the experimental data for *m*-xylene. The highest deviations of the density for every isomer are found with the OPLS force field. The largest differences with the experimental data can be found for the *o*-xylene vapor density at temperatures over 450 K, where all force fields present deviations larger than the statistical uncertainties from the experimental data. Such differences for *o*-xylene can be related to assumptions such as having fixed charges, a rigid molecule, and transferable force field parameters for the three isomers. Assuming fixed charges implies a fixed dipole/quadrupole moment. The aromatic  $\pi$  clouds result in a non-negligible quadrupole moment for the aromatic ring [252], which is only considered by the AUA force field. The dipole polarization changes with the temperature, specially for *m*-xylene and *o*-xylene [301], which is not considered by any of the force fields.

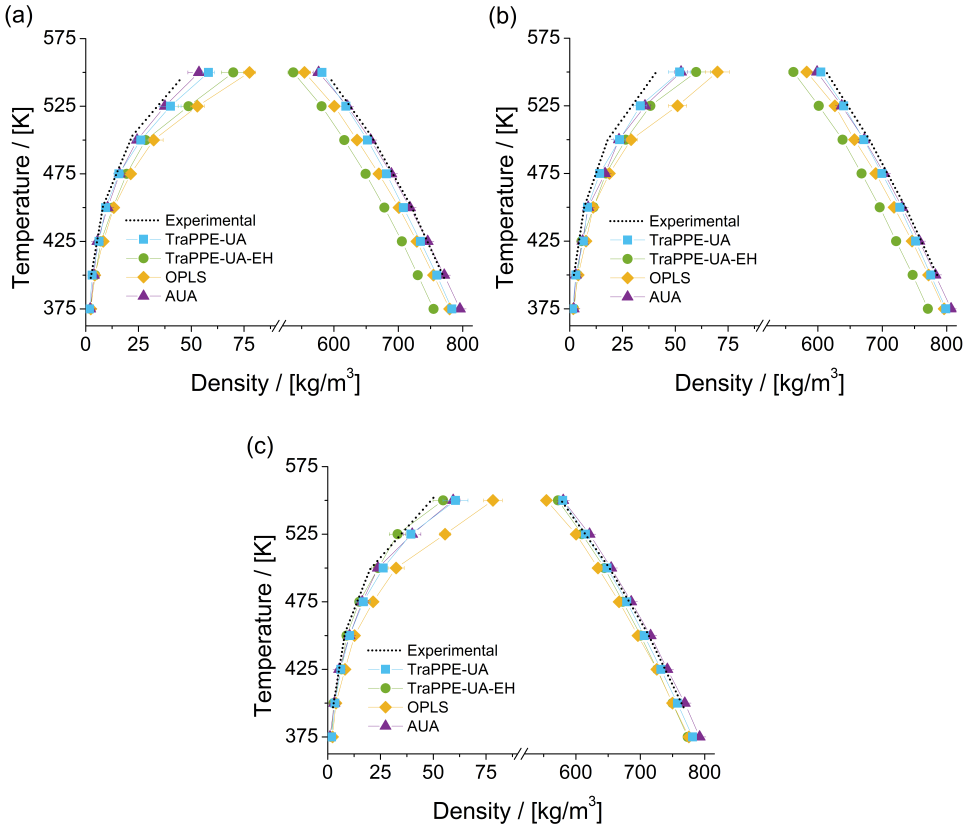


Figure 2.5: Vapor-liquid equilibria of (a) *m*-xylene, (b) *o*-xylene, and (c) *p*-xylene for each force field using the Ewald summation method. Experimental data from ref. [259] is also included.

The critical temperatures ( $T_c$ ) and critical densities ( $\rho_c$ ) are extrapolated using the fitting procedure described by Dinpajoo et al. [302]. The obtained critical points of *m*-xylene, *o*-xylene and *p*-xylene for each force field are listed with experimental data in table 2.1. In general, the differences between the critical point for each force field using the Wolf and Ewald methods are within the statistical error. This is related to the agreement found for the TrapPPE-UA-EH and AUA force fields shown in Fig. 2.5. However, the different densities obtained at high temperature with the Wolf and the Ewald methods for the OPLS force field have an impact on the determined critical point for xylene isomers. The largest difference of the estimated critical temperature between the Wolf and the Ewald methods is 14 K, for *o*-xylene using the OPLS force field. The difference of the critical point of the three isomers and the experimental data is smaller than the statistical uncertainties for TrapPPE-UA and AUA, as well as the experimental critical point of *p*-xylene is predicted by all the simulations within the uncertainties.

Table 2.1: Critical temperatures ( $T_c$ ) and critical densities ( $\rho_c$ ) of pure components extrapolated from VLE simulations using the fitting procedure described by Dinpajooh et al. [302]. (E) and (W) denote the use of the Ewald and the Wolf methods, respectively. The numbers between round brackets denote the uncertainty in the last digit. Experimental data are from Refs. [303–305].

$T_c$ / [K], $\rho_c$ / [ $\text{kg}/\text{m}^3$ ]	<i>m</i> -xylene		<i>o</i> -xylene		<i>p</i> -xylene	
	$T_c$	$\rho_c$	$T_c$	$\rho_c$	$T_c$	$\rho_c$
Experimental [303–305]	616.4(10)	283(4)	630.5(10)	287(4)	617.6(10)	281(4)
TraPPE-UA	620(7)	288(7)	629(7)	297(6)	617(4)	286(8)
TraPPE-UA-EH (E)	604(11)	279(7)	622(6)	278(5)	626(9)	279(6)
TraPPE-UA-EH (W)	610(9)	270(6)	623(5)	275(3)	620(7)	278(7)
OPLS (E)	605(9)	290(9)	626(8)	293(6)	609(8)	285(6)
OPLS (W)	609(9)	279(5)	612(9)	300(9)	611(9)	277(8)
AUA (E)	618(9)	284(6)	625(9)	293(6)	616(8)	290(6)
AUA (W)	618(9)	281(7)	627(8)	286(7)	616(14)	288(8)

### 2.3.2. VAPOR-LIQUID EQUILIBRIA OF BINARY MIXTURES

The VLE of the *p*-xylene/*o*-xylene binary mixture at 6.66 kPa is calculated with *NPT*-Gibbs ensemble Monte Carlo simulations using the CFCMC method [240]. The simulations are performed with each force field using the Ewald and the Wolf methods. The phase compositions obtained with the TraPPE-UA-EH, OPLS, and AUA force fields using the Wolf and Ewald methods are shown in Fig. 2.6. It can be observed that the composition of the liquid phase is not affected by the choice of force field or method for accounting the electrostatic interactions. The statistical uncertainties are larger in the vapor phase than in the liquid phase, and there is a reasonable agreement between the calculated vapor phase compositions with both methods for electrostatic interactions.

The phase diagrams of the *p*-xylene/*o*-xylene binary mixture at 6.66 kPa simulated using the Ewald method with experimental data are shown in Fig. 2.7. Llopis and Monton [263] reported discrete measurements of the phase composition of the mixture. This data is shown as lines to facilitate comparison with the simulations. The experimental uncertainties reported are 0.1 K for the temperature and a standard deviation of 0.001 for reported mole fractions. Small differences from ideality are reported [263] and a small difference between the phase compositions is observed. The experimental data suggests that the vapor does not have the same composition as the liquid. The component with the lowest boiling temperature is expected to have a higher molar fraction in the vapor phase than that with the higher boiling temperature. The simulated composition of the liquid phase is in excellent agreement with the experimental data and the differences are below the statistical uncertainties. Larger differences can be observed for the composition of the vapor phase. For the TraPPE-UA-EH and OPLS force fields, the mole fraction of *p*-xylene in the vapor phase is higher than in the liquid phase at temperatures higher than 335 K, whereas an opposite behavior is predicted by the simulations for temperatures lower than 334 K. This suggests that the vapor phase composition of the component with the highest mole fraction in the liquid phase is underestimated by the simulations. It is important to note that the temperature range of these simulations is out of the fitting range of the force fields, so the observed behavior can

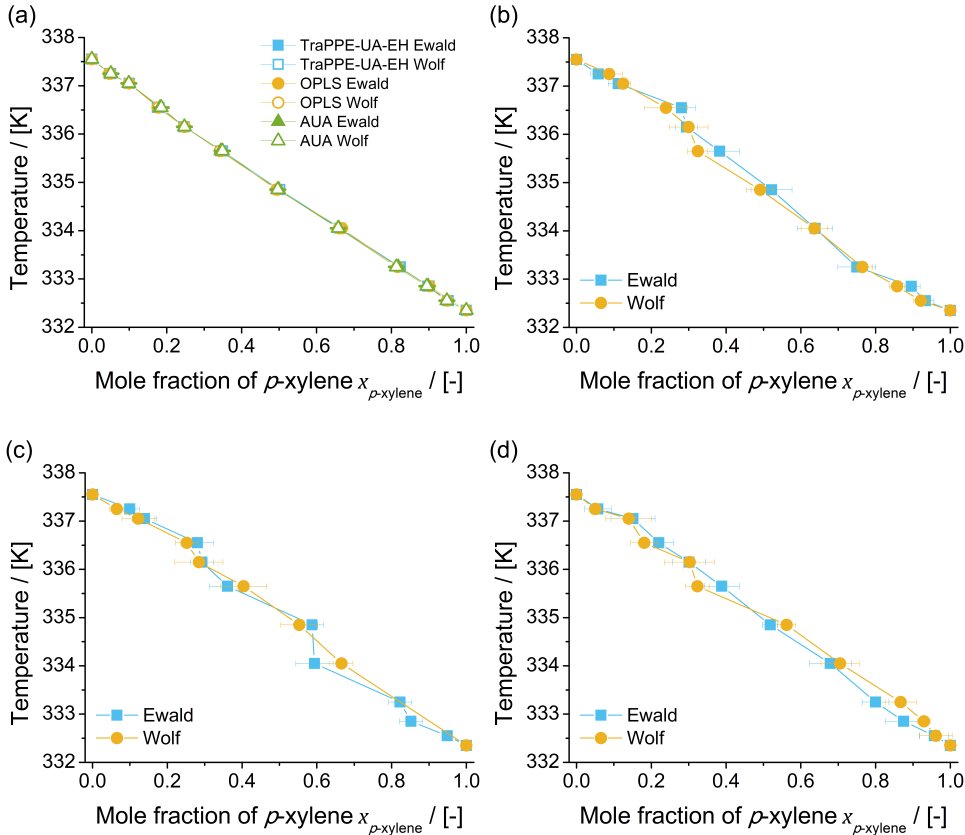


Figure 2.6: Phase composition diagrams of the p-xylene/o-xylene binary mixture at 6.66 kPa using the Wolf and Ewald methods. (a) Liquid phase composition for TraPPE-UA-EH [245, 252], OPLS [253] and AUA [248] force fields. Vapor phase composition for (b) TraPPE-UA-EH [245, 252], (c) OPLS [253], and (d) AUA [248].  $x_{p\text{-xylene}}$  is the mole fraction of p-xylene in the liquid phase.  $y_{p\text{-xylene}}$  is the mole fraction of p-xylene in the vapor phase.

be an artifact of the force field.

The excess chemical potential of *p*-xylene in the liquid phase of the *p*-xylene/o-xylene mixture at 6.66 kPa, as a function of the liquid phase composition is shown in Fig. 2.8. The reference state for the excess chemical potential is the ideal gas. The excess chemical potential computed for each force field with the Wolf and Ewald methods agree between the statistical uncertainties. The excess chemical potential of *p*-xylene in the liquid phase does not change as a function of the mole fraction of *p*-xylene. The excess chemical potential is directly related to the activity coefficient of the component in the mixture [306, 307]. The activity coefficients for *p*-xylene reported by the experimental work [263] do not show dependence on the phase composition of the mixture, which is in agreement with the excess chemical potential calculated in the simulations.

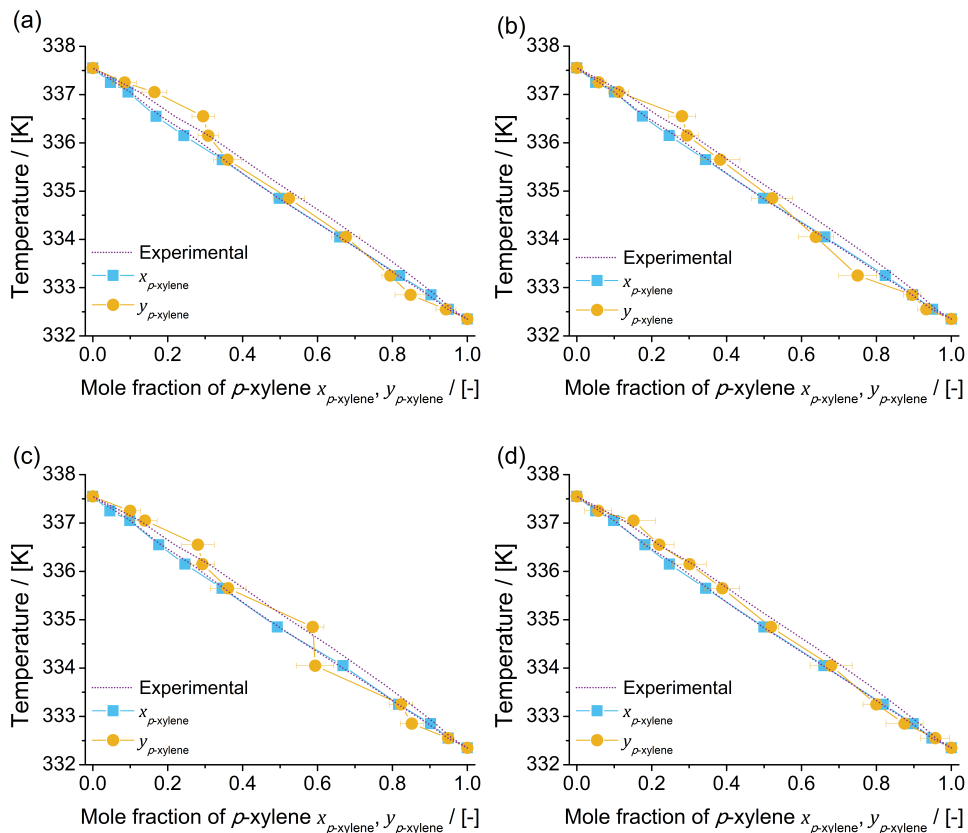


Figure 2.7: Phase diagram of the p-xylene/o-xylene binary mixture at 6.66 kPa for (a) TraPPE-UA [252], (b) TraPPE-UA-EH [245, 252], (c) OPLS [253], and (d) AUA [248], calculated using the Ewald method. Experimental data are from Llopis and Monton [263].  $x_{p\text{-xylene}}$  (blue symbols) is the mole fraction of *p*-xylene in the liquid phase.  $y_{p\text{-xylene}}$  (orange symbols) is the mole fraction of *p*-xylene in the vapor phase.

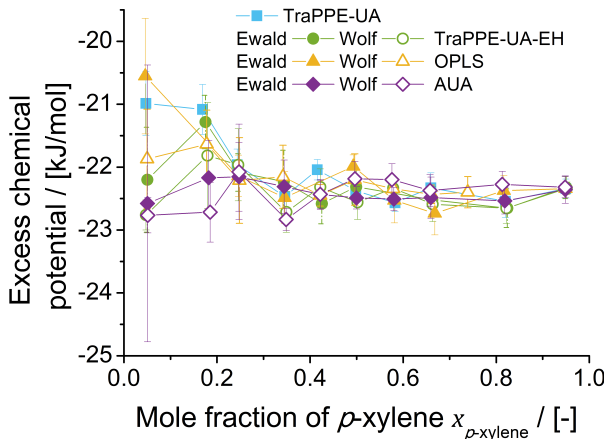


Figure 2.8: Excess chemical potential ( $\mu_e^e_{p\text{-xylene}}$ ) of *p*-xylene in the liquid phase of the *p*-xylene/*o*-xylene binary mixture at 6.66 kPa, as a function of the liquid phase composition ( $x_{p\text{-xylene}}$ ) for all force fields. Closed and open symbols denote the use of the Ewald and the Wolf methods, respectively.

The phase diagrams of the *p*-xylene/*o*-xylene binary mixture at 81.3 kPa simulated using the Ewald summation for all the force fields and experimental data [265] are shown in Fig. 2.9. The reported experimental uncertainty for the temperatures is 0.1 K. Small deviations from ideality are reported [265], and a difference between the phase compositions smaller than in the binary mixture at 6.66 kPa can be observed. The simulations of the composition of the liquid phase are in agreement with the experimental data with all the force fields. The predictions of the composition of the vapor phase agree with the experiments when the mole fraction of *p*-xylene is smaller than 0.5. For larger mole fractions of *p*-xylene (i.e. when the mixture has more *p*-xylene than *o*-xylene), the predicted composition of the vapor phase is the same as for the liquid phase. The simulations suggest that for the tested force fields, the predictions of the composition of the vapor phase are predominantly represented by the properties of the component with the largest mole fraction in the liquid phase. The accuracy of the calculations are related to how well the densities can be calculated for the pure components. The differences on the estimation of the density of *o*-xylene as a pure component play a significant role in the determination of the VLE of binary mixtures of xylenes.

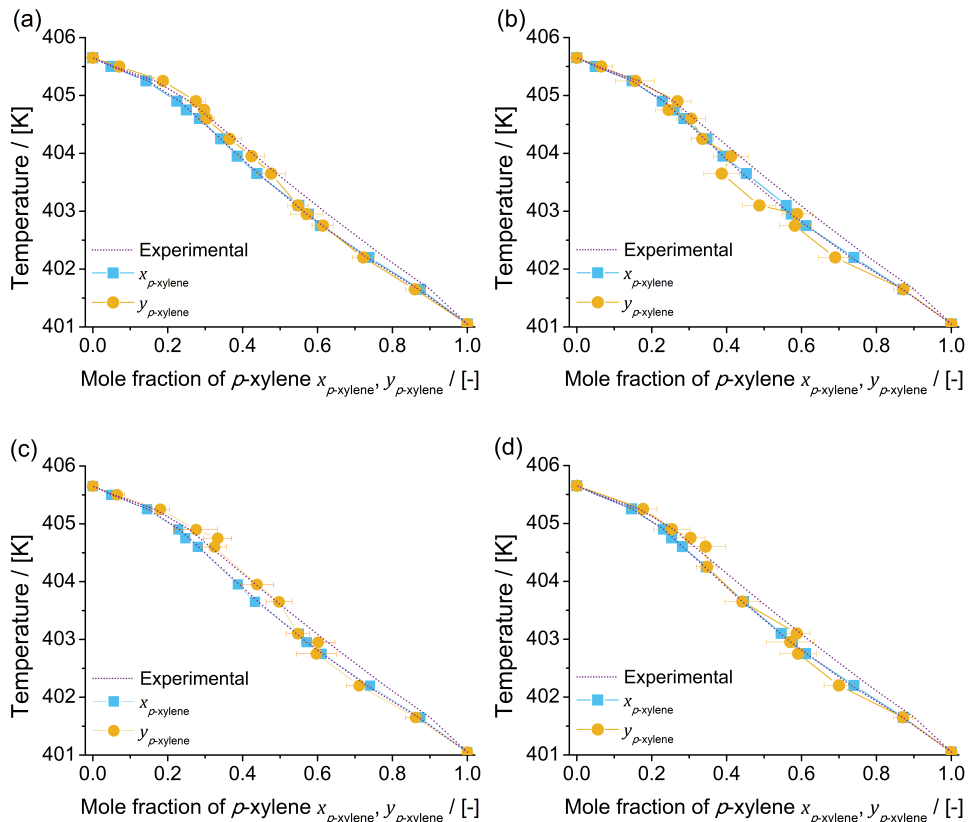


Figure 2.9: Phase diagram of the p-xylene/o-xylene binary mixture at 81.3 kPa for (a) TraPPE-UA [252], (b) TraPPE-UA-EH [245, 252], (c) OPLS [253], and (d) AUA [248], calculated using the Ewald method. Experimental data are from Parvez et al. [265].  $x_{p\text{-xylene}}$  (blue symbols) is the mole fraction of *p*-xylene in the liquid phase.  $y_{p\text{-xylene}}$  (orange symbols) is the mole fraction of *p*-xylene in the vapor phase.

## 2.4. CONCLUSIONS

The VLE of xylenes as a single components and binary mixtures have been calculated using the Wolf and Ewald methods. Comparable results using the Wolf and the Ewald methods can be obtained for the prediction of densities and the phase compositions of binary mixtures. With the Wolf method, up to 50% less CPU time is used compared to the Ewald method, at the cost of accuracy and additional parameter calibration. The performance of the considered force fields to predict the VLE of xylene isomers as pure component has been tested. The TraPPE-UA and AUA force fields provide a reasonable estimate of the experimentally determined densities for *p*-xylene and *m*-xylene. The largest differences with experimental data are observed in the calculations of the vapor density of *o*-xylene. The use of the TraPPE-UA force field yields the best prediction of the experimental density of *o*-xylene. Simulations of *p*-xylene/*o*-xylene binary mixtures at 6.66 and 81.3 kPa are in excellent agreement with the experimental data for the liquid phase composition. The accuracy of the phase composition predictions are related to the quality of the density predictions of the pure component systems. The experimental vapor phase composition is not well predicted by the simulations. This is related to the deviations observed for the prediction of the vapor density of *o*-xylene as a pure component. The simulations have shown the potential to accurately predict the phase compositions of such binary mixture, but the development of force fields that predict the VLE of each xylene isomer more accurately -especially *o*-xylene- is needed. The binary systems of xylenes are very sensitive to the slight density differences in the vapor phase of each xylene isomer and how well these are captured by the force fields.

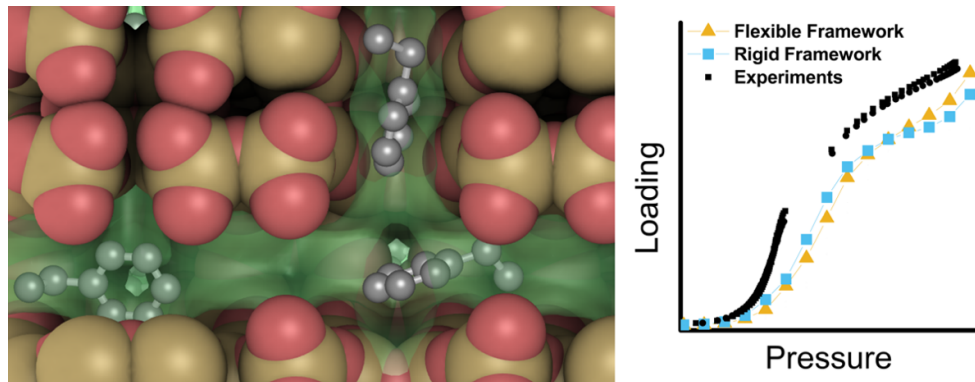


# 3

## EFFECTS OF MODELS FOR FRAMEWORK FLEXIBILITY ON THE ADSORPTION OF AROMATICS IN MFI-TYPE ZEOLITES

This chapter is based on the article:

S. Caro-Ortiz, E. Zuidema, D. Dekker, M. Rigutto, D. Dubbeldam, T. J. H. Vlugt, *Adsorption of aromatics in MFI-type zeolites: Experiments and framework flexibility in Monte Carlo simulations*, *J. Phys. Chem. C* **124**, 21782 (2020) [204].



### 3.1. INTRODUCTION

Knowledge of the adsorption behavior of hydrocarbons in the pores of zeolites is important for the understanding of the catalytic activity of the zeolite [130, 144, 145]. Many industrial processes such as the separation of xylenes, disproportionation of toluene, ethylbenzene dealkylation, strongly rely on the interaction of hydrocarbons within a zeolite [308–311].

3

Zeolites are commonly considered as very rigid structures as their atomic bonds and angles are highly constrained [312, 313]. An inflection point in the adsorption isotherm reflects either that molecules start to fill a new adsorption site [314, 315], and/or that there is a structural change in the zeolite due to the number of adsorbed molecules [316–318] or the temperature [319, 320]. Adsorption of aromatics in MFI-type zeolites is a typical example of a mix of such factors [321]. Talu et al. [316] described the isotherm shapes for benzene, toluene, and *p*-xylene, adsorbed in MFI-type zeolites. It is reported that with increasing temperature the isotherm shape changes from type IV to type I [316]. The observable kink in the isotherm at lower temperatures disappears at temperatures higher than 80°C [316]. The all-silica form of the MFI-type zeolite (silicalite) is known to show a monoclinic or orthorhombic structure depending on the temperature and loading [322, 323]. Van Koningsveld et al. [324] identified three structures of the *p*-xylene/silicalite system: Mono (monoclinic), Ortho (orthorhombic) and Para (also orthorhombic). Very small structural differences are observed between the Ortho and Para lattices [174]. The silicalite/*p*-xylene system is known to have the Ortho structure when the loading is lower than 4 molec./uc [324]. At 8 molec./uc, the silicalite/*p*-xylene system shows the Para structure [322]. Sacerdote et al. [325] reported that silicalite loaded with benzene, toluene or ethylbenzene shows a Mono structure for loadings lower than 4 molecules/unit cell. Sorenson et al. [326] reported that benzene loading does not cause a significant change in the unit cell volume of silicalite. *o*-xylene and *m*-xylene do not access nor cause significant deformations to the zigzag channels relative to the room-temperature empty Mono framework [327]. *o*-xylene is located exclusively in the intersections of the channels at 273 and 315 K [328]. Several experimental studies that describe the adsorption of aromatics in MFI-type zeolites can be found in literature [316, 322, 325, 327–340].

The adsorption of aromatics in MFI-type zeolites has also been studied by molecular simulations. Commonly, Monte Carlo (MC) simulations in the grand-canonical ensemble (GCMC) are used to compute sorbate loadings as a function of temperature and pressure in a zeolite framework [197–199]. Several studies where MC is used to investigate adsorption of aromatics in MFI-type zeolites can be found in literature [135, 200–203, 341–349]. Snurr et al. [200] computed adsorption isotherms of benzene and *p*-xylene in MFI-type zeolites. Large differences in the loadings are found when using the MFI Ortho and Para structures. It is shown that below 4 molecules/unit cell, benzene and *p*-xylene are adsorbed in the intersections of the Ortho structure. Molecules in the intersections are too far apart to strongly interact with each other. The molecules are also located in the channels at higher loadings, allowing sorbate/sorbate interactions [200]. Torres-Knoop et al. [201] reported simulations of adsorption of ethylbenzene and styrene in the Para form of

MFI-type zeolite at 433 K. It is observed that close to saturation conditions, styrene can be located in the zigzag channel. At the same conditions, ethylbenzene suffers from size exclusion effects. Therefore, it is located exclusively in the intersections of the channels. Mohanty et al. [342] reported GCMC simulations of *p*-xylene and *m*-xylene in silicalite. These authors found that *p*-xylene adsorption selectivity over *m*-xylene is due to the difficulty of *m*-xylene to access the adsorption sites of the framework in comparison to *p*-xylene. The large energetic difference between *p*-xylene and *m*-xylene is the primary reason for *p*-selectivity.

Computer simulations of the adsorption of hydrocarbons in zeolites are typically performed using rigid zeolite frameworks [186, 197, 216]. Clark and Snurr [217] performed simulations of the adsorption of benzene in the Ortho and Para structures of silicalite at 343 K. The simulations showed that the computed loadings are very sensitive to small differences in the atom positions of the zeolite. It is found that the Henry coefficient of benzene in the Ortho structure described by Olson et al. [350] is 3.1 times larger than in the Ortho structure described by van Koningsveld et al. [351]. The mean and maximum differences of the atomic positions of these two Ortho structures are only 0.11 Å and 0.41 Å, respectively. It is suggested that interactions that include lattice flexibility and polarizability are required to simulate systems where molecules fit tightly in the pores [217, 218].

Only a limited amount of studies have approached the simulations of adsorption using a flexible zeolite framework. García-Pérez et al. [219] and Sánchez-Gil et al. [220] studied argon adsorption in MFI and MEL, respectively. García-Sánchez et al. [221] described the loadings of methane in LTA. Fang et al. [222] considered framework flexibility for the adsorption of CO<sub>2</sub> in an ammonium MFI-type zeolite. It is observed that the overall effect of framework flexibility is small for the adsorption of CO<sub>2</sub> in the zeolite structure. Vlugt et al. [216, 223] reported the effect of flexibility in the adsorption of n-alkanes and cycloalkanes in a MFI-type zeolite. It is found that for molecules with an inflection behavior in the isotherm, the influence of the flexibility seems to be larger than for molecules without such inflection. The influence of the flexibility on the adsorption of cyclohexane is similar to n-alkanes [223].

Framework flexibility has also been studied in other porous materials [352–359]. Witman et al. [360] studied the effect of framework flexibility on the separation of Xe/Kr mixtures in ~3000 Metal-Organic Frameworks (MOFs). A model that predicts the Henry regime adsorption of each framework and selectivity as a function of framework flexibility is used. The results of this study suggest that the selectivity of the Xe/Kr mixtures can be increased or decreased up to two orders of magnitude when unit cell volume changes are allowed [360]. Agrawal and Sholl [361] examined the adsorption of nine molecules and four mixtures in 100 MOFs. It is observed that adsorption selectivities can be significantly affected by framework flexibility. It is suggested that including framework flexibility is important when attempting to make quantitative predictions of adsorption selectivity in MOFs. Heinen and Dubbeldam [362] review in depth the prospects of development of force fields for framework flexibility in MOFs. In this review it is shown that there is an urgent need for efficient sampling schemes that capture stimuli-driven phase transitions.

This limits the predictive capacity of existing force fields for framework flexibility in MOFs [362].

This chapter explores how the inclusion of framework flexibility in a model affects the adsorption of aromatic hydrocarbons in MFI-type zeolites. Structural changes of MFI-type zeolites (i.e. Mono to Ortho/Para transition) imply small geometry and volume changes in the framework unit cell [326, 363] that are not considered in this work. Instead, framework flexibility aims to study local changes of the MFI-type zeolite framework induced by the presence of guest molecules. Computations of adsorption of n-heptane, ethylbenzene, and xylene isomers are performed in three MFI-type zeolite structures. Several models are considered to describe the flexibility of the zeolite framework. The simulations of n-heptane adsorption aim to investigate if the details of framework flexibility play any role on a system known to be well reproduced with a rigid zeolite structure [364]. Experimental data of adsorption of ethylbenzene in a MFI-type zeolite at 353 K is presented. The new experimental data shows higher loadings than in previously reported isotherms in literature. Pore size distributions are computed to investigate the effect that framework flexibility induces in the MFI-type zeolite structures. The experimental and simulation procedure are explained in Section 3.2. The results of experiments, computed pore-size distributions, and computed loadings are reported and discussed in Section 3.3. It is shown that the intra-framework interactions in flexible framework models induce small but important changes in the atom positions of the zeolite, and hence in the adsorption isotherms. The current challenges to model and predict reliable molecular insight about the system are also discussed in Section 3.3. Our concluding remarks regarding the influence of the force fields for framework flexibility on the adsorption of aromatics in MFI-type zeolites are discussed in Section 3.4.

## 3.2. METHODS

The adsorption computations are performed using the Continuous Fractional Component Monte Carlo (CFCMC) [240–242] algorithm in the grand-canonical ensemble. The RASPA software [22, 365, 366] is used for all simulations. Periodic boundary conditions are applied to a simulation box consisting of 2x2x3 unit cells of MFI-type zeolite. The all silica structures described by van Koningsveld et al. (Mono [363], Ortho [351], Para [324]) are considered. The adsorption of aromatics is computed for the three structures. The Ortho structure is used for n-heptane adsorption simulations. A cutoff radius of 14 Å is applied for all Lennard-Jones (LJ) interactions and analytic tail corrections are used [292, 367]. The interactions between different atom types are obtained using Lorentz-Berthelot mixing rules [292]. The Ewald summation [274] with a relative precision of  $10^{-6}$  is used to account for the long-range electrostatic interactions. In the CFCMC algorithm, the interactions of a fractional molecule are scaled by the  $\lambda$  parameter in the range 0 to 1 (0 for no interactions with surrounding molecules/framework and 1 for full interaction with surrounding molecules/framework). Fig. 3.1 shows how a toluene molecule can be inserted/deleted in the straight channel of an MFI-type zeolite using the CFCMC method.

A MC cycle consists of  $N$ -trial moves with a minimum of 20, with  $N$  being the number of molecules in the system [365]. At each MC cycle, trial moves attempt to rotate, displace, randomly reinsert, and insert adsorbates. Also,  $\lambda$ -trial moves scale the interactions of the fractional molecule (via the CFCMC algorithm [240, 241]). The simulations are started with  $10^5$  MC cycles to initialize the system. The initialization run only allows translation, rotation and insertion trial moves. After that, a stage of  $4 \cdot 10^5$  MC cycles are used to equilibrate the system. All the considered types of trial moves are allowed and the biasing factors for the  $\lambda$ -trial moves of the CFCMC algorithm are calculated.  $\lambda$ -trial moves are biased to obtain a flat  $\lambda$  probability distribution. The use of this trial move is advantageous as it enables an efficient insertion and deletion of sorbate molecules in the system [243, 295]. Ensemble averages are obtained in a  $5 \cdot 10^5$  MC cycles production stage. The reported errors account for the 95% confidence interval calculated by dividing the production run into five parts. An extra MC trial move is included to simulate a flexible zeolite framework, which attempts a random displacement to a randomly selected zeolite atom [216]. Since the volume of the simulation box is fixed, the equilibrium framework density is not affected by framework flexibility.

Force fields that model the flexibility of the zeolite framework (host-host interactions) are commonly based on the description of vibrational properties, such as the infrared spectra of the zeolite atoms [368, 369], and/or ab initio quantum chemical calculations [370, 371]. Several force fields for framework flexibility have been reported in literature [312, 370–378]. Such force fields are typically used in the calculations of diffusion of aromatics in MFI-type zeolites by molecular dynamics simulations [137, 379, 380]. Some sets of zeolite intra-framework interactions only include harmonic potentials between the zeolite atoms, while others also add a combination of LJ and partial charges. Polarization of the zeolite atoms can also be added by using the core-shell method [381]. In this method typically the oxygen atoms of the zeolite are separated into cores and shells [382–384]. Phase transitions and negative thermal expansion can be studied using this method [352]. The predicted crystal structures agree very well with crystallographic data from experiments [385]. The core-shell model requires formal charges that are higher than the partial charges based on ab initio calculations [352]. The computational time using this method is increased due to the use of more particles in the system [352].

The Nicholas [376] model, the Demontis [374] model, and the model reported by Jeffroy et al. [312] are considered for investigating the host-host force field induced effects in MFI-type zeolite frameworks. The force field parameters are listed in tables A.4, A.5, and A.6 of Appendix A.1. The Demontis model [373–375] consists on describing the flexibility of the zeolite only by Si-O bond stretching and O-Si-O Urey-Bradley potentials. More details regarding the Demontis model are discussed in chapter 4. The Nicholas model [376] includes intra-molecular (1-4) LJ and electrostatic interactions, besides torsional, bond-bending, and bond-stretching potentials. The model by Jeffroy et al. [312] is a transferable force field able to predict the structure of zeolites including extra-framework cations. The host-host interactions are determined by electrostatic interactions, bond-stretching, and bend-angle parameters.

3

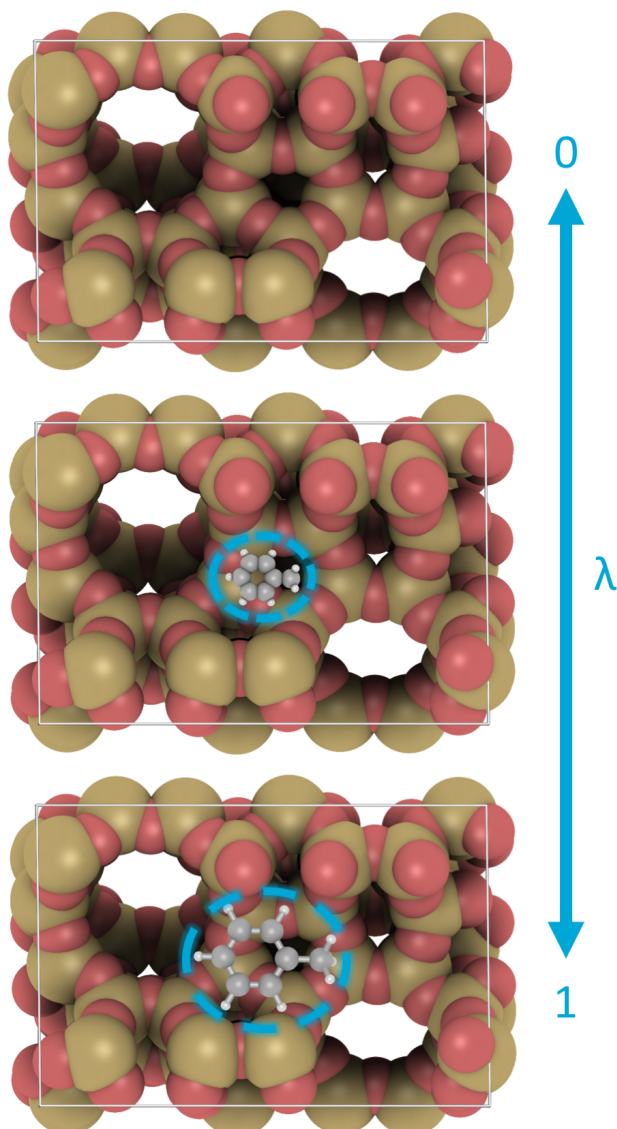


Figure 3.1: Insertion/deletion of a fractional toluene molecule in the straight channel of MFI-type zeolite using the CFCMC algorithm. In this method, a trial move attempts to scale the interactions of a fractional molecule by the so-called  $\lambda$  parameter. The  $\lambda$  parameter is changed by a random value in the range 0 to 1 (0 for no interactions with surrounding molecules/framework and 1 for full interactions with surrounding molecules/framework).

There is a distribution of bond lengths and angles in MFI-type structures from crystallography [324, 351, 363]. The Nicholas model, the Demontis model, and the model by Jeffroy et al. use constant equilibrium bond lengths and angles. The so-called modified form of these models take the equilibrium bond lengths and bend-angles (in the Urey-Bradley term) directly from the crystallographic structure to which the model is applied [216]. As discussed in the following section, this modification is used to avoid large deviations from the experimental crystal structure. In this work, the modified Nicholas [376] model and the modified Demontis [374] model are used for the simulations of adsorption of aromatics.

To take into account the effect that the host-host interactions have on the zeolite structure, an optimization of the atom positions of the zeolite framework at 0 K with the flexible force field is performed. The structure with atom positions optimized is obtained using the mode-following minimization method [386, 387] for each initial experimental zeolite topology subject to the host-host force field. The Pore-size distribution (PSD) of the structures with atom positions optimized at 0 K using each host-host force field is calculated geometrically with the method of Gelb and Gubbins [388, 389]. The MFI-type zeolite atom positions are optimized at 0 K with the Demontis model [374], the Nicholas model [376], and the model reported by Jeffroy et al. [312], as well as the modified forms of each force field. The PSD is also calculated for each of the MFI-type zeolite lattices from crystallographic data. Henry coefficients of ethylbenzene in the MFI-type structures are calculated via the Widom test-particle insertion method [390].

The interactions between the zeolite and guest hydrocarbons (host-guest interactions) are described using several force fields [391–397]. The host-guest force fields are usually obtained by fitting the parameters to experimental data [144], such as adsorption isotherms. The TraPPE-zeo model [396] is used in this work. In this force field, all oxygen and silicon atoms are modeled with Lennard-Jones interactions and partial charges. The development of this force field is focus on transferability and variety of zeolite/guest systems [396]. As such, it is fitted to match the experimental adsorption isotherms of n-heptane, propane, carbon dioxide, and ethanol in zeolites. The partial charges of the zeolite atoms are a critical parameter for the force fields and adsorption [398, 399]. Typical partial charges for silicon atoms have been reported in the range of +0.5 to +4 e [400]. The host-guest electrostatic interactions from TraPPE-zeo [396] (+1.5 and -0.75 e for Si and O, respectively) are fitted considering fixed positions of the zeolite atoms. Zeolite host-host interactions that includes electrostatics are likely to be incompatible with a guest-host force field that also include electrostatics. The combination of two types of force fields can be cumbersome. The Nicholas model, the Demontis model, and the model reported by Jeffroy et al. use different partial charges for the zeolite atoms than the TraPPE-zeo [396] force field. In this work, the electrostatic interactions of the zeolite atoms are modeled by each host-host force field used in the simulation. The interaction parameters of the TraPPE-zeo force field are listed in table A.3 of Appendix A.1. The partial charges are listed in tables A.5 and A.6 of Appendix A.1.

As discussed in chapter 2, molecular simulations of aromatics typically use force

fields (guest-guest interactions) that model the vapor-liquid equilibrium (VLE) with LJ potentials or a combination of LJ and electrostatic interactions. For aromatic species, a common practice in the development of these force fields is to fit the interaction parameters to reproduce the VLE of the pure components [245–248, 253, 297, 299], or by ab initio quantum mechanical calculations [249–251, 401].

Despite the extensive use of guest-guest force fields that use electrostatic interactions (such as OPLS [253, 297]) for the simulation of adsorption of aromatics in zeolites [200–202, 402], the electrostatic interactions are fitted for VLE and not for the interaction with a host framework. In this work, the electrostatic interactions of the zeolite atoms are modeled by each host-host force field used in the simulation. Such electrostatic interactions are not suited for the interaction with an adsorbate, but for the zeolite framework with itself. Therefore, it is convenient to use a guest-guest force field that does not explicitly use partial charges for electrostatic interaction. The uncharged TraPPE-UA [252, 403] force field is chosen for the guest-guest interactions. The TraPPE-UA is a widely used force field that is designed to reproduce the VLE of alkylbenzenes and n-alkanes, among other chemical species. The united atom approach is used by merging a carbon atom and its bonded hydrogen atoms into a single uncharged interaction site representing each  $\text{CH}_x$  group in the n-alkanes and aromatic species. Aromatics are modeled as rigid molecules, except ethylbenzene, that includes a torsional potential in the  $\text{CH}_3\text{-CH}_2\text{-CH}$  bend-angle. The force field parameters are listed in table A.2 of Appendix A.1.

### 3.3. RESULTS AND DISCUSSION

#### 3.3.1. FORCE FIELD INDUCED EFFECTS IN MFI-TYPE ZEOLITES

The effect of each host-host force field on the zeolite pores can be observed in the Pore-size distribution. The PSD of MFI-type zeolite structures with atom positions optimized at 0 K using the Demontis [374] model, the Nicholas [376] model, and the model reported by Jeffroy et al. [312] are calculated. The PSDs are compared with the PSD computed for each experimental crystal structure. The modified form of each force field is also included. As an example, Fig. 3.2 shows the visible differences in the MFI Para structure when using constant equilibrium bond lengths in the Demontis model, compared to the modified Demontis model. For the modified Demontis model, the experimental crystal structure is exactly reproduced when  $T \rightarrow 0$  K. With the original Demontis model, atomic positions are shifted and the shape of the straight channel changes to an oval shape. Fig. 3.3 shows the Si-O bond length distribution of the MFI Para structure from crystallography [324] and the MFI Para structure with atom positions optimized at 0 K using the original Demontis model. The Si-O bond lengths of MFI Para structure from experiments [324] range from 1.58194 to 1.61089 Å. The Si-O bond length distribution of the MFI Para structure with atom positions optimized using the original Demontis model ranges from 1.60398 to 1.60427 Å. The fixed equilibrium bond lengths of the original Demontis model significantly reduce the bond length range. The shape and atom position changes shown in Fig. 3.2 are caused by the use of fixed equilibrium bond lengths and angles and the reduction of the bond length range.

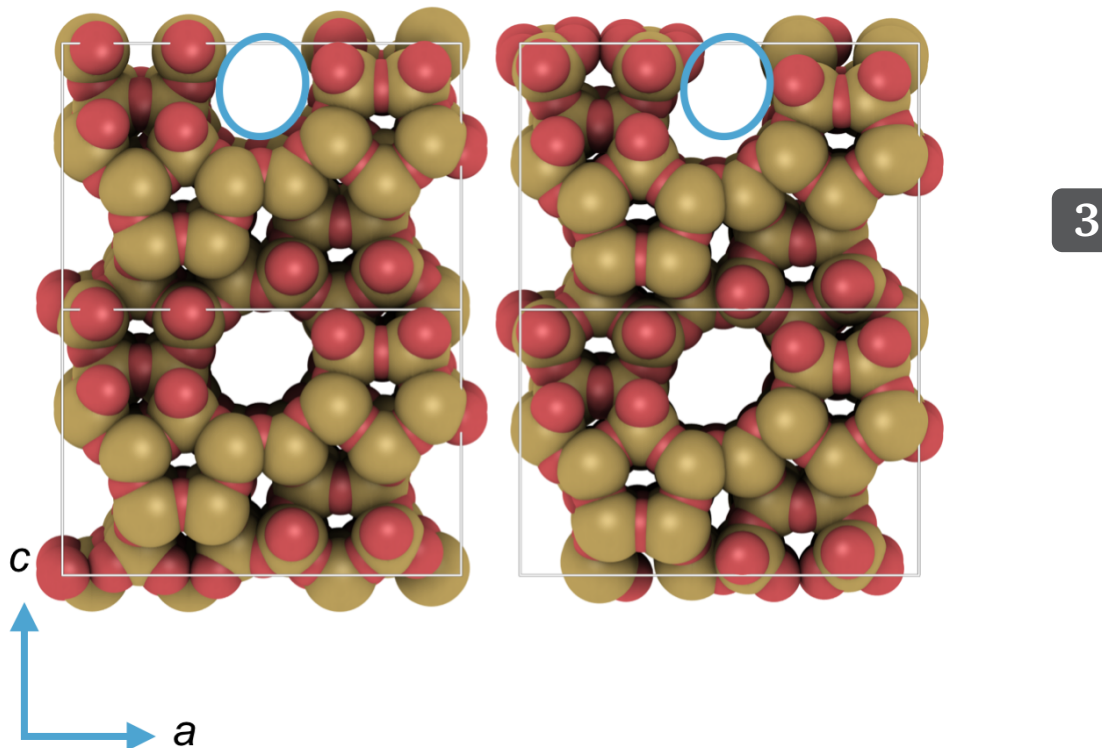


Figure 3.2: Minimum-energy atomic configuration of MFI Para structures with atom positions optimized at 0 K using the modified Demontis model (left) and the original Demontis [374] model (right). The minimum-energy structure exactly reproduces the experimental crystal structure [324] when using the modified Demontis model. The blue ring is the same in both structures. The blue ring highlights differences in the atomic position and the change of shape of the straight channel caused by the use of fixed equilibrium bond lengths with the original Demontis model.

The PSD of MFI-type zeolite structures with atom positions optimized at 0 K using the Demontis [374] model, the Nicholas [376] model, and the model reported by Jeffroy et al. [312] are shown in Figs. 3.4, 3.5, and 3.6. In a PSD of MFI-type zeolites, the peak centered at a diameter of approximately 4 Å corresponds to the zigzag and straight channels. The peak centered at a diameter of approximately 5.5 Å corresponds to the intersection of the channels. Using the Demontis model, significant differences can be observed in the PSD of the Ortho structure. The PSD shows a new peak at a diameter smaller than 4 Å, suggesting that the channels decreased its size. This change in the structure is exclusively related to the use of constant bond lengths and angles. In the Mono and Para structures, the shift of the peak shows that the intersections are smaller.

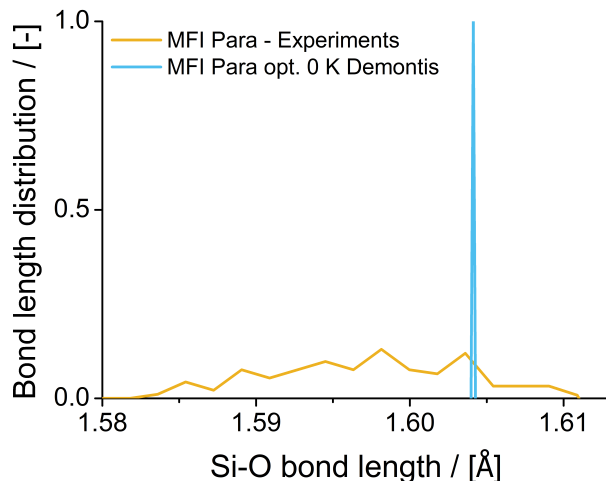


Figure 3.3: Si-O bond length distribution of the MFI Para from the structure from experiments [324] and from the MFI Para minimum-energy structure obtained optimizing the atomic positions at 0 K using the Demontis [374] model. The original Demontis [374] model uses fixed equilibrium Si-O and O-(Si)-O bond lengths. The Si-O bond length distribution of the MFI Para structure with atom positions optimized at 0 K with the modified Demontis model exactly reproduces the Si-O bond length distribution from experiments.

When the Nicholas model and its modified form are used, the PSDs of the Mono structure do not show significant deviations from the experimental structure. The Nicholas model and the modified form induce an expansion of the intersections in the Ortho structure. The peak corresponding to the intersection is shifted approximately +0.5 Å. In the Para structure, the peaks corresponding to the intersections and the channels are shifted approximately 1 Å. This means that the pores are significantly larger than in the Para structure from experiments. As the original and modified forms of the Nicholas model show similar shifts of the pore-size peaks, these shifts can be related to the LJ and the strong electrostatic interactions accounted in the optimization of the atom positions with the force field.

The model presented by Jeffroy et al. [312] induces significant differences in the Ortho structure. The channels are smaller, while the intersections are expanded. The peak corresponding to the channels is shifted approximately -0.5 Å. The peak corresponding to the intersections is shifted approximately +0.5 Å. In addition, the intersections of the Para structure approximately 0.5 Å (in diameter) larger than in the crystal structure from experiments. The modified form of this model shows better agreement with the PSD of the experimental Mono and Ortho structures. A mean displacement of 0.462 Å of the atoms in the Para structure suggest that the zeolite structure is significantly influenced by the force field.

Table 3.1 lists the mean and maximum displacements atomic position induced by each of the host-host force fields, and the Henry coefficient of ethylbenzene at 353 K in the MFI-type structures. The displacements suggest that taking the equi-

librium bond distances and angles from the experimental crystal structure reduces the deformation induced by the host-host force field in the structure. Clark and Snurr [217] observed that a mean displacement of 0.11 Å of the zeolite atoms is enough to significantly influence the adsorption of benzene in MFI-type zeolites. In this work, all mean displacements accounted in the optimized structures at 0 K with the modified forms of the force fields are higher than 0.11 Å (except for the modified Demontis model). Henry coefficients of ethylbenzene significantly vary within MFI-type zeolite structures. For the crystal structures from experiments, the Henry coefficients of ethylbenzene in the Mono and Ortho structure are similar, and larger than in the Para structure.

Significant differences can be observed using the modified and original host-host force fields. For the original Demontis [374] model in the Para structure, the Henry coefficient of ethylbenzene is 3.4 times smaller than when taking the equilibrium bond lengths directly from the crystal structure from experiments in the modified Demontis model. This suggests that Henry coefficients (and hence adsorption) of ethylbenzene in MFI-type zeolites are very sensitive to small deviations in the atom positions of the zeolite framework.

3

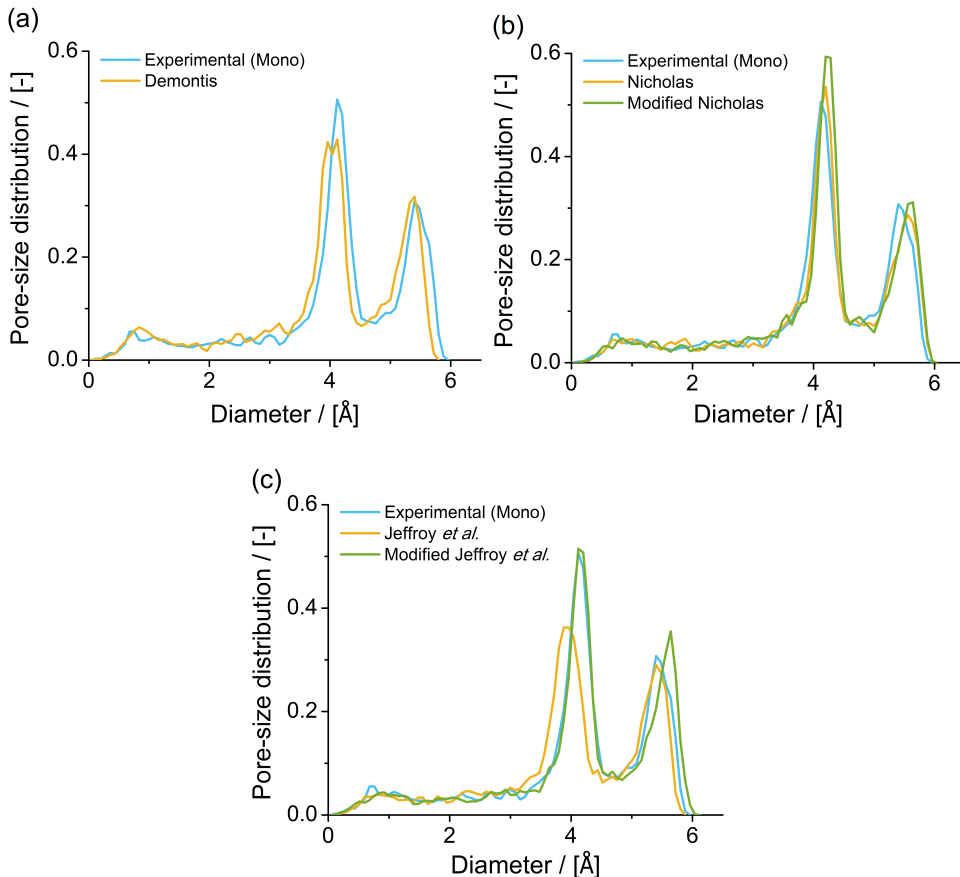


Figure 3.4: Pore-size distributions (PSD) of the MFI Mono structures with atom positions optimized at 0 K using the (a) Demontis [374] model, (b) the original and the modified Nicholas [376] model, and (c) the original and the modified model by Jeffroy et al. [312]. Experiments correspond to the PSD computed in lattices from experiments [363]. In a PSD of MFI-type zeolites, the peak centered at a diameter of approximately 4 Å corresponds to the channels. The peak centered at a diameter of approximately 5.5 Å corresponds to the intersection of the channels.

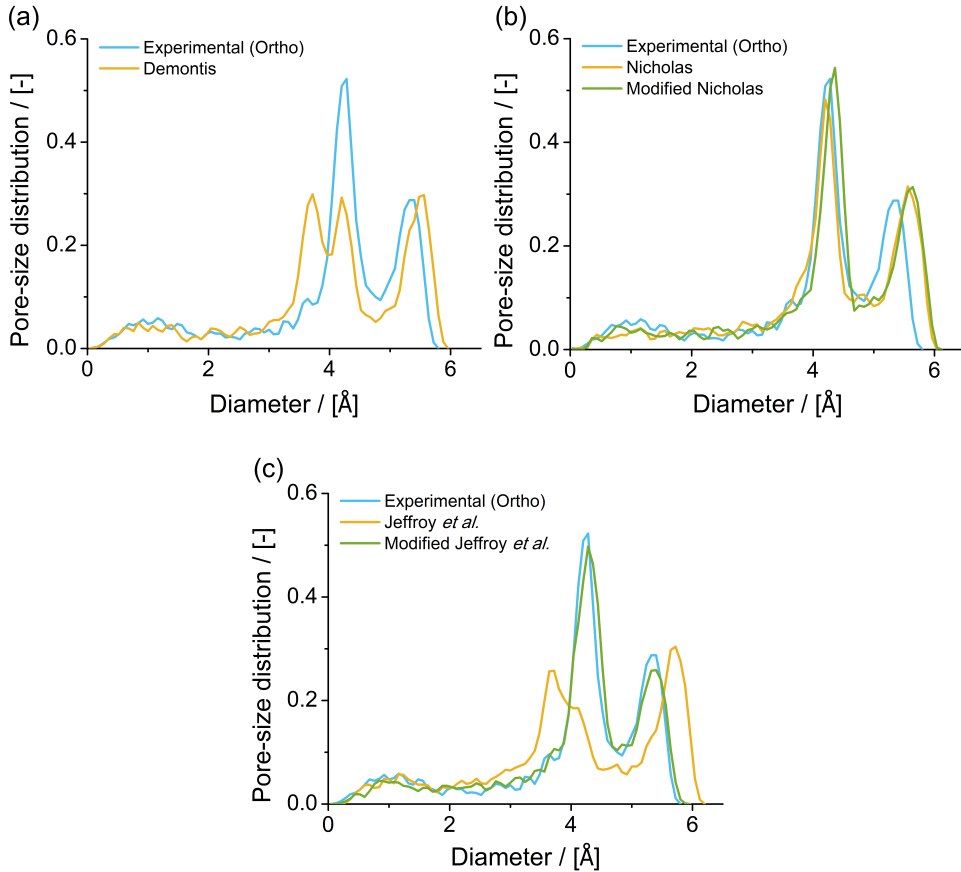


Figure 3.5: Pore-size distributions (PSD) of the MFI Ortho structures with atom positions optimized at 0 K using the (a) Demontis [374] model, (b) the original and the modified Nicholas [376] model, and (c) the original and the modified model by Jeffroy et al. [312]. Experiments correspond to the PSD computed in lattices from experiments [351]. In a PSD of MFI-type zeolites, the peak centered at a diameter of approximately 4 Å corresponds to the channels. The peak centered at a diameter of approximately 5.5 Å corresponds to the intersection of the channels.

3

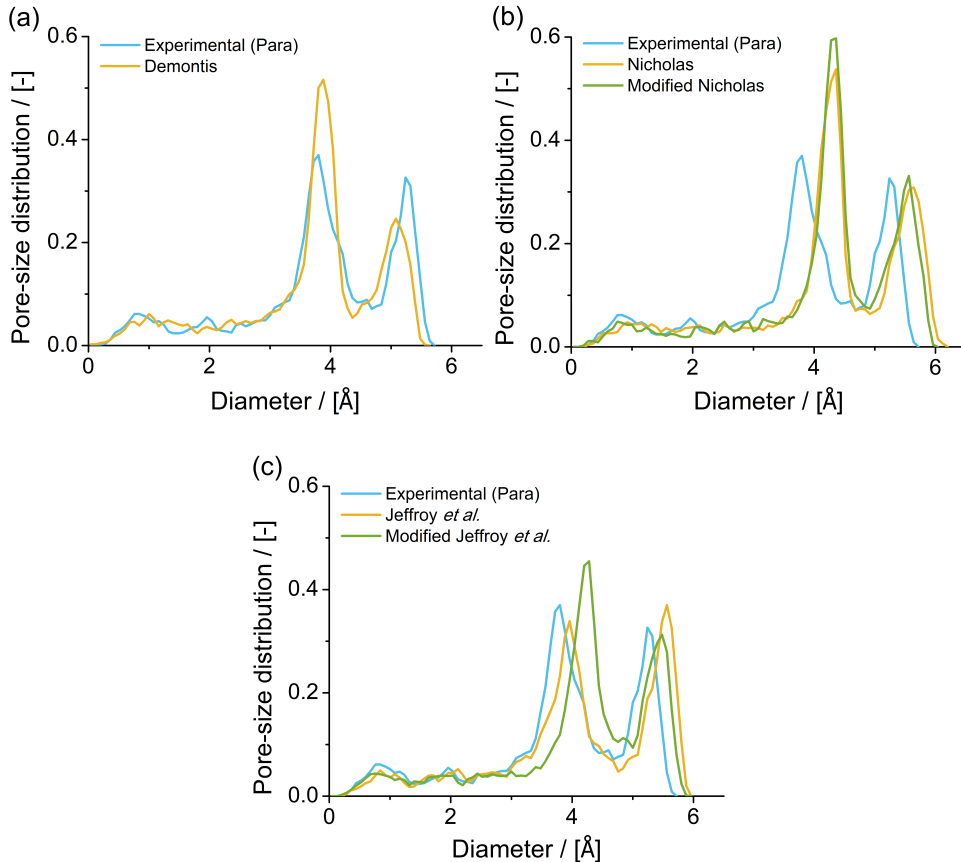


Figure 3.6: Pore-size distributions (PSD) of the MFI Para structures with atom positions optimized at 0 K using the (a) Demontis [374] model, (b) the original and the modified Nicholas [376] model, and (c) the original and the modified model by Jeffroy *et al.* [312]. Experiments correspond to the PSD computed in lattices from experiments [324]. In a PSD of MFI-type zeolites, the peak centered at a diameter of approximately 4 Å corresponds to the channels. The peak centered at a diameter of approximately 5.5 Å corresponds to the intersection of the channels.

Table 3.1: Mean and maximum displacement [ $\text{\AA}$ ] of the atomic positions between the experimental MFI-type structures, the rigid structure with atom positions optimized at 0 K using the host-host force fields, and the modified forms.  $K_{\text{H,eb}}$  is the Henry coefficient of ethylbenzene at 353 K in the MFI-type structures with atom positions optimized at 0 K using the host-host force fields and the modified forms. The Henry coefficient of ethylbenzene in the MFI-type structures with atom positions optimized at 0 K using the modified Demontis [374] model correspond to the Henry coefficient in the crystal structure from experiments. The numbers between round brackets denote the statistical uncertainties in the last digit.

	Mono			Ortho			Para		
	Mean / [ $\text{\AA}$ ]	Max / [ $\text{\AA}$ ]	$K_{\text{H,eb}} /$ [mmol/kg Pa]	Mean / [ $\text{\AA}$ ]	Max / [ $\text{\AA}$ ]	$K_{\text{H,eb}} /$ [mmol/kg Pa]	Mean / [ $\text{\AA}$ ]	Max / [ $\text{\AA}$ ]	$K_{\text{H,eb}} /$ [mmol/kg Pa]
Demontis [374]	0.211	0.582	14.9(11)	0.282	0.679	13.9(5)	0.315	0.786	3.6(3)
Mod. Demontis [374]	0.000	0.000	24.3(11)	0.000	0.000	26.1(24)	0.000	0.000	12.3(8)
Nicholas [376]	0.216	0.511	24.6(13)	0.229	0.497	30.9(15)	0.455	1.081	25.8(9)
Mod. Nicholas [376]	0.164	0.449	30.3(10)	0.189	0.536	44.2(15)	0.342	0.611	31.1(9)
Jeffroy et al. [312]	0.271	0.658	9.8(3)	0.419	1.065	10.8(4)	0.475	1.238	13.2(4)
Mod. Jeffroy et al. [312]	0.137	0.311	29.8(13)	0.226	0.656	27.8(20)	0.462	1.109	22.4(11)

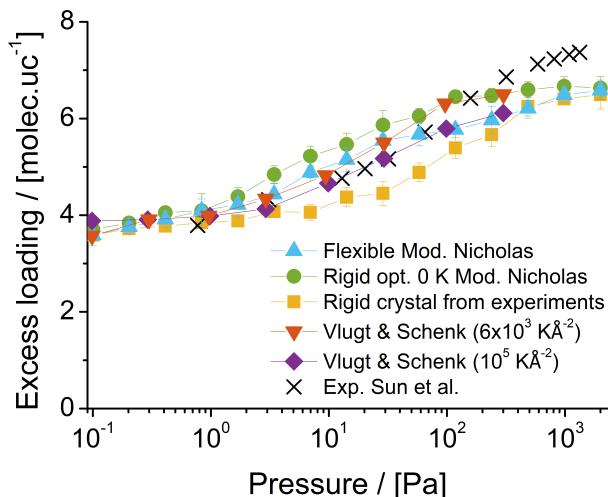


Figure 3.7: Adsorption isotherm of n-heptane in MFI Ortho at 303 K. Experimental data from Sun et al. [404]. Crossed symbols denote the experimental data. Upside down triangle and diamond denote the simulations by Vlugt and Schenk [216]. Triangles, circles, and squares denote simulations using the modified Nicholas [376] model, the rigid structure with atom positions optimized at 0 K with the modified Nicholas model, and the rigid crystal structure from experiments [351], respectively.

### 3.3.2. ADSORPTION OF N-HEPTANE IN MFI-TYPE ZEOLITE

The adsorption of n-heptane in MFI Ortho at 303 K is calculated using the modified Nicholas [376] model, the rigid framework with atomic positions fixed to the crystal from experiments [351] and the rigid framework with atom positions optimized at 0 K using the modified Nicholas [376] model. The adsorption isotherms are shown in Fig. 3.7. Experimental data from Sun et al. [404] is included. The simulation results by Vlugt and Schenk [216] are included. The simulation by Vlugt and Schenk [216] were performed using a modified Demontis-like model, by tuning the spring constants  $k/k_B = k_{O-O}/k_B = 0.2k_{Si-O}/k_B$ , from 6000 to 100000 KÅ<sup>-2</sup> (original Demontis [374] model:  $k_{O-O}/k_B = 51831.61$  KÅ<sup>-2</sup>). The simulations using the rigid framework slightly underestimate the amount of adsorbed molecules when the loading is higher than 4 molec./uc. Using the rigid structure with atom positions optimized at 0 K using the modified Nicholas model, the experimental loadings are slightly overpredicted. These differences between the loadings in the rigid and the rigid structure with atom positions optimized at 0 K are related to the pore size changes induced by the modified Nicholas model. The loadings computed using the modified Nicholas model are close to the experimental loadings. The isotherm computed using the modified Nicholas model is in excellent agreement with the predictions of Vlugt and Schenk [216]. All simulations underestimate the experimental loadings at high pressure. All simulated isotherms converge to the same maximum loading of approximately 6.5 molec./uc. in the studied pressure range. The simulations suggest that there is marginal contribution of the flexibility models in the

prediction of n-heptane loadings in MFI-type zeolites, as the differences are small and below the statistical uncertainties of the simulations.

### 3.3.3. ADSORPTION OF ETHYLBENZENE IN MFI-TYPE ZEOLITE

The adsorption of ethylbenzene in MFI-type zeolites at 353 K is calculated using the modified Nicholas model, the modified Demontis model, the rigid experimental lattice, and the rigid framework with atom positions optimized at 0 K with the modified Nicholas model, in the Mono, Ortho, and Para MFI-type structures. The adsorption isotherms (Si/Al ratio:  $\infty$ ) and the experimental data (Si/Al ratio: 80) from Ref. [204] are shown in Fig. 3.8. Experimental observations reported that the MFI/ethylbenzene system is in the Mono structure when the loading is lower than 4 molec./uc [322]. All simulations using the modified Demontis model reach approximately 4 molec./uc at the high pressure in the considered pressure range. All the molecules are located in the intersections of the channels.

For the Mono and Ortho structures, framework flexibility using the modified Demontis model does not show any contribution to the loadings, compared to the use of the rigid frameworks from crystallography. In the case of the Para structure, the loadings obtained with the modified Demontis model are lower than in the rigid structure at high pressure. In the Mono structure, the use of the modified Nicholas model does not show any influence of the framework flexibility when the loading is lower than 4 molec./uc, compared to the rigid structures. The ethylbenzene loading in the rigid structure with atom positions fixed to the crystal structure from experiments and the rigid structure with atom positions optimized at 0 K both reach 4 molec./uc in the considered pressure range. At 2000 Pa, loading of approximately 0.5 molec./uc higher than in the rigid frameworks are obtained. At pressures higher than 200 Pa, loadings higher than 4 molec./uc are obtained with the modified Nicholas model. When using the modified Nicholas model, the framework flexibility plays a role when loadings are higher than 4 molec./uc.

In the Ortho structure, the simulations using the modified Nicholas model and the rigid structure with atom positions optimized at 0 K predict higher loadings than in the rigid framework from crystallography. Ethylbenzene loadings reach approximately 4 molec./uc with the rigid frameworks, and slightly higher loadings with the modified Nicholas model. In the Para structure, ethylbenzene loadings are similar when using the modified Nicholas model and the rigid structure with atom positions optimized at 0 K for pressures up to 100 Pa. At 2000 Pa, the simulations with the modified Nicholas model predict loadings 0.5 molec./uc higher than in the rigid frameworks. At high pressures, the loadings in the rigid and the rigid structure with atom positions optimized at 0 K are the same. A typical snapshot of the simulation of adsorption in MFI Para using the modified Nicholas model at 353 K and 2000 Pa is included shown in Fig. 3.9. It can be observed that ethylbenzene molecules are located in the channels and in the intersections of the channels.

Obtaining higher loadings in the rigid structure with atom positions optimized at 0 K than in the rigid structure from experiments suggests that the atomic configuration of the optimized structure at 0 K can be related to the pore-size difference shown in Fig. 3.6b. The intersection of the rigid structure with atom positions op-

timized at 0 K using the modified Nicholas model are approximately 0.5 Å larger than in the rigid crystal structure from experiments.

Comparing the Mono, Ortho and Para systems, higher maximum loadings are obtained in the Para structure for all cases. The adsorption of molecules in the Mono structure is less affected by use of the modified Nicholas model at low loadings. There is a qualitatively good agreement between the simulations using the modified Nicholas model and the experimental data. For loadings lower than 4 molec./uc, the simulations using the Mono structure are in good agreement with the experiments, and the flexibility does not play a role in this regime. The loadings computed in the MFI Mono rigid structure with atom positions optimized at 0 K are closer to the experimental loadings than with the rigid structure. At loadings higher than 4 molec./uc, the simulations in the Para structure using the modified Nicholas model show a better agreement with the experiments than using the rigid frameworks and the modified Demontis model.

The adsorption of ethylbenzene in MFI-type zeolites from experiments has been reported by Song et al. [335] at 345 K (Si/Al ratio: 1338) and Schumacher and Karge [330] at 355 K (Si/Al ratio: 34). Type I isotherms are reported with a maximum loadings of approximately 4 and 3.5 molec./uc, respectively. Caro-Ortiz et al. [204] reported adsorption isotherms of ethylbenzene in MFI-type zeolite (Si/Al ratio: 80) at 353 K.

Choudhary and Srinivasan [405] studied the effect of the Si/Al ratio in the adsorption of benzene in MFI-type zeolites at 523 K. It is observed that the loadings of benzene increase with the decrease in the Si/Al ratio. Guo et al. [406] indicate that the pore size of MFI-type zeolites become smaller with increasing Si/Al ratios of the framework. This suggest that the loadings of ethylbenzene from Ref. [204] are expected to be higher than the loadings reported by Song et al. [335], and lower than the loadings reported by Schumacher and Karge [330], due to differences in the Si/Al ratio of the zeolites. Caro-Ortiz et al. [204] reported loadings over 4 molec./uc are observed at pressures higher than 40 Pa. The loadings reached 5 molec./uc at approximately 800 Pa. The maximum loading obtained is 5.21 at 1211 Pa in sample A. The loadings reported in Ref. [204] are higher than the loadings reported in the literature [330, 335]. This suggest that the differences between the loadings reported in Ref. [204] and the isotherms from literature [330, 335] are not related to Si/Al ratio differences and can be compared to simulations considering an all silica MFI-type zeolite. Caro-Ortiz et al. [204] showed that experiments reporting adsorption of aromatics in MFI-type zeolites are scarce and not always consistent under the same temperature/pressure conditions.

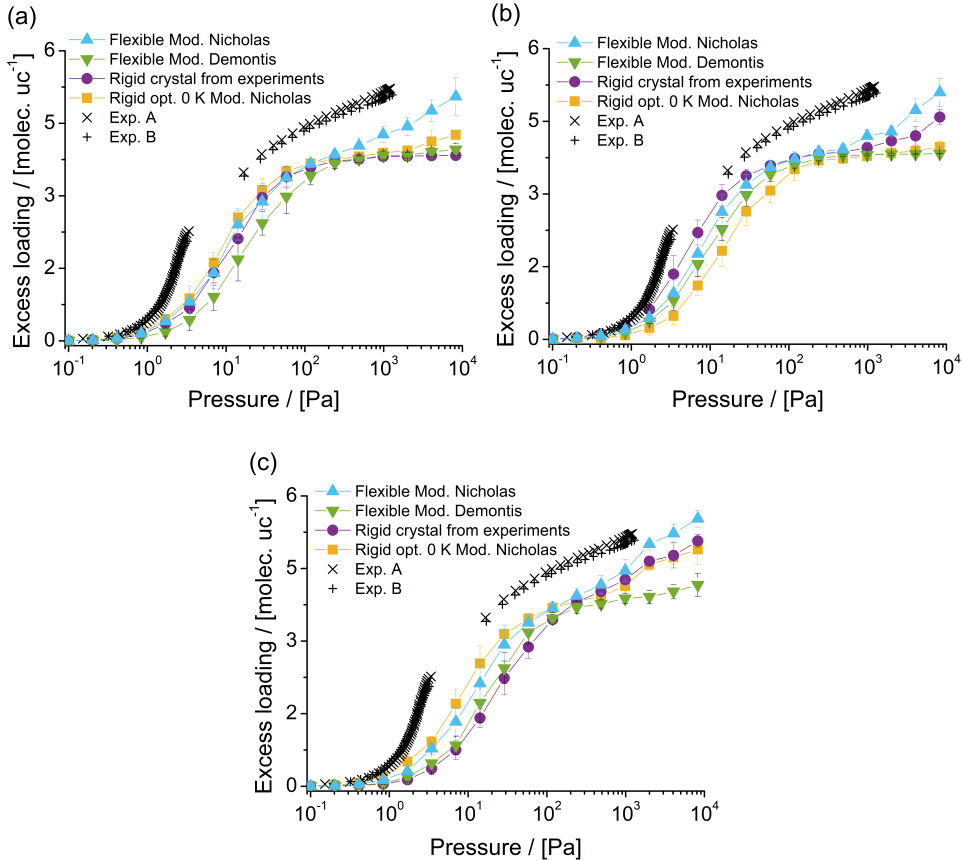


Figure 3.8: Adsorption isotherms of ethylbenzene at 353 K computed for the (a) Mono, (b) Ortho, and (c) Para structures (Si/Al ratio:  $\infty$ ). Crossed symbols denote the experimental data (Sample A and B) from Ref.[204] (Si/Al ratio: 80) . Triangles, upside down triangles, circles, and squares denote the simulations with the modified Nicholas [376] model, the modified Demontis [374] model, the rigid structure from experiments, and the rigid structure with atom positions optimized at 0 K using the modified Nicholas model, respectively.

3

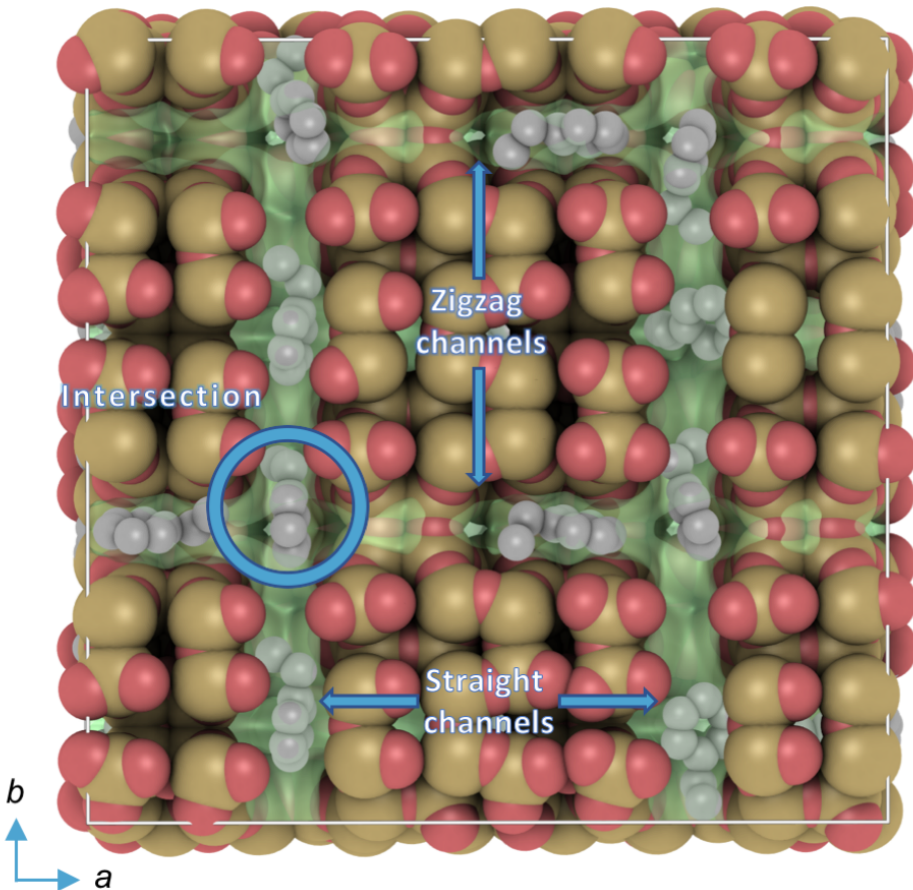


Figure 3.9: Typical snapshot of the simulation of adsorption of ethylbenzene in MFI Para using the modified Nicholas model at 353 K and 2000 Pa. An intersection of the channels is circled. Straight channels and zigzag channels are indicated with arrows. Ethylbenzene molecules are adsorbed in the channels and the intersection of the channels.

### 3.3.4. ADSORPTION OF XYLENE ISOMERS IN MFI-TYPE ZEOLITE

The adsorption of xylene isomers in MFI-type zeolites at 373 K is calculated with the modified Nicholas model, the modified Demontis model, the rigid framework and the rigid structure with atom positions optimized at 0 K with the modified Nicholas model. The adsorption isotherms are shown in Figs. 3.10, 3.11, 3.12. For *m*-xylene (Fig. 3.10) in the Mono structure, framework flexibility does not influence the isotherm. The differences in the loadings using the modified Nicholas model, the modified Demontis model, the rigid structure from experiments and the rigid structure with atom positions optimized at 0 K are below the statistical error of the simulations. In the Ortho structure, the highest loadings are predicted in the rigid structure with atom positions optimized at 0 K. At 800 Pa, all simulations predict a loading of approximately 4 molec./uc. In the Para structure, the modified Nicholas model and the rigid structure with atom positions optimized at 0 K using the modified Nicholas model predict higher loadings than in the rigid structure from experiments and with the modified Demontis model. This suggests that obtaining higher loadings with the modified Nicholas model is due to the deformation of the crystal structure (in the structure with atom positions optimized at 0 K) instead of the vibrations of atoms. In the *m*-xylene/MFI-type zeolite system, the flexibility of the zeolite does not play a large role in the adsorption. All simulations of adsorption of *m*-xylene in the MFI-type zeolites overestimate the experimental data.

For *o*-xylene (Fig. 3.11), the loadings predicted with the modified Nicholas model and the rigid structure with atom positions optimized at 0 K using the modified Nicholas model are higher than in the rigid structure for each MFI-type zeolite lattice. A very small influence of the flexibility of the modified Nicholas model can be observed for each structure. The computed loadings differ within the statistical error with the rigid structure with atom positions optimized at 0 K using the modified Nicholas model. The loadings obtained with the modified Demontis model are lower than in the rigid structure from experiments. It is important to note that the loadings from experiments of adsorption in silicalite [331] at 373 K for *m*-xylene are much lower than those reported for *o*-xylene. The loadings reported by Wu et al. [331] at 293 K show higher loadings for *m*-xylene than for *o*-xylene in silicalite. This suggest that the loadings of *m*-xylene at 373 K in silicalite can be hindered by slow diffusion. The modified Demontis model yields loadings closer to the experimental data than any of the models here considered.

For *p*-xylene (Fig. 3.12) in the Mono and Ortho structures, the modified Nicholas model predicts higher loadings than the rigid structures only at 800 Pa. At lower pressures, the differences are below the statistical uncertainties of the simulations. The modified Demontis model predicts the lowest loadings in all MFI-type zeolite structures. The loadings obtained with the modified Demontis model are lower than in the rigid structure from experiments. The modified Demontis model yields loadings in excellent agreement with the experimental isotherm. In the Para structure, the loadings computed in the rigid structure from experiments are higher than with any flexible model considered. The modified Nicholas model yields loadings close to the rigid structure with atom positions optimized at 0 K, which suggests that the flexibility does not play a role in this case. The large differences between the

3

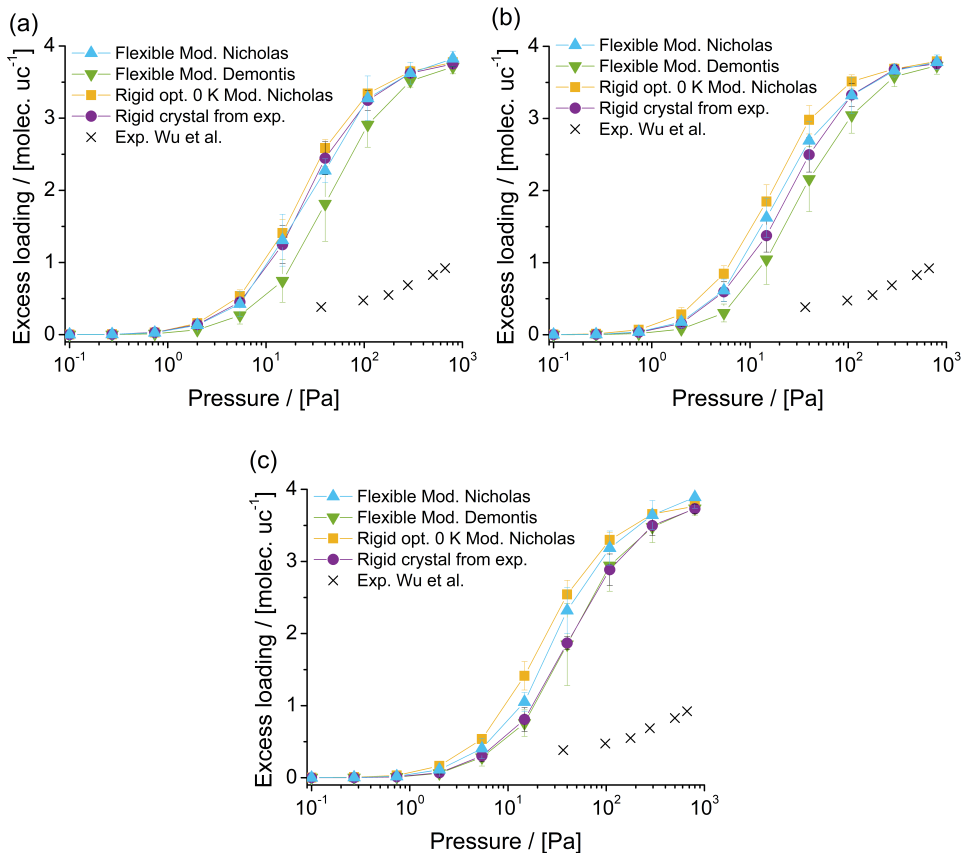


Figure 3.10: Adsorption isotherms of *m*-xylene at 373 K computed in the (a) Mono, (b) Ortho, and (c) Para structures. Triangles, upside down triangles, squares, and circles denote the simulations with the modified Nicholas [376] model, the modified Demontis [374] model, the rigid structure with atom positions optimized at 0 K using the modified Nicholas model, and the rigid structure from experiments, respectively. Crossed symbols denote the experimental data from Wu et al. [331]. The experimental loadings are low (compared to the simulations) and this is indicative of diffusion limitations for *m*-xylene in MFI-type zeolites.

loadings in the rigid structure from experiments and with the modified Demontis model at high pressure suggests that the adsorption in the intersections of the Para structure is affected by the displacement of the zeolite atoms.

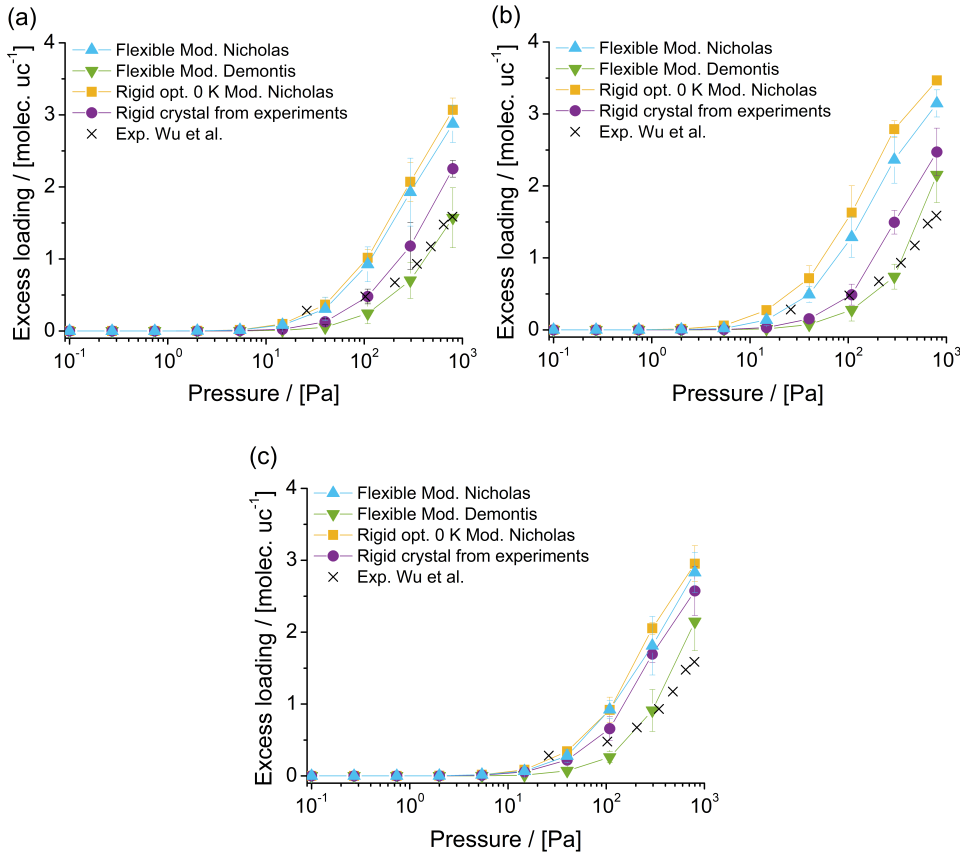


Figure 3.11: Adsorption isotherms of *o*-xylene at 373 K computed in the (a) Mono, (b) Ortho, and (c) Para structures. Crossed symbols denote the experimental data from Wu et al. [331]. Triangles, upside down triangles, squares, and circles denote the simulations with the modified Nicholas [376] model, the modified Demontis [374] model, the rigid structure with atom positions optimized at 0 K using the modified Nicholas model, and the rigid structure from experiments, respectively.

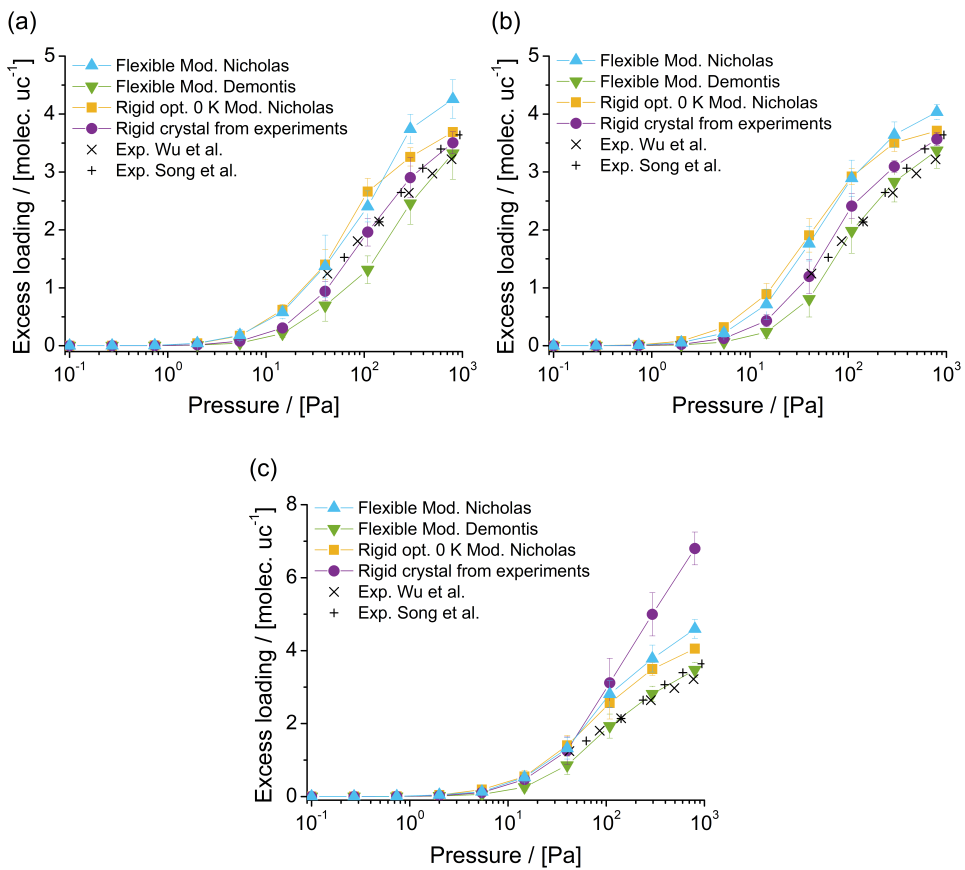


Figure 3.12: Adsorption isotherms of *p*-xylene at 373 K computed in the (a) Mono, (b) Ortho, and (c) Para structures. Crossed symbols denote the experimental data from Wu et al. [331] and Song et al. [335]. Triangles, upside down triangles, squares, and circles denote the simulations with the modified Nicholas [376] model, the modified Demontis [374] model, the rigid structure with atom positions optimized at 0 K using the modified Nicholas model, and the rigid structure from experiments, respectively.

### 3.3.5. DISCUSSION

The simulations from this work underscore the difficulties in modeling the framework flexibility and the adsorption of aromatics in MFI-type zeolites appropriately. Models able to describe the phase transitions that MFI-type zeolites show in experiments -such as core-shell- are difficult to combine with adsorbate models to study adsorption [352]. Also, the use of a core-shell model implies a significant increase in the number of particles in the system, which reduces the efficiency of the simulation [352]. For modeling the phase transitions of MFI-type zeolites, the small volume change and shape differences between the phases cannot be accounted assuming a fixed unit cell volume. Systems where adsorbed molecules induce rearrangement of the zeolite pores require host-host force fields specially designed for this purpose.

The simulations show that the long-range potentials (intra-framework electrostatic and Lennard-Jones interactions) in flexible framework models intrinsically induce small but important changes in the atom positions of the zeolite, and hence in the adsorption isotherms. The incompatibility of the partial charges of the zeolite atoms between host-host and guest-host interactions show the need to consider both aspects for force fields development.

The adsorption of alkylbenzenes in the pores of MFI-type zeolites represents confinement conditions. The confinement affects the physico-chemistry of the adsorbed molecules in different aspects [407–409]. The confinement optimizes van der Waals interactions in zeolite cavities, involving a perturbation of the shape and electronic structure of the sorbate [321]. This suggests that polarizability of sorbate molecules as well as the zeolite framework might have been overlooked.

Macroscopic behavior and properties of alkylbenzenes -such as VLE and critical points- can be well predicted with models that consider rigid molecules in gas and liquid phases [257]. However, benzene rings are flexible [410]. Laaksonen et al. [411] reported that isolated benzene molecules can easily adopt non-planar conformations with torsion angles up to 10° at room temperature. Considering a C-C bond length of 1.4 Å, a C-C-C-C torsion angle of 10° in the aromatic ring induces a displacement of a C atom of approximately 0.24 Å. Such displacement is similar to the mean displacement of the zeolite atoms induced by the force fields for framework flexibility discussed in this work (see table 3.1). This suggests that the intra-molecular flexibility of aromatic molecules can be an important factor in the description of adsorption of aromatics in a zeolite pore.

Experimental work highlights challenges for an accurate description of the adsorption process. Data of adsorption of aromatics in MFI-type zeolites is scarce and not always consistent under the same temperature/pressure conditions. The experiments presented by Caro-Ortiz et al. [204] show important differences with experiments from literature performed decades ago. This suggests that experiments of adsorption of aromatics in MFI-type zeolites are highly dependent on the sample synthesis and detection methods. Such inconsistencies can also be related to diffusion limitations experienced by aromatic bulky molecules, such as *m*-xylene and *o*-xylene [412, 413]. The differences between experiments of adsorption of aromatics in MFI-type zeolites do not provide a clear overview on what to compare with simulations results, what to fit or what to use as input for machine learning

algorithms for force field development.

An accurate experimental description of the internal changes and crystal structure of the zeolite when varying pressure or temperature is needed. To the best of authors' knowledge, detailed experimental insight on how the crystal structure changes hosting different aromatic molecules are not available. All this information is required to develop models able to reproduce and provide reliable molecular insight of the adsorption phenomena. Such requirements, pitfalls, and challenges underline that adsorption of aromatics in MFI-type zeolites is one of the most difficult systems to model.

## 3

### 3.4. CONCLUSIONS

The adsorption of n-heptane, ethylbenzene, and xylene isomers in MFI-type zeolites is computed using rigid and flexible zeolite frameworks. Pore-size distributions (PSD) of the MFI-type zeolite structures subject to three different host-host force field are computed. The PSDs show that the use of constant bond lengths induce displacements of the framework atoms that influences adsorption. Directly taking the bond lengths from the crystallographic structure minimizes this effect. The electrostatic and LJ intra-framework interactions induce displacements of the zeolite atoms that significantly affect the size of the pores and channels of the zeolite. The simulations of the adsorption of n-heptane in MFI-type zeolite at 303 K show a minor influence of framework flexibility for the computed isotherms, compared to simulations using the rigid frameworks and experimental data. The simulations of adsorption of ethylbenzene in MFI-type zeolite at 353 K show that the simulations with the modified Demontis model underestimate experimental loadings. The results suggest that the framework atom displacements using the modified Demontis model hinder the adsorption of aromatics in the zeolite. The use of the modified Nicholas model yields loadings closer to the experimental data. This is due to changes in the average zeolite structure caused by the intra-framework interactions and not to framework flexibility. The vibrations of the zeolite atoms using the modified Nicholas model in the adsorption of ethylbenzene in MFI-type zeolites only plays a role at high pressures/loadings.

The simulations of adsorption of xylene isomers in MFI-type zeolites at 373 K showed that the influence of the flexibility is dependent on the framework. The use of the rigid framework and the modified Demontis model yield loadings close to the experimental isotherm for *o*-xylene and *p*-xylene. All simulations overestimate the experimental isotherm of *m*-xylene. *p*-xylene in the Para structure is the only case where the flexible models show significantly lower loadings than in the rigid structure from experiments. The loadings in the rigid structure are higher than with framework flexibility models and overestimate the experimental loadings.

Using the considered host-host force fields, framework flexibility generates a new structure that is differently 'rigid'. The flexible force fields produce a zeolite structure that vibrates around a new equilibrium configuration that has limited capacity to accommodate to a bulky guest molecule. The vibration of the zeolite atoms only plays role at high loadings, and the adsorption is mainly dependent on the average positions of the atoms. The intra-framework interactions should be treated

carefully, as these interactions cause significant deviations from the experimental zeolite lattice. The adsorption of n-heptane in the MFI-type zeolite is not significantly influenced by the structure changes of the framework due to the force fields for framework flexibility (see Fig. 3.7). The use of a zeolite structure with fixed atom positions is appropriate when the molecule does not fit tightly in the zeolite pores. For aromatics, the influence of the force field for framework flexibility on the adsorption in MFI-type zeolites implies that the structural changes of the zeolite framework are relevant for molecules that fit tightly in the zeolite void spaces. The prediction of different loadings when a force field for framework flexibility is used compared to when a rigid structure is used is an artifact of the force field and not a re-accommodation of the framework atoms to a guest molecule. Force fields for framework flexibility usually do not capture the physics behind the accommodation of the framework atoms to a guest molecule. Obtaining a prediction of the loadings closer to the experiments is an overall effect of the host-host interactions, and not guest interactions as desired. This implies that it is not possible to determine if one of the force fields for framework flexibility performs best for the description of the adsorption of aromatics in MFI-type zeolites. Simulations of MOFs and other porous material considering framework flexibility use similar types of force fields [222, 352]. The findings of this work suggest that similar effects on the framework may be found for other classes of porous materials.

The simulations underline the need of new tailor-made force fields to model the zeolite flexibility for aromatics. Such force fields should focus on the local changes due to the presence of bulky guest molecules, and not only vibrational behavior. As electrostatic interactions are important for adsorption purposes, the intra-framework LJ interactions should also aim to balance the electrostatic interactions to preserve the atomic positions of the zeolite. There are many challenges and difficulties to model the framework flexibility and the adsorption of aromatics in MFI-type zeolites appropriately. An accurate experimental description of the internal changes and crystal structure of the zeolite when varying pressure or temperature is crucial. Data of adsorption of aromatics in MFI-type zeolites is scarce and not always consistent at the same temperature/pressure conditions. The variability on the experiments of adsorption of aromatics in MFI-type zeolites does not provide a clear overview on what to compare to the predictions of the simulations. This knowledge is required to develop models able to reproduce and provide reliable molecular insight of the adsorption phenomena. The simulations from this work show that force fields for framework flexibility should not be blindly applied to zeolites and a general rethinking of the parametrization schemes for such models is needed.

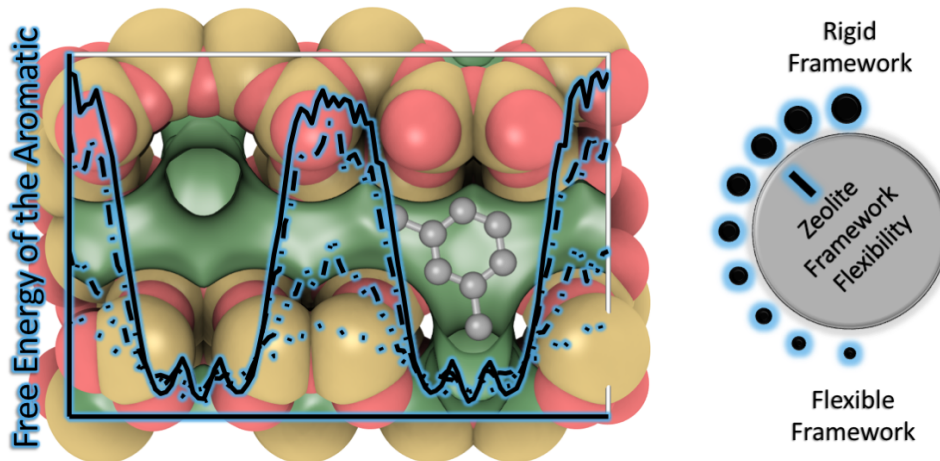


# 4

## INFLUENCE OF FRAMEWORK FLEXIBILITY ON THE ADSORPTION AND DIFFUSION OF AROMATICS IN MFI-TYPE ZEOLITES

This chapter is based on the article:

S. Caro-Ortiz, E. Zuidema, M. Rigo, D. Dubbeldam, T. J. H. Vlugt, *Effects of framework flexibility on the adsorption and diffusion of aromatics in MFI-type zeolites*, *J. Phys. Chem. C*, **124**, 24488 (2020) [187].



## 4.1. INTRODUCTION

Many petrochemical processes strongly rely on the interaction and kinetic behavior of hydrocarbons inside a zeolite [308–311, 414]. For example, xylene molecules diffusing along the zeolite pores can undergo isomerization, disproportionation and transalkylation reactions [137]. Thus, knowledge of the adsorption and diffusion behavior of hydrocarbons in the pores of zeolites is important for the understanding of the catalytic activity of the zeolite [130, 142, 144, 145].

The adsorption and diffusion of aromatics in MFI-type zeolites has been reported by several experimental studies [316, 322, 325, 327–340, 415]. The interaction of an aromatic molecule within a zeolite framework is a complex process [204]. Factors such as molecules filling a new adsorption site [314, 315], structural changes due to the number of adsorbed molecules [316–318] or due to a change of temperature [319, 320], may result in an inflection point in the adsorption isotherm. Talu et al. [316] reported that with increasing temperature, the isotherm shape for benzene, toluene, and *p*-xylene changes from type IV to type I. The combination of such factors also leads to different phases of MFI-type zeolite structures. The all-silica form of the MFI-type zeolite is known to show a monoclinic or orthorhombic structure depending on the temperature and loading [322, 323]. Van Koningsveld et al. [324] identified three structures of the *p*-xylene/silicalite system: Mono (monoclinic), Ortho (orthorhombic), and Para (also orthorhombic). The adsorption and diffusion of aromatics in MFI-type zeolites has also been studied by molecular simulations [144]. Commonly, Monte Carlo (MC) simulations in the grand-canonical ensemble (GCMC) are used to compute sorbate loadings as a function of temperature and pressure in a zeolite framework [197–199]. Several studies where MC is used to study adsorption of aromatics in MFI-type zeolites can be found in literature [135, 200–204, 341–349]. Zeolites are commonly considered as very rigid structures as its atomic bonds and angles are highly constrained [312, 313]. Computer simulations of the adsorption of hydrocarbons in zeolites are typically performed assuming that the zeolite framework taken from crystallographic data is a rigid structure [186, 197, 216]. Nevertheless, Clark and Snurr [217] showed that the computed adsorption isotherms are sensitive to small differences in the atom positions of the zeolite. Framework flexibility is observed to play a role only if the adsorbate fits tightly in the zeolite pore [217]. Vlugt et al. [216, 223] reported the effect of framework flexibility in the adsorption of n-alkanes and cycloalkanes in MFI-type zeolite. It was found that for molecules with an inflection behavior in the isotherm, the influence of the flexibility seems to be larger than for molecules without such inflection. Caro-Ortiz et al. [204] showed that the use of force fields for framework flexibility significantly affects the adsorption isotherm of xylene isomers and ethylbenzene in MFI-type zeolites. Such effect is related to intrinsic changes of the zeolite structure caused by the intra-framework interactions of the force field for framework flexibility. Molecular dynamic studies have shown that accounting for framework flexibility considerably affects the diffusion coefficient of aromatics in zeolites [137]. Forester et al. [224] reported that framework flexibility changes the diffusivity of aromatics in zeolites by an order of magnitude. Toda et al. [137] assessed the performance of several force fields for framework flexibility by comput-

ing diffusion coefficients of *p*-xylene and *o*-xylene in 10-ring zeolites. It is observed that force fields for framework flexibility distort the structure, and that the size and shape of the 10-rings act as bottlenecks for the diffusion [137]. Kolokathis et al. [225] computed self-diffusion coefficients of *p*-xylene and benzene in silicalite-1, based on transition state theory. It is found that *p*-xylene diffuses roughly 100 times faster than benzene when adsorbed at low occupancy in silicalite.

If the diffusion coefficient of a molecule in a zeolite framework is sufficiently high, molecular dynamic simulations can be directly used [144]. Processes such as the separation of aromatic isomer mixtures in zeolites, show self-diffusivity coefficients lower than  $10^{-12} \text{ m}^2\text{s}^{-1}$  [226]. As such, the diffusion behavior may occur outside the time scales accessible to molecular dynamics simulations [227]. The free energy landscape of molecules within the pores of a zeolite show the mobility of the molecules inside the zeolite and can be used in a more quantitative investigation of product shape selectivity of zeolite catalysts [228]. Low diffusion coefficients are observed when the molecules are trapped in low free energy sites in the zeolite framework, and sporadically hop from one low energy site to another [144]. Transition state theory (TST) methods can be used to estimate the diffusion coefficients in porous materials at slow diffusion time scales [229, 230], using the free energy landscape [231]. Such methods have been used for the estimation of diffusion coefficients of aromatics in MFI-type zeolites [224, 225, 232–234]. As discussed in chapter 3, force fields for framework flexibility produce a zeolite structure that vibrates around a new equilibrium configuration with limited capacity to accommodate to bulky guest molecules. To the best of our knowledge, molecular simulation studies where the effect of framework flexibility on the adsorption and diffusion of aromatics in zeolites is systematically studied are not available. This chapter explores how the variation of framework flexibility in a model affects the adsorption and diffusion of aromatic hydrocarbons in MFI-type zeolites. Force fields for framework flexibility that include intra-framework Lennard-Jones (LJ) and electrostatic interactions induce small but important changes in the atom positions of the zeolite, affecting the adsorption isotherm (see chapter 3 for details). The Demontis model [373] consists of modeling zeolite framework flexibility by a bond stretching potential for the Si-O bond, and a bond stretching potential for oxygen atoms linked by a silicon atom, not including intra-framework LJ and electrostatic interactions. Fig. 4.1 shows how the bonds of selected neighboring atoms from the MFI-type zeolite are modeled as rigid bonds and as harmonic oscillators according to the Demontis model [373].

The effect of framework flexibility on the adsorption and diffusion of C<sub>8</sub> aromatics in MFI-type zeolites is studied using a Demontis-like model in which the spring constants of such bond-stretching parameters are varied. MC simulations are used to compute adsorption of ethylbenzene and xylene isomers in an MFI-type zeolite structure when framework flexibility is varied. Also, free energy profiles are used to obtain the self-diffusion coefficients of aromatics in the straight channel of the zeolite.

This chapter aims to study how variations of framework flexibility change the MFI-type zeolite framework, and influence the interactions with guest molecules. The 'flexible snapshot' method has been developed by Sholl et al. [416–418] to cap-

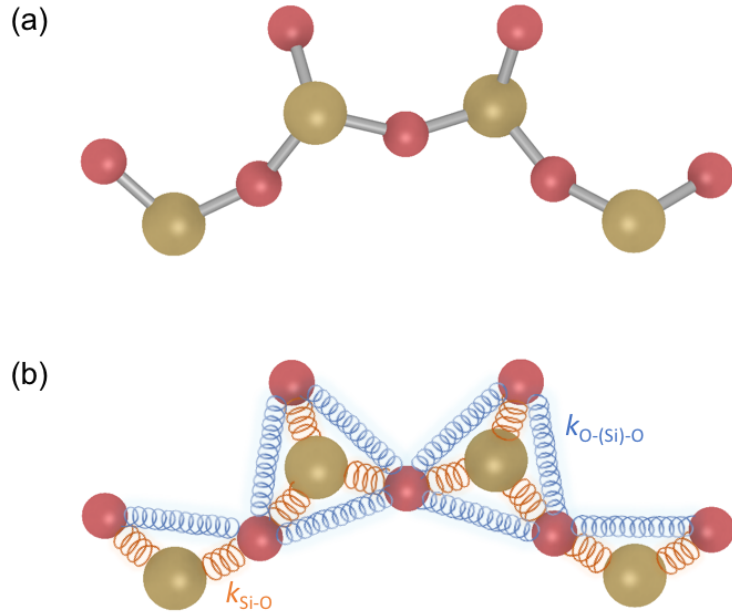


Figure 4.1: Selected neighboring atoms from the 10-ring of MFI-type zeolite with bonds modeled as (a) rigid distances and (b) as harmonic oscillators according to the Demontis model [373]. Silicon and oxygen atoms are shown in yellow and red, respectively. The orange spring represents the harmonic potential between linked silicon and oxygen atoms with spring constant  $k_{\text{Si}-\text{O}}$ . The blue spring represents the harmonic potential for oxygen atoms linked by a silicon atom with spring constant  $k_{\text{O}-(\text{Si})-\text{O}}$ .

ture the effect of framework flexibility on adsorption in nanoporous materials. In this method, snapshots are obtained using fully flexible MD simulation of an empty framework, and has been used to study the selectivities of C<sub>8</sub> aromatics in multiple metal-organic frameworks [418]. In this work, the 'flexible snapshot' method is used to see how the empty zeolite structure changes due to framework flexibility. The potential of this method to describe adsorption at high pressures is briefly assessed. The simulation procedure is explained in Section 4.2. The computed Henry coefficients, diffusion coefficients, and adsorption isotherms of C<sub>8</sub> aromatics in an MFI-type zeolite are reported and discussed in Section 4.3. It is shown that framework flexibility induces small but important changes in the atom positions of the zeolite, and hence in the adsorption isotherm and the diffusion coefficient of aromatics in MFI-type zeolite. The concluding remarks regarding the effect of the framework flexibility on the interaction of aromatics within an MFI-type zeolites are discussed in Section 4.4.

## 4.2. METHODS

The adsorption computations are performed using the Continuous Fractional Component Monte Carlo (CFCMC) [240, 241] algorithm in the grand-canonical ensemble. The RASPA software [365, 366] is used for all simulations. Periodic boundary conditions are applied to a simulation box consisting of 2x2x3 unit cells of the MFI-type zeolite Ortho structure described by van Koningsveld et al. [351]. A cut off radius of 14 Å is applied for all LJ interactions and analytic tail corrections are used [367]. The interactions between different atom types are obtained using Lorentz-Berthelot mixing rules [292]. MC simulations are performed in MC cycles. The number of trial moves per cycle equals the number of adsorbed molecules  $N$  with a minimum of 20. At each MC cycle, trial moves attempt to rotate, displace, randomly reinsert, and insert/remove adsorbates. In the CFCMC algorithm, the interactions of a fractional molecule are scaled by the  $\lambda$  parameter in the range 0 to 1 (0 for no interactions with surrounding molecules/framework and 1 for full interaction with surrounding molecules/framework). The so-called  $\lambda$ -trial moves scale the interactions of the fractional molecule via the CFCMC algorithm [240, 241]. The simulations use  $10^5$  MC cycles to initialize the system. The initialization run only allows translation, rotation, and insertion/deletion, and reinsertion trial moves. After initialization, a stage of  $4 \cdot 10^5$  MC cycles are used to equilibrate the CFCMC biasing factors. All the considered types of trial moves are allowed and the biasing factors for the  $\lambda$ -trial moves of the CFCMC algorithm are calculated.  $\lambda$ -trial moves are biased to obtain a flat  $\lambda$  probability distribution. The use of this trial move is advantageous as it enables an efficient insertion and deletion of sorbate molecules in the system [241, 243]. Ensemble averages are obtained in a  $5 \cdot 10^5$  MC cycles production stage. The reported errors account for the 95% confidence interval calculated by dividing the production run into five parts and computing the standard deviation. An additional MC trial move is included to simulate a flexible zeolite framework, which attempts to give a random displacement to a randomly selected zeolite atom [216]. *p*-Xylene and benzene adsorption cause volume changes of the MFI-type framework lower than 0.4% [329, 419]. As such, the volume of the simulation box is kept fixed.

The framework snapshots considered for the 'flexible snapshot' method [416–418] are obtained by performing simulations of an empty zeolite structure in the *NVT* ensemble. Random framework atom trial moves are allowed. A  $10^5$  MC cycles run is performed as initialization. After that, snapshots are produced every  $10^4$  MC cycles. The average properties for each snapshot are computed and then averaged.

The pore size distribution (PSD) of a MFI-type structure is calculated geometrically with the method of Gelb and Gubbins [388, 389]. Henry coefficients, and free energy profiles of aromatics in the MFI-type zeolite structure are calculated via the Widom test-particle insertion method [390]. In this method, the average Boltzmann weight of a ghost molecule is calculated. Such ghost molecule perceives the same energy as a real particle. The other molecules in the system (zeolite framework in this case) do not feel the presence of the ghost particle [173]. The simulations are started with  $10^5$  MC cycles to initialize the system. The initialization run only allows

framework atom moves. After that, the Henry coefficient and free energy landscape are computed in a  $10^5$  MC cycles production run. The helium void fraction (HVF) is determined using the iRASPA visualization software [22], by probing the framework with a non-adsorbing helium molecule using the Widom test-particle insertion method [390].

Force fields that model the flexibility of the zeolite framework are commonly based on the description of vibrational properties, such as the infrared spectra of the zeolite atoms [368, 369], and/or ab initio quantum chemical calculations [370, 371]. Several force fields for framework flexibility have been reported in literature [312, 370–378]. Such force fields are typically used for the calculations of diffusion of aromatics in MFI-type zeolites by molecular dynamics simulations [137, 380]. In this work, the host-host interaction are modeled using a Demontis-like force field. The Demontis model [373–375] consists on modeling zeolite framework flexibility by a bond stretching potential for the Si-O bond, and a bond stretching potential for the oxygen atoms linked by a silicon atom. The bond stretching potentials  $U(r)$  are modeled using the expression:  $U(r) = 0.5 \cdot k \cdot (r - r_0)^2$ , where  $k$  is the spring constant and  $r_0$  is the equilibrium bond length. The original values of the spring constants are  $k_{\text{O}-(\text{Si})-\text{O}}/k_B = 51831.61 \text{ K}\text{\AA}^{-2}$  and  $k_{\text{Si}-\text{O}}/k_B = 251778.07 \text{ K}\text{\AA}^{-2}$ . The ratio  $k = k_{\text{O}-(\text{Si})-\text{O}} = 0.2 \cdot k_{\text{Si}-\text{O}}$  is kept fixed to reduce the number of parameters [216]. The original Demontis model [373] uses constant equilibrium bond lengths and angles. The so-called modified form of this model takes the equilibrium bond lengths and bend-angles (in the Urey-Bradley term) directly from the crystallographic structure to which the model is applied [216]. This modification is used in this work, and it is used to avoid large deviations from the experimental crystal structure (see chapter 3). When this modification is in use, the minimum energy structure is exactly reproduced when  $k \rightarrow \infty$  [216] or for any value of the spring constant  $k$  when  $T \rightarrow 0 \text{ K}$ .

The interactions between the zeolite and guest hydrocarbons are modeled using the TraPPE-zeo model [396]. In this force field, all oxygen and silicon atoms are modeled with LJ interactions and partial charges. The development of this force field was focus on transferability and variety of zeolite/guest systems [396]. As such, it is fitted to match the experimental adsorption isotherms of n-heptane, propane, carbon dioxide, and ethanol in zeolites.

As discussed in chapter 2, molecular simulations of aromatics typically use force fields (guest-guest interactions) that model the vapor-liquid equilibrium (VLE) with LJ potentials or a combination of LJ and electrostatic interactions [257, 258]. In the case of aromatic species, a common practice in the development of these force fields is to fit the interaction parameters to reproduce the VLE of the pure components [245–248, 253, 297, 299], or by optimizing LJ interactions by a combination of ab initio quantum mechanical calculations and empirical methods [249–251, 401, 420]. In this work, the guest-guest interactions are modeled using the TraPPE-UA [252, 403] force field. The TraPPE-UA is a widely used force field that is designed to reproduce the VLE of alkylbenzenes and n-alkanes, among other chemical species. The united atom approach is used by merging a carbon atom and its bonded hydrogen atoms into a single uncharged interaction site representing

each  $\text{CH}_x$  group in the aromatic species. Aromatics are modeled as rigid molecules, except ethylbenzene, that includes a torsional potential in the  $\text{CH}_3\text{-CH}_2\text{-CH}$  bend-angle. The reader is referred to chapter 3 for details about the choice of force fields and to tables A.2 and A.3 of Appendix A.1 for the force field parameters used here.

## 4.3. RESULTS AND DISCUSSION

### 4.3.1. HENRY COEFFICIENTS OF XYLEMES IN MFI-TYPE ZEOLITE

The Henry coefficients of ethylbenzene and xylene isomers (as single components) in an MFI-type zeolite at 353 K are computed using the flexible framework model and the 'flexible snapshot' method, varying  $k$ . Five snapshots are used for the 'flexible snapshot' method. The computed Henry coefficients as a function of the framework flexibility are shown in Fig. 4.2. It is observed that for all aromatics considered in this study, the 'flexible snapshot' method yields the same Henry coefficient as the simulations using a flexible framework. Fig. 4.2 shows that framework flexibility has a significant influence on the Henry coefficient of aromatics in the MFI-type zeolite. When the framework is very flexible (i.e.  $k/k_B = 500 \text{ K}\text{\AA}^{-2}$ ), the Henry coefficients of ethylbenzene, *p*-xylene, and *o*-xylene are higher than those computed for the structure with atom positions fixed to the crystallographic data (rigid framework). When  $5 \cdot 10^4 \text{ K}\text{\AA}^{-2} \leq k/k_B \leq 5 \cdot 10^6 \text{ K}\text{\AA}^{-2}$ , the Henry coefficients of ethylbenzene and xylene isomers are lower than in the rigid zeolite framework. When  $k/k_B > 5 \cdot 10^7 \text{ K}\text{\AA}^{-2}$ , the Henry coefficient of ethylbenzene and xylene isomers is in agreement with the Henry coefficient computed for the rigid structure. This suggests that when  $k$  is sufficiently high, framework flexibility does not affect the zeolite structure. The Henry coefficients of aromatics in MFI-type zeolite computed with the 'flexible snapshot' method are in excellent agreement with the values computed using the flexible framework for all  $k$ . This suggests that the snapshots can be used to describe the changes that framework flexibility induces on the empty zeolite structure.

### 4.3.2. FRAMEWORK FLEXIBILITY IN MFI-TYPE ZEOLITE

The mean displacement of the zeolite atoms compared to the rigid structure [351], the HVF, and the PSD are computed for the five snapshots used in the 'flexible snapshot' method. Fig. 4.3 shows the mean displacement of the zeolite framework atoms compared to the rigid framework, the HVF, and the PSD, as a function of  $k$ , computed for five MFI-type zeolite snapshots. It is observed that as  $k$  is decreased, the mean displacement of the framework atoms increases. When  $k/k_B = 5 \cdot 10^2 \text{ K}\text{\AA}^{-2}$ , an average displacement of 0.95 Å is observed. For  $k/k_B > 5 \cdot 10^7 \text{ K}\text{\AA}^{-2}$ , the average displacement of framework atoms is close to zero. The HVF of the MFI-type zeolite structures is significantly influenced by framework flexibility. The highest HVF is observed when  $k/k_B = 5 \cdot 10^2 \text{ K}\text{\AA}^{-2}$ . For  $5 \cdot 10^4 \text{ K}\text{\AA}^{-2} \leq k/k_B \leq 5 \cdot 10^5 \text{ K}\text{\AA}^{-2}$ , the HVF of the MFI-type zeolite structure is lower than the HVF computed for the rigid framework. For  $k/k_B > 5 \cdot 10^6 \text{ K}\text{\AA}^{-2}$ , the HVF of the MFI-type zeolite structures is in good agreement with the HVF computed for the rigid zeolite structure. The influence of framework flexibility on the HVF shows that the accessible pore volume

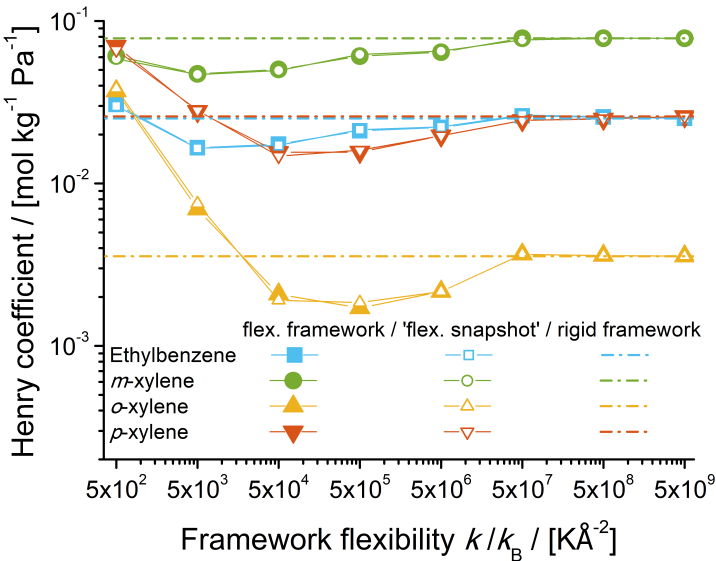


Figure 4.2: Henry coefficient of ethylbenzene, and xylene isomers computed in an MFI-type zeolite at 353 K as a function of framework flexibility  $k$ . Closed symbols denote the computations using the flexible framework. Open symbols denote the computations using the 'flexible snapshot' method [416]. Dashed lines denote the computations using the rigid framework.

of the zeolite is directly related to the Henry coefficient of aromatics in MFI-type zeolites.

For the PSD of MFI-type zeolites, the peak centered at a diameter of approximately 4.3 Å corresponds to the zigzag and straight channels. The peak centered at a diameter of approximately 5.5 Å corresponds to the intersection of the channels. The PSD of the MFI-type zeolite snapshots show the influence of framework flexibility on the zeolite pore sizes. It can be observed that as  $k$  is decreased, the peak that corresponds to the intersections is shifted to lower diameters. The peak that corresponds to the channels is shifted to lower diameters when  $k/k_B \leq 5 \cdot 10^4 \text{ K}\text{\AA}^{-2}$ .

The PSD of the MFI-type structures when  $k/k_B = 5 \cdot 10^2 \text{ K}\text{\AA}^{-2}$  does not show a pore size peak distinction between channels and intersection. The maximum pore size observed is 6.5 Å, suggesting that for very high framework flexibility, the deformation of the zeolite void spaces is very large. As framework flexibility changes the pore size of the zeolite intersections and channels, a decrease of the pore size of the intersection directly affects the adsorption of molecules, and Henry coefficients lower than for the rigid framework are obtained. This suggests that the interaction of the aromatic molecules and the zeolite framework is highly influenced by changes on the pore sizes of the zeolite. Having higher Henry coefficients than in the rigid framework when  $k/k_B \leq 5 \cdot 10^3 \text{ K}\text{\AA}^{-2}$  can be related to an increase of pores with a diameter of approximately 4.7 Å. The PSDs suggest that as  $k$  is decreased, the pore sizes of the channels and the intersections become uniform.

When  $k/k_B = 5 \cdot 10^6 \text{ K\AA}^{-2}$ , a mean displacement of the zeolite atoms of  $0.018 \text{ \AA}$  is enough to induce up to a 42% decrease of the Henry coefficient of *o*-xylene in MFI-type zeolites, compared to the Henry coefficient computed in the rigid framework. With framework flexibility in the range of the original Demontis model (i.e.  $k/k_B = 5 \cdot 10^4 \text{ K\AA}^{-2}$ ), Henry coefficients lower than in the rigid framework are obtained. As the framework is more flexible, Henry coefficients higher than in the rigid framework are obtained. This suggests that the interactions between the aromatic molecules and the zeolite framework are very susceptible to small displacements of the zeolite atoms and the geometry of the zeolite pores.

Since the snapshots are obtained from an empty zeolite structure, the capacity of the 'flexible snapshot' method to describe the adsorption of aromatics outside the Henry regime is of interest. Simulations of adsorption of ethylbenzene and *p*-xylene in an MFI-type structure are computed at 7848 Pa, using different number of snapshots, for different  $k$ . Snapshot 1 corresponds to the crystal structure from experiments [351]. The loadings of ethylbenzene and *p*-xylene in MFI-type zeolite at 7848 Pa and 353 K as a function of the number of snapshots for different  $k$  are shown in Fig. 4.4. The loadings computed using the 'flexible snapshot' method are higher than the loadings computed in the rigid framework. The loadings computed with the 'flexible snapshot' method are lower than the loadings obtained using a flexible framework. It can be observed that the loadings using the 'flexible snapshot' method do not depend on the number of snapshots used if ten or more snapshots are used.

#### 4.3.3. 'FLEXIBLE SNAPSHOT' METHOD FOR ADSORPTION IN MFI-TYPE ZEOLITE

Adsorption isotherms of ethylbenzene and *p*-xylene in an MFI-type zeolite at 353 K are computed using the flexible framework and the 'flexible snapshot' method with ten snapshots, are shown in Fig. 4.4. The adsorption isotherms show the differences between the loadings computed with the flexible framework and the 'flexible snapshot' method. In the 'flexible snapshot' method, it is assumed that the adsorbate does not have a significant effect on the framework dynamics [418]. This assumption has a significant effect on the computed loadings when framework flexibility is high (i.e.  $k$  is low). When  $k/k_B = 5 \cdot 10^2 \text{ K\AA}^{-2}$ , significant differences between the loadings of ethylbenzene and *p*-xylene in MFI-type zeolite computed with the flexible framework and the 'flexible snapshot' method are observed for pressures higher than 10 Pa. For framework flexibility  $k/k_B = 5 \cdot 10^3 \text{ K\AA}^{-2}$  and  $k/k_B = 5 \cdot 10^4 \text{ K\AA}^{-2}$ , the loading differences can be observed when the pressure is higher than 100 Pa, and loadings higher than 4 molec./u.c. are obtained. The 'flexible snapshot' method can be used to understand the effect that bulky aromatic guest molecules produce on the zeolite framework. It can be observed that the loadings computed using the 'flexible snapshot' method account for the molecules that would fit in a new rigid framework with the new average configuration produced by a particular framework flexibility  $k$ . The difference between the loadings computed with the 'flexible snapshot' method and the flexible framework correspond to the effect on the isotherm of how the framework accommodates to the guest molecules. The 'flexible snapshot'

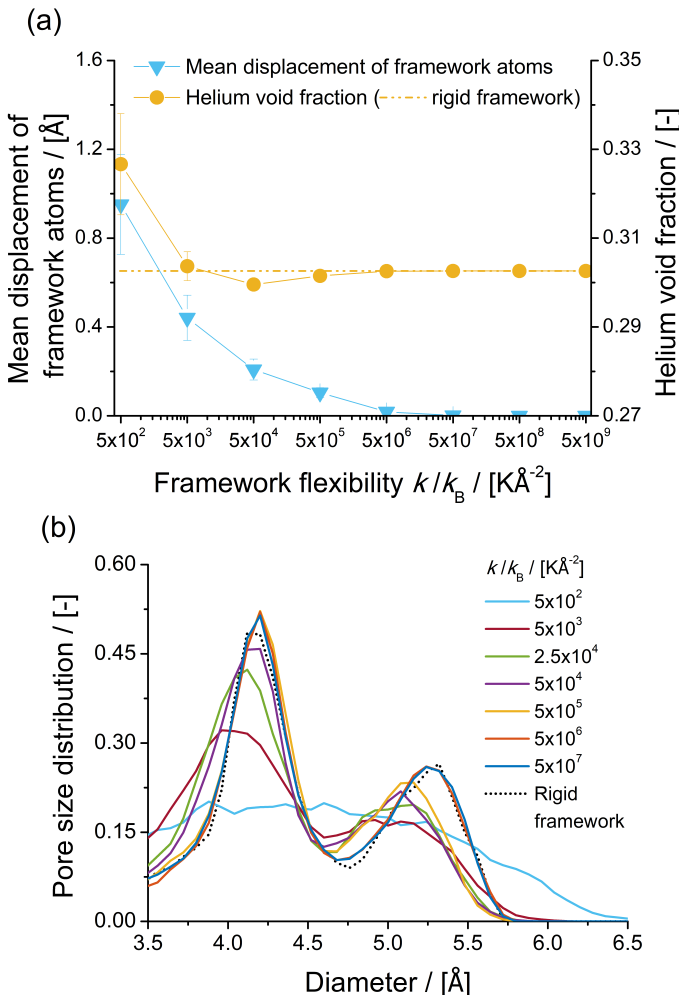


Figure 4.3: (a) Mean displacement of framework atoms compared to the rigid structure [351] and helium void fraction, and (b) Pore size distribution of the five empty MFI-type zeolite snapshots used for the 'flexible snapshot' method [416] at 353 K as a function of framework flexibility  $k$ .

method is useful for the description of the adsorption behavior at very low loadings/infinite dilution. For high pressures/loadings, the 'flexible snapshot' method does not yield the same loading as when the flexible framework is used. This suggests that the effect of the guest aromatic molecules on the zeolite framework should not be neglected.

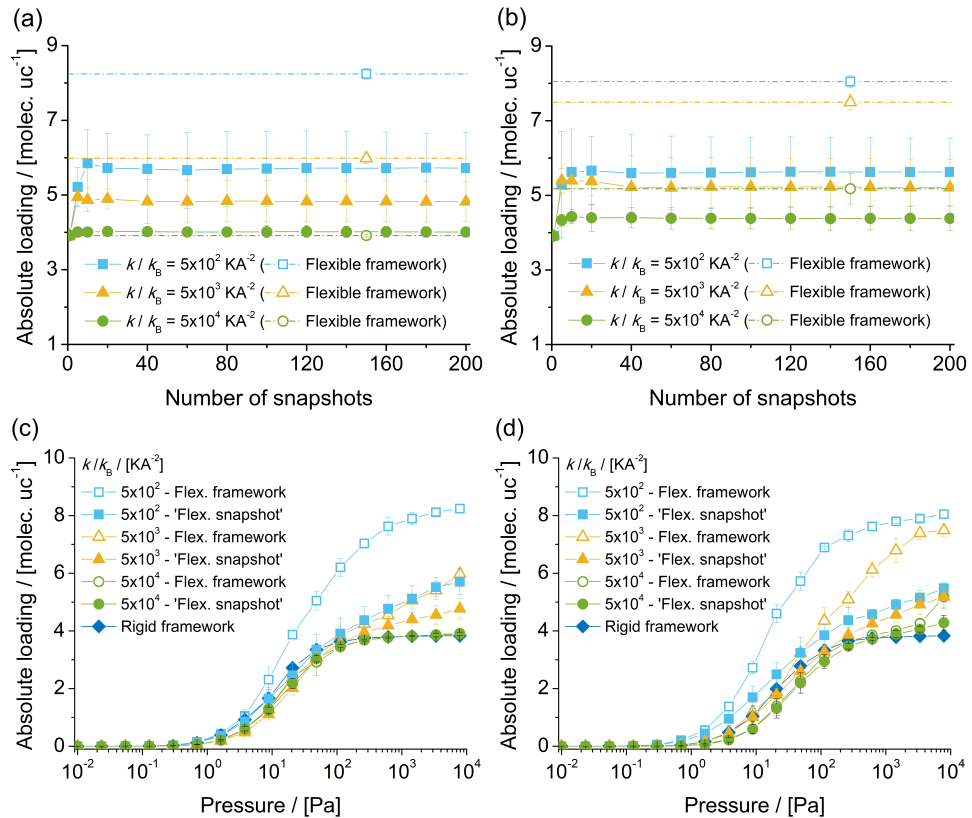


Figure 4.4: Absolute loadings of (a) ethylbenzene and (b) *p*-xylene at 7848 Pa in an MFI-type zeolite [351] at 353 K computed using the flexible framework and the 'flexible snapshot' method, as a function of the number of snapshots considered in the 'flexible snapshot' method, for different framework flexibility  $k$ . Adsorption isotherms of (c) ethylbenzene and (d) *p*-xylene in an MFI-type zeolite [351] at 353 K computed using the flexible framework and the 'flexible snapshot' method using ten snapshots, for different framework flexibility  $k$ .

#### 4.3.4. ADSORPTION OF AROMATICS IN MFI-TYPE ZEOLITE

Adsorption isotherms of ethylbenzene and xylene isomers at 353 K in an MFI-type zeolite varying framework flexibility  $k$  are shown in Fig 4.5. Framework flexibility influences the adsorption isotherm of aromatics in MFI-type zeolite. In the low pressure regime (i.e.  $P < 10^2$  Pa), the loadings of ethylbenzene are similar for  $k/k_B \geq 5 \cdot 10^3$  KÅ<sup>-2</sup>. At higher pressures, the effect of framework flexibility is observed, yielding higher loadings as  $k$  is decreased. The highest loadings of ethylbenzene in the considered pressure range are obtained when  $k/k_B = 5 \cdot 10^2$  KÅ<sup>-2</sup>, having up to 8.2 molec./u.c. at 7848 Pa.

At pressures lower than 20 Pa, framework flexibility does not play a role in the loadings of *m*-xylene. When  $k/k_B = 5 \cdot 10^2$  KÅ<sup>-2</sup>, loadings of 7.8 molec./u.c. of *m*-

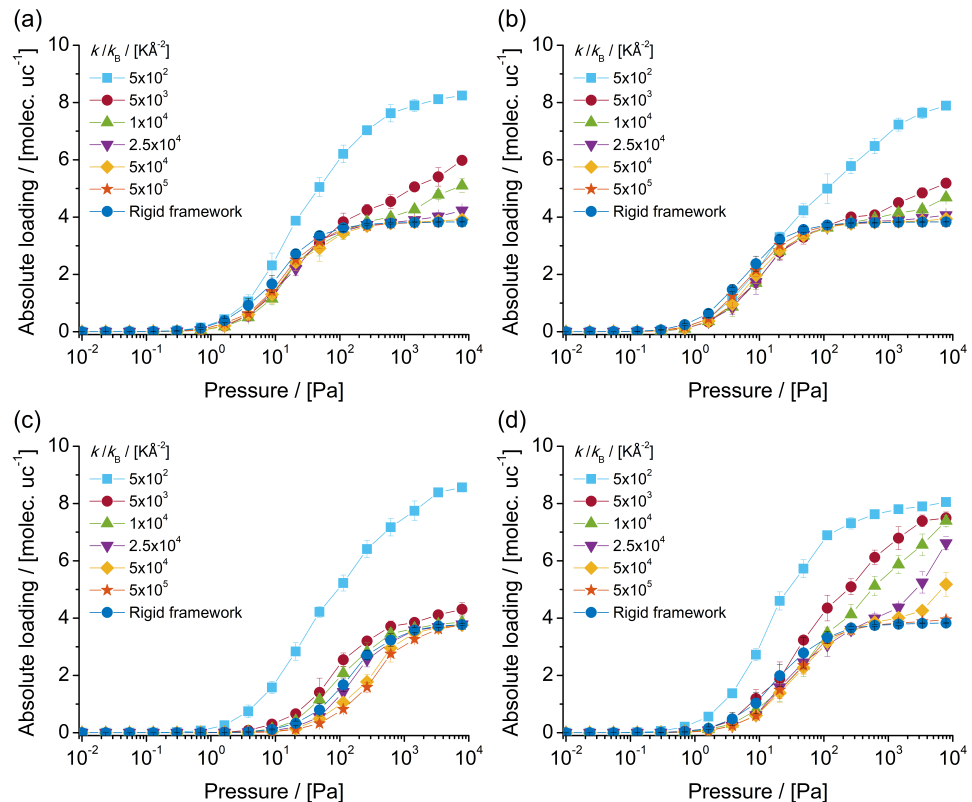
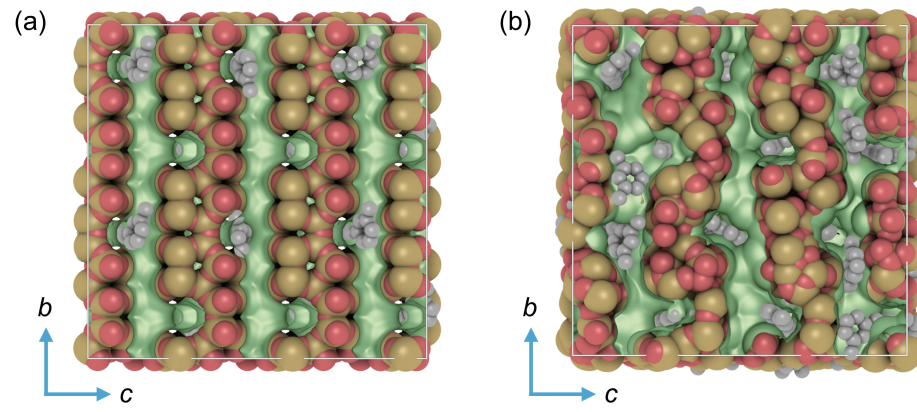


Figure 4.5: Adsorption isotherms for (a) ethylbenzene, (b) *m*-xylene, (c) *o*-xylene, and (d) *p*-xylene in an MFI-type zeolite [351] at 353 K, varying framework flexibility  $k$ .

xylene are observed at 7848 Pa. For  $5 \cdot 10^3 \text{ K\AA}^{-2} \leq k/k_B \leq 10^4 \text{ K\AA}^{-2}$ , framework flexibility influences adsorption only when the pressure is higher than  $6 \cdot 10^2 \text{ Pa}$ . Fig. 4.6 shows two typical snapshots of the simulation of adsorption of *m*-xylene in an MFI-type zeolite at 353 K and 7848 Pa, using a rigid zeolite framework (Fig. 4.6a), and a flexible zeolite framework with  $k/k_B = 5 \cdot 10^2 \text{ K\AA}^{-2}$  (Fig. 4.6b). It can be observed that when using the rigid zeolite framework, *m*-xylene molecules are located exclusively in the intersection of the zigzag and the straight channel. When  $k/k_B = 5 \cdot 10^2 \text{ K\AA}^{-2}$ , *m*-xylene molecules are located in the intersections of the channels, as well as in the channels.

Unlike ethylbenzene and *m*-xylene, *o*-xylene adsorption is affected by framework flexibility already at very low pressures. The effects of framework flexibility are noticeable when the pressure is higher than 10 Pa. Framework flexibility has a significant influence on the Henry coefficient of *o*-xylene (Fig. 4.2); the Henry coefficient of *o*-xylene is 1.9 times higher than for the rigid structure when  $k/k_B = 5 \cdot 10^3 \text{ K\AA}^{-2}$ , and 0.48 times smaller when than for the rigid structure



4

Figure 4.6: Typical snapshots of the simulations of adsorption of *m*-xylene in an MFI-type zeolite at 353 K and 7848 Pa. (a) Simulation using the rigid zeolite framework. (b) Simulations using framework flexibility  $k/k_B = 5 \cdot 10^2 \text{ K}^\circ\text{A}^{-2}$ . The adsorption surface computed with iRASPA [22] is shown in green.

when  $k/k_B = 5 \cdot 10^5 \text{ K}^\circ\text{A}^{-2}$ . This suggest that the adsorption of *o*-xylene in MFI-type zeolite is sensitive to the changes of the zeolite structure caused by framework flexibility already at low loadings. When  $k/k_B = 5 \cdot 10^2 \text{ K}^\circ\text{A}^{-2}$ , *o*-xylene loadings of up to 8.5 molec./u.c. are obtained. For  $k/k_B = 5 \cdot 10^3 \text{ K}^\circ\text{A}^{-2}$ , the maximum loading obtained is 4.3 molec./u.c. As  $k/k_B \geq 10^4 \text{ K}^\circ\text{A}^{-2}$ , maximum loadings of approximately 3.8 molec./u.c. are obtained. *p*-xylene adsorption is highly affected by framework flexibility, specially at high pressures. The maximum loading of *p*-xylene (8.1 molec./u.c.) is obtained for  $k/k_B = 5 \cdot 10^2 \text{ K}^\circ\text{A}^{-2}$ . Only when  $k/k_B \geq 5 \cdot 10^5 \text{ K}^\circ\text{A}^{-2}$ , the loadings obtained with the flexible framework are the same as the loadings obtained in the rigid framework. In the case of C<sub>8</sub> aromatics, and inflection point in the isotherm can be an indication of the occupancy of new adsorption sites [314], such as the zigzag and straight channels. For adsorption of aromatics in MFI-type zeolites, when the loadings are lower than 4 molec./u.c., the molecules occupy the intersection of the channels. At higher loadings, the molecules occupy the void spaces in the channels. It can be observed that as  $k$  is decreased to  $k/k_B = 5 \cdot 10^2 \text{ K}^\circ\text{A}^{-2}$ , the shape of the isotherms for ethylbenzene and xylene isomers changes from type IV to type I. The PSD of the empty zeolite structure for  $k/k_B = 5 \cdot 10^2 \text{ K}^\circ\text{A}^{-2}$  (Fig. 4.3b) shows the absence of a pore size peak distinction between the channels and the intersections. This suggests that the changes that framework flexibility induces in the zeolite structure can change the shape of the adsorption isotherm of aromatics in MFI-type zeolites.

#### 4.3.5. DIFFUSION OF AROMATICS IN MFI-TYPE ZEOLITE

The free energy profiles of ethylbenzene and xylene isomers in an MFI-type zeolite as a function of framework flexibility are shown in Fig. 4.7. The dimensionless coordinate correspond to the dimensionless position across the *b*-crystallographic axis

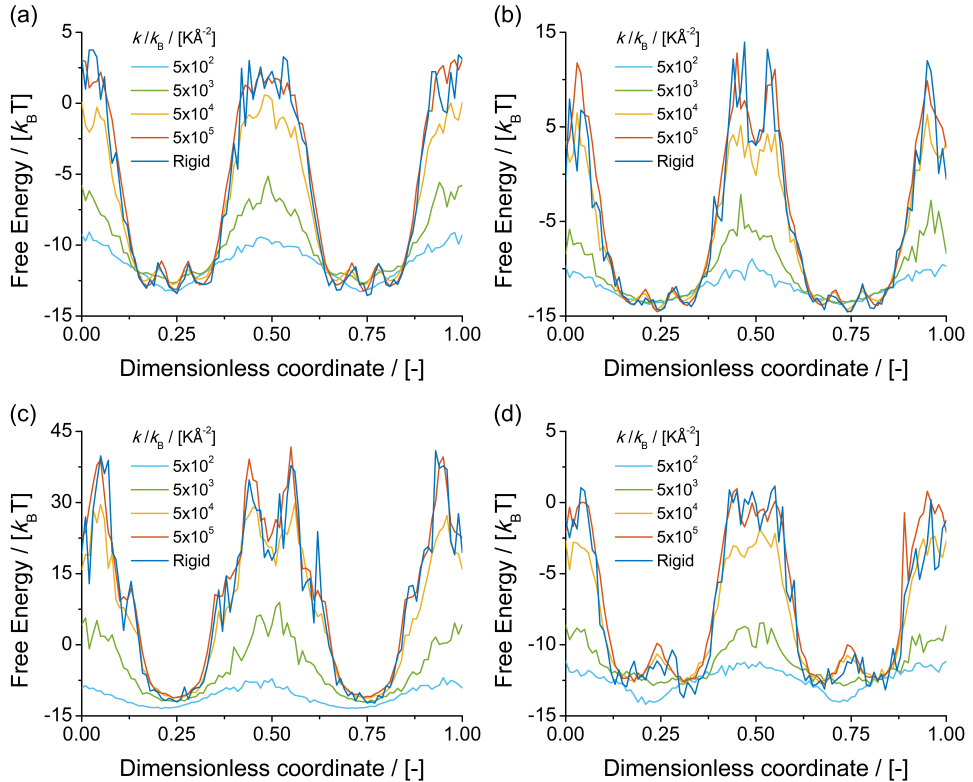


Figure 4.7: Free Energy profiles in the *b*-crystallographic axis (parallel to the straight channel) for (a) ethylbenzene, (b) *m*-xylene, (c) *o*-xylene, and (d) *p*-xylene at infinite dilution in an MFI-type zeolite [351] at 353 K, varying framework flexibility  $k$ . The dimensionless coordinate correspond to the dimensionless position across the *b*-crystallographic axis of the MFI-type zeolite unit cell.

of the MFI-type zeolite unit cell. The free energy profiles suggest that framework flexibility significantly influences the free energy barrier between the low energy states (intersections). As  $k$  is decreased, the free energy barrier between the intersections of the channels is decreased. This suggests that the pore size changes that framework flexibility induces on the zeolite framework have an important effect on the free energy of aromatic molecules in MFI-type zeolites.

The free energy profiles are used to compute the hopping rate  $k_{A \rightarrow B}^{\text{TST}}$  and the self-diffusion coefficient ( $D$ ) at infinite dilution of aromatics in the straight channel of a MFI-type zeolite framework using TST. In TST, it is assumed that all particles that reach the free energy barrier from a low energy site A to a low energy site B, eventually end up in B [227]. The hopping rates  $k_{A \rightarrow B}^{\text{TST}}$  are obtained by computing the relative probability to find a molecule on top of the free energy barrier, and the velocity of the molecule is given by a Maxwell distribution corresponding to the temperature of the system [144]. The hopping distance  $\lambda_{A \rightarrow B}$  is the distance between A and B.

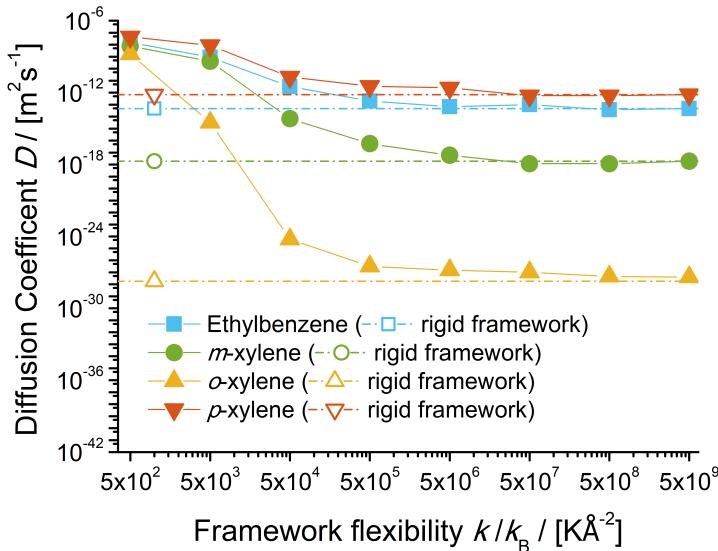


Figure 4.8: Self-diffusion coefficient  $D$  computed using Transition State Theory for ethylbenzene and xylene isomers in the straight channel of an MFI-type zeolite [351] at 353 K, varying framework flexibility  $k$ .

At infinite dilution, the self-diffusion coefficient is calculated using the expression  $D = k_{A \rightarrow B}^{\text{TST}} \cdot \lambda_{A \rightarrow B}^2$ . The reader is referred to refs. [144, 227, 230] for details about the calculation of diffusion coefficients from TST. The self-diffusion coefficients of ethylbenzene and xylene isomers in the straight channel of MFI-type zeolite at 353 K are shown in Fig. 4.8. It can be observed that framework flexibility has an important effect on the self-diffusion coefficient of aromatics in MFI-type zeolites. The highest self-diffusivity coefficients  $D$  are obtained when  $k/k_B = 5 \cdot 10^2 \text{ K\AA}^{-2}$  for all aromatics considered. As  $k$  is increased, the computed  $D$  are in agreement with the self-diffusion coefficient computed in the rigid framework. For all values of  $k$  considered (and the rigid structures),  $D_{p\text{-xylene}} > D_{\text{ethylbenzene}} > D_{m\text{-xylene}} > D_{o\text{-xylene}}$ . Comparing the self diffusion coefficients obtained when  $k/k_B = 5 \cdot 10^2 \text{ K\AA}^{-2}$  and  $D$  obtained in the rigid structure, framework flexibility affects the diffusion of aromatics molecules in an MFI-type zeolite differently:  $D_{\text{ethylbenzene}}$  increased from  $4.7 \cdot 10^{-14}$  to  $1.5 \cdot 10^{-8} \text{ m}^2 \text{s}^{-1}$ ;  $D_{m\text{-xylene}}$  increased from  $1.9 \cdot 10^{-18}$  to  $7.6 \cdot 10^{-9} \text{ m}^2 \text{s}^{-1}$ ;  $D_{o\text{-xylene}}$  increased from  $1.9 \cdot 10^{-28}$  to  $1.6 \cdot 10^{-9} \text{ m}^2 \text{s}^{-1}$ ;  $D_{p\text{-xylene}}$  increased from  $6.8 \cdot 10^{-13}$  to  $4.5 \cdot 10^{-8} \text{ m}^2 \text{s}^{-1}$ . Framework flexibility significantly changes  $D$  when  $k/k_B \leq 5 \cdot 10^6 \text{ K\AA}^{-2}$ . This suggests that the changes that framework flexibility induces on the pore sizes of the channels of the zeolite framework notably influence the estimation of  $D$ .

#### 4.4. CONCLUSIONS

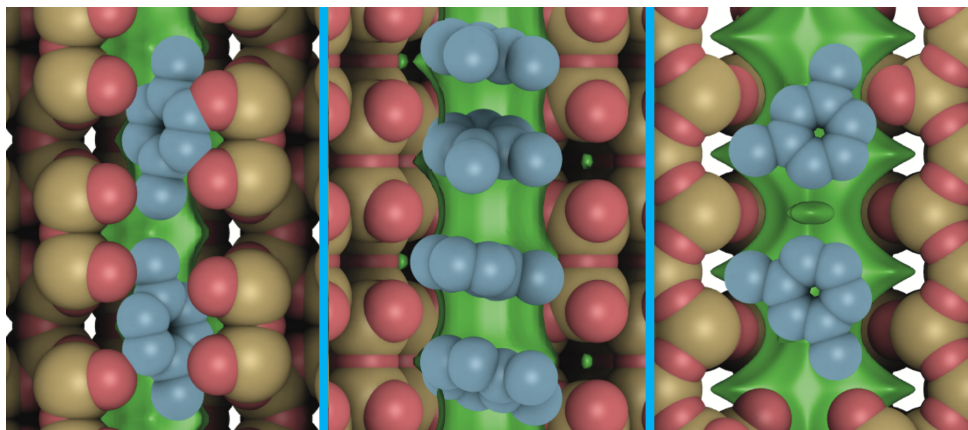
The influence of framework flexibility on the adsorption and diffusion behavior of C<sub>8</sub> aromatics in an MFI-type zeolite has been investigated using molecular simulations. It has been observed that -regardless of taking the bond lengths and angles from the crystallographic data- framework flexibility induces changes on the average zeolite structure. As the framework is more flexible, it is difficult to discriminate the channels and the intersections based on pore sizes. This has a significant effect on the Henry coefficient and the adsorption isotherms of aromatics in MFI-type zeolites. The Henry coefficient of aromatics in MFI-type zeolites is significantly affected by framework flexibility. With framework flexibility in the range of the original Demontis model (i.e.  $k/k_B = 5 \cdot 10^4 \text{ K\AA}^{-2}$ ), computed Henry coefficients of aromatics in MFI-type zeolites are lower than in the rigid framework. As the framework is more flexible, Henry coefficients are higher than in the rigid framework. When  $k/k_B = 5 \cdot 10^6 \text{ K\AA}^{-2}$ , a mean displacement of the zeolite atoms of 0.018 Å is enough to induce a significant change in the Henry coefficient of aromatics in MFI-type zeolites. This suggests that the interactions between the aromatic molecules and the zeolite framework are very susceptible to small displacements of the zeolite atoms affect and changes of the geometry of the zeolite pores. The 'flexible snapshot' method is useful for the description of the adsorption behavior at very low loadings/infinite dilution. For high pressures/loadings, the 'flexible snapshot' method does not yield the same loading as when the flexible framework is used. This suggests that the effect of the guest molecules on the zeolite framework should not be neglected. The adsorption isotherms are affected by framework flexibility. At low loadings, the influence of the framework flexibility on the adsorption is small. When the loadings are higher than 4 molec./u.c., small, lower framework flexibility  $k$  yields higher loadings than in the rigid framework. In the pressure range considered, the maximum loadings of aromatics in MFI-type zeolites computed depend on the framework flexibility. Higher maximum loadings are obtained when the framework is more flexible (i.e.  $k/k_B = 5 \cdot 10^2 \text{ K\AA}^{-2}$ ). For ethylbenzene, *m*-xylene and *p*-xylene, framework flexibility plays an important role when the loadings are higher than 4 molec./u.c.. For *o*-xylene, framework flexibility plays a role when the loadings are lower than 4 molec./u.c. The changes that framework flexibility induces in the zeolite structure can change the shape of the adsorption isotherm of aromatics in MFI-type zeolites for very flexible zeolite frameworks. Framework flexibility significantly decreases the free energy barriers of aromatics between the low energy sites of the zeolite framework. As the zeolite framework is more flexible, the self-diffusion coefficient is significantly increased. Framework flexibility has a remarkable effect on the adsorption and diffusion of aromatics in MFI-type zeolites. In the future, the development of force fields for zeolite framework flexibility should have a special focus on the interactions of bulky aromatic guest molecules with and within a zeolite framework.

# 5

## COMPETITIVE ADSORPTION OF XYLEMES AT CHEMICAL EQUILIBRIUM IN ZEOLITES

This chapter is based on the article:

S. Caro-Ortiz, E. Zuidema, M. Rigitto, D. Dubbeldam, T. J. H. Vlugt, *Competitive adsorption of xylenes at chemical equilibrium in zeolites*, *J. Phys. Chem. C*, [10.1021/acs.jpcc.0c09411](https://doi.org/10.1021/acs.jpcc.0c09411) (in press) [421].



## 5.1. INTRODUCTION

Several mechanisms influence the selective adsorption of molecules in zeolites [144, 422]. These mechanisms are based on enthalpy, shape, and entropy differences between the competing guest molecules [423]. The enthalpy difference between competing molecules is relevant when the change of enthalpy of the molecules transferred from the bulk phase into the zeolite is even slightly different. In this mechanism, the adsorption is driven by the attractions between the molecules and the zeolite atoms. At low loadings, when interactions among adsorbates can be neglected, there is selectivity towards molecules with stronger attractive interactions with the zeolite [424]. In the shape selectivity mechanism, the adsorption of molecules that do not fit in the pores of the zeolite is hindered [231]. Instead, only molecules that are smaller than the zeolite pores -and that can diffuse through the pores- are adsorbed. This size exclusion mechanism is related to entropic effects [425]. In the entropic selectivity mechanism, packing effects drive the selectivity. The efficiency with which the adsorbed molecules are arranged within the channels of the zeolite determines which molecules are preferentially adsorbed [425, 426]. This mechanism is particularly important at high loadings [427].

Molecular simulations are an extensively used tool to predict the thermodynamic properties of a wide diversity of systems [173]. Molecular simulations have been extensively used to predict the adsorption properties of hydrocarbons in zeolites [179–186, 188] and other nanoporous materials [190–193]. Commonly, Monte Carlo simulations (MC) in the grand-canonical ensemble (GCMC) can be used to compute sorbate loadings in a zeolite for different temperatures and pressures [197–199]. Several studies where MC are used to study adsorption of aromatics in zeolites can be found in literature [135, 200–210]. Most molecular simulations studies of adsorption of hydrocarbons in zeolites have focused on adsorption from a vapor-phase [202]. This is due to the difficult insertion and deletion of molecules at conditions close to saturation, leading to inefficient simulations [239]. However, advanced biasing techniques -such as Continuous Fractional Component (CFCMC) or Configurational-Bias (CBMC)[243]- can be used nowadays in Monte Carlo simulations to overcome this issue. In practice, most C<sub>8</sub> processing technologies have classically considered adsorption from a vapor phase. More recently, there has been interest in adsorption from a liquid phase [236]. This leads to an efficient use of all the pore volume of the zeolite. Liquid phase adsorption is preferred due to its operational, maintenance and environmental advantages over other processing technologies [237].

The adsorption of xylene isomers in zeolites and the mechanisms that drive adsorption are studied using Monte Carlo simulations. This article aims to study the competitive adsorption of xylene isomers in selected zeolite frameworks at conditions relevant for industrial purposes. The prediction of the adsorption equilibrium of multiple components is one of the most challenging problems in adsorption [159, 160, 428]. Typical processing of xylenes use the mixture of xylenes at chemical equilibrium as feedstock. For this reason, the composition of a mixture of xylene isomers at chemical equilibrium is computed by MC simulations and used as a input for GCMC simulations of adsorption in zeolites. The calculations of the compositions

of the mixtures at chemical equilibrium also yield the chemical potentials and fugacity coefficients of xylene isomers [295]. For the grand-canonical ensemble ( $\mu VT$ ), there is thermodynamic equilibrium between the adsorbed molecules and the reservoir [429]. The fugacity coefficients and the composition of the mixture at chemical equilibrium are used to describe the reservoir for GCMC simulations. As there is chemical equilibrium in the reservoir, there must be chemical equilibrium for the molecules adsorbed in the zeolite framework. The adsorption of xylenes in zeolites from a vapor and a liquid phase is computed at 523 K as a function of the total pressure. This temperature is chosen as it is high enough to promote isomerization of xylene isomers catalyzed by acid sites in zeolites [311, 430–432]. Pressures of interest for industrial processing of xylenes in the liquid phase using zeolites at temperatures close to 523 K are in the range of 15 to 40 bar [433–435]. In this work, the pressures considered for the simulations are in the range of 0.03 to 300 bar. To investigate the dependence of xylenes adsorption on the zeolite structure, nine different zeolite types are chosen: FAU, MWW, AFI, MEL, MOR, BEA, MRE, MFI, and MTW. These zeolite types are considered as part of the most commonly used in industry, including four out of the so-called 'big five' zeolite types [107, 128]. These zeolite types are shown in Figs. 1.3 and 5.1. Also, a characterization of the selected zeolite frameworks is presented.

This chapter is organized as follows. The methods are explained in section 5.2. The characterization of the selected zeolite frameworks, computed heats of adsorption and adsorption isotherms of xylenes in the zeolite frameworks are reported and discussed in section 5.3. It is shown that the type and topology of the zeolite framework influence the mechanisms for selective adsorption of xylene isomers in different zeolites. The concluding remarks regarding the competitive adsorption of xylenes in zeolites are discussed in Section 5.4.

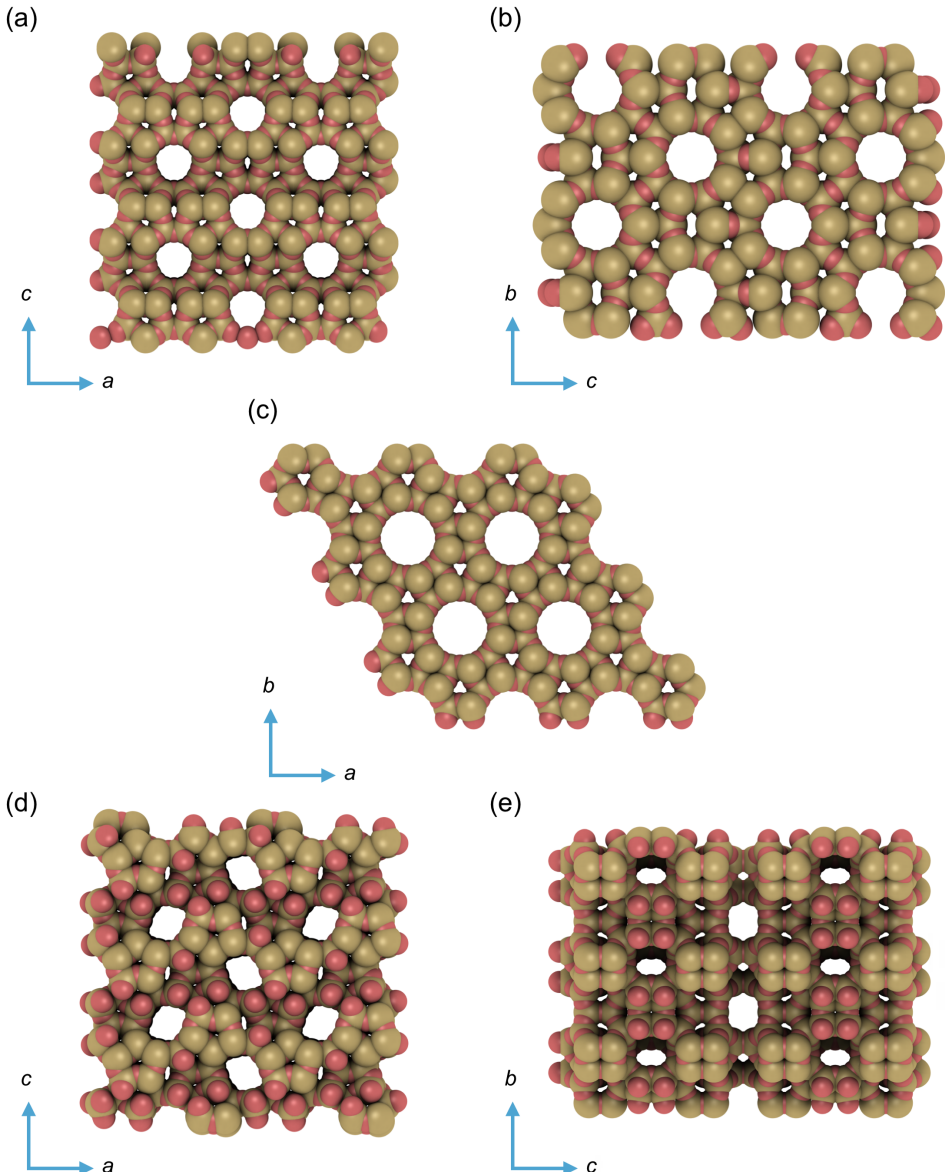


Figure 5.1: Framework structures of (a) MEL-type zeolite, (b) MRE-type zeolite, (c) AFI-type zeolite, (d) MTW-type zeolite, and (e) MWW-type zeolite. The framework structures of the other zeolite types considered in this chapter can be found in Fig. 1.3. Silicon and oxygen atoms are shown in yellow and red, respectively. The maximum diameter of a sphere that can fit in these zeolite types are: 7.72, 6.36, 8.3, 6.08, and 9.69 Å, respectively [123]. MEL- and MRE-type zeolites contain 10-membered ring (mr) channels. MTW- and AFI-type zeolites contain 12-mr channels. MWW-type zeolites contain 12-mr cages and 10-mr channels.

## 5.2. METHODS

The compositions of the mixture at chemical equilibrium and densities of the mixture of xylene isomers are obtained using force field-based Monte Carlo simulations in the isothermal-isobaric ensemble (*NPT*), combined with the Reaction ensemble [436–439]. In the reaction ensemble, trial moves are attempted to transform reactant molecules of a chemical reaction into reaction product molecules. This method considers chemical reactions as Monte Carlo trial moves, without considering kinetics or the reaction mechanism. The Brick-CFCMC software [295] is used for these simulations. The Continuous Fractional Component Monte Carlo (CFCMC) [240, 241] algorithm is used for having efficient insertions and deletions of molecules in the system [241–243]. Fugacity coefficients of xylene isomers in the mixture are obtained from the chemical potential computed with the CFCMC algorithm [242, 294, 439]. Details about the conversion of chemical potentials to fugacity coefficients can be found in Appendix A.4. A MC cycle is defined as the maximum between 20 and  $N$ -move-attempts, with  $N$  being the number of molecules in the system [295, 365].

In the CFCMC algorithm, the interactions of a fractional molecule are scaled by the so-called  $\lambda$  parameter. The  $\lambda$  parameter scales the interactions of the fractional molecule in the range 0 to 1 (0 for no interactions with surrounding molecules, and 1 for full interaction with surrounding molecules). The  $\lambda$ -trial moves are biased to obtain a flat probability distribution of  $\lambda$ . The simulations are initialized with  $10^5$  MC cycles and only translation and rotation trial moves are attempted. After initialization, an equilibration run of  $5 \cdot 10^5$  MC cycles is performed. All the types of trial moves considered are allowed and the biasing factors for the  $\lambda$ -trial moves of the CFCMC algorithm are calculated. After equilibration, ensemble averages are obtained in a  $5 \cdot 10^5$  MC cycles production stage. The reported errors account for the 95% confidence interval calculated by dividing the production run into five parts and computing the standard deviation. The initial system contains a total of 300 molecules (200 *m*-xylene, 50 *o*-xylene, and 50 *p*-xylene). The simulations are performed at pressures ranging between 0.03 bar and 300 bar. This pressure range considers both a vapor and a liquid phase. The initial volume of the simulation box for the simulations in the vapor phase is estimated assuming ideal gas behavior. The initial volume of the simulation box for the simulations of the liquid phase is  $40^3 \text{ \AA}^3$ .

Two isomerization reactions are considered:  $m\text{-xylene} \leftrightarrow o\text{-xylene}$  and  $m\text{-xylene} \leftrightarrow p\text{-xylene}$ . The simulations using the reaction ensemble require the partition functions of the isolated molecules of all the species involved in the reaction as input. The partition functions of isolated molecules can be obtained using standard thermodynamic tables (e.g. JANAF tables [440]) or by quantum mechanic calculations [441]. Mullen and Maginn [442] computed the composition of xylene mixtures at chemical equilibrium as a function of temperature using the reaction ensemble Monte Carlo simulations. These authors found that the use of tabulated free energies of reaction for the calculation of partition functions yield the best agreement with experimental composition of the bulk fluid phase of xylene mixtures. The Brick software [295] uses the ideal gas partition function of each component as input. In this work, the isolated molecule partition functions are obtained using thermody-

namic tables. The reader is referred to Appendix A.2 for detailed steps to obtain the partition functions of xylenes using thermodynamic tables for simulations of the reaction ensemble in Brick-CFCMC [295]. The ideal gas partition function of each component as input for Brick-CFCMC are listed in table A.9 of Appendix A.2.

The composition of the mixture at chemical equilibrium and the fugacity coefficients of xylene isomers computed in the *NPT*-ensemble combined with the reaction ensemble are used as input for the computations of adsorption in zeolites. The computations of adsorption are performed using the CFCMC [240, 241] algorithm in the grand-canonical ensemble. The RASPA software [365, 366] is used for all the simulations of adsorption. The all-silica zeolite structures are obtained from the IZA-SC Database of Zeolite Structures [123]. The volume of the simulation box is kept fixed. Periodic boundary conditions are applied. The computations of adsorption do not consider reaction trial moves.

The interactions between the zeolite and guest hydrocarbons are modeled using the TraPPE-zeo model [396]. In this force field, all oxygen and silicon atoms are modeled with LJ interactions and partial charges. As discussed in chapter 3, it is known that framework flexibility plays a significant role in the adsorption of aromatics in zeolites. For very flexible zeolite frameworks, loadings up to two times larger than in a rigid zeolite framework are obtained at a given pressure (see chapter 4). However, models for framework flexibility should not be blindly applied to zeolites [204]. The intra-framework interactions in flexible framework models induce small but important changes in the atom positions of the zeolite, and hence in the adsorption isotherms [204]. The effects of using models for framework flexibility in different zeolite types is unknown. For these reasons, the zeolite frameworks are considered rigid. As discussed in chapter 2, force fields for the interactions between aromatic molecules are typically fitted to model the vapor-liquid equilibrium with LJ potentials or a combination of LJ and electrostatic interactions [257, 258]. Guest-guest force field that use electrostatic interactions (such as OPLS [253, 297]) have been used to a great extend for the simulation of adsorption of aromatics in zeolites [200–202, 402]. The electrostatic interactions of guest-guest force fields of aromatics are fitted for VLE and not for the interaction with a host framework [204]. Also, the electrostatic interactions included in the TraPPE-zeo model [396] are fitted and tested for the adsorption of CO<sub>2</sub>, and not for aromatic/zeolite systems. It is convenient to use a guest-guest force field that does not include electrostatic interactions. In this work, the guest-guest interactions are modeled using the TraPPE-UA [252, 403] force field. This force field considers single uncharged interaction site representing each CH<sub>x</sub> group in the aromatic molecules. Electrostatic interactions are not considered in this work. Although the presence of non-framework cations may change the adsorption of xylenes [443], this is not considered in this work as it would interfere with understanding the effect of the zeolite type on adsorption. The interactions between different atom types are obtained using Lorentz-Berthelot mixing rules [292]. A cut off radius of 14 Å is applied for all LJ interactions and analytic tail corrections are used [367]. All force field parameters are listed in tables A.2 and A.3 of Appendix A.1.

At each MC cycle, trial moves attempt to rotate, displace, randomly reinsert, and

insert/remove adsorbates. Also,  $\lambda$ -trial moves scale the interactions of the fractional molecule (via the CFCMC algorithm [240, 241]). The simulations use  $10^5$  MC cycles to initialize the system. The initialization run only allows translation, rotation, and insertion/deletion, and reinsertion trial moves. After initialization, a stage of  $5 \cdot 10^5$  MC cycles are used to equilibrate the CFCMC biasing factors. Ensemble averages are obtained in a  $5 \cdot 10^5$  MC cycles production stage. The reported errors account for the 95% confidence interval calculated by dividing the production run into five parts and computing the standard deviation.

The pore size distribution (PSD) of each zeolite structure considered in this work is calculated geometrically with the method of Gelb and Gubbins [388, 389]. The heat of adsorption of xylenes at infinite dilution in the zeolite structures are calculated via Widom's test-particle insertion method [390]. The heat of adsorption is computed in a  $10^5$  MC cycles production run. Enthalpies of adsorption at 523 K from the mixture at chemical equilibrium to the zeolite frameworks at 0.3 and 30 bar are computed by grand-canonical Monte Carlo simulations in a production stage of  $5 \cdot 10^6$  MC cycles. The helium void fraction (HVF) and the gravimetric surface area of the zeolite frameworks used in this work are determined using the iRASPA visualization software [22]. The HVF is determined by probing the framework with a non-adsorbing helium molecule using Widom's test-particle insertion method [390]. The surface area is determined by probing the zeolite framework with a nitrogen molecule. The HVF, surface area, and the amount of unit cells considered for each zeolite framework used in this work are listed in table 5.1. The discussion of the zeolite types is ordered based on the maximum diameter of a sphere that can be included in the zeolite framework [123]. This diameter is listed in table 5.1.

For comparison with the adsorption of the mixture of xylene isomers, the Ideal Adsorbed Solution Theory (IAST) [444, 445] is used to predict the loadings of the xylene mixture using single component adsorption isotherms. The single component adsorption isotherms are computed using the fugacity coefficients for each xylene isomer as input. The IAST predictions are computed using the pyIAST software [446].

Multiple linear regression [447, 448] is used to compute changes in enthalpy and entropy due to the transfer of one xylene molecule from the bulk phase to the zeolite framework. Details about these calculations can be found in Appendix A.3.

Table 5.1: Helium void fraction and gravimetric surface area computed using iRASPA [22], unit cell parameters, and amount of unit cells considered for the simulations of each zeolite framework used in this work. \*Maximum diameter of a sphere that can be included in the zeolite framework [123].

Zeolite type	Helium void fraction / [-]	Surface area / [ $\text{m}^2/\text{g}$ ]	Unit cells	Unit cell dimensions / [ $\text{\AA}$ ]			Unit cell angles / [ $^\circ$ ]			Max. diam. sphere* / [ $\text{\AA}$ ]
				a	b	c	$\alpha$	$\beta$	$\gamma$	
FAU	0.494	1212.8	2 x 2 x 2	24.345	24.345	24.345	90	90	90	11.24
MWW	0.395	965.1	3 x 3 x 2	14.390	14.390	25.198	90	90	120	9.69
AFI	0.291	602.4	3 x 3 x 4	13.8271	13.8271	8.58035	90	90	120	8.3
MEL	0.309	736.1	2 x 2 x 3	20.270	20.270	13.459	90	90	90	7.72
MOR	0.309	1002.9	2 x 2 x 4	18.256	20.534	7.542	90	90	90	6.7
BEA	0.415	1063.5	3 x 3 x 2	12.632	12.632	26.186	90	90	90	6.68
MRE	0.172	354.2	4 x 2 x 2	8.257	14.562	20.314	90	90	90	6.36
MFI	0.265	657.5	2 x 2 x 3	20.090	19.738	13.142	90	90	90	6.36
MTW	0.238	537.4	2 x 6 x 3	25.552	5.256	12.117	90	109.312	90	6.08

## 5.3. RESULTS AND DISCUSSION

### 5.3.1. PROPERTIES OF MIXTURE OF XYLEMES

The properties of the mixture of xylene isomers at chemical equilibrium are calculated by Monte Carlo simulations in the *NPT*-ensemble, combined with the reaction ensemble. Fig. 5.2 shows the computed equilibrium composition, density of the mixture, and fugacity coefficients of xylenes as a function of pressure at 523 K. The simulations suggest that the composition of xylene isomers in the mixture at chemical equilibrium does not significantly vary with changes of pressure at 523 K. Taylor et al. [449] reported that at 500 K the mixture of C<sub>8</sub> aromatic mixture has an equilibrium composition of: 3.7% ethylbenzene, 52.8% *m*-xylene, 20.4% *o*-xylene, and 23.2% *p*-xylene. In this work, the equilibrium composition of the mixture of xylenes at 0.94 bar and 523 K is: 54.6% *m*-xylene, 21.5% *o*-xylene, and 23.9% *p*-xylene. The computed composition of the mixture at chemical equilibrium is in agreement with the experimental data. The computed composition of the mixture at chemical equilibrium are in excellent agreement with the equilibrium composition estimated by Mullen and Maginn [442] at 1 bar by MC simulations in the reaction ensemble.

Given the similarity of the thermodynamic properties of xylene isomers [257, 258], it is expected that the vapor pressure of the mixture of xylenes is close to the vapor pressure of the xylene isomers. From experiments, it is known that the vapor pressure of *m*-xylene (at 523 K) is 9.85 bar [450], for *o*-xylene (at 523 K) is 8.83 bar [451], and for *p*-xylene (at 520 K) is 9.419 bar [452]. It is expected that the vapor pressure of the mixture of xylenes at chemical equilibrium is close to these pressures. From the computed densities of the mixture of xylene isomers, it is observed that the mixture is in vapor phase when the pressure is lower than 5.3 bar, and that the mixture is in liquid state when the pressure is higher than 16.8 bar. The density of the mixture of xylenes as a function of pressure suggests that the phase change from vapor to liquid occurs at some point between 5.3 and 16.8 bar. From the bulk phase simulations, only an estimation of the composition of the mixture at chemical equilibrium and the fugacity coefficients are required. As such, the properties for pressures close to the phase change at 523 K are not computed. The computed fugacity coefficients significantly decrease from pressures higher than 5.3 bar. The fugacity coefficients of the three xylene isomers are nearly identical at 523 K and pressures between 0.03 and 300 bar.

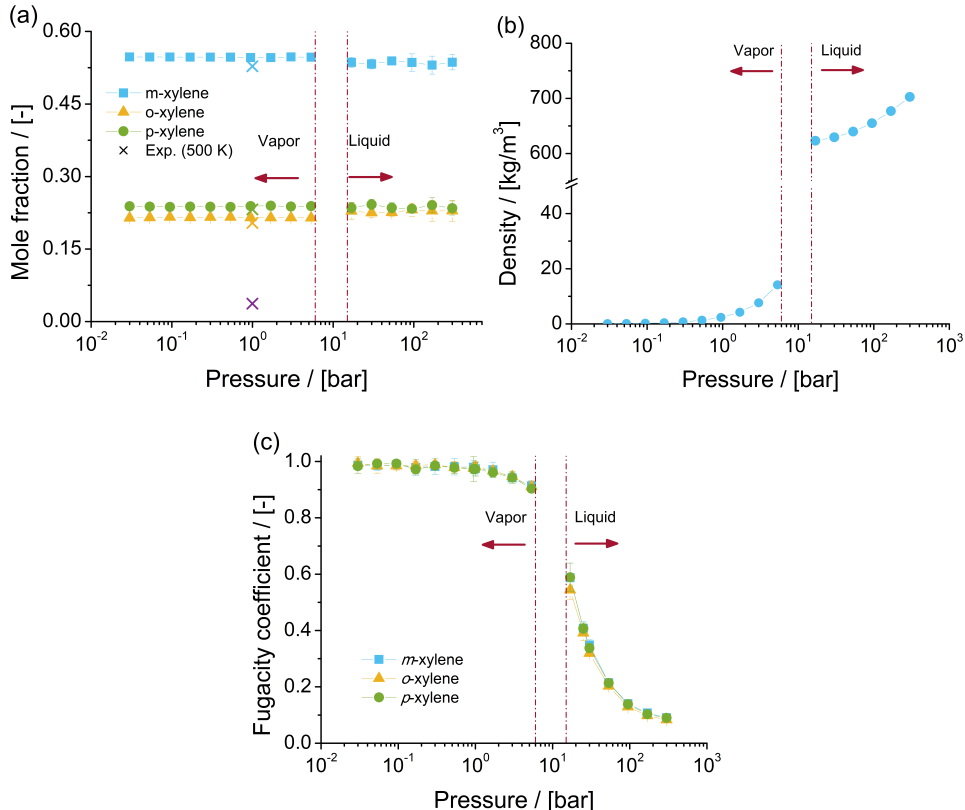


Figure 5.2: Properties of the mixture of xylene isomers at 523 K as computed in this work by Monte Carlo simulations in the *NPT*-ensemble combined with the reaction ensemble. (a) Composition of the mixture of xylene isomers at chemical equilibrium as a function of pressure. Crossed symbols denote the mole fractions of xylenes and ethylbenzene (purple) in the mixture at chemical equilibrium determined from experiments by Taylor et al. [449] at 500 K. The mole fraction of ethylbenzene in the experiments is very low, and the computed mole fractions of xylenes match the experimental mole fractions well. (b) Density of the mixture of xylene isomers as a function of pressure. (c) Fugacity coefficients of xylene isomers as a function of pressure.

### 5.3.2. ZEOLITE STRUCTURES

The pore size distribution (PSD) of the zeolite frameworks considered in this work are shown in Fig. 5.3. The PSD is calculated geometrically with the method of Gelb and Gubbins [388, 389]. In this method, the diameter of the largest sphere that does not intercept any framework atoms is computed for each point in the void space of the framework. In a PSD of zeolite frameworks, a peak in the distribution denotes the diameter of a cavity or a channel. For FAU-type zeolite, the cages are denoted at a diameter of *ca.* 9.5 Å. For MWW-type zeolite, the two independent pore systems are represented by two ranges of diameters in the pore-size distribution. The 10-ring pore system is denoted between 3-5 Å approximately. The 12-ring pore system is denoted between 6-8.5 Å. For AFI-type zeolite, the channel is denoted at a diameter of approx. 7 Å. For MEL-type zeolite, a peak at a diameter of approx. 4.5 Å denotes the channels, and the distribution at diameters larger than 5.5 Å denote the intersections of the channels. For MOR-type zeolite, the peak at a diameter of approx. 5.5 Å denote the 12-ring channels. The small peak at a diameter of approx. 4 Å denotes the 8-ring side pockets that link the 12-ring channels. For BEA-type zeolite, the channel and the intersection of the channels are denoted at a diameter of approx. 5.5 Å. For MFI-type zeolite, two peaks are observed: one at a diameter of approx. 3.5 Å and one at approx. 5 Å. These peaks correspond to the channels (zigzag and straight) and intersection of the channels, respectively. For MRE-type and MTW-type zeolite, the peaks at a diameter of approx. 5 and 4.5 Å denote the channels, respectively.

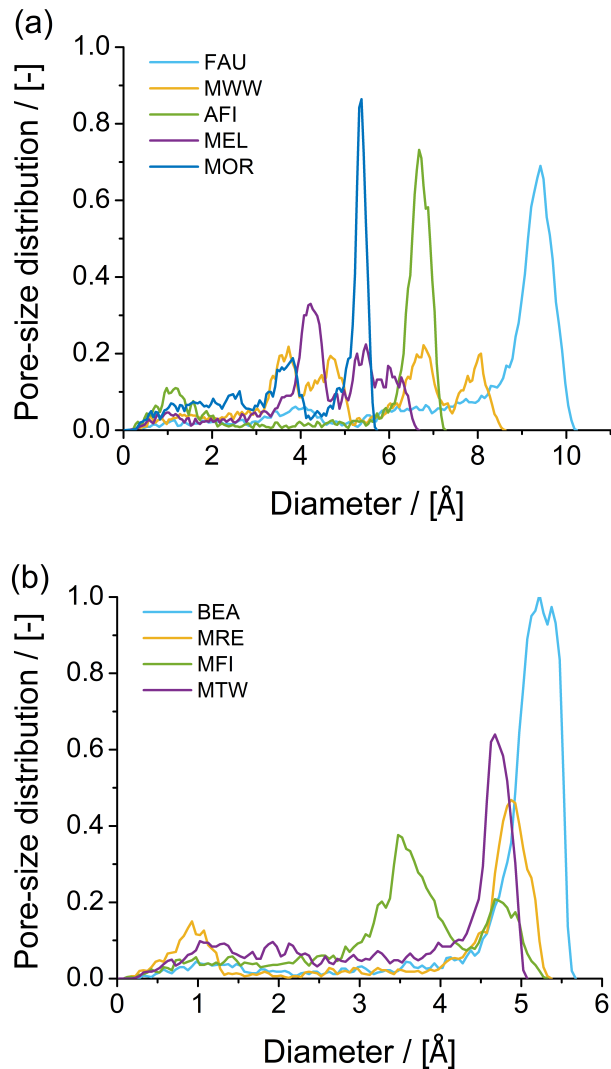


Figure 5.3: Pore size distribution (PSD) of the zeolite frameworks considered in this work computed with the method of Gelb and Gubbins [388]. In this method, the diameter of the largest sphere that does not intercept any framework atoms is computed for each point in the void space of the zeolite framework. (a) PSD for FAU-type, MWW-type, AFI-type, MEL-type, and MOR-type zeolites. (b) PSD for BEA-type, MRE-type, MFI-type, and MTW-type zeolites.

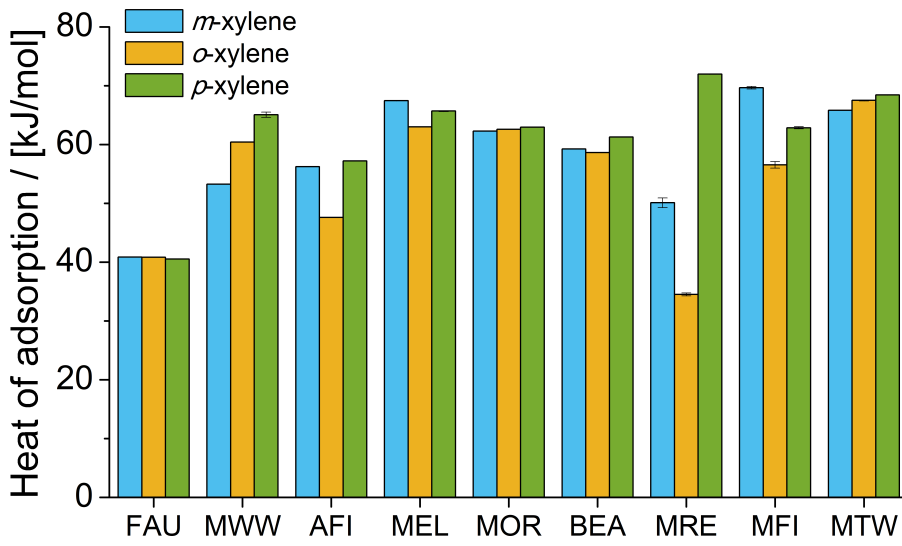


Figure 5.4: Heat of adsorption at infinite dilution of xylene isomers at 523 K in the zeolite framework types considered in this work as computed by Monte Carlo simulations.

### 5.3.3. ADSORPTION OF XYLEMES IN ZEOLITES

The heats of adsorption at infinite dilution of xylene isomers at 523 K in the zeolite frameworks considered in this work are shown in Fig. 5.4. In FAU-type zeolite, there is enthalpic preference for *m*-xylene and *o*-xylene over *p*-xylene. In AFI-type, MWW-type, BEA-type, MRE-type, and MTW-type zeolite, there is an enthalpic preference for *p*-xylene over *o*-xylene and *m*-xylene. For MOR-type zeolite, *p*-xylene and *o*-xylene are preferentially adsorbed based on enthalpy. For MFI-type and MEL-type zeolite, there is an enthalpic preference for *m*-xylene. In the following section, the siting of the xylene molecules in each zeolite framework is discussed and linked to the heat of adsorption and changes in enthalpy and entropy due to the transfer of xylenes from the bulk mixture to the zeolite. Table 5.2 lists the preferential adsorption of xylene isomers based on the heat of adsorption at infinite dilution. The computed heat of adsorption of xylenes adsorbed from the mixture at chemical equilibrium at 30 bar and 523 K in the zeolite types considered in this work are shown in Fig. A.1.

The adsorption isotherms of single component xylene isomers and the mixture of isomers at chemical equilibrium in FAU-type zeolite at 523 K are shown in Fig. 5.5. The single component isotherms of the three isomers suggest that there is no preferential adsorption for any isomer. Zheng et al. [206] reported the adsorption of aromatics in FAU-type zeolites. The same packing efficiency of C<sub>8</sub> aromatics in the cages of FAU-type zeolites is observed. In Fig. 5.5a, it is observed that nearly identical loadings of the three xylene isomers in FAU-type zeolite as a function of pressure are computed. This is expected due to the large pore size of FAU-type zeolite.

Fig. 5.5b shows the adsorption isotherm of the mixture of xylenes at chemical equilibrium in FAU-type zeolite. It is observed that the loadings of *m*-xylene are higher than for the other isomers. This is related to the high mole fraction of *m*-xylene in the bulk phase, compared to the mole fractions of the other isomers. The loadings of *o*-xylene in FAU-type zeolite are higher than the loadings of *p*-xylene.

Fig. 5.5c shows the composition of the mixture of xylenes adsorbed in FAU-type zeolite compared to the composition of mixture in the bulk phase (Fig 5.2a). It is observed that the composition of the adsorbed fluid does not change with the pressure. The mole fractions of *p*-xylene in the adsorbed phase are lower than the mole fractions of *p*-xylene in the bulk phase. Fig 5.5d shows the changes in enthalpy and entropy due to the transfer of a xylene molecule between the bulk mixture and FAU-type zeolite for 0.3 and 30 bar and 523 K. At 0.3 bar, adsorption is driven by enthalpic changes. At 30 bar, the changes in entropy (multiplied by the absolute temperature) are larger than the changes in enthalpy. This suggests that for adsorption from the liquid phase, changes in entropy significantly influence adsorption and the arrangement of xylenes in the cages of FAU-type zeolite. The changes in enthalpy and entropy due to the transfer of xylene molecules from the bulk phase to the zeolite (either at 0.3 or 30 bar) do not show any selectivity for a xylene isomer.

A typical snapshot of the simulation of adsorption of the mixture of xylene isomers at 523 K and 300 bar is shown in Fig. 5.5e. It is observed that xylene molecules are almost fluid-like in the cages of FAU-type zeolite. At high pressure -or when molecules are adsorbed from the liquid phase-, each cage hosts two or more xylene molecules. The loadings predicted with IAST are in agreement with the simulations of adsorption of the mixture of xylenes. This suggest that xylene molecules compete for the same adsorption sites in the FAU-type zeolite.

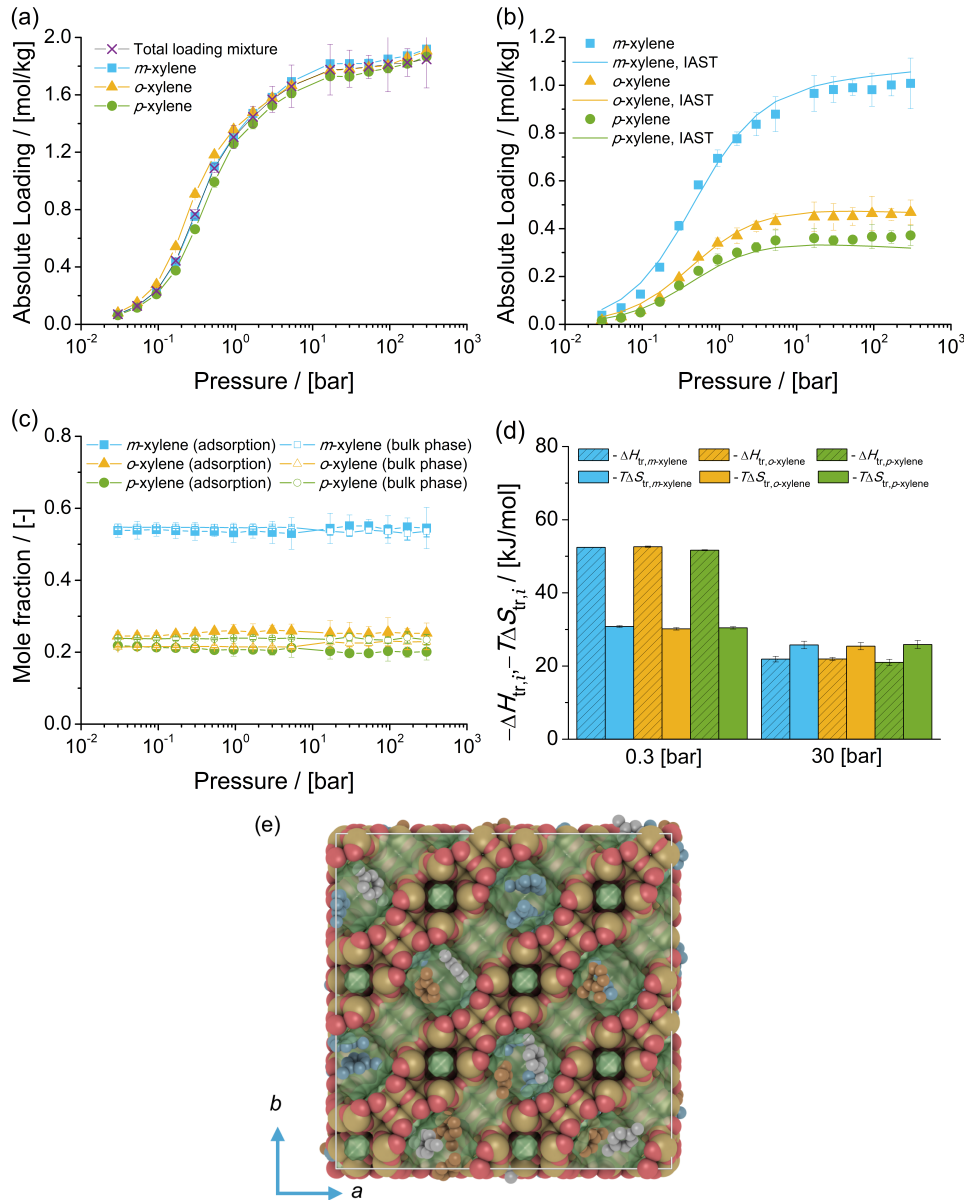


Figure 5.5: Adsorption isotherms of xylene isomers as (a) single components (total loading mixture is the sum of the loadings of xylenes from the mixture at chemical equilibrium), and (b) mixture at chemical equilibrium in FAU-type zeolite at 523 K. For adsorption of xylenes in FAU-type zeolite, 1 mol/kg is equal to 11.5 molecules/unit cell. (c) Mole fractions of xylene isomers as a function of total pressure for the mixture at chemical equilibrium adsorbed in FAU-type zeolite, and for the bulk phase. The composition in the bulk phase follows from Fig 5.2a. (d) Changes in enthalpy  $\Delta H_{\text{tr},i}$  and entropy  $T\Delta S_{\text{tr},i}$  at 523 K due to the transfer of xylene *i* from the fluid phase mixture at chemical equilibrium to FAU-type zeolite at 0.3 bar and 30 bar. (e) Typical snapshot of the simulation of adsorption of the mixture of xylene isomers in FAU-type zeolite at 523 K and 300 bar. *m*-Xylene is shown in blue, *p*-xylene in grey, and *o*-xylene in orange. The snapshot shows how several xylenes are hosted in the cages of FAU-type zeolite.

The adsorption isotherms of xylene isomers as single components and the mixture of xylenes at chemical equilibrium in MWW-type zeolite at 523 K are shown in Fig. 5.6. The single components isotherms show that for pressures lower than 5.3 bar (adsorption from vapor phase), the loadings of *o*-xylene are higher than for *p*-xylene and *m*-xylene. For pressures higher than 16.8 bar (i.e. adsorption from liquid phase), the loadings of *m*-xylene are higher than for *p*-xylene and *o*-xylene.

For the adsorption isotherm of the mixture of xylenes at chemical equilibrium, there is a preferential adsorption of *o*-xylene over *m*-xylene and *p*-xylene. Fig. 5.6c shows the composition of the mixture of xylenes adsorbed in MWW-type zeolite compared to the composition of the mixture in the bulk phase as a function of pressure. It is observed that for the adsorbed molecules, the mole fractions of *m*-xylene and *p*-xylene are nearly identical. The heat of adsorption of xylenes in MWW-type zeolite at infinite dilution show an energetic preference for *p*-xylene over the other isomers. Fig 5.6d shows the changes in enthalpy and entropy due to the transfer of a xylene molecule between the bulk mixture and MWW-type zeolite for 0.3 and 30 bar at 523 K. At 0.3 bar, adsorption is driven by enthalpy and there is an enthalpic preference for *p*-xylene over *o*-xylene and *m*-xylene. At 30 bar, the changes in entropy (multiplied by the absolute temperature) are larger than the changes in enthalpy for each xylene isomer. The adsorption of *o*-xylene is almost equally driven by enthalpic and entropic changes. For *m*-xylene and *p*-xylene, adsorption is hindered by entropic effects. For pressures higher than 16.8 bar, the loadings predicted with IAST are not in agreement with the simulations of adsorption of the mixture of xylenes. IAST does not provide a suitable prediction of the component loadings if there is a segregation of the preferential adsorption sites [453–455]. For the adsorption of xylene isomers in MWW-type zeolite, the isomers do not compete for the same adsorption sites. *o*-Xylene is preferentially adsorbed in the 12-ring cages. *m*-Xylene and *p*-xylene are preferentially adsorbed in the 10-ring channels. Fig. 5.6e shows a typical snapshot of the simulation of adsorption of the mixture of xylenes at chemical equilibrium at 523 K and 300 bar. It is observed that for the mixture of xylenes at chemical equilibrium, the 12-ring cages preferentially host *o*-xylene. *m*-Xylene and *p*-xylene are hosted in the 10-ring channels.

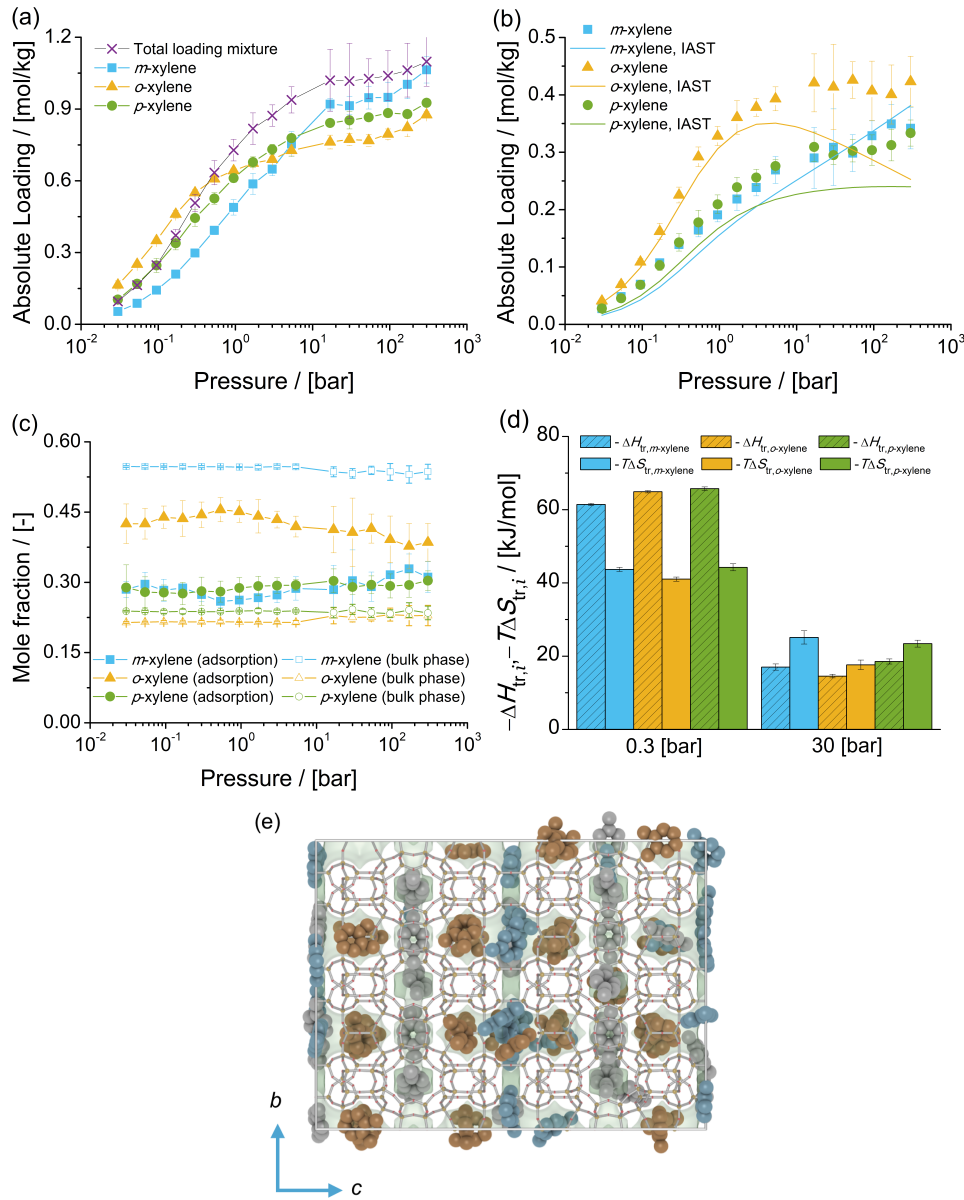


Figure 5.6: Adsorption isotherms of xylene isomers as (a) single components (total loading mixture is the sum of the loadings of xylenes from the mixture at chemical equilibrium), and (b) mixture at chemical equilibrium in MWW-type zeolite at 523 K. For adsorption of xylenes in MWW-type zeolite, 1 mol/kg is equal to 4.3 molecules/unit cell. (c) Mole fractions of xylene isomers as a function of total pressure for the mixture at chemical equilibrium adsorbed in MWW-type zeolite, and for the bulk phase. The composition in the bulk phase follows from Fig 5.2a. (d) Changes in enthalpy  $\Delta H_{\text{tr},i}$  and entropy  $T\Delta S_{\text{tr},i}$  at 523 K due to the transfer of xylene *i* from the fluid phase mixture at chemical equilibrium to MWW-type zeolite at 0.3 bar and 30 bar. (e) Typical snapshot of the simulation of the mixture of xylene isomers at chemical equilibrium at 523 K and 300 bar. *m*-Xylene is shown in blue, *p*-xylene in grey, and *o*-xylene in orange. *o*-Xylene is located in the 12-ring cages of the MWW-type zeolite. *m*-Xylene and *p*-xylene are located in the 10-ring channels.

The adsorption isotherms of xylene isomers as single components and the mixture of isomers at chemical equilibrium in AFI-type zeolite at 523 K are shown in Fig. 5.7. The single component isotherms show a significant adsorption selectivity of *o*-xylene over *m*-xylene and *p*-xylene. This is in agreement with the observations of Chiang et al. [456] who studied the adsorption of xylenes in AlPO<sub>4</sub>-5 (an AFI-type zeolite) via experiments.

The adsorption isotherm of the mixture of xylenes at chemical equilibrium shows a significant selectivity of *o*-xylene over *m*-xylene and *p*-xylene for pressures higher than 16.8 bar, i.e. adsorption from the liquid phase. The total loading of the mixture is lower than the single component isotherm for *o*-xylene (Fig. 5.7a). This suggest that the preferential adsorption of *o*-xylene from the mixture is affected by guest-guest interactions between *o*-xylene and the other isomers. The loadings predicted with IAST agree with the simulations of adsorption of the mixture of xylenes. Fig. 5.7c shows the composition of the mixture of xylenes adsorbed in AFI-type zeolite compared to the composition of the mixture in the bulk phase as a function of pressure. It is observed that for pressures higher than 0.53 bar, the composition of the adsorbed molecules significantly changes as a function of the pressure. At low pressures, the adsorption of *m*-xylene is higher than for the other isomers. At pressures higher than 0.53 bar, the mole fraction of *o*-xylene is significantly higher than for the other isomers. At 300 bar, the mole fraction of *o*-xylene in the adsorbed phase is 0.92. The heats of adsorption of xylene isomers at infinite dilution in AFI-type zeolite show an energetic preference for *p*-xylene. Fig 5.7d shows the changes in enthalpy and entropy due to the transfer of a xylene molecule between the bulk mixture and AFI-type zeolite for 0.3 and 30 bar at 523 K. At 0.3 bar, adsorption is driven by enthalpic changes due to the transfer of xylenes to the zeolite. At 30 bar, adsorption of *m*-xylene and *p*-xylene is significantly affected by entropic changes. For *o*-xylene, adsorption is almost equally driven by entropic and enthalpic changes. Fig. 5.7e shows a typical snapshot of the adsorption of *m*-xylene and *p*-xylene in AFI-type zeolite. At least one methyl group of these molecules is aligned with the channel direction. Fig. 5.7f shows a typical snapshot of the adsorption of *o*-xylene in AFI-type zeolite. Face-to-face stacking of *o*-xylene molecules is observed. The aromatic ring of *o*-xylene is perpendicular to the direction of the channel. This arrangement of *o*-xylene molecules has been previously observed by Torres-Knoop et al. [457] for the adsorption of an equimolar mixture of xylene isomers and ethylbenzene in AFI-type zeolite. In literature, the face-to-face stacking has been related to entropic effects [426, 457], i.e. how efficiently xylene molecules are arranged. The simulations from this work suggest that the preferential adsorption of *o*-xylene over the other isomers is related to enthalpic changes affecting adsorption of the other isomers.

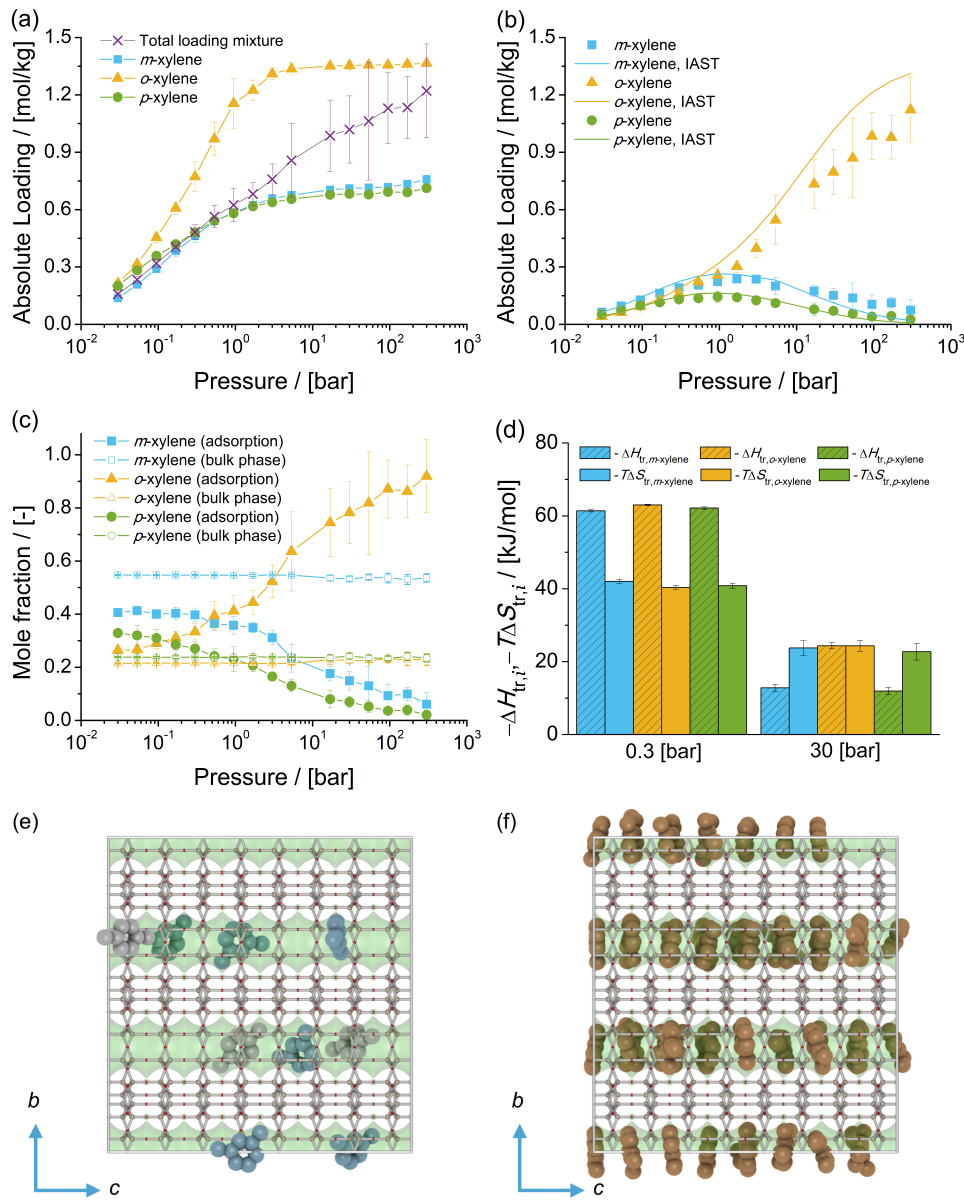


Figure 5.7: Adsorption isotherms of xylene isomers as (a) single components (total loading mixture is the sum of the loadings of xylenes from the mixture at chemical equilibrium), and (b) mixture at chemical equilibrium in AFI-type zeolite at 523 K. For adsorption of xylenes in AFI-type zeolite, 1 mol/kg is equal to 1.44 molecules/unit cell. (c) Mole fractions of xylene isomers as a function of total pressure for the mixture at chemical equilibrium adsorbed in AFI-type zeolite, and for the bulk phase. The composition in the bulk phase follows from Fig 5.2a. (d) Changes in enthalpy  $\Delta H_{\text{tr},i}$  and entropy  $T\Delta S_{\text{tr},i}$  at 523 K due to the transfer of xylene *i* from the fluid phase mixture at chemical equilibrium to AFI-type zeolite at 0.3 bar and 30 bar. Typical snapshots of the simulation of adsorption from the mixture of xylenes at chemical equilibrium at 523 K and 300 bar showing (e) *m*-xylene + *p*-xylene, and (f) *o*-xylene. *m*-Xylene is shown in blue, *p*-xylene in grey, and *o*-xylene in orange. The snapshots show the face-to-face stacking of *o*-xylene molecules, in comparison to how *m*-xylene and *p*-xylene molecules are arranged in the channels of AFI-type zeolite.

The adsorption isotherms of xylene isomers as single components and the mixture at chemical equilibrium in MEL-type zeolite at 523 K are shown in Fig. 5.8. The single component isotherms show that the loadings of *m*-xylene and *p*-xylene are higher than the loadings of *o*-xylene for pressures lower than 5.3 bar. For pressures higher than 16.8 bar (adsorption from the liquid phase), almost identical loadings are obtained for the three isomers. This suggest that the three xylene isomers are adsorbed on the same sites of MEL-type zeolite.

For the mixture of xylene isomers at chemical equilibrium, there is a strong selectivity of *m*-xylene adsorption over *o*-xylene and *p*-xylene. Fig. 5.8c shows the composition of the mixture of xylenes adsorbed in MEL-type zeolite compared to the composition of the mixture in the bulk phase as a function of pressure. It is observed that the composition of the adsorbed phase does not depend on the pressure. The mole fractions of *p*-xylene in the adsorbed phase are the same as in the bulk phase.

The loadings predicted with IAST are in agreement with the simulations of adsorption of the mixture. Based on the heat of adsorption at infinite dilution, there is a preferential adsorption of *m*-xylene > *p*-xylene > *o*-xylene. Fig 5.8d shows the changes in enthalpy and entropy due to the transfer of a xylene molecule between the bulk mixture and MEL-type zeolite for 0.3 and 30 bar at 523 K. At both 0.3 and 30 bar, adsorption is driven by enthalpic changes due to the transfer of xylenes to the zeolite. The changes of enthalpy due to the transfer of xylenes between the fluid phase and MEL-type zeolite (as computed using Eq. A.8) become positive when xylenes are adsorbed from the liquid phase. Fig. A.1 shows the computed heat of adsorption of xylenes in MEL-type zeolite at 30 bar and 523 K. It can be observed that the heat of adsorption of xylenes in MEL-type zeolite at 30 bar are significantly smaller than the heat of adsorption at infinite dilution (see Fig. 5.4). This is in agreement with the observations from experiments of *m*-xylene adsorption in ZSM-11 (an MEL-type zeolite) at 315 K by Guil et al. [458], where this decrease of the heat of adsorption at high loadings compared to low loadings is related to the complete filling of the pores of MEL-type zeolite. At high pressures, the heat of adsorption of xylenes in the bulk phase is higher than the heat of adsorption of xylenes in MEL-type zeolite (due to the complete pore filling), yielding to a positive change of enthalpy. Fig. 5.8e shows a typical snapshot of the simulation of adsorption of the mixture of xylenes at chemical equilibrium at 523 K and 300 bar. The snapshot shows that the three xylene isomers are located in the intersections of the channels of MEL-type zeolite.

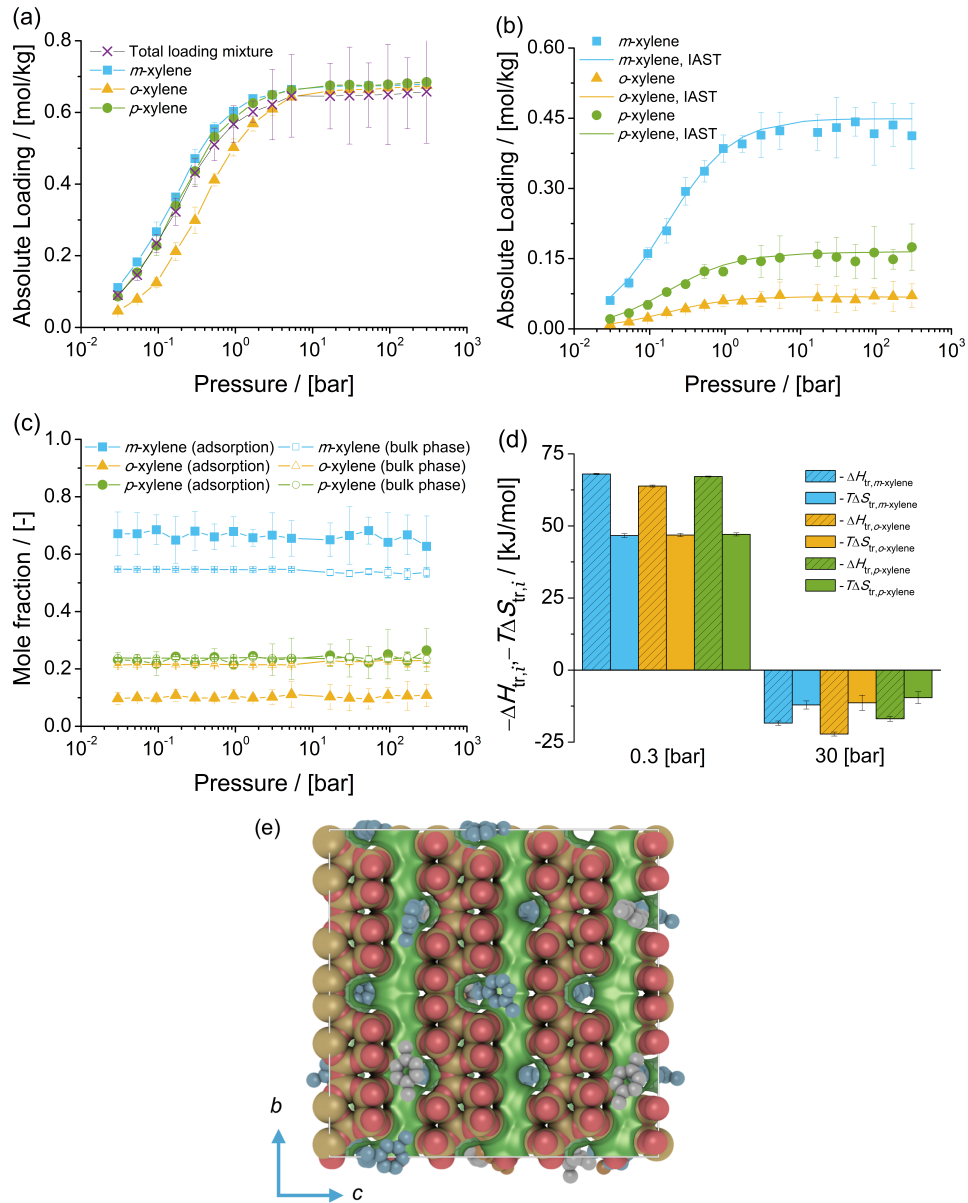


Figure 5.8: Adsorption isotherms of xylene isomers as (a) single components (total loading mixture is the sum of the loadings of xylenes from the mixture at chemical equilibrium), and (b) mixture at chemical equilibrium in MEL-type zeolite at 523 K. For adsorption of xylenes in MEL-type zeolite, 1 mol/kg is equal to 5.7 molecules/unit cell. (c) Mole fractions of xylene isomers as a function of total pressure for the mixture at chemical equilibrium adsorbed in MEL-type zeolite, and for the bulk phase. The composition in the bulk phase follows from Fig 5.2a. (d) Changes in enthalpy  $\Delta H_{\text{tr},i}$  and entropy  $T\Delta S_{\text{tr},i}$  at 523 K due to the transfer of xylene *i* from the fluid phase mixture at chemical equilibrium to MEL-type zeolite at 0.3 bar and 30 bar. (e) Typical snapshot of the simulation of adsorption of the mixture of xylenes in MEL-type zeolite at 300 bar and 523 K. *m*-Xylene is shown in blue, *p*-xylene in grey, and *o*-xylene in orange. The snapshot shows how xylenes are located in the intersection of the channels of MEL-type zeolite.

The adsorption isotherms of xylene isomers as single components and the mixture at chemical equilibrium in MOR-type zeolite at 523 K are shown in Fig. 5.9. The single components isotherms (Fig. 5.9a) show that for pressures lower than 0.94 bar, the loadings the three xylene isomers are nearly identical. For pressures higher than 0.94 bar, the loadings of *o*-xylene are higher than for the other isomers. The preferential adsorption of xylene isomers in MOR-type zeolites based on the heat of adsorption is *p*-xylene > *o*-xylene > *m*-xylene. This suggest that entropic effects are important for the arrangement of *o*-xylene molecules in the 12-ring channels of MOR-type zeolites for adsorption from the liquid phase.

For the adsorption isotherm of the mixture of xylenes at chemical equilibrium in MOR-type zeolite (Fig. 5.9b), there is a preferential adsorption of *m*-xylene and *p*-xylene for pressures lower than 5.3 bar (i.e. adsorption from the vapor phase). For adsorption from the liquid phase, there is preferential adsorption of *m*-xylene, and nearly identical loadings of *o*-xylene and *p*-xylene. Fig. 5.9c shows the composition of the mixture of xylenes adsorbed in MOR-type zeolite compared to the composition of the mixture in the bulk phase as a function of pressure. It is observed that the composition of the adsorbed fluid changes as a function of the pressure. For pressures higher than 0.94 bar, the mole fractions of *p*-xylene in MOR-type zeolite decrease with increasing total pressure, while the mole fractions of *o*-xylene increase with increasing total pressure. The mole fractions of *p*-xylene for the mixture adsorbed in MOR-type zeolite does not change as a function of the total pressure. Fig 5.9d shows the changes in enthalpy and entropy due to the transfer of a xylene molecule between the bulk mixture and MOR-type zeolite for 0.3 and 30 bar at 523 K. At 0.3 bar, adsorption is driven by changes in enthalpy due to the transfer of xylenes to the zeolite. At 30 bar, adsorption of xylene isomers is affected by entropic changes. However, there is a small enthalpic preference for *o*-xylene over the other xylene isomers. This suggest that at higher pressures there is a competition between enthalpic and entropic effects for accommodating *p*-xylene and *o*-xylene molecules in MOR-type zeolites.

Figs. 5.9e and 5.9f show typical snapshots of the adsorption at 523 K and 300 bar of *o*-xylene and *p*-xylene, respectively. At high pressures, adsorption of *o*-xylenes is favored by the alignment of its methyl groups. These can be aligned with the direction of the channel (*c*-crystallographic axis) or perpendicular to the channel (*a*-crystallographic axis). This favors an efficient pore volume occupancy of *o*-xylenes in MOR-type zeolites. The total loading of the mixture is lower than the single component isotherm for *o*-xylene (Fig. 5.9a). The preferential adsorption of *o*-xylene from the mixture is affected by guest-guest interactions between *o*-xylene and the other isomers. This leads to a disagreement between the computed loadings of *o*-xylenes with the predictions of IAST. For *p*-xylene, the methyl groups are typically aligned with the channel direction. The grooves of the surface of the 12-ring channel also typically allow the methyl groups of *p*-xylene to align with and inclination of ca. 45° from the channel direction.

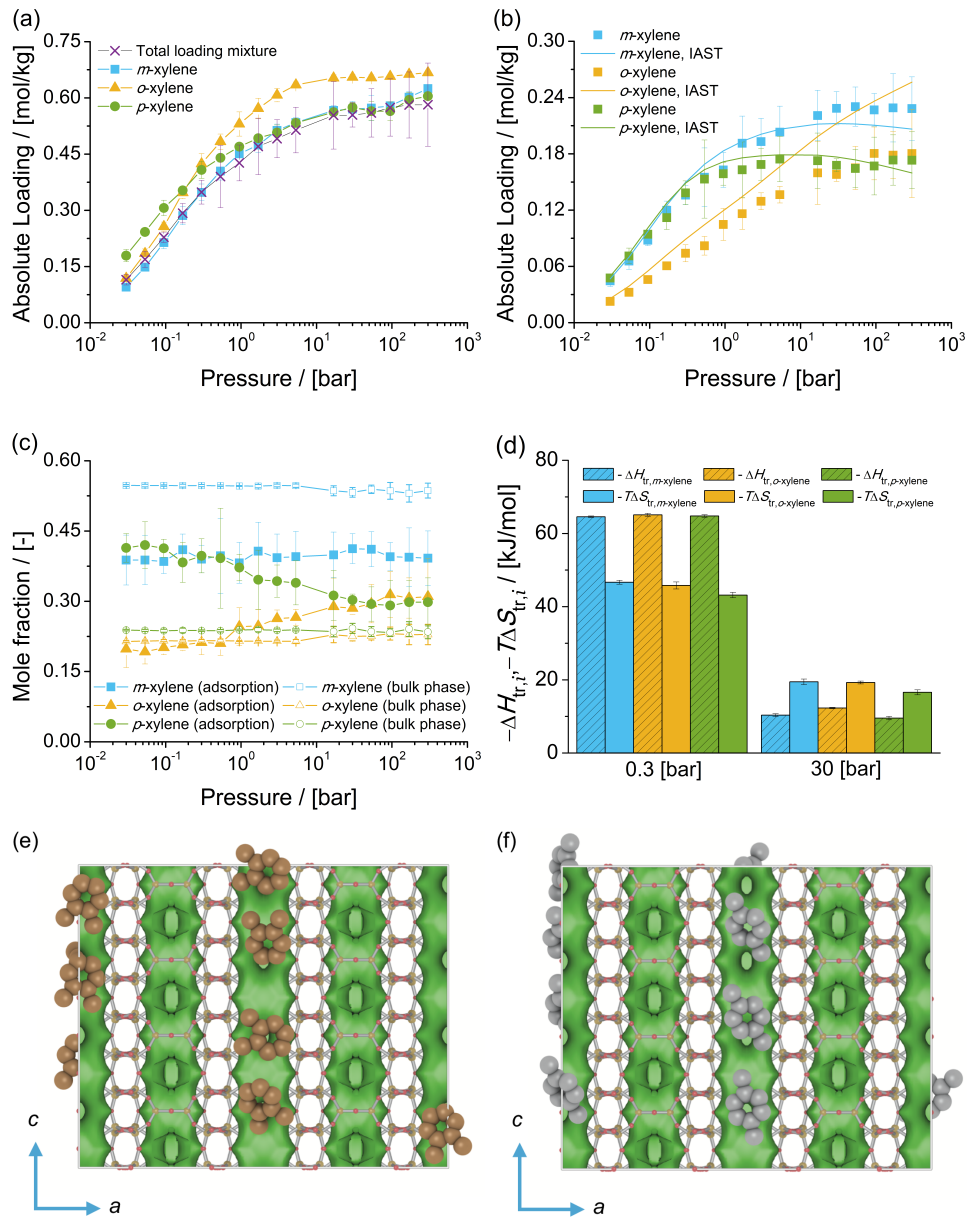


Figure 5.9: Adsorption isotherms of xylene isomers as (a) single components (total loading mixture is the sum of the loadings of xylenes from the mixture at chemical equilibrium), and (b) mixture at chemical equilibrium in MOR-type zeolite at 523 K. For adsorption of xylenes in MOR-type zeolite, 1 mol/kg is equal to 2.9 molecules/unit cell. (c) Mole fractions of xylene isomers as a function of total pressure for the mixture at chemical equilibrium adsorbed in MOR-type zeolite, and for the bulk phase. The composition in the bulk phase follows from Fig 5.2a. (d) Changes in enthalpy  $\Delta H_{\text{tr},i}$  and entropy  $T\Delta S_{\text{tr},i}$  at 523 K due to the transfer of xylene *i* from the fluid phase mixture at chemical equilibrium to MOR-type zeolite at 0.3 bar and 30 bar. Typical snapshots of the simulations of adsorption of (e) *o*-xylene and (f) *p*-xylene in MOR-type zeolite at 300 bar and 523 K. *p*-Xylene is shown in grey, and *o*-xylene is shown in orange. The snapshots show the typical configuration of xylene isomers in the channels of MOR-type zeolite.

The adsorption isotherms of xylene isomers as single components and the mixture at chemical equilibrium in BEA-type zeolite at 523 K are shown in Fig. 5.10. The single component isotherms show that for pressures lower than 1 bar, there is *p*-xylene selectivity over *m*-xylene and *o*-xylene. For the adsorption from a liquid phase (pressure higher than 16.8 bar), loadings of *o*-xylene higher than *p*-xylene and *m*-xylene are obtained.

The adsorption isotherm of the mixture at chemical equilibrium suggest that there is a preferential adsorption of *p*-xylene and *m*-xylene over *o*-xylene. The loadings predicted with IAST are in agreement with the simulations of adsorption of the mixture of xylenes. Fig. 5.10c shows the composition of the mixture of xylenes adsorbed in BEA-type zeolite compared to the composition of the mixture in the bulk phase as a function of pressure. It is observed that the composition of the adsorbed phase does not significantly vary with the pressure. Based on the heat of adsorption at infinite dilution, there is a preferential adsorption of *p*-xylene > *m*-xylene > *o*-xylene. Fig 5.10d shows the changes in enthalpy and entropy due to the transfer of a xylene molecule between the bulk mixture and BEA-type zeolite for 0.3 and 30 bar at 523 K. At 0.3 bar, adsorption is driven by changes in enthalpy due to the transfer of xylenes to the zeolite. At 30 bar, adsorption of xylene isomers is driven by changes in entropy. However, there is a small enthalpic preference for the adsorption of *p*-xylene over the other isomers. Fig. 5.10e and 5.10f show typical snapshots of the simulation of adsorption of the *m*-xylene and *p*-xylene at 30 bar and 523 K. It is observed that *m*-xylene molecules are located in the intersection of the channels and that the methyl groups align with the two intersecting channels. For *p*-xylene molecules, the methyl groups can either align with the channel direction or with an intersecting channel. This suggests that the differences between the loadings of the xylene isomers in the adsorbed mixture are related to the shape of the molecules.

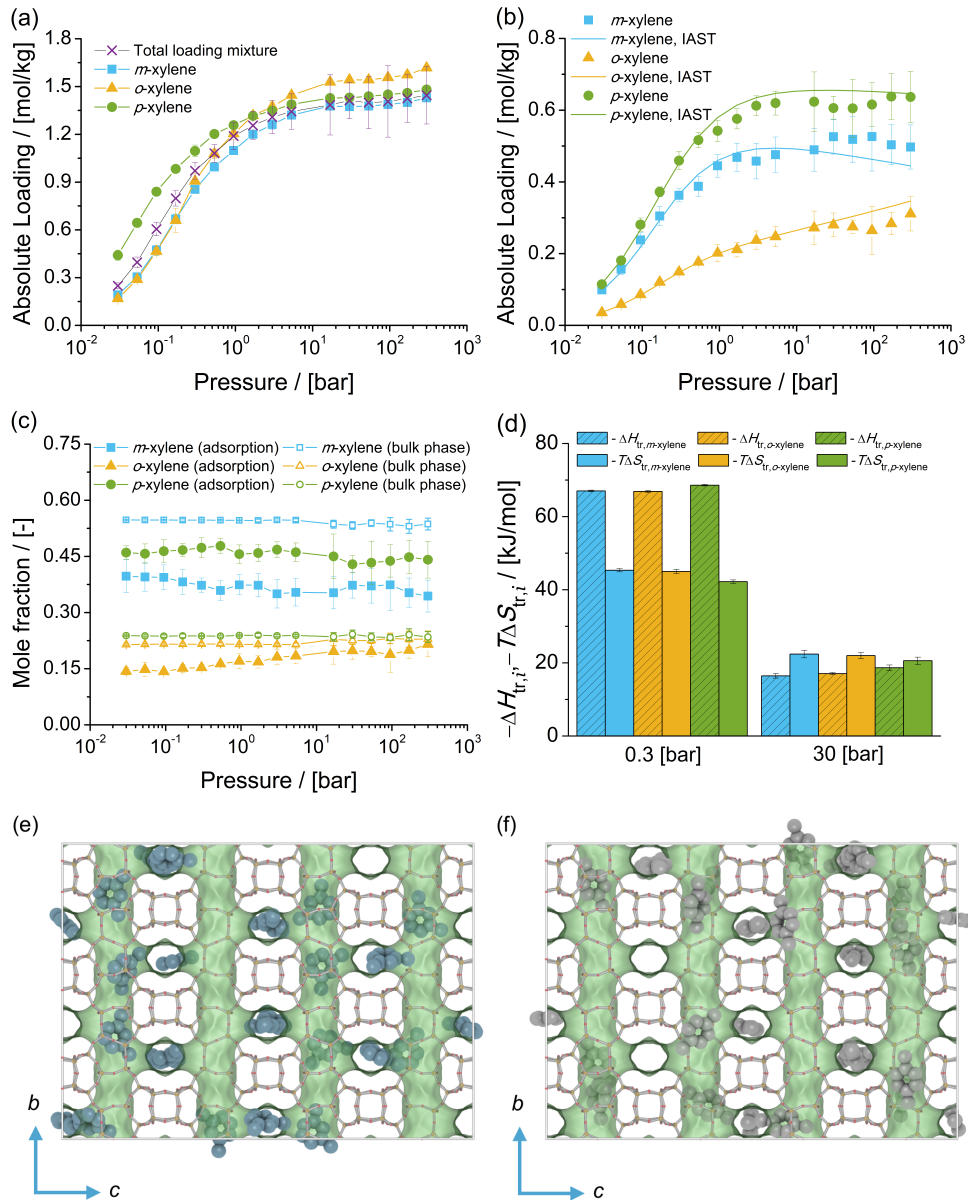


Figure 5.10: Adsorption isotherms of xylene isomers as (a) single components (total loading mixture is the sum of the loadings of xylenes from the mixture at chemical equilibrium), and (b) mixture at chemical equilibrium in BEA-type zeolite at 523 K. For adsorption of xylenes in BEA-type zeolite, 1 mol/kg is equal to 3.8 molecules/unit cell. (c) Mole fractions of xylene isomers as a function of total pressure for the mixture at chemical equilibrium adsorbed in the BEA-type zeolite, and for the bulk phase. The composition in the bulk phase follows from Fig 5.2a. (d) Changes in enthalpy  $\Delta H_{\text{tr},i}$  and entropy  $T\Delta S_{\text{tr},i}$  at 523 K due to the transfer of xylene *i* from the fluid phase mixture at chemical equilibrium to BEA-type zeolite at 0.3 bar and 30 bar. Typical snapshot of the simulation of adsorption of the mixture of xylenes in BEA-type zeolite at 523 K and 30 bar showing (e) *m*-xylene and (f) *p*-xylene. *m*-Xylene is shown in blue, and *p*-xylene in grey. The snapshot shows how *m*-xylene and *p*-xylene are arranged in the intersection of the channels.

The adsorption isotherms of xylene isomers as single components and the mixture at chemical equilibrium in MRE-type zeolite at 523 K are shown in Fig. 5.11. The single component isotherms show a strong preference for the adsorption of *p*-xylene over the adsorption of *m*-xylene and *o*-xylene. The loadings of *m*-xylene and *o*-xylene are below 0.05 mol/kg for the considered pressure range. This can be related to the size of the channel of MRE-type zeolite. Fig. 5.11c shows the composition of the mixture of xylenes adsorbed in MRE-type zeolite compared to the composition of the mixture in the bulk phase as a function of pressure. The composition of the adsorbed phase does not vary as a function of pressure. The mole fraction of *p*-xylene in the adsorbed phase is 0.999 for the considered pressure range. The loadings predicted with IAST are in agreement with the simulations of adsorption of the mixture of xylenes. The PSD (Fig. 5.3) shows a peak in the distribution for MRE-type zeolite at a diameter of *ca.* 5 Å, which suggest that there size restriction and shape selectivity for molecules larger *p*-xylene. Fig 5.11d shows the changes in enthalpy and entropy due to the transfer of a xylene molecule between the bulk mixture and MRE-type zeolite for 0.3 and 30 bar at 523 K. At 0.3 bar, adsorption of *p*-xylene is driven by changes in enthalpy due to the transfer to the zeolite. For *m*-xylene and *o*-xylene, the shape exclusion is shown as changes in entropy. This is also observed for adsorption at 30 bar, as only *p*-xylene is adsorbed from the mixture of xylenes at chemical equilibrium. Fig 5.11e shows a snapshot of the simulation of adsorption of the mixture of xylenes. It is observed that the methyl groups of *p*-xylene are aligned with the channel.

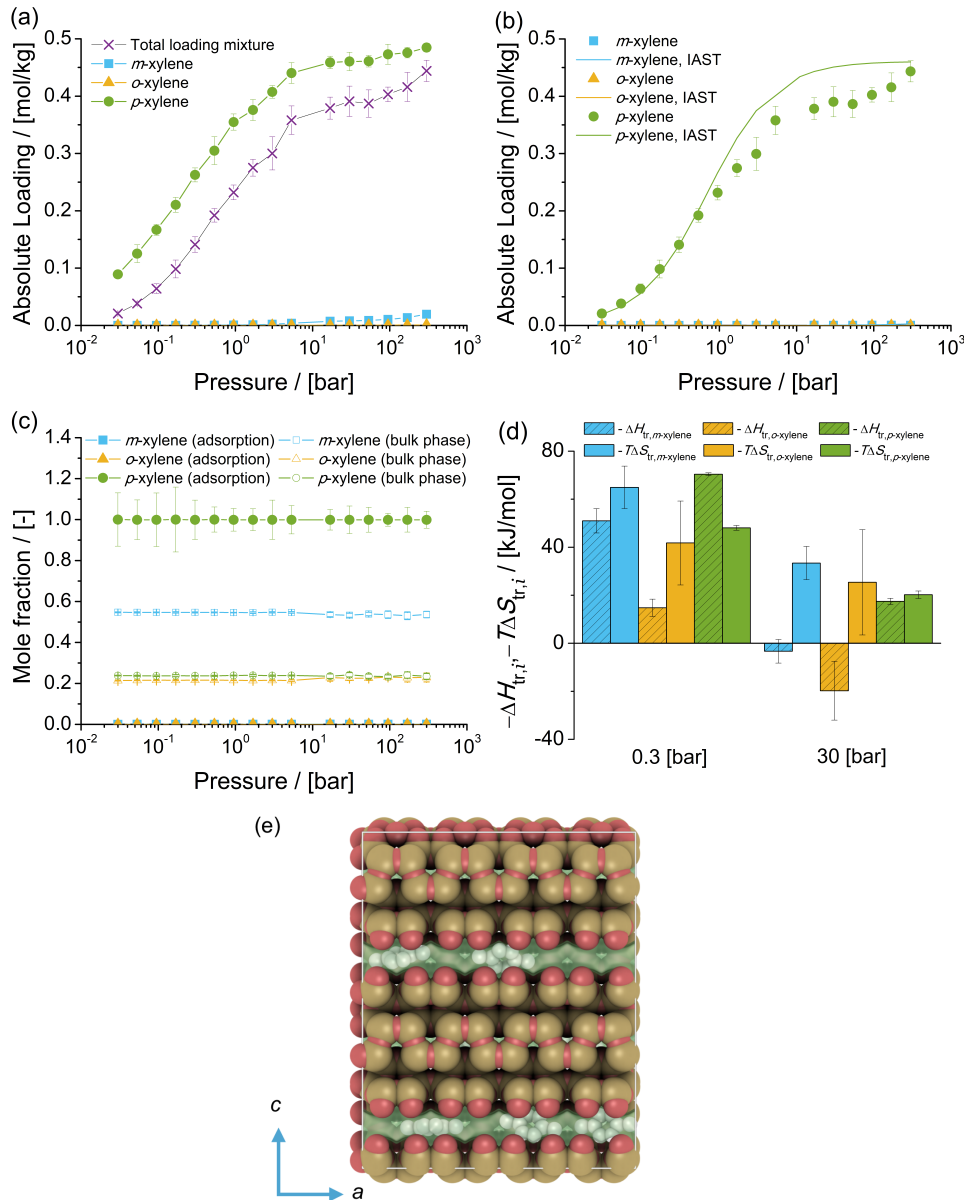


Figure 5.11: Adsorption isotherms of xylene isomers as (a) single components (total loading mixture is the sum of the loadings of xylenes from the mixture at chemical equilibrium), and (b) mixture at chemical equilibrium in MRE-type zeolite at 523 K. For adsorption of xylenes in MRE-type zeolite, 1 mol/kg is equal to 2.9 molecules/unit cell. (c) Mole fractions of xylene isomers as a function of total pressure for the mixture at chemical equilibrium adsorbed in MRE-type zeolite, and for the bulk phase. The composition in the bulk phase follows from Fig 5.2a. (d) Changes in enthalpy  $\Delta H_{tr,i}$  and entropy  $T\Delta S_{tr,i}$  at 523 K due to the transfer of xylene *i* from the fluid phase mixture at chemical equilibrium to MRE-type zeolite at 0.3 bar and 30 bar. (e) Typical snapshot of the simulation of adsorption of the mixture of xylenes at chemical equilibrium in MRE-type zeolite at 300 bar and 523 K. *p*-Xylene is shown in grey. The snapshot shows how *p*-xylene molecules are aligned with the channel of MRE-type zeolite.

The adsorption isotherms of xylene isomers as single components and the mixture at chemical equilibrium in MFI-type zeolite at 523 K are shown in Fig. 5.12. The single component isotherms show that the loadings of *m*-xylene are higher than the loadings of *p*-xylene and *o*-xylene in the considered pressure range. In this pressure range, the adsorption site for all isomers is nearly identical. It is known that *p*-xylene molecules are hosted in the channels of MFI-type zeolites when the loadings are higher than 4 molecules/unit cell (ca. 0.693 mol/kg) [200, 204]. The simulations show that all the molecules are located in the intersections of the zigzag and straight channel. The preference for *m*-xylene is due to an alignment of the methyl groups with the zigzag and straight channels. Fig. 5.12e shows how as one methyl group of *m*-xylene is aligned in the direction of the straight channel (*b*-crystallographic axis), the other methyl group is aligned with the direction of the zigzag channel (*c*-crystallographic axis). It can be also observed how this arrangement of the methyl groups is difficult for *o*-xylene molecules. *p*-Xylenes are aligned with the straight channel (*b*-crystallographic axis).

For the mixture of xylene isomers at chemical equilibrium, there is a strong selectivity of *m*-xylene adsorption over *o*-xylene and *p*-xylene. Fig. 5.12c shows the composition of the mixture of xylenes adsorbed in MFI-type zeolite compared to the composition of the mixture in the bulk phase as a function of pressure. It is observed that the composition of the adsorbed phase does not depend on the pressure. The loadings predicted with IAST are in agreement with the simulations of adsorption of the mixture. Based on the heat of adsorption at infinite dilution, there is a preferential adsorption of *m*-xylene > *p*-xylene > *o*-xylene. Fig. 5.12d shows the changes in enthalpy and entropy due to the transfer of a xylene molecule between the bulk mixture and MFI-type zeolite for 0.3 and 30 bar at 523 K. At 0.3 bar, adsorption of *m*-xylene and *o*-xylene are almost equally driven by changes in enthalpy and entropy due to the molecule transfer to the zeolite. For *p*-xylene, adsorption is driven by changes in enthalpy. For adsorption of *m*-xylene at 30 bar the changes in enthalpy and entropy (multiplied by the absolute temperature) due to the transfer to the zeolite are almost equal.

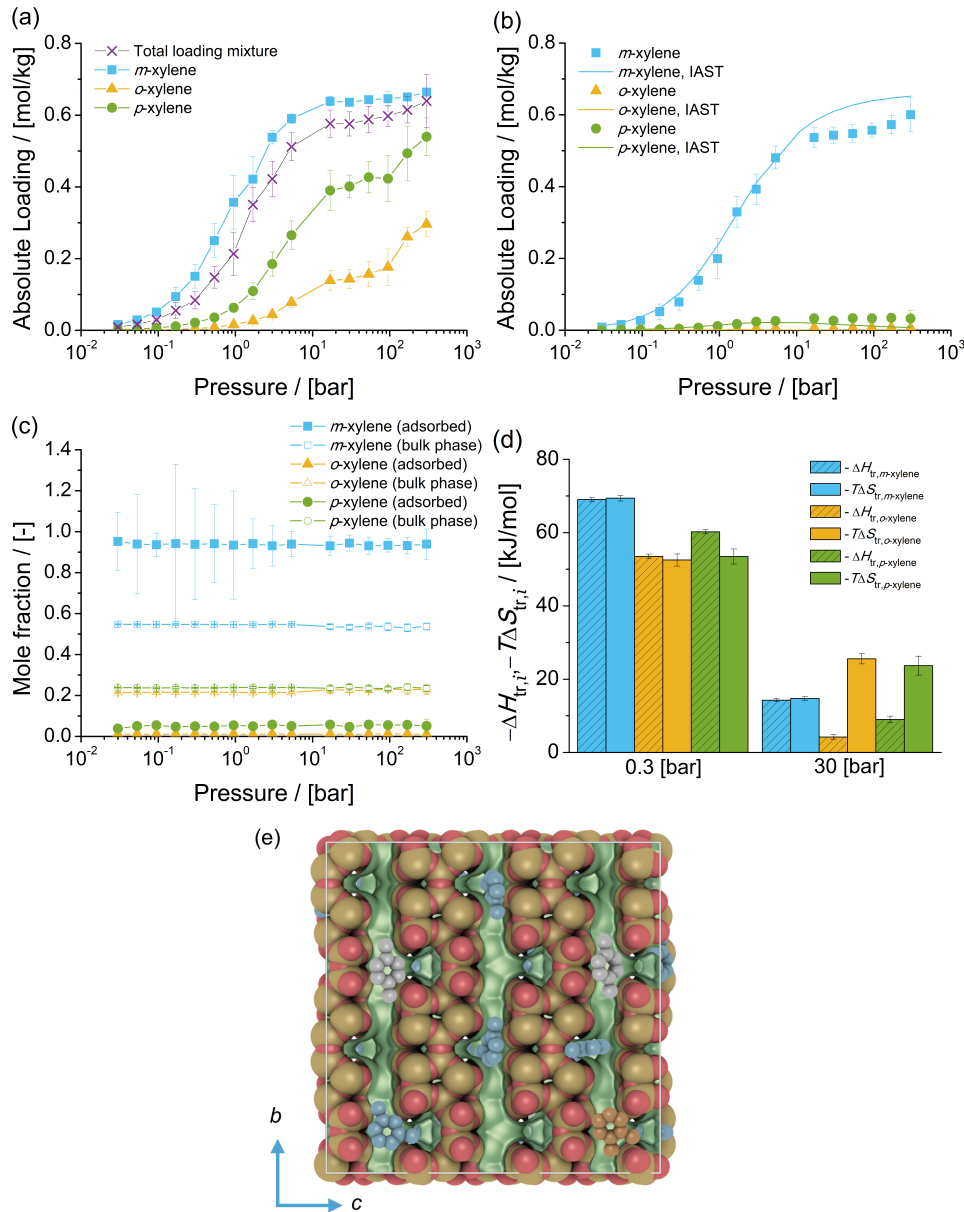


Figure 5.12: Adsorption isotherms of xylene isomers as (a) single components (total loading mixture is the sum of the loadings of xylenes from the mixture at chemical equilibrium), and (b) mixture at chemical equilibrium in MFI-type zeolite at 523 K. For adsorption of xylenes in MFI-type zeolite, 1 mol/kg is equal to 5.7 molecules/unit cell. (c) Mole fractions of xylene isomers as a function of total pressure for the mixture at chemical equilibrium adsorbed in MFI-type zeolite, and for the bulk phase. The composition in the bulk phase follows from Fig 5.2a. (d) Changes in enthalpy  $\Delta H_{\text{tr},i}$  and entropy  $T\Delta S_{\text{tr},i}$  at 523 K due to the transfer of xylene *i* from the fluid phase mixture at chemical equilibrium to MFI-type zeolite at 0.3 bar and 30 bar. (d) Typical snapshot of the simulation of adsorption of the mixture of xylenes in the MFI-type zeolite at 300 bar and 523 K. *m*-Xylene is shown in blue, *p*-xylene in grey, and *o*-xylene in orange. The snapshot shows how xylenes are located in the intersection of the zigzag and straight channels of MFI-type zeolite.

The adsorption isotherms of xylene isomers as single components and the mixture at chemical equilibrium in MTW-type zeolite at 523 K are shown in Fig. 5.13. The single components isotherms show that for pressures lower than 5.3 bar, the loadings of *p*-xylene are higher than for *o*-xylene and *m*-xylene. For pressures higher than 16.8 bar, the loadings of *m*-xylene are higher than for *o*-xylene and *p*-xylene.

For the adsorption of the mixture of xylenes at chemical equilibrium, there is a preferential adsorption of *p*-xylene, over *m*-xylene and *o*-xylene. The isotherm predicted with IAST is in agreement with the simulations of adsorption of the mixture of xylenes at chemical equilibrium. This implies that the adsorbed molecules compete for the same adsorption sites. Fig. 5.13c shows the composition of the mixture of xylenes adsorbed in MTW-type zeolite compared to the composition of the mixture in the bulk phase as a function of pressure. It is observed that the phase composition of the adsorbed fluid changes as a function of the pressure. The mole fractions of *p*-xylene for the mixture adsorbed in MTW-type zeolite decrease from 0.6 at 0.03 bar to 0.4 at 300 bar. For *m*-xylene, the mole fractions increase from 0.27 at 0.03 bar to 0.4 at 300 bar. Based on the heat of adsorption at infinite dilution, there is a preferential adsorption of *p*-xylene > *o*-xylene > *m*-xylene. Fig. 5.13d shows the changes in enthalpy and entropy due to the transfer of a xylene molecule between the bulk mixture and MTW-type zeolite for 0.3 and 30 bar at 523 K. At 0.3 bar, adsorption of xylenes is driven by changes in enthalpy due to the transfer of molecules between the bulk mixture and MTW-type zeolite. For 30 bar, the adsorption of xylenes is influenced by changes in entropy. The changes in entropy and enthalpy due to the transfer of xylenes to MTW-type zeolite suggest that the preferential adsorption of *p*-xylene is due to entropic effects, and that the preferential adsorption of *m*-xylene over *o*-xylene is due to its large mole fraction in the bulk phase. Figs. 5.13e and 5.13f show typical snapshots of the location of xylene molecules in the channel of a MTW-type zeolite. It is observed that *m*-xylene and *o*-xylene molecules fit tightly in the channel due to the direction of the methyl groups.

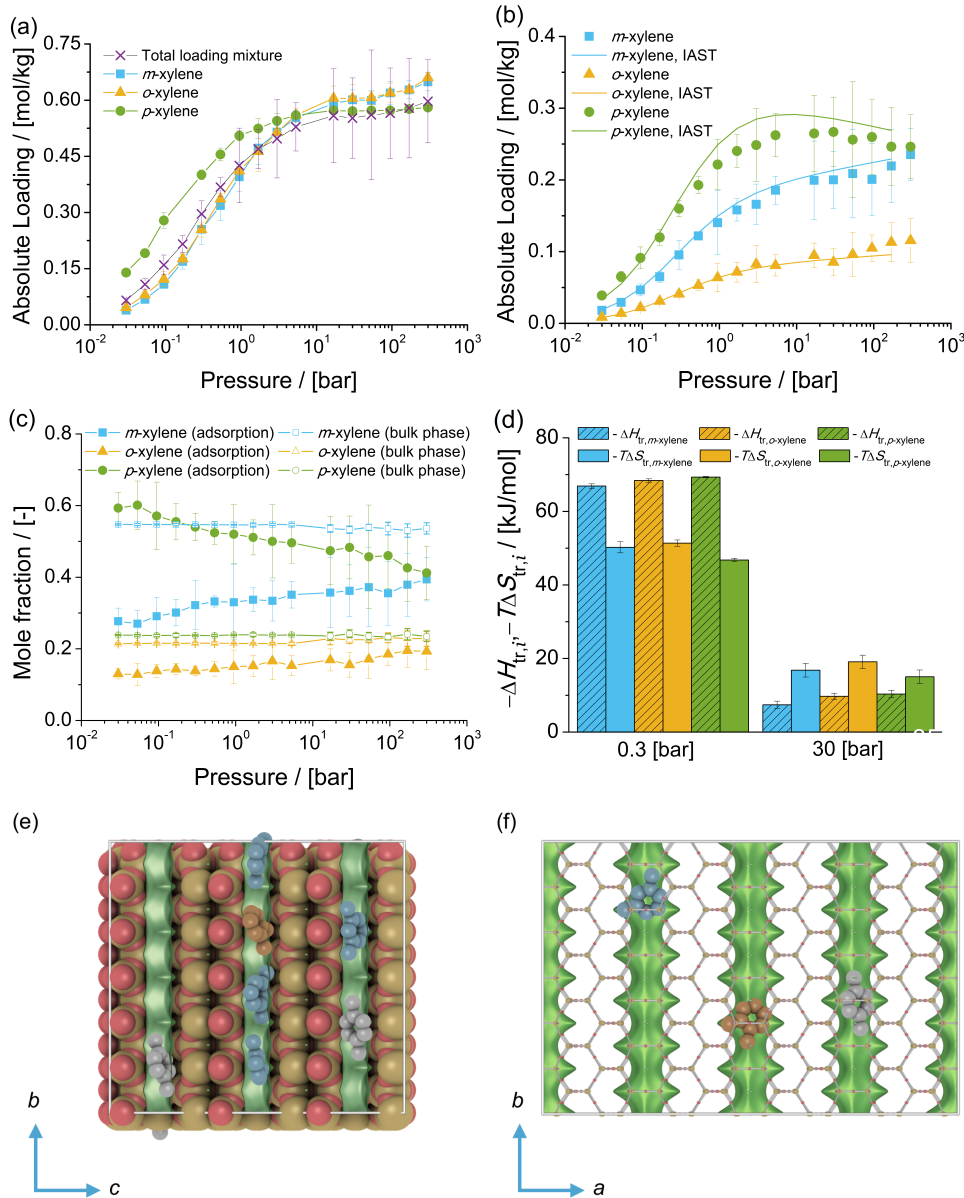


Figure 5.13: Adsorption isotherms of xylene isomers as (a) single components (total loading mixture is the sum of the loadings of xylenes from the mixture at chemical equilibrium), and (b) mixture at chemical equilibrium in MTW-type zeolite at 523 K. For adsorption of xylenes in MTW-type zeolite, 1 mol/kg is equal to 1.7 molecules/unit cell. (c) Mole fractions of xylene isomers adsorbed in MTW-type zeolite, and for the bulk phase. The composition in the bulk phase follows from Fig 5.2a. (d) Changes in enthalpy  $\Delta H_{tr,i}$  and entropy  $T\Delta S_{tr,i}$  at 523 K due to the transfer of xylene *i* from the fluid phase mixture at chemical equilibrium to MTW-type zeolite at 0.3 bar and 30 bar. (e) and (f) are typical snapshots of the simulation of adsorption of the mixture of xylene isomers in MTW-type zeolite at 300 bar and 523 K. *m*-Xylene is shown in blue, *p*-xylene is shown in grey, and *o*-xylene is shown in orange. The snapshots show the typical configuration of xylene isomers in the channels of MTW-type zeolite.

Table 5.2 lists a summary of the observed preferential adsorption of the single components and for the mixture at chemical equilibrium for each zeolite type considered in this work. It is observed that *m*-xylene is preferentially adsorbed in FAU-, MEL-, and MFI-type zeolites. The preferential adsorption of *m*-xylene in the FAU-type zeolite is related to the large mole fraction of *m*-xylene in the bulk phase, compared to mole fraction of the other isomers. In MEL- and MFI-type zeolites, the preferential adsorption of *m*-xylene is related to the shape of the adsorption site in which xylene molecules are located. Xylene molecules are located in the intersections of two channel systems. The methyl groups of *m*-xylene are aligned with these two channel systems. For *p*-xylene, the methyl groups are aligned with one of the channels. One of the methyl groups of *o*-xylene is in alignment with one of the channels, while the other methyl group is not.

BEA-type zeolite shows a preferential adsorption of *p*-xylene. Also significant adsorption of *m*-xylene is observed. This is related to *m*-xylene molecules located in the intersection of the channels and that the methyl groups are aligned with the two intersecting channels, and to the large mole fraction of *m*-xylene in the bulk mixture of xylenes. For *p*-xylene molecules, the methyl groups can either align with the channel direction or with an intersecting channel.

The PSD of BEA-type zeolite shows a peak of the distribution at a diameter of approx. 5.5 Å. This diameter is larger than for MFI- and MEL-type zeolites (intersections with diameters of approx. 5 Å). This suggest that the preferential adsorption of *m*-xylene in zeolites with an intersecting channel system depends on the size of such channel systems. If the channel intersection is large, molecules such as *p*-xylene can be accommodated in configurations different than in alignment with the channel direction. This influences the preferential adsorption of *p*-xylene over the other xylene isomers in zeolites with intersecting channel systems. The preferential adsorption of *m*-xylene in zeolites with intersecting channel systems occurs when the molecules fit tightly in the adsorption site.

For MRE-type zeolite, only *p*-xylene molecules are adsorbed in the 10-ring channel. *m*-Xylene and *o*-xylene are not adsorbed. In this zeolite type, the methyl groups of *p*-xylene are in alignment with the 10-ring channel. Steric effects hinder the adsorption of *m*-xylene and *o*-xylene in MRE-type zeolite. For MTW-type zeolites, *p*-xylene is preferentially adsorbed. At high pressures, significant loadings of *m*-xylene are observed. MTW-type zeolites have small 12-ring one dimensional channels [459]. In these channels, the methyl groups of *p*-xylene are in alignment with the channel. Also, these 12-ring channels can host *m*-xylene and *o*-xylene when one of its methyl groups is accommodated in the cavity (Fig. 5.13e). In this case, there is an enthalpic preference for *p*-xylene.

MOR-type zeolites have a 12-ring channel wider than the one dimensional channel of MTW-type zeolite (see Fig. 5.3). In these channels, entropic effects favor the adsorption of *o*-xylenes. This is caused by the alignment of its methyl groups. These can be aligned with the direction of the channel or perpendicular to the channel. For the adsorption of the mixture at chemical equilibrium this entropic effect is hindered by the other isomers in the neighborhood. The adsorption is driven by a competition between entropic and enthalpic effect.

The AFI-type zeolite has a 12-ring one dimensional channel even wider than the channel of MOR-type zeolite (see Fig. 5.3). The size of such channel can host *o*-xylene molecules that align perpendicular to the channel direction. In such channel, *m*-xylene and *p*-xylene molecules accommodate in alignment with the direction of the channel. In this case, the *o*-xylene preference is related to entropic effects.

In zeolites with one dimensional channel systems, the size of the such channels determines the selective mechanism for a particular xylene isomer. *p*-Xylene is preferentially adsorbed in the 10-ring channel of MRE-type zeolite due to size exclusion of the other isomers. Entropic and enthalpic factors compete for the preferential adsorption of xylenes in the 12-ring channels of MTW-type and MOR-type zeolites. Entropic effects yield a preferential adsorption of *o*-xylene in the 12-ring channels of AFI-type zeolite.

In the case of MWW-type zeolite, there is a preferential adsorption of *o*-xylene, and significant loadings of *m*-xylene and *p*-xylene. It is observed that for the adsorption of the mixture of xylenes at chemical equilibrium, *o*-xylene molecules are located in the 12-ring cages. The 10-ring channels host *m*-xylene and *p*-xylene. MWW-type zeolite can accommodate xylene isomers in different channel systems depending on the size of the channel.

The insight from this work can be considered for the design and/or improvement of applications of zeolites for the processing of xylenes. However, it is known that the predictions of adsorption of aromatics in zeolites are sensitive to the flexibility of the framework [187, 217], the flexibility of aromatic molecules [410], and to the partial charges used for the models [181]. These factors are not considered in this work. Models that capture the physics behind the flexibility of the zeolite and aromatics in confinements are needed [204]. The insight shown here is based on the thermodynamic stability of the isomers inside the zeolite pores. Thus, diffusion limitations of xylenes in the channels of the zeolite types considered should be thoroughly assessed. As such, future work on experimental testing of these findings is encouraged.

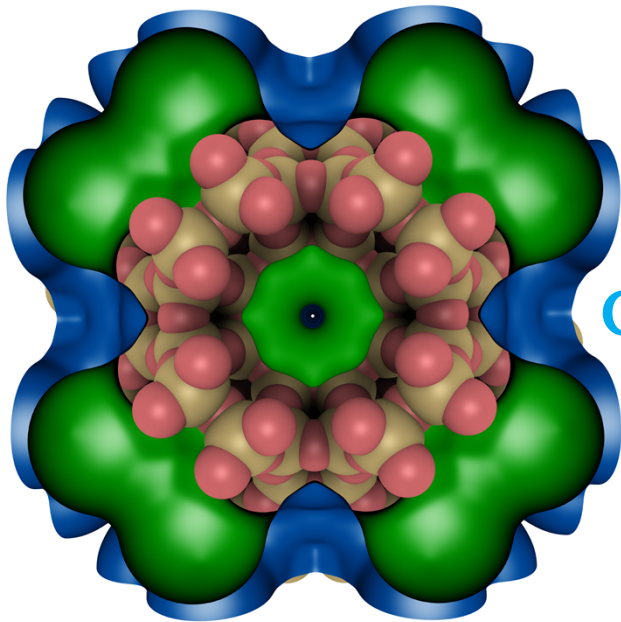
Table 5.2: Summary of the observed preferential adsorption of xylene isomers in zeolites for pure components and for the adsorption of the mixture of xylenes at chemical equilibrium at 523 K. The preferences are observed for two pressure ranges:  $0.03 \leq P \leq 5.3$  bar (i.e. adsorption from the vapor phase), and  $16.8 \leq P \leq 300$  bar (i.e. adsorption from a liquid phase). The preferential adsorption based on the heat of adsorption at infinite dilution is also listed. The xylene isomers are represented as: *m* for *m*-xylene, *o* for *o*-xylene, and *p* for *p*-xylene.

Zeolite framework type	Observed preferential adsorption of xylenes as single components				Observed preferential adsorption of xylenes for the mixture at chemical equilibrium				Preference based on the heat of adsorption at infinite dilution	
	$0.03 \leq P \leq 5.3$ bar	$16.8 \leq P \leq 300$ bar	$0.03 \leq P \leq 5.3$ bar	$16.8 \leq P \leq 300$ bar	$0.03 \leq P \leq 5.3$ bar	$16.8 \leq P \leq 300$ bar	$0.03 \leq P \leq 5.3$ bar	$16.8 \leq P \leq 300$ bar		
FAU	<i>m</i>	=	<i>o</i>	=	<i>p</i>	<i>m</i>	=	<i>o</i>	=	<i>p</i>
AFI	<i>o</i>	>	<i>m</i>	$\sim$	<i>p</i>	<i>o</i>	$\gg$	<i>m</i>	$>$	<i>p</i>
MWW	<i>o</i>	$\vee$	<i>p</i>	$\vee$	<i>m</i>	<i>m</i>	$\vee$	<i>p</i>	$\gg$	<i>m</i>
MEL	<i>m</i>	$\vee$	<i>p</i>	$\vee$	<i>o</i>	<i>m</i>	$\vee$	<i>p</i>	$\vee$	<i>m</i>
MFI	<i>m</i>	$\vee$	<i>p</i>	$\vee$	<i>o</i>	<i>m</i>	$\sim$	<i>p</i>	$\gg$	<i>p</i>
BFA	<i>p</i>	$\vee$	<i>m</i>	$\sim$	<i>o</i>	<i>o</i>	$\vee$	<i>p</i>	$\gg$	<i>p</i>
MRE	<i>p</i>	$\gg$	<i>m</i>	$\sim$	<i>o</i>	<i>p</i>	$\gg$	<i>m</i>	$\vee$	<i>m</i>
MTW	<i>p</i>	$\vee$	<i>o</i>	$\sim$	<i>p</i>	$\gg$	<i>m</i>	$\sim$	$\gg$	<i>p</i>
MOR	<i>m</i>	$\sim$	<i>p</i>	$\sim$	<i>m</i>	$\sim$	<i>p</i>	$\sim$	$\gg$	<i>m</i>
	<i>o</i>	$\vee$	<i>m</i>	$\sim$	<i>p</i>	$\vee$	<i>m</i>	$\sim$	$\gg$	<i>m</i>

## 5.4. CONCLUSIONS

The adsorption of xylenes as single components and as a mixture at chemical equilibrium in several zeolites has been computed by Monte Carlo simulations. The simulations show the role of the different mechanisms that drive adsorption in several zeolite types. It is observed that for zeolites with one dimensional channels, the selectivity for a xylene isomer is determined by a competition of entropic and enthalpic effects. Each of these effects is related to the diameter of the zeolite channel. Shape and size selectivity entropic effects are predominant for small one dimensional systems. Entropic effects due to the efficient arrangement of xylenes become relevant for large one dimensional systems. For zeolites with two intersecting channels, the selectivity is determined by a competition between enthalpic and entropic effects. Such effects are related to the orientation of the methyl groups of the competing xylenes. *m*-Xylene is preferentially adsorbed if xylenes fit tightly in the intersection of the channels. If the intersection is much larger than the adsorbed molecules, *p*-xylene molecules are adsorbed and can be efficiently arranged in the void volumes of the zeolite. The simulations show that different selectivity mechanisms are predominant when the vapor phase mixture of xylenes is adsorbed in a zeolite compared to the adsorption from the liquid phase. This suggests that screening studies that consider adsorption only from a vapor phase may have overlooked well-performing candidates for C<sub>8</sub> aromatics processing. MRE-type and AFI-type zeolites exclusively adsorb *p*-xylene and *o*-xylene from the mixture of xylenes in the liquid phase, respectively. These zeolite types show potential to be used as high-performing molecular sieves for xylene separation and catalysis.





# 6

## CONCLUSIONS

The separation and catalytic transformations of aromatic hydrocarbons are one of the most important processes in the petrochemical industry. In this work, the separation of these molecules in zeolites is studied using classical molecular simulations. Importance is given to the factors that are required to predict reliable molecular insight from simulations.

The intermolecular interactions between aromatic molecules are studied by computing vapor-liquid equilibria of pure xylenes and binary mixtures using four different force fields. The densities of pure *p*-xylene and *m*-xylene are well estimated using the TraPPE-UA and AUA force fields. The largest differences of computed VLEs with experiments are observed for *o*-xylene. *p*-Xylene/*o*-xylene binary mixtures are simulated, leading to an excellent agreement for the prediction of the composition of the liquid phase compared to experiments. For the vapor phase, the accuracy of the predictions of the composition are closely related to the quality of the density predictions of the pure components of the mixture. The simulations have shown the potential to accurately predict the phase compositions of such binary mixtures, but the development of force fields that predict the VLE of each xylene isomer more accurately -especially *o*-xylene- is needed. The phase composition of the binary system of xylenes is very sensitive to slight differences in the vapor phase densities of each xylene isomer, and how well the differences are captured by the force fields.

Most of the models commonly used for framework flexibility in zeolites include a combination of Lennard-Jones (LJ) and electrostatic intra-framework interactions,

and impose fixed lengths for the covalent bonds between zeolite framework atoms. The effect of these models for framework flexibility on the predictions of adsorption of aromatics in zeolites is studied. The adsorption of n-heptane and C<sub>8</sub> in MFI-type zeolites is computed using rigid and flexible zeolite frameworks. Pore-size distributions (PSD) of the MFI-type zeolite structures using three different force fields for framework flexibility are computed. The results show that the use of constant bond lengths induce displacements of the framework atoms that influences adsorption. Directly taking the bond lengths from the crystallographic structure minimizes this effect. Also, the electrostatic and LJ intra-framework interactions induce small displacements of the zeolite atoms that significantly affect the size of the pores and channels of the zeolite. Using the considered host-host force fields, framework flexibility generates a new structure that is differently 'rigid'. The flexible force fields produce a zeolite structure that vibrates around a new equilibrium configuration that has only a limited capacity to accommodate to a bulky guest molecule. The vibration of the zeolite atoms only plays role at high loadings, and the adsorption is mainly dependent on the average positions of the atoms. The intra-framework interactions should be treated carefully, as these interactions cause significant deviations from the experimental zeolite lattice. In sharp contrast to the adsorption of aromatics, the adsorption of n-heptane in MFI-type zeolite showed that the use of a zeolite structure with fixed atom positions is appropriate when the molecule does not fit tightly in the zeolite pores. For aromatics, the influence of the force field for framework flexibility on the adsorption in MFI-type zeolites implies that structural changes of the zeolite framework are relevant for molecules that fit tightly in the zeolite pores. The prediction of loadings when a force field for framework flexibility is used compared to when a rigid structure is used can be considered an artifact of the force field and not a re-accommodation of the framework atoms to a guest molecule. The simulations underline the need of new tailor-made force fields to model the zeolite flexibility for hosting aromatics. Such force fields should focus on the local changes due to the presence of bulky guest molecules, and not only vibrational behavior. The models for framework flexibility such as the ones considered in this work have been extensively used in literature to compute diffusion of many kinds of molecules in zeolites. The artifacts that these force fields produce for predictions of adsorption may have affected the prediction of other thermodynamic properties in these systems. The simulations from this work show that force fields for framework flexibility should not be blindly applied to zeolites and that a general rethinking of the parametrization schemes for such models is needed.

The effect of framework flexibility on the adsorption and diffusion of aromatics in MFI-type zeolites has been systematically studied. It has been observed that framework flexibility induces changes of the average zeolite structure. As the framework is more flexible, it is difficult to distinguish the channels and the intersections based on pore sizes. This has a significant effect on the Henry coefficient and the adsorption isotherms of aromatics in MFI-type zeolites. This suggests that the interactions between the aromatic molecules and the zeolite framework are very susceptible to small displacements of the zeolite atoms and changes of the geometry of the zeolite pores. The 'flexible snapshot' method is useful for the description of adsorp-

tion behavior at very low loadings/infinite dilution. For high pressures/loadings, the 'flexible snapshot' method does not yield the same loading compared to a flexible framework. This suggests that the effect of the guest molecules on the zeolite framework should not be neglected. The adsorption isotherms are affected by framework flexibility. At low loadings, the influence of the framework flexibility on the adsorption is small. When the loadings are higher than 4 molec./u.c., a small framework flexibility  $k$  yields higher loadings than in the rigid framework. Framework flexibility significantly decreases the free energy barriers of aromatics between the low energy sites of the zeolite framework. As the zeolite framework is more flexible, the self-diffusion coefficient is significantly increased. Framework flexibility has a remarkable effect on the adsorption and diffusion of aromatics in MFI-type zeolites. In the future, the development of force fields for zeolite framework flexibility should specifically focus on the interactions of bulky aromatic guest molecules within a zeolite framework.

The interactions of aromatic molecules within different zeolite types are studied by computing adsorption isotherms of pure xylenes and a mixture of xylenes at chemical equilibrium. It is observed that for zeolites with one dimensional channels, the selectivity for a xylene isomer is determined by a competition of entropic and enthalpic effects. Shape and size selectivity entropic effects are predominant for small one dimensional systems. Entropic effects due to the efficient arrangement of xylenes become relevant for large one dimensional systems. For zeolites with two intersecting channels, the selectivity is determined by a competition between enthalpic and entropic effects. Such effects are related to the orientation of the methyl groups of the competing xylenes. *m*-Xylene is preferentially adsorbed if xylenes fit tightly in the intersection of the channels. If the intersection is much larger than the adsorbed molecules, *p*-xylene molecules are adsorbed and can be efficiently arranged in the void volumes of the zeolite. The zeolite type can influence the competitive adsorption and selectivity of xylenes at reaction conditions. Different selectivities are observed when molecules are adsorbed from a vapor phase compared to the adsorption from a liquid phase. This suggests that screening studies that consider adsorption only from a vapor phase may have overlooked well-performing candidates for C<sub>8</sub> aromatics processing. This insight has a direct impact on the design criteria for future applications of zeolites in industry. More specifically, it is observed that MRE-type and AFI-type zeolites exclusively adsorb *p*-xylene and *o*-xylene from the mixture of xylenes in the liquid phase, respectively. These zeolite types show potential to be used as high-performing molecular sieves for xylene separation and catalysis. The insight from this work reflect the thermodynamic equilibrium of the molecules in the zeolites, so experimental work testing these findings is encouraged.

Regarding molecular simulations of aromatics and zeolites, future work should focus on the development of accurate descriptions of: vapor-liquid equilibria, specially for the vapor phase of xylenes; zeolite framework flexibility, aiming to properly describe the accommodation of bulky guest molecules in the framework without inducing artificial changes on the structure; and screening different zeolite types at reaction conditions considering the different mechanisms that drive adsorption at

high pressures. The development of appropriate models for the adsorption of aromatics in zeolites could be assisted by artificial intelligence algorithms. However, there are many challenges to model the framework flexibility and the adsorption of aromatics in zeolites appropriately. An accurate experimental description of the internal changes and crystal structure of the zeolite when varying pressure or temperature is crucial. Data of adsorption of aromatics in zeolites is scarce and not always consistent at the same temperature/pressure conditions. The variability of the adsorption experiments of aromatics in zeolites prevents a clear overview on what to compare to the predictions of the simulations. This knowledge is required to develop models able to reproduce and provide reliable molecular insight of adsorption phenomena. The insight provided in this work contributes to the development of knowledge at the molecular level of the chemistry and physics behind the complex interactions of C<sub>8</sub> aromatics hydrocarbons in zeolites.

# APPENDIX

## A.1. FORCE FIELD PARAMETERS AND INITIAL CONDITIONS

Table A.1: Force field parameters for xylene isomers used for chapter 2. All molecules are considered as rigid. \*Carbon atom bonded with a methyl group. For the bond lengths and angles between pseudo-atoms, the reader is referred to the original publications of the force fields [245, 248, 252, 253, 297, 299].

Force field	Pseudo-atom	$\epsilon/k_B$ / [K]	$\sigma$ / Å	$q$ / [e]
TraPPE-UA [252]	C	21.00	3.880	0
	CH	50.50	3.695	0
	CH <sub>3</sub>	98.00	3.750	0
TraPPE-UA-EH [245, 252]	C	30.70	3.600	-0.095
	C*	21.00	3.880	0
	H	25.50	2.360	0.095
	CH <sub>3</sub>	98.00	3.750	0
OPLS [253, 297]	C	35.24	3.550	-0.115
	H	15.03	2.420	0.115
	CH <sub>3</sub>	85.51	3.800	0.115
AUA [248, 299]	C	35.43	3.361	0
	CH	75.60	3.361	0
	CH <sub>3</sub>	120.15	3.607	0
	Center site (+)	0	0	8.130
	$\pi$ -site (-)	0	0	-4.065

Table A.2: Force field parameters of the guest-guest interactions used in chapters 3, 4, and 5. Lennard-Jones, partial charges, bending and torsion parameters are listed. The reader is referred to the original publications of the force fields for further details [252, 403].

Molecule	Pseudo-atom	$\epsilon/k_B / [\text{K}]$	$\sigma / [\text{\AA}]$	$q / [\text{e}]$
n-Heptane [403]	CH <sub>2</sub>	46.0	3.950	0
	CH <sub>3</sub>	98.0	3.750	0
Ethylbenzene [252]	C	21.0	3.880	0
	CH	50.5	3.695	0
	CH <sub>2</sub>	46.0	3.950	0
	CH <sub>3</sub>	98.0	3.750	0
Xylenes [252]	C	21.0	3.880	0
	CH	50.5	3.695	0
	CH <sub>3</sub>	98.0	3.750	0

Molecule	Bend	$\theta_0 / [\text{^\circ}]$	$k_\theta/k_B / [\text{K}]$
n-Heptane [403]	CH <sub>3</sub> -CH <sub>2</sub> -CH <sub>2</sub>	114	62500
	CH <sub>2</sub> -CH <sub>2</sub> -CH <sub>2</sub>	114	62500
	CH <sub>2</sub> -CH <sub>2</sub> -CH <sub>3</sub>	114	62500
Ethylbenzene [252]	C-CH <sub>2</sub> -CH <sub>3</sub>	114	62500

$$U_{\text{bend}} = 0.5k_\theta[\theta - \theta_0]^2$$

Molecule	n-Heptane [403]
Torsion	CH <sub>3</sub> -CH <sub>2</sub> -CH <sub>2</sub> -CH <sub>2</sub>
	CH <sub>2</sub> -CH <sub>2</sub> -CH <sub>2</sub> -CH <sub>3</sub>
$c_0/k_B / [\text{K}]$	0.00
$c_1/k_B / [\text{K}]$	355.03
$c_2/k_B / [\text{K}]$	-68.19
$c_3/k_B / [\text{K}]$	791.32

$$U_{\text{torsion}} = c_0 + c_1[1 + \cos \phi] + c_2[1 - \cos 2\phi] + c_3[1 - \cos 3\phi]$$

Molecule	Torsion	$e_1 / [\text{^\circ}]$	$e_0/k_B / [\text{K}]$
Ethylbenzene [252]	CH-C-CH <sub>2</sub> -CH <sub>3</sub>	180	131
$U_{\text{torsion}} = e_0[1 - \cos(2\phi + e_1)]$			

Table A.3: Force field parameters of the host-guest interactions used in chapters 3, 4, and 5. Lennard-Jones parameters listed. The interactions between different host-guest atom types are obtained using Lorentz-Berthelot mixing rules [292]. \*For chapter 3, the partial charges of the host-host force field [312, 373, 376] are used instead of the partial charges reported in the original TraPPE-zeo [396] force field. The reader is referred to the original publication of the force field for further details [396].

Pseudo-atom	$\epsilon/k_B / [\text{K}]$	$\sigma / [\text{\AA}]$	$q / [\text{e}]$
Si	22.0	2.3	+1.50*
O	53.0	3.3	-0.75*

Table A.4: Force field parameters of the Demontis [374] model. Intra-framework bond bending parameters are listed. \*The modified form of the model takes these lengths directly from the experimental crystal structure. The reader is referred to the original publication of the force field for further details [374].

#### Demontis [374] model

Bond	Type	$k/k_B / [\text{\AA}^{-2}]$	$r_0 / [\text{\AA}]$
Si-O	Harmonic bond stretch	251778.08	1.605*
O-(Si)-O	Urey-Bradley	51866.28	2.61786*

$U_{\text{Harmonic bond stretch}} = 0.5k[r - r_0]^2$   
 $U_{\text{Urey-Bradley}} = 0.5k[r - r_0]^2$

A

Table A.5: Force field parameters of the Nicholas [376] model. Intra-framework Lennard-Jones, partial charges, bond stretching, bending and torsion parameters are listed. \*The modified form of the model takes these lengths directly from the experimental crystal structure. The reader is referred to the original publications of the force fields for further details [376].

Nicholas [376] model				
Pseudo-atom		$\epsilon/k_B / [\text{K}]$	$\sigma / [\text{\AA}]$	$q / [\text{e}]$
Si		81.76	3.96	+1.10
O		29.43	3.06	-0.55
Bond	Type	$k / [\text{K\AA}^{-2}]$	$r_0 / [\text{\AA}]$	
Si-O	Harmonic bond stretch	300724.77	1.61*	
O-(Si)-O	Urey-Bradley	27488.74	3.1261*	
$U_{\text{Harmonic bond stretch}} = 0.5k[r - r_0]^2$				
$U_{\text{Urey-Bradley}} = 0.5k[r - r_0]^2$				
Bond bending		Si-O-Si		
Type		Quartic bend		
$k_1 / [\text{K}/\text{rad}^2]$		5462.50		
$k_2 / [\text{K}/\text{rad}^3]$		-17157.80		
$k_3 / [\text{K}/\text{rad}^4]$		13351.67		
$\theta_0 / [\text{^\circ}]$		149.5		
$U_{\text{Quartic bend}} = 0.5(k_1[\theta - \theta_0]^2 - k_2[\theta - \theta_0]^3 + k_3[\theta - \theta_0]^4)$				
Bond bending	Type	$k / [\text{K\AA}^{-2}]$	$\theta_0 / [\text{^\circ}]$	
O-Si-O	Harmonic bend	69537.44	109.5	
$U_{\text{Harmonic bend}} = 0.5k[\theta - \theta_0]^2$				
Bend-Torsion		Si-O-Si-O		
Type		Smoothed three cosine dihedral		
$p_0/k_B / [\text{K}]$		0.0		
$p_1/k_B / [\text{K}]$		0.0		
$p_2/k_B / [\text{K}]$		-352.42		
$U_{\text{Bend-torsion}} = 0.5p_0[1 + \cos \phi_{ijkl}]S(\theta_{ijk})S(\theta_{jkl})$				
		$+ 0.5p_1[1 - \cos 2\phi_{ijkl}]S(\theta_{ijk})S(\theta_{jkl})$		
		$+ 0.5p_2[1 + \cos 3\phi_{ijkl}]S(\theta_{ijk})S(\theta_{jkl})$		
$S(\theta) = \begin{cases} 1 & \theta < \theta_{\text{on}} \\ (\theta_{\text{off}} - \theta)^2 \frac{\theta_{\text{off}} + 2\theta - 3\theta_{\text{on}}}{(\theta_{\text{off}} - \theta_{\text{on}})^3} & \theta \geq \theta_{\text{on}} \end{cases}$				
with $\theta_{\text{on}} = 170^\circ$ and $\theta_{\text{off}} = 180^\circ$ .				

A

Table A.6: Force field parameters of the zeolite model by Jeffroy et al. [312] used in chapter 3. Intra-framework Lennard-Jones, partial charges, bond stretching, and bending parameters are listed. The reader is referred to the original publication of the force fields for further details [312]. \*The modified form of the model takes these lengths directly from the experimental crystal structure. \*\*Partial charges for silicalite are not reported by Jeffroy et al. [312]. In the original model [312], the partial charges are linearly extrapolated based on the aluminum content of the zeolite structure. The partial charges reported for Si atoms increase from +1.270530 e to +1.452410 e as the Si:Al ratio is increased from 1 to 3. Such linear extrapolation yields very high values of partial charges for high Si:Al ratios/all silica zeolites. Typical partial charges for Si atoms have been reported in the range of +0.5 to +4 e [400]. The values +1.5 e and -0.75 e are chosen for the Si and O atoms of silicalite, respectively.

### Jeffroy et al. [312] model

Pseudo-atom	$\epsilon/k_B / [\text{K}]$	$\sigma / [\text{\AA}]$	$q / [\text{e}]$
Si	0.0	0.0	+1.50**
O	0.0	0.0	-0.75**
Bond	Type	$k / [\text{K\AA}^{-2}]$	$r_0 / [\text{\AA}]$
Si-O	Harmonic bond stretch	1392000	1.65*
		$U_{\text{Harmonic bond stretch}} = 0.5k[r - r_0]^2$	
Bond bending	Type	$k / [\text{K/rad}^2]$	$\theta_0 / [^\circ]$
O-Si-O	Harmonic bend	300000	110
Si-O-Si	Harmonic bend	60000	145
		$U_{\text{Harmonic bend}} = 0.5k[\theta - \theta_0]^2$	

A

Table A.7: Input for the simulations of vapor-liquid equilibrium of chapter 2 for *m*-xylene, *o*-xylene and *p*-xylene.  $T$  is the temperature,  $N$  the number of molecules,  $L$  the initial length of one side of the (cubic) simulation box.

$T / [\text{K}]$	$N_{\text{Liquid}}$	$N_{\text{Vapor}}$	$L_{\text{Liquid}} / [\text{\AA}]$	$L_{\text{Vapor}} / [\text{\AA}]$
375	965	35	60	142
400	933	67	60	142
425	899	101	60	130
450	863	137	60	126
475	830	170	60	114
500	797	203	60	112
525	760	240	60	112
550	745	255	60	105

Table A.8: Change of ideal gas free energy  $\Delta G_{A \leftrightarrow B}^{\text{ideal}}$  of a reaction  $A \leftrightarrow B$  at 523 K computed using tabulated data [460–463] with Eq. A.1 for the reactions considered in chapter 5.

Reaction $A \leftrightarrow B$	$\Delta G_{A \leftrightarrow B}^{\text{ideal}} / [\text{kJ/mol}]$
$m\text{-xylene} \leftrightarrow o\text{-xylene}$	4.06
$m\text{-xylene} \leftrightarrow p\text{-xylene}$	3.62

## A.2. PARTITION FUNCTIONS OF XYLEMES FROM THERMODYNAMIC TABLES

The partition functions of xylene isomers at 523 K are computed from the change of the ideal gas free energy  $\Delta G_{A \leftrightarrow B}^{\text{ideal}}$  of a reaction  $A \leftrightarrow B$  using the procedure outlined in Ref. [295]. The change of the ideal gas free energy  $\Delta G_{A \leftrightarrow B}^{\text{ideal}}$  of a reaction  $A \leftrightarrow B$  is computed with tabulated enthalpies and entropies of formation using [442]:

$$\Delta G_{A \leftrightarrow B}^{\text{ideal}} = \Delta H_{f,B}^o - \Delta H_{f,A}^o + \int_{298K}^T \Delta C_{p,A \leftrightarrow B} dT - T \left( S_{f,B}^o - S_{f,A}^o + \int_{298K}^T \frac{\Delta C_{p,A \leftrightarrow B}}{T} dT \right) \quad (\text{A.1})$$

A

where  $\Delta H_{f,A}^o$ ,  $\Delta H_{f,B}^o$  and  $S_{f,A}^o$ ,  $S_{f,B}^o$  are the enthalpy and entropy of formation of components  $A$  and  $B$  at 298 K and 1 atm.  $\Delta C_{p,A \leftrightarrow B}$  is the difference between the constant pressure heat capacities of component  $A$  and  $B$  at temperature  $T$ . The enthalpies and entropies of formation, and the constant pressure heat capacities of xylene isomers are obtained from Refs. [460–463]. The computed change of ideal gas free energy  $\Delta G_{A \leftrightarrow B}^{\text{ideal}}$  of a reaction  $A \leftrightarrow B$  for the reactions considered in chapter 5 are listed in table A.8.

The change of the ideal gas free energy  $\Delta G_{A \leftrightarrow B}^{\text{ideal}}$  of a reaction  $A \leftrightarrow B$  with  $S$  components is related to the chemical potential of reactants and products (and the equilibrium constant  $K(T)$ ) by [295]:

$$\Delta G_{A \leftrightarrow B}^{\text{ideal}} = -RT \ln K(T) = -RT \sum_{i=1}^S \nu_i \ln \left( \frac{q_i V_0}{\Lambda_i^3} \right) \quad (\text{A.2})$$

Where  $\nu_i$  is the stoichiometric coefficient of component  $i$ ,  $q_i$  is the partition function of an isolated molecule of component  $i$ ,  $V_0$  is the reference volume (for the input of Brick-CFCMC:  $V_0 = 1 \text{ \AA}^3$ ). The thermal de Broglie wavelength  $\Lambda_i$  can be calculated using:

$$\Lambda_i = \frac{h}{\sqrt{2\pi M_i k_B T}} \quad (\text{A.3})$$

in which  $h$  is the Planck constant,  $M_i$  is the mass of one molecule of component  $i$ ,  $k_B$  is the Boltzmann constant, and  $T$  is the temperature [464]. Using the computed change of ideal gas free energy  $\Delta G_{A \leftrightarrow B}^{\text{ideal}}$  of a reaction  $A \leftrightarrow B$  for the reactions considered in chapter 5, Eq. A.2 becomes Eqs. A.4 and A.5:

Table A.9: Partition functions of xylene isomers at 523 K as input for reaction ensemble simulations in Brick-CFCMC [295] computed using Eqs. A.4 and A.5 by setting  $\ln\left(\frac{q_m V_0}{\Lambda^3}\right) = 0$ .

Molecule	$\ln(q_i V_0 / \Lambda_i^3) / [-]$
<i>m</i> -xylene	0
<i>o</i> -xylene	-0.9329943
<i>p</i> -xylene	-0.8324533

$$\frac{\Delta G_{m \leftrightarrow o}^{\text{ideal}}}{RT} = \ln\left(\frac{q_m V_0}{\Lambda_m^3}\right) - \ln\left(\frac{q_o V_0}{\Lambda_o^3}\right) \quad (\text{A.4})$$

$$\frac{\Delta G_{m \leftrightarrow p}^{\text{ideal}}}{RT} = \ln\left(\frac{q_m V_0}{\Lambda_m^3}\right) - \ln\left(\frac{q_p V_0}{\Lambda_p^3}\right) \quad (\text{A.5})$$

where *m* is *m*-xylene, *o* is *o*-xylene, and *p* is *p*-xylene. For the simulations of the reaction ensemble in Brick-CFCMC, only the relative difference between the partition functions is needed. The partition functions as input for Brick-CFCMC are obtained by setting  $\ln\left(\frac{q_m V_0}{\Lambda^3}\right) = 0$  in Eqs. A.4 and A.5. The partition functions used as input of Brick-CFCMC for the simulations of chapter 5 are listed in table A.9.

### A.3. MULTIPLE LINEAR REGRESSION FOR COMPUTING THERMODYNAMIC PROPERTIES OF ADSORPTION

Multiple linear regression [447, 448] is used to compute changes in enthalpy and entropy due to the transfer of one xylene molecule from the bulk phase (mixture of xylenes at chemical equilibrium) to the zeolite framework in chapter 5. The change in free energy  $\Delta G_{\text{tr},i}$  due to the transfer of one xylene molecule  $i$  from the bulk phase to the zeolite is related to the change of enthalpy  $\Delta H_{\text{tr},i}$  and entropy  $\Delta S_{\text{tr},i}$  by:

$$\Delta G_{\text{tr},i} = \Delta H_{\text{tr},i} - T\Delta S_{\text{tr},i} \quad (\text{A.6})$$

The change in free energy due to the transfer of one xylene molecule between the bulk phase and the zeolite is obtained using [465, 466]:

$$\Delta G_{\text{tr},i} = RT \ln \frac{\rho_{\text{bulk},i}}{\rho_{\text{ads},i}} \quad (\text{A.7})$$

where  $\rho_{\text{bulk},i}$  and  $\rho_{\text{ads},i}$  are the number densities of molecule  $i$  in bulk phase and zeolite, respectively. The change in enthalpy  $\Delta H_{\text{tr},i}$  due to the transfer of one xylene molecule  $i$  from the bulk phase to the zeolite is obtained from:

$$\Delta H_{\text{tr},i} = H_{\text{ads},i} - H_{\text{bulk},i} - RT \quad (\text{A.8})$$

where  $H_{\text{ads},i}$  is the enthalpy of adsorption of component  $i$  from the mixture of xylenes at chemical equilibrium in the zeolite framework, and  $H_{\text{bulk},i}$  is the enthalpy of adsorption of component  $i$  in the bulk phase mixture of xylenes at chemical equilibrium. Both  $H_{\text{ads},i}$  and  $H_{\text{bulk},i}$  are computed by Monte Carlo simulations in the grand-canonical ensemble using multiple linear regression [447, 448].

### A.4. FUGACITY COEFFICIENT FROM CHEMICAL POTENTIALS

In chapter 5, the Brick-CFCMC software [295] was used to compute fugacity coefficients  $\phi_i$  for component  $i$  from the excess chemical potential  $\mu_{\text{excess},i}$  obtained with the CFCMC method using [295]:

$$\phi_i = \frac{N}{\beta V} \exp(\beta\mu_{\text{excess},i}) \quad (\text{A.9})$$

where  $N$  is the total number of whole molecules, and  $V$  is the volume of the simulation box.

For the input for grand-canonical Monte Carlo simulations using the RASPA software [22, 365, 366], the fugacity coefficients are transformed to chemical potentials  $\mu_i$  using [366]:

$$\beta\mu_i = \beta\mu_{\text{IG},i}^0 + \ln(\beta\phi_i P) \quad (\text{A.10})$$

where  $P$  is the pressure, and  $\mu_{\text{IG},i}^0$  is the the chemical potential of the reference state.

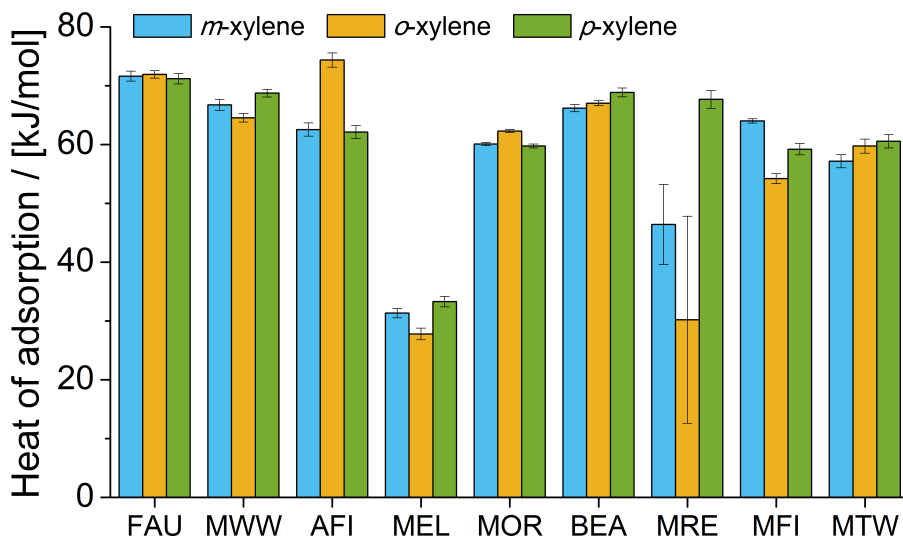


Figure A.1: Heat of adsorption of xylene isomers at 523 K and 30 bar in the zeolite framework types considered in chapter 5, adsorbed from the mixture at chemical equilibrium as computed by Monte Carlo simulations.

A



# REFERENCES

- [1] R. Agrawal, *Separations: Perspective of a process developer/designer*, *AIChE J.* **47**, 967 (2001).
- [2] National Research Council, *Separation Technologies for the Industries of the Future* (The National Academies Press, Washington, DC, 1998).
- [3] J. L. Humphrey and G. Keller, *Separation Process Technology* (McGraw-Hill, New York, 1997).
- [4] J. L. Humphrey and A. F. Siebert, *Separation technologies; an opportunity for energy savings*, *Chem. Eng. Prog.* **88**, 32 (1992).
- [5] D. S. Sholl and R. P. Lively, *Seven chemical separations to change the world*, *Nature* **532**, 435 (2016).
- [6] J. G. Speight, *The chemistry and technology of petroleum*, 5th ed. (CRC Press, Boca Raton, FL, 2014).
- [7] R. A. Kinsara and A. Demirbas, *Upgrading of crude oil via distillation processes*, *Pet. Sci. Technol.* **34**, 1300 (2016).
- [8] R. A. Ristinen, J. J. Kraushaar, and J. Brack, *Energy and the Environment* (John Wiley & Sons Inc, New York, 2007).
- [9] J. D. Gilchrist, *Fuels, Furnaces and Refractories* (Pergamon, Oxford, 1977).
- [10] BP p.l.c., *Statistical Review of World Energy*, 69th ed. (BP p.l.c., London, 2020).
- [11] J. G. Speight, *Handbook of Petroleum Product Analysis*, 2nd ed. (John Wiley & Sons, Hoboken, NJ, 2015).
- [12] T. Siddique, P. M. Fedorak, M. D. MacKinnon, and J. M. Foght, *Metabolism of BTEX and naphtha compounds to methane in oil sands tailings*, *Environ. Sci. Technol.* **41**, 2350 (2007).
- [13] J. G. Speight, *Production, properties and environmental impact of hydrocarbon fuel conversion*, in *Advances in Clean Hydrocarbon Fuel Processing*, Woodhead Publishing Series in Energy, edited by M. R. Khan (Woodhead Publishing, Oxford, 2011) pp. 54 – 82.
- [14] E. de Jong and R. J. Gosselink, *Lignocellulose-based chemical products*, in *Bioenergy Research: Advances and Applications*, edited by V. K. Gupta, M. G. Tuohy, C. P. Kubicek, J. Saddler, and F. Xu (Elsevier, Amsterdam, 2014) pp. 277 – 313.
- [15] H. H. Szmant, *Organic Building Blocks of the Chemical Industry* (Wiley, New York, 1989).
- [16] S. Matar and L. F. Hatch, *Chemistry of Petrochemical Processes*, 2nd ed. (Butterworth-Heinemann, Boston, 2001).
- [17] J. G. Speight, *The Refinery of the Future*, 2nd ed. (Gulf Professional Publishing, Cambridge, MA, 2020).

- [18] International Energy Agency, *Energy Technology Perspectives 2020* (OECD Publishing, Paris, 2020) Available: <http://dx.doi.org/10.1787/ab43a9a5-en>.
- [19] International Energy Agency, *World Energy Outlook 2019* (IEA, Paris, 2019) Available: <https://www.iea.org/reports/world-energy-outlook-2019>.
- [20] Y. Xiang, H. Wang, J. Cheng, and J. Matsubu, *Progress and prospects in catalytic ethane aromatization*, *Catal. Sci. Technol.* **8**, 1500 (2018).
- [21] Y. H. Kim, *Energy savings in the benzene-toluene-xylene separation process using an extended divided-wall column*, *Chem. Eng. Technol.* **39**, 2312 (2016).
- [22] D. Dubbeldam, S. Calero, and T. J. H. Vlugt, *iRASPA: GPU-accelerated visualization software for materials scientists*, *Mol. Simulat.* **44**, 653 (2018).
- [23] T. F. Degnan, C. Morris Smith, and C. R. Venkat, *Alkylation of aromatics with ethylene and propylene: recent developments in commercial processes*, *Appl. Catal. Gen.* **221**, 283 (2001).
- [24] F. Cavani and F. Trifirò, *Alternative processes for the production of styrene*, *Appl. Catal. A-Gen.* **133**, 219 (1995).
- [25] R. J. Schmidt, *Industrial catalytic processes-phenol production*, *Appl. Catal. A-Gen.* **280**, 89 (2005).
- [26] R. P. Eganhouse, *Long-chain alkylbenzenes: Their analytical chemistry, environmental occurrence and fate*, *Int. J. Environ. Anal. Chem.* **26**, 241 (1986).
- [27] H. Franck and J. W. Stadelhofer, *Industrial Aromatic Chemistry: Raw Materials - Processes - Products* (Springer-Verlag, Berlin, 1988).
- [28] J. Hancsók, *Gasoline fuels for spark-ignition internal combustion engines*, in *Kirk-Othmer Encyclopedia of Chemical Technology* (Wiley-Interscience, New York, NY, 2016).
- [29] H. A. Wittcoff, B. G. Reuben, and J. S. Plotkin, *Industrial Organic Chemicals*, 3rd ed. (John Wiley & Sons, Hoboken, NJ, 2013).
- [30] E. D. Ozokwelu, *Toluene*, in *Kirk-Othmer Encyclopedia of Chemical Technology* (Wiley-Interscience, New York, NY, 2000).
- [31] D. Stoye and W. Freitag, *Paints, coatings and solvents*, 2nd ed. (Wiley-Blackwell, Weinheim, 2007).
- [32] L. Fishbein, *An overview of environmental and toxicological aspects of aromatic hydrocarbons III. Xylene*, *Sci. Total Environ.* **43**, 165 (1985).
- [33] J. Das, Y. Bhat, and A. Halgeri, *Aromatization of C<sub>4</sub>-C<sub>6</sub> hydrocarbons to benzene, toluene and para xylene over pore size controlled ZnO-HZSM-5 zeolite*, in *Recent advances in basic and applied aspects of industrial catalysis*, Studies in surface science and catalysis, Vol. 113, edited by T. S. R. P. Rao and G. M. Dhar (Elsevier, Amsterdam, 1998) pp. 447 – 453.
- [34] C. J. Egan and R. V. Luthy, *Separation of xylenes*, *Ind. Eng. Chem.* **47**, 250 (1955).
- [35] J. Caro and J. Kärger, *From computer design to gas separation*, *Nature Mater.* **19**, 375 (2020).
- [36] R. A. F. Tomás, J. C. M. Bordado, and J. F. P. Gomes, *p-Xylene oxidation to terephthalic acid: A literature review oriented toward process optimization and development*, *Chem. Rev.* **113**, 7421 (2013).

- [37] A. Maneffa, P. Priecel, and J. A. Lopez-Sanchez, *Biomass-derived renewable aromatics: Selective routes and outlook for p-xylene commercialisation*, *ChemSusChem* **9**, 2736 (2016).
- [38] PlasticsEurope, *Plastics - The Facts 2019: An analysis of European plastics production, demand and waste data*. (PlasticsEurope, 2019) Available: <https://www.plasticseurope.org/en/resources/publications/1804-plastics-facts-2019>.
- [39] Ellen MacArthur Foundation, *The new plastics economy: Catalysing action* (Ellen MacArthur Foundation, 2017) Available: <https://www.newplasticseconomy.org/about/publications/report-2017>.
- [40] R. Ashby, *Migration from polyethylene terephthalate under all conditions of use*, *Food Addit. Contam* **5**, 485 (1988).
- [41] S. Keresztes, E. Tatár, V. G. Mihucz, I. Virág, C. Majdik, and G. Záray, *Leaching of antimony from polyethylene terephthalate (PET) bottles into mineral water*, *Sci. Total Environ.* **407**, 4731 (2009).
- [42] Ellen MacArthur Foundation, *The new plastics economy: Rethinking the future of plastics* (Ellen MacArthur Foundation, 2016) Available: <https://www.newplasticseconomy.org/about/publications/report-2016>.
- [43] H. Y. Choi and J. S. Lee, *The physiological response on wear comfort of polyethylene terephthalate irradiated by ultra-violet*, *Fibers Polym.* **7**, 446–449 (2006).
- [44] B. Kuczenski and R. Geyer, *Material flow analysis of polyethylene terephthalate in the US, 1996-2007*, *Resour. Conserv. Recy.* **54**, 1161 (2010).
- [45] M. Sulyman, J. Haponiuk, and K. Formela, *Utilization of recycled polyethylene terephthalate (PET) in engineering materials: A review*, *Int. J. Environ. Sci. Dev.* **7**, 100 (2016).
- [46] J. R. Ajmeri and C. Joshi Ajmeri, *Nonwoven materials and technologies for medical applications*, in *Handbook of Medical Textiles*, Woodhead Publishing Series in Textiles, edited by V. T. Bartels (Woodhead Publishing, Oxford, 2011) pp. 106 – 131.
- [47] R. Gadhave, S. Vineeth, and P. Gadekar, *Polymers and polymeric materials in COVID-19 pandemic: A review*. *Open J. Polym. Chem.* **10**, 66 (2020).
- [48] International Energy Agency, *The Future of Petrochemicals* (OECD/IEA, Paris, 2018) Available: <https://webstore.iea.org/the-future-of-petrochemicals>.
- [49] M. Minceva and A. E. Rodrigues, *Adsorption of xylenes on faujasite-type zeolite: Equilibrium and kinetics in batch adsorber*, *Chem. Eng. Res. Des.* **82**, 667 (2004).
- [50] V. Nikolov, D. Klissurski, and A. Anastasov, *Phthalic anhydride from o-xylene catalysis: Science and engineering*, *Catal. Rev.* **33**, 319 (1991).
- [51] K. Gupta and M. Yaseen, *Influence of xylene concentration and temperature on the intrinsic parameters of PVC in cyclohexanone–xylene blends*, *Polym. Int.* **46**, 303 (1998).
- [52] G. Wypych, *PVC Degradation and Stabilization*, 3rd ed. (ChemTec, Toronto, 2015).

- [53] M. Mock Carroll, *Polyvinylchloride (PVC) pipe reliability and failure modes*, *Reliab. Eng.* **13**, 11 (1985).
- [54] S. Biedermann-Brem, M. Biedermann, S. Pfenninger, M. Bauer, W. Altkofer, K. Rieger, U. Hauri, C. Droz, and K. Grob, *Plasticizers in PVC toys and child-care products: What succeeds the phthalates? Market survey 2007*, *Chroma.* **68**, 227–234 (2008).
- [55] N. Henry, *How Protective Is Protective Clothing?* in *Performance of Protective Clothing*, edited by R. Barker and G. Coletta (ASTM International, West Conshohocken, PA, 1986) pp. 51–58.
- [56] J. Leadbitter, *PVC and sustainability*, *Prog. Polym. Sci.* **27**, 2197 (2002).
- [57] L. Ciacci, F. Passarini, and I. Vassura, *The European PVC cycle: In-use stock and flows*, *Resour. Conserv. Recy.* **123**, 108 (2017).
- [58] W. J. Cannella, *Xylenes and ethylbenzene*, in *Kirk-Othmer Encyclopedia of Chemical Technology* (Wiley-Interscience, New York, NY, 2007).
- [59] L. B. Young, S. A. Butter, and W. W. Kaeding, *Shape selective reactions with zeolite catalysts: III. selectivity in xylene isomerization, toluene-methanol alkylation, and toluene disproportionation over ZSM-5 zeolite catalysts*, *J. Catal.* **76**, 418 (1982).
- [60] J. F. M. Denayer, D. De Vos, and P. Leflaive, *Separation of xylene isomers*, in *Metal-Organic Frameworks: Applications from Catalysis to Gas Storage*, edited by D. Farrusseng (John Wiley & Sons, Weinheim, 2011) Chap. 8, pp. 171–190.
- [61] M. S. P. Silva, J. P. B. Mota, and A. E. Rodrigues, *Fixed-bed adsorption of aromatic C<sub>8</sub> isomers: Breakthrough experiments, modeling and simulation*, *Sep. Purif. Technol.* **90**, 246 (2012).
- [62] Z.-Y. Gu and X.-P. Yan, *Metal-organic framework MIL-101 for high-resolution gas-chromatographic separation of xylene isomers and ethylbenzene*, *Angew. Chem. Int. Ed.* **49**, 1477 (2010).
- [63] M. T. Ashraf, R. Chebbi, and N. A. Darwish, *Process of p-xylene production by highly selective methylation of toluene*, *Ind. Eng. Chem. Res.* **52**, 13730 (2013).
- [64] Y. Ma, F. Zhang, S. Yang, and R. P. Lively, *Evidence for entropic diffusion selection of xylene isomers in carbon molecular sieve membranes*, *J. Membrane Sci.* **564**, 404 (2018).
- [65] R. Paludetto, G. Storti, G. Gamba, S. Carra, and M. Morbidelli, *On multicomponent adsorption equilibria of xylene mixtures on zeolites*, *Ind. Eng. Chem. Res.* **26**, 2250 (1987).
- [66] Y. Zhou, J. Wu, and E. W. Lemmon, *Thermodynamic properties of o-xylene, m-xylene, p-xylene, and ethylbenzene*, *J. Phys. Chem. Ref. Data* **41**, 023103 (2012).
- [67] D. L. Terrill, L. F. Sylvestre, and M. F. Doherty, *Separation of closely boiling mixtures by reactive distillation. 1. Theory*, *Ind. Eng. Chem. Process. Des. Dev.* **24**, 1062 (1985).
- [68] D. W. Green and M. Z. Southard, *Perry's chemical engineers' handbook*, 9th ed. (McGraw-Hill, New York, NY, 2018).

- [69] R. M. Lima and I. E. Grossmann, *Optimal synthesis of p-xylene separation processes based on crystallization technology*, *AIChE J.* **55**, 354 (2009).
- [70] B. Obama, *The irreversible momentum of clean energy*, *Science* **355**, 126 (2017).
- [71] M. Toledo, F. Gracia, S. Caro, J. Gómez, and V. Jovicic, *Hydrocarbons conversion to syngas in inert porous media combustion*, *Int. J. Hydrg. Energ.* **41**, 5857 (2016).
- [72] S. Zhang, M. K. Taylor, L. Jiang, H. Ren, and G. Zhu, *Light hydrocarbon separations using porous organic framework materials*, *Cem.-Eur. J.* **26**, 3205 (2020).
- [73] B. Crittenden and W. John Thomas, *Adsorption technology and design*, 1st ed. (Butterworth-Heinemann, Oxford, 1998).
- [74] Y. Wang, S. B. Peh, and D. Zhao, *Alternatives to cryogenic distillation: Advanced porous materials in adsorptive light olefin/paraffin separations*, *Small* **15**, 1900058 (2019).
- [75] W.-G. Cui, T.-L. Hu, and X.-H. Bu, *Metal-organic framework materials for the separation and purification of light hydrocarbons*, *Adv. Mater* **32**, 1806445 (2020).
- [76] R. P. Lively and M. J. Realff, *On thermodynamic separation efficiency: Adsorption processes*, *AIChE J.* **62**, 3699 (2016).
- [77] M. Minceva and A. E. Rodrigues, *Understanding and revamping of industrial scale SMB units for p-xylene separation*, *AIChE J.* **53**, 138 (2007).
- [78] R. T. Yang, *Gas separation by adsorption processes* (Butterworth Publishers, Stoneham, MA, 1987).
- [79] D. M. Ruthven, *Principles of adsorption and adsorption processes* (Wiley, New York, 1984).
- [80] A. E. Rodrigues, C. Pereira, M. Minceva, L. S. Pais, A. M. Ribeiro, A. Ribeiro, M. Silva, N. Graça, and J. C. Santos, *The Parex process for the separation of p-xylene*, in *Simulated Moving Bed Technology*, edited by A. E. Rodrigues, C. Pereira, M. Minceva, L. S. Pais, A. M. Ribeiro, A. Ribeiro, M. Silva, N. Graça, and J. C. Santos (Butterworth-Heinemann, Oxford, 2015) pp. 117 – 144.
- [81] D. B. Broughton, R. W. Neuzil, J. M. Pharis, and C. S. Brearley, *The Parex process for recovering paraxylene*, *Chem. Eng. Prog.* **66**, 70–75 (1970).
- [82] G. Ash, K. Barth, G. Hotier, L. Mank, and P. Renard, *Eluxyl: a new paraxylene separation process*, *P. Rev. Inst. Fr. Pet.* **49**, 541–549 (1994).
- [83] W. Jin and P. C. Wankat, *Hybrid simulated moving bed processes for the purification of p-xylene*, *Sep. Sci. Technol.* **42**, 669 (2007).
- [84] W. Jin and S. Zhu, *Study of adsorption equilibrium and dynamics of benzene, toluene, and xylene on zeolite NaY*, *Chem. Eng. Technol.* **23**, 151 (2000).
- [85] V. Cottier, J.-P. Bellat, M.-H. Simonot-Grange, and A. Méthivier, *Adsorption of p-xylene/m-xylene gas mixtures on BaY and NaY zeolites. Coadsorption equilibria and selectivities*, *J. Phys. Chem. B* **101**, 4798 (1997).

- [86] J.-P. Bellat and M.-H. Simonot-Grange, *Adsorption of gaseous p-xylene and m-xylene on NaY, KY, and BaY zeolites. Part 2: Modeling. Enthalpies and entropies of adsorption*, *Zeolites* **15**, 219 (1995).
- [87] V. Cottier, E. Pilverdier, M.-H. Simonot-Grange, and J.-P. Bellat, *Derivative enthalpies of adsorption of p-xylene and m-xylene onto NaY and BaY Zeolites at 150°C: Contribution to the prediction of adsorption selectivity*, *J. Therm. Anal. Calorim.* **58**, 121 (1999).
- [88] I. Daems, P. Leflaive, A. Méthivier, J. Denayer, and G. Baron, *Size and packing related adsorption effects in the liquid phase adsorption of aromatics and alkenes on FAU type zeolites*, (Elsevier, 2005) pp. 1177 – 1184.
- [89] I. Daems, P. Leflaive, A. Méthivier, G. V. Baron, and J. F. Denayer, *Influence of si:al-ratio of faujasites on the adsorption of alkanes, alkenes and aromatics*, *Microporous Mesoporous Mat.* **96**, 149 (2006).
- [90] Z.-Y. Gu, D.-Q. Jiang, H.-F. Wang, X.-Y. Cui, and X.-P. Yan, *Adsorption and separation of xylene isomers and ethylbenzene on two Zn-terephthalate metal-organic frameworks*, *J. Phys. Chem C* **114**, 311 (2010).
- [91] A. Torres-Knoop, R. Krishna, and D. Dubbeldam, *Separating xylene isomers by commensurate stacking of p-xylene within channels of MAF-X8*, *Angew. Chem.* **126**, 7908 –7912 (2014).
- [92] D. Peralta, G. Chaplais, A. Simon-Masseron, K. Barthelet, C. Chizallet, A.-A. Quoineaud, and G. D. Pirngruber, *Comparison of the behavior of metal-organic frameworks and zeolites for hydrocarbon separations*, *J. Am. Chem. Soc.* **134**, 8115 (2012).
- [93] B. Bozbiyik, J. Lannoeye, D. E. De Vos, G. V. Baron, and J. F. M. Denayer, *Shape selective properties of the Al-fumarate metal-organic framework in the adsorption and separation of n-alkanes, iso-alkanes, cyclo-alkanes and aromatic hydrocarbons*, *Phys. Chem. Chem. Phys.* **18**, 3294 (2016).
- [94] M. E. Davis, *Distinguishing the (almost) indistinguishable*, *Science* **300**, 438 (2003).
- [95] A. Martínez, M. A. Arribas, and S. Moussa, *Application of zeolites in the production of light olefins and BTX petrochemical intermediates*, in *Zeolites in catalysis: Properties and applications*, edited by J. Čejka, R. E. Morris, and P. Nachtigall (The Royal Society of Chemistry, London, 2017) pp. 351–408.
- [96] E. A. Uslamin, H. Saito, N. Kosinov, E. Pidko, Y. Sekine, and E. J. M. Hensen, *Aromatization of ethylene over zeolite-based catalysts*, *Catal. Sci. Technol.* **10**, 2774 (2020).
- [97] M. Rigutto, *Cracking and hydrocracking*, in *Zeolites and Catalysis*, edited by J. Čejka, A. Corma, and S. Zones (John Wiley & Sons, Weinheim, 2010) pp. 547–584.
- [98] E. T. C. Vogt and B. M. Weckhuysen, *Fluid catalytic cracking: recent developments on the grand old lady of zeolite catalysis*, *Chem. Soc. Rev.* **44**, 7342 (2015).
- [99] Y. Li, L. Li, and J. Yu, *Applications of zeolites in sustainable chemistry*, *Chem* **3**, 928 (2017).

- [100] P. Princz, J. Olah, S. Smith, K. Hatfield, and M. Litrico, *Wastewater treatment using modified natural Zeolites*, in *Use of humic substances to remediate polluted environments: From theory to practice*, edited by I. V. Perminova, K. Hatfield, and N. Hertkorn (Springer Netherlands, Dordrecht, 2005) pp. 267–282.
- [101] Z. Milán, C. de Las Pozas, M. Cruz, R. Borja, E. Sánchez, K. Ilangovan, Y. Espinosa, and B. Luna, *The removal of bacteria by modified natural zeolites*, *J. Environ. Sci. Health A* **36**, 1073 (2001).
- [102] K. B. Tankersley, N. P. Dunning, C. Carr, D. L. Lentz, and V. L. Scarborough, *Zeolite water purification at Tikal, an ancient Maya city in Guatemala*, *Sci. Rep.* **10**, 18021 (2020).
- [103] H. G. Karge and J. Weitkamp, *Zeolites as catalysts, sorbents and detergent builders: applications and innovations* (Elsevier, Amsterdam, 1989).
- [104] L. Cai, J. A. Koziel, Y. Liang, A. T. Nguyen, and H. Xin, *Evaluation of zeolite for control of odorants emissions from simulated poultry manure storage*, *J. Environ. Qual.* **36**, 184 (2007).
- [105] E. Borai, R. Harjula, L. Malinen, and A. Paajanen, *Efficient removal of cesium from low-level radioactive liquid waste using natural and impregnated zeolite minerals*, *J. Hazard. Mater.* **172**, 416 (2009).
- [106] H. Valdés, S. Alejandro, and C. A. Zaror, *Natural zeolite reactivity towards ozone: The role of compensating cations*, *J. Hazard. Mater.* **227-228**, 34 (2012).
- [107] V. Van Speybroeck, K. Hemelsoet, L. Joos, M. Waroquier, R. G. Bell, and C. R. A. Catlow, *Advances in theory and their application within the field of zeolite chemistry*, *Chem. Soc. Rev.* **44**, 7044 (2015).
- [108] M. Kubů, R. Millini, and N. Žilková, *10-ring zeolites: Synthesis, characterization and catalytic applications*, *Catal. Today* **324**, 3 (2019).
- [109] N. Jiang, M. Erdős, O. A. Moulton, R. Shang, T. J. H. Vlugt, S. G. J. Heijman, and L. C. Rietveld, *The adsorption mechanisms of organic micropollutants on high-silica zeolites causing S-shaped adsorption isotherms: An experimental and monte carlo simulation study*, *Chem. Eng. J.* **389**, 123968 (2020).
- [110] S. Ozaydin, G. Kocer, and A. Hepbasli, *Natural zeolites in energy applications*, *Energ. Source Part A* **28**, 1425 (2006).
- [111] A. Luna-Triguero, J. M. Vicent-Luna, M. J. Jansman, G. Zafeiropoulos, M. N. Tsampas, M. C. M. van de Sanden, H. N. Akse, and S. Calero, *Enhancing separation efficiency in european syngas industry by using zeolites*, *Catal. Today* **362**, 113 (2020).
- [112] C. J. Rhodes, *Properties and applications of zeolites*, *Sci. Prog.* **93**, 223 (2010).
- [113] N. Kosinov, J. Gascon, F. Kapteijn, and E. J. Hensen, *Recent developments in zeolite membranes for gas separation*, *J. Membr. Sci.* **499**, 65 (2016).
- [114] M. Fischer, *Simulation-based evaluation of zeolite adsorbents for the removal of emerging contaminants*, *Mater. Adv.* **1**, 86 (2020).
- [115] S. Alejandro, H. Valdés, M.-H. Manero, and C. A. Zaror, *BTX abatement using Chilean natural zeolite: the role of Brønsted acid sites*, *Water Sci. Technol.* **66**, 1759 (2012).

- [116] M. E. Davis, *Zeolites and molecular sieves: not just ordinary catalysts*, *Ind. Eng. Chem. Res.* **30**, 1675 (1991).
- [117] B. Coasne, J. Haines, C. Levelut, O. Cambon, M. Santoro, F. Gorelli, and G. Garbarino, *Enhanced mechanical strength of zeolites by adsorption of guest molecules*, *Phys. Chem. Chem. Phys.* **13**, 20096 (2011).
- [118] Y. Li, H. Cao, and J. Yu, *Toward a new era of designed synthesis of nanoporous zeolitic materials*, *ACS Nano* **12**, 4096 (2018).
- [119] M. O'Keeffe, *Rigid, flexible and impossible zeolite and related structures*, *Philos. Trans. Royal Soc. A* **372**, 20120034 (2014).
- [120] A. Corma, F. Rey, S. Valencia, J. L. Jordá, and J. Rius, *A zeolite with interconnected 8-, 10- and 12-ring pores and its unique catalytic selectivity*, *Nature Mater.* **2**, 493–497 (2003).
- [121] E. M. Flanigen, *Zeolites and molecular sieves: An historical perspective*, in *Introduction to Zeolite Science and Practice*, Studies in Surface Science and Catalysis, Vol. 137, edited by H. van Bekkum, E. Flanigen, P. Jacobs, and J. Jansen (Elsevier, Amsterdam, 2001) pp. 11 – 35.
- [122] G. Sastre and A. Corma, *Rings and strain in pure silica zeolites*, *J. Phys. Chem. B* **110**, 17949 (2006).
- [123] C. Baerlocher and L. B. McCusker, *Database of zeolite structures*, <http://www.iza-structure.org/databases/>, Accessed: 25-09-2020.
- [124] D. J. Earl and M. W. Deem, *Toward a database of hypothetical zeolite structures*, *Ind. Eng. Chem. Res.* **45**, 5449 (2006).
- [125] E. Haldoupis, S. Nair, and D. S. Sholl, *Pore size analysis of >250.000 hypothetical zeolites*, *Phys. Chem. Chem. Phys.* **13**, 5053 (2011).
- [126] R. Pophale, P. A. Cheeseman, and M. W. Deem, *A database of new zeolite-like materials*, *Phys. Chem. Chem. Phys.* **13**, 12407 (2011).
- [127] M. Król, *Natural vs. synthetic zeolites*, *Crystals* **10**, 622 (2020).
- [128] R. Bingre, B. Louis, and P. Nguyen, *An overview on zeolite shaping technology and solutions to overcome diffusion limitations*, *Catalysts* **8**, 163 (2018).
- [129] W. Chaikittisilp and T. Okubo, *Zeolite and zeolite-like materials*, in *Handbook of Solid State Chemistry* (John Wiley & Sons, Weinheim, 2017) pp. 97–119.
- [130] S. Kulprathipanja, ed., *Zeolites in industrial separation and catalysis*, 1st ed. (John Wiley & Sons, Weinheim, 2010).
- [131] W. Vermeiren and J. P. Gilson, *Impact of zeolites on the petroleum and petrochemical industry*, *Top. Catal.* **52**, 1131–1161 (2009).
- [132] M. W. Ackley, S. U. Rege, and H. Saxena, *Application of natural zeolites in the purification and separation of gases*, *Microporous Mesoporous Mat.* **61**, 25 (2003).
- [133] A. Ramirez, A. Dutta Chowdhury, A. Dokania, P. Cnudde, M. Caglayan, I. Yarulina, E. Abou-Hamad, L. Gevers, S. Ould-Chikh, K. De Wispelaere, V. van Speybroeck, and J. Gascon, *Effect of zeolite topology and reactor configuration on the direct conversion of CO<sub>2</sub> to light olefins and aromatics*, *ACS Catal.* **9**, 6320 (2019).

- [134] J. Shi, Y. Wang, W. Yang, Y. Tang, and Z. Xie, *Recent advances of pore system construction in zeolite-catalyzed chemical industry processes*, *Chem. Soc. Rev.* **44**, 8877 (2015).
- [135] V. Sánchez-Gil, E. G. Noya, A. Sanz, S. J. Khatib, J. M. Guil, E. Lomba, R. Marguta, and S. Valencia, *Experimental and simulation studies of the stepped adsorption of toluene on pure-silica MEL zeolite*, *J. Phys. Chem. C* **120**, 8640 (2016).
- [136] K. Gołębek, K. A. Tarach, and K. Góra-Marek, *2D COS analysis of m-xylene transformation over medium-pore zeolites*, *Microporous Mesoporous Mat.* **266**, 90 (2018).
- [137] J. Toda, A. Corma, R. H. Abudawoud, M. S. Elanany, I. M. Al-Zahrani, and G. Sastre, *Influence of force fields on the selective diffusion of para-xylene over ortho-xylene in 10-ring zeolites*, *Mol. Simulat.* **41**, 1438 (2015).
- [138] S. Al-Khattaf, S. A. Ali, A. M. Aitani, N. Žilková, D. Kubička, and J. Čejka, *Recent advances in reactions of alkylbenzenes over novel zeolites: The effects of zeolite structure and morphology*, *Catal. Rev.* **56**, 333 (2014).
- [139] J. Toda, A. Corma, and G. Sastre, *Diffusion of trimethylbenzenes and xylenes in zeolites with 12- and 10-ring channels as catalyst for toluene-trimethylbenzene transalkylation*, *J. Phys. Chem. C* **120**, 16668 (2016).
- [140] J. M. Thomas, *Solid acid catalysts*, *Sci. Am.* **266**, 112 (1992).
- [141] M. Shamzhy, M. Opanasenko, P. Concepción, and A. Martínez, *New trends in tailoring active sites in zeolite-based catalysts*, *Chem. Soc. Rev.* **48**, 1095 (2019).
- [142] B. Smit, L. Daniël J. C. Loyens, and G. L. M. M. Verbist, *Simulation of adsorption and diffusion of hydrocarbons in zeolites*, *Faraday Discuss.* **106**, 93 (1997).
- [143] B. Smit, *Molecular simulations of the adsorption and diffusion of hydrocarbons in molecular sieves*, in *From Zeolites to Porous MOF Materials - The 40th Anniversary of International Zeolite Conference*, Studies in Surface Science and Catalysis, Vol. 170, edited by R. Xu, Z. Gao, J. Chen, and W. Yan (Elsevier, Amsterdam, 2007) pp. 121 – 129.
- [144] B. Smit and T. L. M. Maesen, *Molecular simulations of zeolites: Adsorption, diffusion, and shape selectivity*, *Chem. Rev.* **108**, 4125 (2008).
- [145] T. J. H. Vlugt, W. Zhu, F. Kapteijn, J. A. Moulijn, B. Smit, and R. Krishna, *Adsorption of linear and branched alkanes in the zeolite silicalite-1*, *J. Am. Chem. Soc.* **120**, 5599 (1998).
- [146] S. F. Garcia and P. B. Weisz, *Effective diffusivities in zeolites 1. Aromatics in ZSM-5 crystals*, *J. Catal.* **121**, 294 (1990).
- [147] J. Toda and G. Sastre, *Diffusion of trimethylbenzenes, toluene, and xylenes in UWY zeolite as a catalyst for transalkylation of trimethylbenzenes with toluene*, *J. Phys. Chem. C* **122**, 7885 (2018).
- [148] J. Kärger, D. M. Ruthven, and R. Valiullin, *Diffusion in nanopores: inspecting the grounds*, *Adsorption* (2020), 10.1007/s10450-020-00277-6.

- [149] A. Sharma and P. K. Ghorai, *Effect of host framework on the diffusion process in microporous material: A molecular dynamics simulation investigation*, *J. Mol. Model.* **23**, 324 (2017).
- [150] D. P. Broom and K. M. Thomas, *Gas adsorption by nanoporous materials: Future applications and experimental challenges*, *MRS Bull.* **38**, 412–421 (2013).
- [151] A. L. Myers and P. A. Monson, *Adsorption in porous materials at high pressure: Theory and experiment*, *Langmuir* **18**, 10261 (2002).
- [152] Y. Belmabkhout, M. Frère, and G. De Weireld, *High-pressure adsorption measurements. a comparative study of the volumetric and gravimetric methods*, *Meas. Sci. Technol.* **15**, 848 (2004).
- [153] P. Pendleton and A. Badalyan, *Gas adsorption data uncertainty and propagation analyses*, *Adsorption* **11**, 61–66 (2006).
- [154] S. Brandani, E. Mangano, and L. N. Sarkisov, *Net, excess and absolute adsorption and adsorption of helium*, *Adsorption* **22**, 261–276 (2016).
- [155] S. Gumma and O. Talu, *Net adsorption: A thermodynamic framework for supercritical gas adsorption and storage in porous solids*, *Langmuir* **26**, 17013 (2010).
- [156] J. U. Keller and R. Staudt, *Gas adsorption equilibria: Experimental methods and adsorptive isotherms* (Springer, New York, NY, 2005).
- [157] O. Talu, *Measurement and analysis of mixture adsorption equilibrium in porous solids*, *Chem. Ing. Tech.* **83**, 67 (2011).
- [158] D. P. Broom, O. Talu, and M. J. Benham, *Integral Mass Balance (IMB) method for measuring multicomponent gas adsorption equilibria in nanoporous materials*, *Ind. Eng. Chem. Res.* **59**, 20478–20491 (2020).
- [159] O. Talu, *Needs, status, techniques and problems with binary gas adsorption experiments*, *Adv. Colloid Interface Sci.* **76-77**, 227 (1998).
- [160] F. R. Siperstein and A. L. Myers, *Mixed-gas adsorption*, *AIChE J.* **47**, 1141 (2001).
- [161] K. S. Walton and D. S. Sholl, *Predicting multicomponent adsorption: 50 years of the ideal adsorbed solution theory*, *AIChE J.* **61**, 2757 (2015).
- [162] O. Talu, *Needs, status, techniques and problems with binary gas adsorption experiments*, *Adv. Colloid Interface Sci.* **76-77**, 227 (1998).
- [163] J. Jansen, *The preparation of oxide molecular sieves a. synthesis of zeolites*, in *Introduction to Zeolite Science and Practice*, Studies in Surface Science and Catalysis, Vol. 137, edited by H. van Bekkum, E. Flanigen, P. Jacobs, and J. Jansen (Elsevier, Amsterdam, 2001) pp. 175 – 227.
- [164] J. Čejka, R. Millini, M. Opanasenko, D. P. Serrano, and W. J. Roth, *Advances and challenges in zeolite synthesis and catalysis*, *Catal. Today* **345**, 2 (2020).
- [165] S. Mintova, J.-P. Gilson, and V. Valtchev, *Advances in nanosized zeolites*, *Nanoscale* **5**, 6693 (2013).
- [166] M. Moliner, C. Martínez, and A. Corma, *Synthesis strategies for preparing useful small pore zeolites and zeotypes for gas separations and catalysis*, *Chem. Mater.* **26**, 246 (2014).

- [167] K. G. Strohmaier, *Synthesis of zeolites*, in *Zeolites in catalysis: Properties and applications*, edited by J. Čejka, R. E. Morris, and P. Nachtigall (The Royal Society of Chemistry, London, 2017) pp. 73–102.
- [168] A. Sayari, *Catalysis by crystalline mesoporous molecular sieves*, *Chem. Mater.* **8**, 1840 (1996).
- [169] A. Korzeniowska, J. Grzybek, K. Kałahurska, M. Kubu, W. J. Roth, and B. Gil, *The structure-catalytic activity relationship for the transient layered zeolite MCM-56 with MW topology*, *Catal. Today* **345**, 116 (2020).
- [170] L. Lin, A. H. Berger, R. L. Martin, J. Kim, J. A. Swisher, K. Jariwala, C. H. Rycroft, A. S. Bhowm, M. W. Deem, M. Haranczyk, and B. Smit, *In silico screening of carbon-capture materials*, *Nature Mater.* **11**, 633–641 (2012).
- [171] T. Düren, Y.-S. Bae, and R. Q. Snurr, *Using molecular simulation to characterise metal-organic frameworks for adsorption applications*, *Chem. Soc. Rev.* **38**, 1237 (2009).
- [172] S. A. Hollingsworth and R. O. Dror, *Molecular dynamics simulation for all*, *Neuron* **99**, 1129 (2018).
- [173] D. Frenkel and B. Smit, *Understanding molecular simulation*, 2nd ed. (Academic Press, San Diego, CA, 2002).
- [174] M. O. Daramola, A. J. Burger, M. Pera-Titus, A. Giroir-Fendler, S. Miachon, J.-A. Dalmon, and L. Lorenzen, *Separation and isomerization of xylenes using zeolite membranes: a short overview*, *Asia-Pac. J. Chem. Eng.* **5**, 815 (2010).
- [175] X. Nie, L. Zhao, S. Deng, W. Su, and Y. Zhang, *A review of molecular simulation applied in vapor-liquid equilibria (VLE) estimation of thermodynamic cycles*, *J. Mol. Liq.* **264**, 652 (2018).
- [176] N. V. Choudary, R. V. Jasra, S. G. T. Bhat, and T. S. R. Prasada Rao, *Liquid phase adsorption, diffusion and counter diffusion of aromatic hydrocarbons on ZSM-5 zeolites*, in *Zeolites: Facts, Figures, Future Part A*, Studies in Surface Science and Catalysis, Vol. 49, edited by P. Jacobs and R. van Santen (Elsevier, 1989) pp. 867 – 876.
- [177] S. Sircar, *Basic research needs for design of adsorptive gas separation processes*, *Ind. Eng. Chem. Res.* **45**, 5435 (2006).
- [178] C. Chmelik, J. Caro, D. Freude, J. Haase, R. Valiullin, and J. Kärger, *Diffusive spreading of molecules in nanoporous materials*, in *Diffusive Spreading in Nature, Technology and Society*, edited by A. Bunde, J. Caro, J. Kärger, and G. Vogl (Springer International Publishing, Cham, 2018) pp. 171–202.
- [179] F. J. Keil, *Molecular simulation of adsorption in zeolites and carbon nanotubes*, in *Adsorption and Phase Behaviour in Nanochannels and Nanotubes*, edited by L. J. Dunne and G. Manos (Springer, Dordrecht, 2010).
- [180] R. Babarao and J. Jiang, *Molecular computations of adsorption in nanoporous materials*, in *Adsorption and phase behaviour in nanochannels and nanotubes*, edited by L. J. Dunne and G. Manos (Springer, Dordrecht, 2010).
- [181] T. J. H. Vlugt, E. García-Pérez, D. Dubbeldam, S. Ban, and S. Calero, *Computing the heat of adsorption using molecular simulations: The effect of strong coulombic interactions*, *J. Chem. Theory Comput.* **4**, 1107 (2008).

- [182] C. González-Galán, A. Luna-Triguero, J. Vicent-Luna, A. Zaderenko, A. Ślawek, R. Sánchez-de-Armas, and S. Calero, *Exploiting the  $\pi$ -bonding for the separation of benzene and cyclohexane in zeolites*, *Chem. Eng. J.* **398**, 125678 (2020).
- [183] J. Perez-Carbajo, P. Gómez-Álvarez, R. Bueno-Perez, P. J. Merkling, and S. Calero, *Optimisation of the Fischer–Tropsch process using zeolites for tail gas separation*, *Phys. Chem. Chem. Phys.* **16**, 5678 (2014).
- [184] E. Rezlerová, A. Zukal, J. Čejka, F. R. Siperstein, J. K. Brennan, and M. Lísal, *Adsorption and diffusion of  $C_1$  to  $C_4$  alkanes in dual-porosity zeolites by molecular simulations*, *Langmuir* **33**, 11126 (2017).
- [185] P. Bai, M. Y. Jeon, L. Ren, C. Knight, M. W. Deem, M. Tsapatsis, and J. I. Siepmann, *Discovery of optimal zeolites for challenging separations and chemical transformations using predictive materials modeling*, *Nat. Commun.* **6**, 5912 (2015).
- [186] A. H. Fuchs and A. K. Cheetham, *Adsorption of guest molecules in zeolitic materials: Computational aspects*, *J. Phys. Chem. B* **105**, 7375 (2001).
- [187] S. Caro-Ortiz, E. Zuidema, M. Rigutto, D. Dubbeldam, and T. J. H. Vlugt, *Effects of framework flexibility on the adsorption and diffusion of aromatics in MFI-type zeolites*, *J. Phys. Chem. C* **124**, 24488–24499 (2020).
- [188] T. R. Josephson, P. J. Dauenhauer, M. Tsapatsis, and J. I. Siepmann, *Adsorption of furan, hexanoic acid, and alkanes in a hierarchical zeolite at reaction conditions: Insights from molecular simulations*, *J. Comput. Sci.* **48**, 101267 (2021).
- [189] F. Gracia and E. E. Wolf, *Monte Carlo simulations of the effect of crystallite size on the activity of a supported catalyst*, *Chem. Eng. J.* **82**, 291 (2001).
- [190] N. Lamia, M. Jorge, M. A. Granato, F. A. Almeida Paz, H. Chevreau, and A. E. Rodrigues, *Adsorption of propane, propylene and isobutane on a metal–organic framework: Molecular simulation and experiment*, *Chem. Eng. Sci.* **64**, 3246 (2009).
- [191] T. M. Becker, A. Luna-Triguero, J. M. Vicent-Luna, L.-C. Lin, D. Dubbeldam, S. Calero, and T. J. H. Vlugt, *Potential of polarizable force fields for predicting the separation performance of small hydrocarbons in M-MOF-74*, *Phys. Chem. Chem. Phys.* **20**, 28848 (2018).
- [192] M. J. Lennox and T. Düren, *Understanding the kinetic and thermodynamic origins of xylene separation in UiO-66(Zr) via molecular simulation*, *J. Phys. Chem. C* **120**, 18651 (2016).
- [193] W.-G. Cui, T.-L. Hu, and X.-H. Bu, *Metal–organic framework materials for the separation and purification of light hydrocarbons*, *Adv. Mater.* **32**, 1806445 (2020).
- [194] A. Ślawek, K. Roztocki, D. Majda, S. Jaskaniec, T. J. H. Vlugt, and W. Makowski, *Adsorption of  $n$ -alkanes in ZIF-8: Influence of crystal size and framework dynamics*, *Microporous Mesoporous Mat.* **312**, 110730 (2020).
- [195] D. Dubbeldam, S. Calero, and T. J. Vlugt, *Exploring new methods and materials for enantioselective separations and catalysis*, *Mol. Simulat.* **40**, 585 (2014).

- [196] A. Torres-Knoop and D. Dubbeldam, *Exploiting large-pore metal-organic frameworks for separations through entropic molecular mechanisms*, *ChemPhysChem* **16**, 2046 (2015).
- [197] S. Calero, *Modeling of transport and accessibility in zeolites*, in *Zeolites and Catalysis*, edited by J. Čejka, A. Corma, and S. Zones (John Wiley & Sons, Weinheim, 2010) pp. 335–360.
- [198] H. Fang, H. Demir, P. Kamakoti, and D. S. Sholl, *Recent developments in first-principles force fields for molecules in nanoporous materials*, *J. Mater. Chem. A* **2**, 274 (2014).
- [199] P. Ungerer, B. Tavitian, and A. Boutin, *Applications of molecular simulation in the oil and gas industry - Monte-Carlo methods*, 1st ed. (Editions Technip, Paris, 2005).
- [200] R. Q. Snurr, A. T. Bell, and D. N. Theodorou, *Prediction of adsorption of aromatic hydrocarbons in silicalite from grand-canonical Monte Carlo simulations with biased insertions*, *J. Phys. Chem.* **97**, 13742 (1993).
- [201] A. Torres-Knoop, J. Heinen, R. Krishna, and D. Dubbeldam, *Entropic separation of styrene/ethylbenzene mixtures by exploitation of subtle differences in molecular configurations in ordered crystalline nanoporous adsorbents*, *Langmuir* **31**, 3771 (2015).
- [202] S. Chempath, R. Q. Snurr, and J. J. Low, *Molecular modeling of binary liquid-phase adsorption of aromatics in silicalite*, *AIChE J.* **50**, 463 (2004).
- [203] Y. Zeng, P. Z. Moghadam, and R. Q. Snurr, *Pore size dependence of adsorption and separation of thiophene/benzene mixtures in zeolites*, *J. Phys. Chem. C* **119**, 15263 (2015).
- [204] S. Caro-Ortiz, E. Zuidema, D. Dekker, M. Rigutto, D. Dubbeldam, and T. J. H. Vlugt, *Adsorption of aromatics in MFI-type zeolites: Experiments and framework flexibility in Monte Carlo simulations*, *J. Phys. Chem. C* **124**, 21782 (2020).
- [205] V. Lachet, A. Boutin, B. Tavitian, and A. H. Fuchs, *Grand-canonical Monte Carlo simulations of adsorption of mixtures of xylene molecules in faujasite zeolites*, *Faraday Discuss.* **106**, 307 (1997).
- [206] H. Zheng, L. Zhao, J. Ji, J. Gao, C. Xu, and F. Luck, *Unraveling the adsorption mechanism of mono- and diaromatics in faujasite zeolite*, *ACS Appl. Mater. Inter.* **7**, 10190 (2015).
- [207] S. M. P. Lucena, R. Q. Snurr, and C. L. Cavalcante, *Monte Carlo and energy minimization studies of binary xylene adsorption in AEL and AFI networks*, *Adsorption* **13**, 477–484 (2007).
- [208] F. Zhao, X. Sun, R. Lu, and L. Kang, *Adsorption of methanol, methanal, toluene, ethylbenzene, and styrene in zeolites: A grand-canonical Monte Carlo simulation study*, *Can. J. Chem.* **95**, 1241 (2017).
- [209] P. He, H. Liu, Y. Li, J. Zhu, S. Huang, Z. Lei, P. Wang, and H. Tian, *Adsorption of benzene and propene in zeolite MCM-22: A grand-canonical Monte Carlo study*, *Adsorption* **18**, 31 (2012).

- [210] V. Lachet, A. Boutin, B. Tavitian, and A. H. Fuchs, *Molecular simulation of p-xylene and m-xylene adsorption in Y zeolites. single components and binary mixtures study*, *Langmuir* **15**, 8678 (1999).
- [211] J. J. Gutiérrez-Sevillano and S. Calero, *Computational approaches to zeolite-based adsorption processes*, in *Structure and Bonding* (Springer Berlin Heidelberg, Berlin, Heidelberg, 2020) pp. 1–27.
- [212] S. Sircar and D. V. Cao, *Heat of adsorption*, *Chem. Eng. Technol.* **25**, 945 (2002).
- [213] S. Sircar, R. Mohr, C. Ristic, and M. B. Rao, *Isosteric heat of adsorption: Theory and experiment*, *J. Phys. Chem. B* **103**, 6539 (1999).
- [214] D. Newsome and M.-O. Coppens, *Molecular dynamics as a tool to study heterogeneity in zeolites - Effect of Na<sup>+</sup> cations on diffusion of CO<sub>2</sub> and N<sub>2</sub> in Na-ZSM-5*, *Chem. Eng. Sci.* **121**, 300 (2015).
- [215] S. M. Auerbach and H. I. Metiu, *Diffusion in zeolites via cage-to-cage kinetics: Modeling benzene diffusion in Na-Y*, *J. Chem. Phys.* **105**, 3753 (1996).
- [216] T. J. H. Vlugt and M. Schenk, *Influence of framework flexibility on the adsorption properties of hydrocarbons in the zeolite silicalite*, *J. Phys. Chem. B* **106**, 12757 (2002).
- [217] L. A. Clark and R. Q. Snurr, *Adsorption isotherm sensitivity to small changes in zeolite structure*, *Chem. Phys. Lett.* **308**, 155 (1999).
- [218] J. M. Castillo, D. Dubbeldam, T. J. H. Vlugt, B. Smit, and S. Calero, *Evaluation of various water models for simulation of adsorption in hydrophobic zeolites*, *Mol. Simulat.* **35**, 1067 (2009).
- [219] E. García-Pérez, J. B. Parra, C. O. Ania, D. Dubbeldam, T. J. H. Vlugt, J. M. Castillo, P. J. Merkling, and S. Calero, *Unraveling the argon adsorption processes in MFI-type zeolite*, *J. Phys. Chem. C* **112**, 9976 (2008).
- [220] V. Sánchez-Gil, E. G. Noya, J. M. Guil, E. Lomba, and S. Valencia, *Adsorption of argon on pure silica MEL. Volumetric experiments and grand-canonical Monte Carlo simulations*, *Microporous Mesoporous Mat.* **222**, 218 (2016).
- [221] A. García-Sánchez, D. Dubbeldam, and S. Calero, *Modeling adsorption and self-diffusion of methane in LTA zeolites: The influence of framework flexibility*, *J. Phys. Chem. C* **114**, 15068 (2010).
- [222] H. Fang, J. Findley, G. Muraro, P. I. Ravikovitch, and D. S. Sholl, *A strong test of atomically detailed models of molecular adsorption in zeolites using multilaboratory experimental data for CO<sub>2</sub> adsorption in ammonium ZSM-5*, *J. Phys. Chem. Letters* **11**, 471 (2020).
- [223] M. Schenk, B. Smit, T. L. M. Maesen, and T. J. H. Vlugt, *Molecular simulations of the adsorption of cycloalkanes in MFI-type silica*, *Phys. Chem. Chem. Phys.* **7**, 2622 (2005).
- [224] T. R. Forester and W. Smith, *Bluemoon simulations of benzene in silicalite-1 prediction of free energies and diffusion coefficients*, *J. Chem. Soc. Faraday Trans.* **93**, 3249 (1997).
- [225] P. D. Kolokathis, G. Káli, H. Jobic, and D. N. Theodorou, *Diffusion of aromatics in silicalite-1: Experimental and theoretical evidence of entropic barriers*, *J. Phys. Chem. C* **120**, 21410 (2016).

- [226] R. Nagumo, H. Takaba, and S. Nakao, *Accelerated computation of extremely ‘slow’ molecular diffusivity in nanopores*, *Chem. Phys. Lett.* **458**, 281 (2008).
- [227] E. Beerdsen, B. Smit, and D. Dubbeldam, *Molecular simulation of loading dependent slow diffusion in confined systems*, *Phys. Rev. Lett.* **93**, 248301 (2004).
- [228] A. Poursaeidesfahani, M. F. de Lange, F. Khodadadian, D. Dubbeldam, M. Rigutto, N. Nair, and T. J. H. Vlugt, *Product shape selectivity of MFI-type, MEL-type, and BEA-type zeolites in the catalytic hydroconversion of heptane*, *J. Catal.* **353**, 54 (2017).
- [229] J. S. Camp and D. S. Sholl, *Transition state theory methods to measure diffusion in flexible nanoporous materials: Application to a porous organic cage crystal*, *J. Phys. Chem. C* **120**, 1110 (2016).
- [230] D. Dubbeldam, E. Beerdsen, T. J. H. Vlugt, and B. Smit, *Molecular simulation of loading-dependent diffusion in nanoporous materials using extended dynamically corrected transition state theory*, *J. Chem. Phys.* **122**, 224712 (2005).
- [231] B. Smit and T. L. M. Maesen, *Towards a molecular understanding of shape selectivity*, *Nature* **451**, 671–678 (2008).
- [232] R. Q. Snurr, A. T. Bell, and D. N. Theodorou, *Investigation of the dynamics of benzene in silicalite using transition-state theory*, *J. Phys. Chem.* **98**, 11948 (1994).
- [233] P. D. Kolokathis, E. Pantatosaki, C.-A. Gatsiou, H. Jobic, G. K. Papadopoulos, and D. N. Theodorou, *Dimensionality reduction of free energy profiles of benzene in silicalite-1: Calculation of diffusion coefficients using transition state theory*, *Mol. Simulat.* **40**, 80 (2014).
- [234] P. D. Kolokathis and O. M. Braun, *Kobra: A rate constant method for prediction of the diffusion of sorbates inside nanoporous materials at different loadings*, *J. Comput. Chem.* **40**, 2053 (2019).
- [235] R. V. Jasra and S. G. T. Bhat, *Adsorptive bulk separations by zeolite molecular sieves*, *Sep. Sci. Technol.* **23**, 945 (1988).
- [236] C. Perego and P. Ingallina, *Recent advances in the industrial alkylation of aromatics: new catalysts and new processes*, *Catal. Today* **73**, 3 (2002).
- [237] M. Rasouli, N. Yaghobi, S. Chitsazan, and M. H. Sayyar, *Effect of nanocrystalline zeolite Na-Y on meta-xylene separation*, *Microporous Mesoporous Mat.* **152**, 141 (2012).
- [238] A. Torres-Knoop, A. Poursaeidesfahani, T. J. H. Vlugt, and D. Dubbeldam, *Behavior of the enthalpy of adsorption in nanoporous materials close to saturation conditions*, *J. Chem. Theory Comput.* **13**, 3326 (2017).
- [239] S. Chempath, J. F. M. Denayer, K. M. A. De Meyer, G. V. Baron, and R. Q. Snurr, *Adsorption of liquid-phase alkane mixtures in silicalite: Simulations and experiment*, *Langmuir* **20**, 150 (2004).
- [240] A. Poursaeidesfahani, A. Torres-Knoop, D. Dubbeldam, and T. J. H. Vlugt, *Direct free energy calculation in the Continuous Fractional Component Gibbs ensemble*, *J. Chem. Theory Comput.* **12**, 1481 (2016).
- [241] W. Shi and E. J. Maginn, *Continuous Fractional Component Monte Carlo: An adaptive biasing method for open system atomistic simulations*, *J. Chem. Theory Comput.* **3**, 1451 (2007).

- [242] A. Rahbari, R. Hens, M. Ramdin, O. A. Moulton, D. Dubbeldam, and T. J. H. Vlugt, *Recent advances in the continuous fractional component Monte Carlo methodology*, *Mol. Simulat.* (2020), [10.1080/08927022.2020.1828585](https://doi.org/10.1080/08927022.2020.1828585).
- [243] A. Torres-Knoop, S. P. Balaji, T. J. H. Vlugt, and D. Dubbeldam, *A comparison of advanced Monte Carlo methods for open systems: CFCMC vs CBMC*, *J. Chem. Theory Comput.* **10**, 942 (2014).
- [244] J. I. Siepmann and D. Frenkel, *Configurational bias Monte Carlo: a new sampling scheme for flexible chains*, *Mol. Phys.* **75**, 59 (1992).
- [245] N. Rai and J. I. Siepmann, *Transferable potentials for phase equilibria. 9. Explicit hydrogen description of benzene and five-membered and six-membered heterocyclic aromatic compounds*, *J. Phys. Chem. B* **111**, 10790 (2007).
- [246] N. Rai and J. I. Siepmann, *Transferable potentials for phase equilibria. 10. Explicit-hydrogen description of substituted benzenes and polycyclic aromatic compounds*, *J. Phys. Chem. B* **117**, 273 (2013).
- [247] P. Bonnaud, C. Nieto-Draghi, and P. Ungerer, *Anisotropic united atom model including the electrostatic interactions of benzene*, *J. Phys. Chem. B* **111**, 3730 (2007).
- [248] C. Nieto-Draghi, P. Bonnaud, and P. Ungerer, *Anisotropic united atom model including the electrostatic interactions of methylbenzenes. I. Thermodynamic and structural properties*, *J. Phys. Chem. C* **111**, 15686 (2007).
- [249] I. Cacelli, G. Cinacchi, G. Prampolini, and A. Tani, *Computer simulation of solid and liquid benzene with an atomistic interaction potential derived from ab initio calculations*, *J. Am. Chem. Soc.* **126**, 14278 (2004).
- [250] P. E. M. Lopes, G. Lamoureux, B. Roux, and A. D. MacKerell, *Polarizable empirical force field for aromatic compounds based on the classical Drude oscillator*, *J. Phys. Chem. B* **111**, 2873 (2007).
- [251] H. Sun, *COMPASS: An ab initio force-field optimized for condensed-phase applications - Overview with details on alkane and benzene compounds*, *J. Phys. Chem. B* **102**, 7338 (1998).
- [252] C. D. Wick, M. G. Martin, and J. I. Siepmann, *Transferable potentials for phase equilibria. 4. United-atom description of linear and branched alkenes and alkylbenzenes*, *J. Phys. Chem. B* **104**, 8008 (2000).
- [253] W. L. Jorgensen, E. R. Laird, T. B. Nguyen, and J. Tirado-Rives, *Monte Carlo simulations of pure liquid substituted benzenes with OPLS potential functions*, *J. Comput. Chem.* **14**, 206 (1993).
- [254] A. K. Rappe, C. J. Casewit, K. S. Colwell, W. A. Goddard, and W. M. Skiff, *UFF, a full periodic table force field for molecular mechanics and molecular dynamics simulations*, *J. Am. Chem. Soc.* **114**, 10024 (1992).
- [255] K. Chenoweth, A. C. T. van Duin, and W. A. Goddard, *ReaxFF Reactive force field for molecular dynamics simulations of hydrocarbon oxidation*, *J. Phys. Chem. A* **112**, 1040 (2008).
- [256] K. A. O. Santos, A. A. Dantas Neto, M. C. P. A. Moura, and T. N. Castro Dantas, *Separation of xylene isomers through adsorption on mesoporous materials: A review*, *Braz. J. Petroleum Gas* **5**, 255 (2011).

- [257] S. Caro-Ortiz, R. Hens, E. Zuidema, M. Rigitto, D. Dubbeldam, and T. J. H. Vlugt, *Molecular simulation of the vapor-liquid equilibria of xylene mixtures: Force field performance, and Wolf vs. Ewald for electrostatic interactions*, *Fluid Phase Equilib.* **485**, 239 (2019).
- [258] S. Caro-Ortiz, R. Hens, E. Zuidema, M. Rigitto, D. Dubbeldam, and T. J. H. Vlugt, *Corrigendum to “Molecular simulation of the vapor-liquid equilibria of xylene mixtures: Force field performance, and Wolf vs. Ewald for electrostatic Interactions” [Fluid Phase Equilib.] 485 (2019) 239–247*, *Fluid Phase Equilib.* **506**, 112370 (2020).
- [259] B. D. Smith and R. Srivastava, *Thermodynamic data for pure compound: Part A, hydrocarbons and ketones* (Elsevier, Amsterdam, 1986).
- [260] W. L. Rodrigues, S. Mattedi, and J. C. N. Abreu, *Experimental vapor-liquid equilibria data for binary mixtures of xylene isomers*, *Braz. J. Chem. Eng.* **22**, 453 (2005).
- [261] M. Kato, T. Sato, and M. Hirata, *Vapor-liquid equilibrium relationship of para-xylene meta-xylene system at atmospheric pressure*, *J. Chem. Eng. Jpn.* **4**, 305 (1971).
- [262] U. Onken and W. Arlt, *Recommended test mixtures for distillation columns*, 2nd ed. (IChemE, Warwickshire, 1990).
- [263] F. J. Llopis and J. B. Monton, *Isobaric vapor-liquid equilibria of p-xylene + o-xylene and m-xylene + o-xylene systems at 6.66 and 26.66 kPa*, *J. Chem. Eng. Data* **39**, 53 (1994).
- [264] F. J. Llopis and J. B. Monton, *Isobaric vapor-liquid equilibria for binary and ternary systems composed of 1,4-dimethylbenzene, 1,3-dimethylbenzene, and 1,2-dimethylbenzene at 6.66 and 26.66 kPa*, *J. Chem. Eng. Data* **39**, 643 (1994).
- [265] M. Parvez, G. Singh, S. Tyagi, S. Kumar, and S. Khan, *Experimental determination of vapour-liquid equilibrium data for the binary mixtures p-xylene and o-xylene at 81.3 kPa*, *Int. J. Sci. Tech. Adv.* **1**, 263 (2015).
- [266] I. Wichterle, J. Linek, Z. Wagner, J.-C. Fontaine, K. Sosnkowska-Kehiaian, and H. Kehiaian, *Vapor-liquid equilibrium of the mixture  $C_8H_{10} + C_8H_{10}$  (LB3761, EVLM 1211)*, in *Binary liquid systems of nonelectrolytes. Part 2*, edited by H. Kehiaian (Springer Berlin Heidelberg, Berlin, Heidelberg, 2008) pp. 1221–1222.
- [267] A. Z. Panagiotopoulos and M. R. Stapleton, *The Gibbs method for molecular-based computer simulations of phase equilibria*, *Fluid Phase Equilib.* **53**, 133 (1989).
- [268] M. Ramdin, S. H. Jamali, T. M. Becker, and T. J. H. Vlugt, *Gibbs ensemble Monte Carlo simulations of multicomponent natural gas mixtures*, *Mol. Simulat.* **44**, 377 (2018).
- [269] A. Z. Panagiotopoulos, N. Quirke, M. Stapleton, and D. J. Tildesley, *Phase equilibria by simulation in the Gibbs ensemble*, *Mol. Phys.* **63**, 527 (1988).
- [270] A. D. Cortés Morales, I. G. Economou, C. J. Peters, and J. I. Siepmann, *Influence of simulation protocols on the efficiency of Gibbs ensemble Monte Carlo simulations*, *Mol. Simulat.* **39**, 1135 (2013).

- [271] M. Ramdin, T. M. Becker, S. H. Jamali, M. Wang, and T. J. H. Vlugt, *Computing equation of state parameters of gases from Monte Carlo simulations*, *Fluid Phase Equilib.* **428**, 174 (2016).
- [272] P. Ungerer, C. Nieto-Draghi, B. Rousseau, G. Ahunbay, and V. Lachet, *Molecular simulation of the thermophysical properties of fluids: From understanding toward quantitative predictions*, *J. Mol. Liq.* **134**, 71 (2007).
- [273] A. Torres-Knoop, N. C. Burtch, A. Poursaeidesfahani, S. P. Balaji, R. Kools, F. X. Smit, K. S. Walton, T. J. H. Vlugt, and D. Dubbeldam, *Optimization of particle transfers in the Gibbs Ensemble for systems with strong and directional interactions using CBMC, CFCMC, and CB/CFCMC*, *J. Phys. Chem. C* **120**, 9148 (2016).
- [274] P. P. Ewald, *Die Berechnung optischer und elektrostatischer Gitterpotentiale*, *Ann. Phys.* **369**, 253 (1921).
- [275] B. A. Wells and A. L. Chaffee, *Ewald summation for molecular simulations*, *J. Chem. Theory Comput.* **11**, 3684 (2015).
- [276] J. W. Eastwood, R. W. Hockney, and D. N. Lawrence, *P3M3DP — The three-dimensional periodic particle-particle/particle-mesh program*, *Comput. Phys. Commun.* **19**, 215 (1980).
- [277] L. Onsager, *Electric moments of molecules in liquids*, *J. Am. Chem. Soc.* **58**, 1486 (1936).
- [278] L. Greengard and V. Rokhlin, *A fast algorithm for particle simulations*, *J. Comput. Phys.* **73**, 325 (1987).
- [279] D. Wolf, P. Kebblinski, S. R. Phillpot, and J. Eggebrecht, *Exact method for the simulation of Coulombic systems by spherically truncated, pairwise  $r^{-1}$  summation*, *J. Chem. Phys.* **110**, 8254 (1999).
- [280] A. Cisneros, M. Karttunen, P. Ren, and C. Sagui, *Classical electrostatics for biomolecular simulations*, *Chem. Rev.* **114**, 779 (2014).
- [281] G. S. Fanourgakis, *An extension of Wolf's method for the treatment of electrostatic interactions: Application to liquid water and aqueous solutions*, *J. Phys. Chem. B* **119**, 1974 (2015).
- [282] P. Demontis, S. Spanu, and G. B. Suffritti, *Application of the Wolf method for the evaluation of Coulombic interactions to complex condensed matter systems: Aluminosilicates and water*, *J. Chem. Phys.* **114**, 7980 (2001).
- [283] C. Avendaño and A. Gil-Villegas, *Monte Carlo simulations of primitive models for ionic systems using the Wolf method*, *Mol. Phys.* **104**, 1475 (2006).
- [284] P. X. Viveros-Méndez and A. Gil-Villegas, *Computer simulation of sedimentation of ionic systems using the Wolf method*, *J. Chem. Phys.* **136**, 154507 (2012).
- [285] D. Zahn, B. Schilling, and S. M. Kast, *Enhancement of the Wolf Damped Coulomb potential: Static, dynamic, and dielectric properties of liquid water from molecular simulation*, *J. Phys. Chem. B* **106**, 10725 (2002).
- [286] C. J. Fennell and J. D. Gezelter, *Is the Ewald summation still necessary? Pairwise alternatives to the accepted standard for long-range electrostatics*, *J. Chem. Phys.* **124**, 234104 (2006).

- [287] J. Kolafa, F. Močka, and I. Nezbeda, *Handling electrostatic interactions in molecular simulations: A systematic study*, *Collect. Czech. Chem. Commun.* **73**, 481 (2008).
- [288] A. Rahbari, R. Hens, S. H. Jamali, M. Ramdin, D. Dubbeldam, and T. J. H. Vlugt, *Effect of truncating electrostatic interactions on predicting thermodynamic properties of water-methanol systems*, *Mol. Simulat.*, 336 (2019).
- [289] R. Hens, *Molecular Simulation of Phase and Reaction Equilibria*, Ph.D. thesis, Delft University of Technology (2020).
- [290] R. Hens and T. J. H. Vlugt, *Molecular simulation of vapor-liquid equilibria using the Wolf method for electrostatic interactions*, *J. Chem. Eng. Data* **63**, 1096 (2018).
- [291] C. Waibel and J. Gross, *Modification of the Wolf Method and evaluation for molecular simulation of vapor liquid equilibria*, *J. Chem. Theory Comput.* **14**, 2198 (2018).
- [292] M. P. Allen and D. Tildesley, *Computer simulation of liquids*, 2nd ed. (Oxford University Press, Oxford, 2017).
- [293] A. Poursaeidesfahani, A. Rahbari, A. Torres-Knoop, D. Dubbeldam, and T. J. H. Vlugt, *Computation of thermodynamic properties in the continuous fractional component Monte Carlo Gibbs ensemble*, *Mol. Simulat.* **43**, 189 (2017).
- [294] A. Rahbari, R. Hens, I. K. Nikolaidis, A. Poursaeidesfahani, M. Ramdin, I. G. Economou, O. A. Mourtos, D. Dubbeldam, and T. J. H. Vlugt, *Computation of partial molar properties using continuous fractional component Monte Carlo*, *Mol. Phys.* **116**, 3331 (2018).
- [295] R. Hens, A. Rahbari, S. Caro-Ortiz, N. Dawass, M. Erdős, A. Poursaeidesfahani, H. S. Salehi, A. T. Celebi, M. Ramdin, O. A. Mourtos, D. Dubbeldam, and T. J. H. Vlugt, *Brick-CFCMC: Open source software for Monte Carlo simulations of phase and reaction equilibria using the Continuous Fractional Component Method*, *J. Chem. Inf. Model.* **60**, 2678–2682 (2020).
- [296] F. Wang and D. P. Landau, *Efficient, multiple-range random walk algorithm to calculate the density of states*, *Phys. Rev. Lett.* **86**, 2050 (2001).
- [297] W. L. Jorgensen, D. S. Maxwell, and J. Tirado-Rives, *Development and testing of the OPLS all-atom force field on conformational energetics and properties of organic liquids*, *J. Am. Chem. Soc.* **118**, 11225 (1996).
- [298] J. M. Castillo, T. J. H. Vlugt, and S. Calero, *Molecular simulation study on the separation of xylene isomers in MIL-47 metal-organic frameworks*, *J. Phys. Chem. C* **113**, 20869 (2009).
- [299] C. Nieto-Draghi, P. Bonnaud, and P. Ungerer, *Anisotropic united atom model including the electrostatic interactions of methylbenzenes. II. Transport properties*, *J. Phys. Chem. C* **111**, 15942 (2007).
- [300] A. Rahbari, R. Hens, D. Dubbeldam, and T. J. H. Vlugt, *Improving the accuracy of computing chemical potentials in CFCMC simulations*, *Mol. Phys.* **117**, 3493 (2019).

- [301] H. Kanai, V. Inouye, L. Yazawa, R. Goo, and H. Wakatsuki, *Importance of Debye and Keesom interactions in separating m-xylene and p-xylene in GC-MS analysis utilizing PEG stationary phase*, *J. Chromatogr. Sci.* **43**, 57 (2005).
- [302] M. Dinpajoooh, P. Bai, D. A. Allan, and J. I. Siepmann, *Accurate and precise determination of critical properties from Gibbs ensemble Monte Carlo simulations*, *J. Chem. Phys.* **143**, 114113 (2015).
- [303] R. D. Chirico, S. E. Knipmeyer, A. Nguyen, J. W. Reynolds, and W. V. Steele, *Thermodynamic equilibria in xylene isomerization. 2. The thermodynamic properties of m-xylene*, *J. Chem. Eng. Data* **42**, 475 (1997).
- [304] R. D. Chirico, S. E. Knipmeyer, A. Nguyen, A. B. Cowell, J. W. Reynolds, and W. V. Steele, *Thermodynamic equilibria in xylene isomerization. 3. The thermodynamic properties of o-xylene*, *J. Chem. Eng. Data* **42**, 758 (1997).
- [305] R. D. Chirico, S. E. Knipmeyer, A. Nguyen, and W. V. Steele, *Thermodynamic equilibria in xylene isomerization. 1. The thermodynamic properties of p-xylene*, *J. Chem. Eng. Data* **42**, 248 (1997).
- [306] S. Hempel, J. Fischer, D. Paschek, and G. Sadowski, *Activity coefficients of complex molecules by molecular simulation and Gibbs-Duhem integration*, *Soft Mater.* **10**, 26 (2012).
- [307] S. P. Balaji, S. K. Schnell, E. S. McGarry, and T. J. H. Vlugt, *A direct method for calculating thermodynamic factors for liquid mixtures using the Permuted Widom test particle insertion method*, *Mol. Phys.* **111**, 287 (2013).
- [308] W. A. Sweeney and P. F. Bryan, *BTX processing*, in *Kirk-Othmer Encyclopedia of Chemical Technology* (Wiley-Interscience, New York, NY, 2000).
- [309] G. Bellussi, *Zeolite catalysts for the production of chemical commodities: BTX derivatives*, in *Recent advances in the science and technology of zeolites and related materials*, Studies in surface science and catalysis, Vol. 154, edited by E. van Steen, I. Claeys, and L. Callanan (Elsevier Science, Amsterdam, 2004) pp. 53 – 65.
- [310] S. A. Ali, A. M. Aitani, J. Čejka, and S. S. Al-Khattaf, *Selective production of xylenes from alkyl-aromatics and heavy reformates over dual-zeolite catalyst*, *Catal. Today* **243**, 118 (2015).
- [311] K. Gołębek, K. A. Tarach, and K. Góra-Marek, *Xylenes transformation over zeolites ZSM-5 ruled by acidic properties*, *Spectrochim. Acta A* **192**, 361 (2018).
- [312] M. Jeffroy, C. Nieto-Draghi, and A. Boutin, *Molecular simulation of zeolite flexibility*, *Mol. Simulat.* **40**, 6 (2014).
- [313] A. Sartbaeva, S. A. Wells, M. M. J. Treacy, and M. F. Thorpe, *The flexibility window in zeolites*, *Nature Mater.* **5**, 962 (2006).
- [314] A. Poursaeidesfahani, A. Torres-Knoop, M. Rigutto, N. Nair, D. Dubbeldam, and T. J. H. Vlugt, *Computation of the heat and entropy of adsorption in proximity of inflection points*, *J. Phys. Chem. C* **120**, 1727 (2016).
- [315] B. Smit and T. L. M. Maesen, *Commensurate ‘freezing’ of alkanes in the channels of a zeolite*, *Nature* **374**, 42 (1995).
- [316] O. Talu, C. J. Guo, and D. T. Hayhurst, *Heterogeneous adsorption equilibria with comparable molecule and pore sizes*, *J. Phys. Chem.* **93**, 7294 (1989).

- [317] N. Floquet, J. P. Coulomb, G. Weber, O. Bertrand, and J. P. Bellat, *Structural signatures of type IV isotherm steps: Sorption of trichloroethene, tetrachloroethene, and benzene in silicalite-I*, *J. Phys. Chem. B* **107**, 685 (2003).
- [318] C. A. Fyfe, H. Strobl, G. T. Kokotailo, G. J. Kennedy, and G. E. Barlow, *Ultrahigh-resolution silicon-29 solid-state MAS NMR investigation of sorbate and temperature-induced changes in the lattice structure of zeolite ZSM-5*, *J. Am. Chem. Soc.* **110**, 3373 (1988).
- [319] E. de Vos Burchart, H. van Bekkum, and B. van de Graaf, *Molecular mechanics studies on MFI-type zeolites: Part 3. The monoclinic-orthorhombic phase transition*, *Zeolites* **13**, 212 (1993).
- [320] B. Ilić and S. G. Wettstein, *A review of adsorbate and temperature-induced zeolite framework flexibility*, *Microporous Mesoporous Mat.* **239**, 221 (2017).
- [321] M. Pera-Titus, *Thermodynamic analysis of type VI adsorption isotherms in MFI zeolites*, *J. Phys. Chem. C* **115**, 3346 (2011).
- [322] C.-K. Lee and A. S. T. Chiang, *Adsorption of aromatic compounds in large MFI zeolite crystals*, *J. Chem. Soc. Faraday Trans.* **92**, 3445 (1996).
- [323] L. Song and L. V. C. Rees, *Adsorption and diffusion of cyclic hydrocarbon in mfi-type zeolites studied by gravimetric and frequency-response techniques*, *Microporous Mesoporous Mat.* **35-36**, 301 (2000).
- [324] H. van Koningsveld, F. Tuinstra, H. van Bekkum, and J. C. Jansen, *The location of p-xylene in a single crystal of zeolite H-ZSM-5 with a new, sorbate-induced, orthorhombic framework symmetry*, *Acta Crystallogr. B* **45**, 423 (1989).
- [325] M. Sacerdote, F. Bosselet, and B. Mentzen, *The MFI(ZSM-5)/sorbate systems. Comparison between structural, theoretical and calorimetric results. Part II - The MFI/benzene system*, *Mater. Res. Bull.* **25**, 593 (1990).
- [326] S. G. Sorenson, J. R. Smyth, M. Kocirik, A. Zikanova, R. D. Noble, and J. L. Falconer, *Adsorbate-induced expansion of silicalite-1 crystals*, *Ind. Eng. Chem. Res.* **47**, 9611 (2008).
- [327] S. Nair and M. Tsapatsis, *The location of o- and m-xylene in silicalite by powder X-ray diffraction*, *J. Phys. Chem. B* **104**, 8982 (2000).
- [328] C. A. Fyfe and J. S. J. Lee, *Solid-state NMR determination of the zeolite ZSM-5/ortho-xylene host-guest crystal structure*, *J. Phys. Chem. C* **112**, 500 (2008).
- [329] B. Mentzen and F. Lefebvre, *Flexibility of the MFI silicalite framework upon benzene adsorption at higher pore-fillings: A study by X-ray power diffraction, NMR and molecular mechanics*, *Mater. Res. Bull.* **32**, 813 (1997).
- [330] R. Schumacher and H. G. Karge, *Sorption and sorption kinetics of ethylbenzene in MFI-Type zeolites studied by a barometric technique*, *Collect. Czech. Chem. Commun.* **64**, 483 (1999).
- [331] P. Wu, A. Debebe, and Y. H. Ma, *Adsorption and diffusion of C<sub>6</sub> and C<sub>8</sub> hydrocarbons in silicalite*, *Zeolites* **3**, 118 (1983).
- [332] R. Cartarius, H. Vogel, and J. Dembowski, *Investigation of sorption and intracrystalline diffusion of benzene and toluene on silicalite-1*, *Ber. Bunsenges. Phys. Chem.* **101**, 193 (1997).

- [333] S. G. Hill and D. Seddon, *Comparison of the sorption of benzene in ZSM-5, silicalite-1, and silicalite-2*, *Zeolites* **11**, 699 (1991).
- [334] D. Malović and D. Vučelić, *Application of thermal analysis for explaining the sorption of benzene and n-hexane on silicalite*, *J. Therm. Anal. Calorim.* **53**, 835 (1998).
- [335] L. Song, Z. Sun, L. Duan, J. Gui, and G. S. McDougall, *Adsorption and diffusion properties of hydrocarbons in zeolites*, *Microporous Mesoporous Mat.* **104**, 115 (2007).
- [336] R. E. Richards and L. V. C. Rees, *The sorption of p-xylene in ZSM-5*, *Zeolites* **8**, 35 (1988).
- [337] H. Ban, J. Gui, L. Duan, X. Zhang, L. Song, and Z. Sun, *Sorption of hydrocarbons in silicalite-1 studied by intelligent gravimetry*, *Fluid Phase Equilib.* **232**, 149 (2005).
- [338] H. Thamm, *Calorimetric study on the state of aromatic molecules sorbed on silicalite*, *J. Phys. Chem.* **91**, 8 (1987).
- [339] W. Rudziński, J. Narkiewicz-Michałek, P. Szabelski, and A. S. T. Chiang, *Adsorption of aromatics in zeolites ZSM-5: A thermodynamic-calorimetric study based on the model of adsorption on heterogeneous adsorption sites*, *Langmuir* **13**, 1095 (1997).
- [340] E. Rodeghero, T. Chenet, A. Martucci, M. Ardit, E. Sarti, and L. Pasti, *Selective adsorption of toluene and n-hexane binary mixture from aqueous solution on zeolite ZSM-5: Evaluation of competitive behavior between aliphatic and aromatic compounds*, *Catal. Today* **345**, 157 (2019).
- [341] J. Li and O. Talu, *Structural effect on molecular simulations of tight-pore systems*, *J. Chem. Soc. Faraday Trans.* **89**, 1683 (1993).
- [342] S. Mohanty, H. T. Davis, and A. V. McCormick, *Shape selective adsorption in atomistic nanopores - A study of xylene isomers in silicalite*, *Chem. Eng. Sci.* **55**, 2779 (2000).
- [343] X. Yue and X. Yang, *Molecular simulation study of adsorption and diffusion on silicalite for a benzene/CO<sub>2</sub> mixture*, *Langmuir* **22**, 3138 (2006).
- [344] Y. Zeng, S. Ju, W. Xing, and C. Chen, *Computer simulation of the adsorption of thiophene/benzene mixtures on MFI and MOR*, *Sep. Purif. Technol.* **55**, 82 (2007).
- [345] S. Ban, A. van Laak, P. E. de Jongh, J. P. J. M. van der Eerden, and T. J. H. Vlugt, *Adsorption selectivity of benzene/propene mixtures for various zeolites*, *J. Phys. Chem. C* **111**, 17241 (2007).
- [346] P. Cosoli, M. Fermeglia, and M. Ferrone, *GCMC simulations in zeolite MFI and activated carbon for benzene removal from exhaust gaseous streams*, *Mol. Simulat.* **34**, 1321 (2008).
- [347] M. Jeffroy, A. H. Fuchs, and A. Boutin, *Structural changes in nanoporous solids due to fluid adsorption: Thermodynamic analysis and Monte Carlo simulations*, *Chem. Commun.*, 3275 (2008).
- [348] R. Krishna and J. M. van Baten, *Influence of adsorption thermodynamics on guest diffusivities in nanoporous crystalline materials*, *Phys. Chem. Chem. Phys.* **15**, 7994 (2013).

- [349] P. Boulet, L. Narasimhan, D. Berg'e-Lefranc, B. Kuchta, O. Schäf, and R. Denoyel, *Adsorption into the MFI zeolite of aromatic molecule of biological relevance. investigations by monte carlo simulations*, *J. Mol. Model.* **15**, 573 (2009).
- [350] D. H. Olson, G. T. Kokotailo, S. L. Lawton, and W. M. Meier, *Crystal structure and structure-related properties of ZSM-5*, *J. Phys. Chem.* **85**, 2238 (1981).
- [351] H. van Koningsveld, H. van Bekkum, and J. C. Jansen, *On the location and disorder of the tetrapropylammonium (TPA) ion in zeolite ZSM-5 with improved framework accuracy*, *Acta Crystallogr. B* **43**, 127 (1987).
- [352] D. Dubbeldam, K. S. Walton, T. J. H. Vlugt, and S. Calero, *Design, parameterization, and implementation of atomic force fields for adsorption in nanoporous materials*, *Adv. Theory Simul.* **2**, 1900135 (2019).
- [353] J. Park, M. Agrawal, D. F. Sava Gallis, J. A. Harvey, J. A. Greathouse, and D. S. Sholl, *Impact of intrinsic framework flexibility for selective adsorption of sarin in non-aqueous solvents using metal–organic frameworks*, *Phys. Chem. Chem. Phys.* **22**, 6441 (2020).
- [354] K. B. Sezginel, S. Lee, H. Babaei, and C. E. Wilmer, *Effect of flexibility on thermal transport in breathing porous crystals*, *J. Phys. Chem. C* **124**, 18604 (2020).
- [355] G. Kupgan, A. G. Demidov, and C. M. Colina, *Plasticization behavior in polymers of intrinsic microporosity (PIM-1): A simulation study from combined Monte Carlo and Molecular Dynamics*, *J. Membrane Sci.* **565**, 95 (2018).
- [356] S. M. J. Rogge, R. Goeminne, R. Demuynck, J. J. Gutiérrez-Sevillano, S. Vandenbrande, L. Vanduyfhuys, M. Waroquier, T. Verstraelen, and V. Van Speybroeck, *Modeling gas adsorption in flexible metal–organic frameworks via Hybrid Monte Carlo/Molecular Dynamics schemes*, *Adv. Theory Simul.* **2**, 1800177 (2019).
- [357] T. Chokbunpiam, S. Fritzsche, J. Caro, C. Chmelik, W. Janke, and S. Hannongbua, *Importance of ZIF-90 lattice flexibility on diffusion, permeation, and lattice structure for an adsorbed H<sub>2</sub>/CH<sub>4</sub> gas mixture: A re-examination by Gibbs ensemble Monte Carlo and Molecular Dynamics simulations*, *J. Phys. Chem. C* **121**, 10455 (2017).
- [358] J. Hajek, C. Caratelli, R. Demuynck, K. De Wispelaere, L. Vanduyfhuys, M. Waroquier, and V. Van Speybroeck, *On the intrinsic dynamic nature of the rigid UiO-66 metal–organic framework*, *Chem. Sci.* **9**, 2723 (2018).
- [359] S. Namsani, A. Ozcan, and A. Ö. Yazaydin, *Direct simulation of ternary mixture separation in a ZIF-8 membrane at molecular scale*, *Adv. Theory Simul.* **2**, 1900120 (2019).
- [360] M. Witman, S. Ling, S. Jawahery, P. G. Boyd, M. Haranczyk, B. Slater, and B. Smit, *The influence of intrinsic framework flexibility on adsorption in nanoporous materials*, *J. Am. Chem. Soc.* **139**, 5547 (2017).
- [361] M. Agrawal and D. S. Sholl, *Effects of intrinsic flexibility on adsorption properties of metal–organic frameworks at dilute and nondilute loadings*, *ACS Appl. Mater. Interfaces* **11**, 31060 (2019).

- [362] J. Heinen and D. Dubbeldam, *On flexible force fields for metal–organic frameworks: Recent developments and future prospects*, *WIREs Comput. Mol. Sci.* **8**, e1363 (2018).
- [363] H. van Koningsveld, J. Jansen, and H. van Bekkum, *The monoclinic framework structure of zeolite H-ZSM-5. Comparison with the orthorhombic framework of as-synthesized ZSM-5*, *Zeolites* **10**, 235 (1990).
- [364] A. Ślawek, J. M. Vicent-Luna, B. Marszałek, S. R. G. Balestra, W. Makowski, and S. Calero, *Adsorption of n-alkanes in MFI and MEL: Quasi-equilibrated thermodesorption combined with molecular simulations*, *J. Phys. Chem. C* **120**, 25338 (2016).
- [365] D. Dubbeldam, S. Calero, D. E. Ellis, and R. Q. Snurr, *RASPA: molecular simulation software for adsorption and diffusion in flexible nanoporous materials*, *Mol. Simulat.* **42**, 81 (2016).
- [366] D. Dubbeldam, A. Torres-Knoop, and K. S. Walton, *On the inner workings of Monte Carlo codes*, *Mol. Simulat.* **39**, 1253 (2013).
- [367] K. M. Jablonka, D. Ongari, and B. Smit, *Applicability of tail corrections in the molecular simulations of porous materials*, *J. Chem. Theory Comput.* **15**, 5635–5641 (2019).
- [368] R. Bueno-Pérez, S. Calero, D. Dubbeldam, C. O. Ania, J. B. Parra, A. P. Zaderenko, and P. J. Merkling, *Zelite force fields and experimental siliceous frameworks in a comparative infrared study*, *J. Phys. Chem. C* **116**, 25797 (2012).
- [369] J. Guo and K. D. Hammond, *Comparison of siliceous zeolite potentials from the perspective of infrared spectroscopy*, *J. Phys. Chem. C* **122**, 6093 (2018).
- [370] B. van Beest, G. Kramer, and R. van Santen, *Force fields for silicas and aluminophosphates based on ab initio calculations*, *Phys. Rev. Lett.* **64**, 1955 (1990).
- [371] G. J. Kramer, N. P. Farragher, B. W. H. van Beest, and R. A. van Santen, *Interatomic force fields for silicas, aluminophosphates, and zeolites: Derivation based on ab initio calculations*, *Phys. Rev. B* **43**, 5068 (1991).
- [372] J. R. Hill and J. Sauer, *Molecular mechanics potential for silica and zeolite catalysts based on ab initio calculations. 2. Aluminosilicates*, *J. Phys. Chem.* **99**, 9536 (1995).
- [373] P. Demontis, G. Suffritti, S. Quartieri, E. Fois, and A. Gamba, *Molecular dynamics studies on zeolites. II: A simple model for silicates applied to anhydrous natrolite*, *Zeolites* **7**, 522 (1987).
- [374] P. Demontis, G. B. Suffritti, S. Quartieri, E. S. Fois, and A. Gamba, *Molecular dynamics studies on zeolites. 3. Dehydrated zeolite A*, *J. Phys. Chem.* **92**, 867 (1988).
- [375] P. Demontis, G. Suffritti, E. Fois, A. Gamba, and G. Morosi, *A potential for molecular dynamics simulations of structural and dynamic properties of hydrate aluminosilicates*, *Mater. Chem. Phys.* **29**, 357 (1991).
- [376] J. B. Nicholas, A. J. Hopfinger, F. R. Trouw, and L. E. Iton, *Molecular modeling of zeolite structure. 2. Structure and dynamics of silica sodalite and silicate force field*, *J. Am. Chem. Soc.* **113**, 4792 (1991).

- [377] A. Gabrieli, M. Sant, P. Demontis, and G. B. Suffritti, *Development and optimization of a new force field for flexible aluminosilicates, enabling fast molecular dynamics simulations on parallel architectures*, *J. Phys. Chem. C* **117**, 503 (2013).
- [378] A. Ghysels, S. L. Moors, K. Hemelsoet, K. De Wispelaere, M. Waroquier, G. Sastre, and V. Van Speybroeck, *Shape-selective diffusion of olefins in 8-ring solid acid microporous zeolites*, *J. Phys. Chem. C* **119**, 23721 (2015).
- [379] P. Demontis and G. B. Suffritti, *Structure and dynamics of zeolites investigated by molecular dynamics*, *Chem. Rev.* **97**, 2845 (1997).
- [380] G. Sastre, J. Kärger, and D. M. Ruthven, *Molecular dynamics study of diffusion and surface permeation of benzene in silicalite*, *J. Phys. Chem. C* **122**, 7217 (2018).
- [381] B. G. Dick and A. W. Overhauser, *Theory of the dielectric constants of alkali halide crystals*, *Phys. Rev.* **112**, 90 (1958).
- [382] K.-P. Schröder and J. Sauer, *Potential functions for silica and zeolite catalysts based on ab initio calculations. 3. A shell model ion pair potential for silica and aluminosilicates*, *J. Phys. Chem.* **100**, 11043 (1996).
- [383] M. J. Sanders, M. Leslie, and C. R. A. Catlow, *Interatomic potentials for  $\text{SiO}_2$* , *J. Chem. Soc., Chem. Commun.*, 1271 (1984).
- [384] M. Sierka and J. Sauer, *Structure and reactivity of silica and zeolite catalysts by a combined quantum mechanics-shell-model potential approach based on DFT*, *Faraday Discuss.* **106**, 41 (1997).
- [385] N. J. Henson, A. K. Cheetham, and J. D. Gale, *Theoretical calculations on silica frameworks and their correlation with experiment*, *Chem. Mater.* **6**, 1647 (1994).
- [386] J. Baker, *An algorithm for the location of transition states*, *J. Comput. Chem.* **7**, 385 (1986).
- [387] A. Banerjee, N. Adams, J. Simons, and R. Shepard, *Search for stationary points on surfaces*, *J. Phys. Chem.* **89**, 52 (1985).
- [388] L. D. Gelb and K. E. Gubbins, *Pore size distributions in porous glasses: A computer simulation study*, *Langmuir* **15**, 305 (1999).
- [389] L. Sarkisov and A. Harrison, *Computational structure characterisation tools in application to ordered and disordered porous materials*, *Mol. Simulat.* **37**, 1248 (2011).
- [390] B. Widom, *Some topics in the theory of fluids*, *J. Chem. Phys.* **39**, 2808 (1963).
- [391] A. G. Bezus, A. V. Kiselev, A. A. Lopatkin, and P. Q. Du, *Molecular statistical calculation of the thermodynamic adsorption characteristics of zeolites using the atom-atom approximation. Part 1. Adsorption of methane by zeolite NaX*, *J. Chem. Soc. Faraday Trans. 2* **74**, 367 (1978).
- [392] P. Pascual, P. Ungerer, B. Tavitian, P. Pernot, and A. Boutin, *Development of a transferable guest-host force field for adsorption of hydrocarbons in zeolites I. Reinvestigation of alkane adsorption in silicalite by grand-canonical Monte Carlo simulation*, *Phys. Chem. Chem. Phys.* **5**, 3684 (2003).

- [393] P. Pascual, P. Ungerer, B. Tavitian, and A. Boutin, *Development of a transferable guest-host force field for adsorption of hydrocarbons in zeolites. II. Prediction of alkenes adsorption and alkane/alkene selectivity in silicalite*, *J. Phys. Chem. B* **108**, 393 (2004).
- [394] D. Dubbeldam, S. Calero, T. J. H. Vlugt, R. Krishna, T. L. M. Maesen, and B. Smit, *United atom force field for alkanes in nanoporous materials*, *J. Phys. Chem. B* **108**, 12301 (2004).
- [395] B. Liu, B. Smit, F. Rey, S. Valencia, and S. Calero, *A new united atom force field for adsorption of alkenes in zeolites*, *J. Phys. Chem. C* **112**, 2492 (2008).
- [396] P. Bai, M. Tsapatsis, and J. I. Siepmann, *TraPPE-zeo: Transferable potentials for phase equilibria force field for all-silica zeolites*, *J. Phys. Chem. C* **117**, 24375 (2013).
- [397] A. García-Sánchez, C. O. Ania, J. B. Parra, D. Dubbeldam, T. J. H. Vlugt, R. Krishna, and S. Calero, *Transferable force field for carbon dioxide adsorption in zeolites*, *J. Phys. Chem. C* **113**, 8814 (2009).
- [398] J. J. Wolffis, D. E. Vanpoucke, A. Sharma, K. V. Lawler, and P. M. Forster, *Predicting partial atomic charges in siliceous zeolites*, *Microporous Mesoporous Mat.* **277**, 184 (2019).
- [399] A. Abdelrasoul, H. Zhang, C.-H. Cheng, and H. Doan, *Applications of molecular simulations for separation and adsorption in zeolites*, *Microporous Mesoporous Mat.* **242**, 294 (2017).
- [400] N. Desbiens, A. Boutin, and I. Demachy, *Water condensation in hydrophobic silicalite-1 zeolite: A molecular simulation study*, *J. Phys. Chem. B* **109**, 24071 (2005).
- [401] K. M. Visscher and D. P. Geerke, *Deriving force-field parameters from first principles using a polarizable and higher order dispersion model*, *J. Chem. Theory Comput.* **15**, 1875 (2019).
- [402] R. Q. Snurr, A. T. Bell, and D. N. Theodorou, *A hierarchical atomistic/lattice simulation approach for the prediction of adsorption thermodynamics of benzene in silicalite*, *J. Phys. Chem.* **98**, 5111 (1994).
- [403] M. G. Martin and J. I. Siepmann, *Transferable potentials for phase equilibria. 1. United-atom description of n-alkanes*, *J. Phys. Chem. B* **102**, 2569 (1998).
- [404] M. S. Sun, O. Talu, and D. B. Shah, *Adsorption equilibria of C<sub>5</sub>-C<sub>10</sub> normal alkanes in silicalite crystals*, *J. Phys. Chem.* **100**, 17276 (1996).
- [405] V. Choudhary and K. Srinivasan, *Sorption and diffusion of benzene in H-ZSM-5: Effect of Si/Al ratio, degree of cation exchange and pretreatment conditions*, *J. Catal.* **102**, 328 (1986).
- [406] G.-Q. Guo, H. Chen, and Y.-C. Long, *Separation of p-xylene from C<sub>8</sub> aromatics on binder-free hydrophobic adsorbent of MFI zeolite. I. Studies on static equilibrium*, *Microporous Mesoporous Mat.* **39**, 149 (2000).
- [407] E. G. Derouane, *Shape selectivity in catalysis by zeolites: The nest effect*, *J. Catal.* **100**, 541 (1986).
- [408] G. Sastre and A. Corma, *The confinement effect in zeolites*, *J. Mol. Catal. A-Chem.* **305**, 3 (2009).

- [409] L. Firlej, J. Rogacka, F. Formalik, and B. Kuchta, *How dense is the gas adsorbed in nanopores?* *Microporous Mesoporous Mat.* **304**, 109240 (2020).
- [410] K. B. Lipkowitz and M. A. Peterson, *Benzene is not very rigid*, *J. Comput. Chem.* **14**, 121 (1993).
- [411] A. Laaksonen, J. Wang, and R. J. Boyd, *Internal motion of benzene. a molecular dynamics simulation study*, *Chem. Phys. Lett.* **241**, 380 (1995).
- [412] D. M. Ruthven, M. Eic, and E. Richard, *Diffusion of C<sub>8</sub> aromatic hydrocarbons in silicalite*, *Zeolites* **11**, 647 (1991).
- [413] J. Kärger and D. M. Ruthven, *Diffusion in zeolites and other microporous solids*, 1st ed. (Wiley-Interscience, New York, NY, 1992).
- [414] R. Mihályi, S. Klébert, M. Kollár, and V. Mavrodinova, *Transformation of ethylbenzene-m-xylene mixture on zeolites with different structures*, *J. Porous Mater.* **21**, 485 (2014).
- [415] O. C. Gobin, S. J. Reitmeier, A. Jentys, and J. A. Lercher, *Diffusion pathways of benzene, toluene and p-xylene in MFI*, *Microporous Mesoporous Mat.* **125**, 3 (2009).
- [416] R. V. Awati, P. I. Ravikovitch, and D. S. Sholl, *Efficient and accurate methods for characterizing effects of framework flexibility on molecular diffusion in zeolites: CH<sub>4</sub> diffusion in eight member ring zeolites*, *J. Phys. Chem. C* **117**, 13462 (2013).
- [417] R. V. Awati, P. I. Ravikovitch, and D. S. Sholl, *Efficient calculation of gas diffusivity in single-component and binary mixtures of spherical adsorbates in flexible 8MR zeolites*, *J. Phys. Chem. C* **119**, 16596 (2015).
- [418] J. A. Gee and D. S. Sholl, *Effect of framework flexibility on C<sub>8</sub> aromatic adsorption at high loadings in metal-organic frameworks*, *J. Phys. Chem. C* **120**, 370 (2016).
- [419] B. Mentzen and P. Gelin, *The silicalite/p-xylene system : Part I - Flexibility of the MFI framework and sorption mechanism observed during p-xylene pore-filling by X-ray powder diffraction at room temperature*, *Mater. Res. Bull.* **30**, 373 (1995).
- [420] D. Yin and A. D. MacKerell Jr., *Combined ab initio/empirical approach for optimization of Lennard-Jones parameters*, *J. Comput. Chem.* **19**, 334 (1998).
- [421] S. Caro-Ortiz, E. Zuidema, M. Rigutto, D. Dubbeldam, and T. J. H. Vlugt, *Competitive adsorption of xylenes at chemical equilibrium in zeolites*, *J. Phys. Chem. C* **10.1021/acs.jpcc.0c09411**, in press.
- [422] A. Jentys, R. R. Mukti, H. Tanaka, and J. A. Lercher, *Energetic and entropic contributions controlling the sorption of benzene in zeolites*, *Microporous Mesoporous Mat.* **90**, 284 (2006).
- [423] J.-R. Li, R. J. Kuppler, and H.-C. Zhou, *Selective gas adsorption and separation in metal-organic frameworks*, *Chem. Soc. Rev.* **38**, 1477 (2009).
- [424] J. F. M. Denayer, R. A. Ocakoglu, K. De Meyer, and G. V. Baron, *Exploiting pore or cavity size and shape in separating linear and branched hydrocarbons by inverse selectivity: Enthalpy, entropy and packing effects*, *Adsorption* **11**, 49–53 (2005).

- [425] M. Schenk, S. Calero, T. L. M. Maesen, T. J. H. Vlugt, L. L. van Benthem, M. G. Verbeek, B. Schnell, and B. Smit, *Shape selectivity through entropy*, *J. Catal.* **214**, 88 (2003).
- [426] R. Krishna, *Elucidation and characterization of entropy effects in mixture separations with micro-porous crystalline adsorbents*, *Sep. Purif. Technol.* **215**, 227 (2019).
- [427] D. Keffer, H. T. Davis, and A. V. McCormick, *Effect of loading and nanopore shape on binary adsorption selectivity*, *J. Phys. Chem.* **100**, 638 (1996).
- [428] J. I. Siepmann, J. F. Brennecke, D. T. Allen, M. T. Klein, P. E. Savage, G. C. Schatz, and F. M. Winnik, *ACS virtual issue on multicomponent systems: Adsorption, adsorption, and diffusion*, *J. Chem. Eng. Data* **63**, 3651 (2018).
- [429] B. Smit, *Grand-canonical Monte Carlo simulations of chain molecules: Adsorption isotherms of alkanes in zeolites*, *Mol. Phys.* **85**, 153 (1995).
- [430] D. J. Collins, R. J. Medina, and B. H. Davis, *Xylene isomerization by ZSM-5 zeolite catalyst*, *Can. J. Chem. Eng.* **61**, 29 (1983).
- [431] X. Chang, Y. Li, and Z. Zeng, *Kinetics study of the isomerization of xylene on HZSM-5 zeolite. 1. Kinetics model and reaction mechanism*, *Ind. Eng. Chem. Res.* **31**, 187 (1992).
- [432] J. C. Gonçalves and A. E. Rodrigues, *Xylene isomerization in the liquid phase using large-pore zeolites*, *Chem. Eng. Technol.* **39**, 225 (2016).
- [433] J. D.-Y. Ou, A. D. Ross, D. Levin, M. Kalyanaraman, and W. F. Lai, *Xylene isomerization process and catalyst therefor*, (U.S. Patent 8,697,929 B2, Apr. 15, 2014).
- [434] J. Magne-Drisch, F. Alario, J.-F. Joly, A. Minkkinen, and E. Merlen, *Process for the production of paraxylene that comprises an adsorption stage, a liquid phase isomerization stage and a gas phase isomerization stage with an EUO-type zeolite*, (U.S. Patent 6,448,459 B1, Sep. 10, 2002).
- [435] L. Wolff, P. Leflaive, and A. Methivier, *Process for co-producing para-xylene and styrene*, (U.S. Patent 7,592,499 B2, Sep. 22, 2009).
- [436] J. Karl Johnson, A. Z. Panagiotopoulos, and K. E. Gubbins, *Reactive canonical Monte Carlo*, *Mol. Phys.* **81**, 717 (1994).
- [437] W. R. Smith and B. Triska, *The reaction ensemble method for the computer simulation of chemical and phase equilibria. I. Theory and basic examples*, *J. Chem. Phys.* **100**, 3019 (1994).
- [438] C. Heath Turner, J. K. Brennan, M. Lísal, W. R. Smith, J. Karl Johnson, and K. E. Gubbins, *Simulation of chemical reaction equilibria by the reaction ensemble Monte Carlo method: A review*, *Mol. Simulat.* **34**, 119 (2008).
- [439] A. Poursaeidesfahani, R. Hens, A. Rahbari, M. Ramdin, D. Dubbeldam, and T. J. H. Vlugt, *Efficient application of Continuous Fractional Component Monte Carlo in the reaction ensemble*, *J. Chem. Theory Comput.* **13**, 4452 (2017).
- [440] M. W. Chase, *NIST-JANAF thermodynamic tables, Fourth edition*, Journal of Physical and Chemical Reference Data Monographs (American Chemical Society, American Institute of Physics, 1998).

- [441] D. A. McQuarrie, J. D. Simon, H. A. Cox, and J. Choi, *Physical chemistry: A molecular approach*, Reference, Information and Interdisciplinary Subjects Series (University Science Books, Herndon, VA, 1997).
- [442] R. G. Mullen and E. J. Maginn, *Reaction ensemble Monte Carlo simulation of xylene isomerization in bulk phases and under confinement*, *J. Chem. Theory Comput.* **13**, 4054 (2017).
- [443] V. Lachet, S. Buttefey, A. Boutin, and A. H. Fuchs, *Molecular simulation of adsorption equilibria of xylene isomer mixtures in faujasite zeolites. A study of the cation exchange effect on adsorption selectivity*, *Phys. Chem. Chem. Phys.* **3**, 80 (2001).
- [444] A. L. Myers and J. M. Prausnitz, *Thermodynamics of mixed-gas adsorption*, *AIChE J.* **11**, 121 (1965).
- [445] A. Tarafder and M. Mazzotti, *A method for deriving explicit binary isotherms obeying the ideal adsorbed solution theory*, *Chem. Eng. Technol.* **35**, 102 (2012).
- [446] C. M. Simon, B. Smit, and M. Haranczyk, *pyIAST: Ideal adsorbed solution theory (IAST) python package*, *Comput. Phys. Commun.* **200**, 364 (2016).
- [447] T. R. Josephson, R. Singh, M. S. Minkara, E. O. Fetisov, and J. I. Siepmann, *Partial molar properties from molecular simulation using multiple linear regression*, *Mol. Phys.* **117**, 3589 (2019).
- [448] A. Rahbari, T. R. Josephson, Y. Sun, O. A. Moulton, D. Dubbeldam, J. I. Siepmann, and T. J. H. Vlugt, *Multiple linear regression and thermodynamic fluctuations are equivalent for computing thermodynamic derivatives from molecular simulation*, *Fluid Phase Equilib.* **523**, 112785 (2020).
- [449] W. J. Taylor, D. D. Wagman, M. G. Williams, K. S. Pitzer, and F. D. Rossini, *Heats, equilibrium constants, and free energies of formation of the alkylbenzenes*, *J. Res. Nat. Bur. Stand.* **37**, 95 (1946).
- [450] A. M. Mamedov, T. S. Akhundov, and N. N. Asadulaeva, *Experimentelle Untersuchung der Dichte und Sättigungsdruckes von m-Xylool*, *Teploenerg.* **5**, 81–82 (1967).
- [451] D. Ambrose, *Vapour pressures of some aromatic hydrocarbons*, *J. Chem. Thermodyn.* **19**, 1007 (1987).
- [452] D. Ambrose, B. E. Broderick, and R. Townsend, *The vapour pressures above the normal boiling point and the critical pressures of some aromatic hydrocarbons*, *J. Chem. Soc. A*, 633 (1967).
- [453] M. Murthi and R. Q. Snurr, *Effects of molecular siting and adsorbent heterogeneity on the ideality of adsorption equilibria*, *Langmuir* **20**, 2489 (2004).
- [454] R. Krishna and J. van Baten, *Segregation effects in adsorption of CO<sub>2</sub>-containing mixtures and their consequences for separation selectivities in cage-type zeolites*, *Sep. Purif. Technol.* **61**, 414 (2008).
- [455] J. A. Swisher, L.-C. Lin, J. Kim, and B. Smit, *Evaluating mixture adsorption models using molecular simulation*, *AIChE Journal* **59**, 3054 (2013).
- [456] A. S. T. Chiang, C.-K. Lee, and Z.-H. Chang, *Adsorption and diffusion of aromatics in AlPO4-5*, *Zeolites* **11**, 380 (1991).

- [457] A. Torres-Knoop, S. R. G. Balestra, R. Krishna, S. Calero, and D. Dubbeldam, *Entropic separations of mixtures of aromatics by selective face-to-face molecular stacking in one-dimensional channels of metal–organic frameworks and zeolites*, *ChemPhysChem* **16**, 532 (2015).
- [458] J. M. Guil, R. Guil-López, J. A. Perdigón-Melón, and A. Corma, *Determining the topology of zeolites by adsorption microcalorimetry of organic molecules*, *Microporous Mesoporous Mat.* **22**, 269 (1998).
- [459] C. W. Jones, S. I. Zones, and M. E. Davis, *m-Xylene reactions over zeolites with unidimensional pore systems*, *Appl. Catal. A-Gen.* **181**, 289 (1999).
- [460] E. J. Prosen, W. H. Johnson, and F. D. Rossini, *Heats of combustion and formation at 25 degrees C of the alkylbenzenes through  $C_{10}H_{14}$ , and of the higher normal monoalkylbenzenes*, *J. Res. Natl. Inst. Stan.* **36**, 455 (1946).
- [461] K. S. Pitzer and D. W. Scott, *The thermodynamics and molecular structure of benzene and its methyl derivatives*, *J. Am. Chem. Soc.* **65**, 803 (1943).
- [462] J. A. Draeger, *The methylbenzenes II. Fundamental vibrational shifts, statistical thermodynamic functions, and properties of formation*, *J. Chem. Thermodyn.* **17**, 263 (1985).
- [463] J. Chao, K. R. Hall, K. N. Marsh, and R. C. Wilhoit, *Thermodynamic properties of key organic oxygen compounds in the carbon range  $C_1$  to  $C_4$ . Part 2. Ideal gas properties*, *J. Phys. Chem. Ref. Data* **15**, 1369 (1986).
- [464] C. Kittel and H. Kroemer, *Thermal Physics*, 2nd ed. (W. H. Freeman, New York, NY, 1980).
- [465] M. G. Martin and J. I. Siepmann, *Calculating Gibbs free energies of transfer from Gibbs ensemble Monte Carlo simulations*, *Theor. Chem. Acc.* **99**, 347–350 (1998).
- [466] A. Ben-Naim, *Statistical thermodynamics for chemists and biochemists*, 1st ed. (Plenum Press, New York, 1992).

# SUMMARY

The separation of C<sub>8</sub> aromatic hydrocarbons (e.g. xylenes) is one of the most important processes in the petrochemical industry. Current research efforts are focused on materials that can decrease the energy consumption and increase the efficiency of the separation process. Industrial processing of C<sub>8</sub> aromatics typically considers adsorption in a zeolite from a vapor or liquid stream of mixed aromatics. Adsorption in porous materials can be used to separate the isomers or to promote catalytic reactions to transform aromatics into high value products. However, little is known about the chemical equilibrium of the adsorbed phase at reaction conditions. Most studies of adsorption of aromatics in zeolites, either experimental or computational, have focused on adsorption of pure components from the vapor phase. Experimentally, it is very difficult to determine adsorption equilibrium at saturation conditions. In molecular simulations, very difficult insertions and deletions of molecules make simulations very inefficient. Nowadays, advanced simulations techniques can be used to overcome this issue. Computer simulations of adsorption of aromatics in zeolites are typically performed using rigid zeolite frameworks. However, it is known that adsorption isotherms for aromatics are very sensitive to small differences in the atomic positions of the zeolite. In this thesis, the following types of questions are addressed: (1) how does framework flexibility influence adsorption and diffusion of C<sub>8</sub> aromatics in zeolites?; (2) what is the role of the pore topology? For the separation and catalytic conversion of xylenes; (3) how does the type of framework influence the product distribution of xylene isomers?; (4) are there any possible zeolite structures that may have been overlooked for the processing of aromatics? For this, the different aspects that affect the interactions between aromatic molecules and the aromatics/zeolite systems in the simulations are discussed.

The intermolecular interactions between aromatic molecules are studied by computing the vapor-liquid equilibria of pure xylenes and binary mixtures using four different force fields. The densities of pure *p*-xylene and *m*-xylene can be well estimated using the TraPPE-UA and AUA force fields. The largest differences of computed VLEs with experiments are observed for *o*-xylene. Binary mixtures of *p*-xylene and *o*-xylene are simulated, leading to an excellent agreement for the predictions of the composition of the liquid phase compared to experiments. For the vapor phase, the accuracy of the predictions of the composition are linked to the quality of the density predictions of the pure components of the mixture. The phase composition of the binary system of xylenes is very sensitive to small differences in vapor phase density of each xylene isomer, and how well the differences are captured by the force fields.

Most of the models commonly used for framework flexibility in zeolites include a combination of Lennard-Jones and electrostatic intra-framework interactions. The effect of these models for framework flexibility on the predictions of adsorption

of aromatics in zeolites is studied. It is observed that the intra-framework interactions in flexible framework models induce small but important changes in the atom positions of the zeolite, and hence in the adsorption isotherms. Framework flexibility is differently 'rigid': flexible force fields produce a zeolite structure that vibrates around a new equilibrium configuration with limited capacity to accommodate to bulky guest molecules. The simulations show that models for framework flexibility should not be blindly applied to zeolites and a general reconsideration of the parametrization schemes for such models is needed. The effect of framework flexibility on the adsorption and diffusion of aromatics in MFI-type zeolite is systematically studied. It is found that framework flexibility has a significant effect on the adsorption of aromatics in zeolites, specially at high pressures. For very flexible zeolite frameworks, loadings up to two times larger than in a rigid zeolite framework are obtained at a given pressure. Framework flexibility increases the rate of diffusion of aromatics in the straight channel of MFI-type zeolites by many orders of magnitude compared to a rigid zeolite framework. The simulations show that framework flexibility should not be neglected and that it significantly affects the diffusion and adsorption properties of aromatics in a MFI-type zeolite.

The interactions of aromatic molecules inside different zeolite types are studied by computing adsorption isotherms of pure xylenes and a mixture of xylenes at chemical equilibrium. It is observed that for zeolites with one dimensional channels, the selectivity for a xylene isomer is determined by a competition of entropic and enthalpic effects. Each of these effects is related to the diameter of the zeolite channel. For zeolites with two intersecting channels, the selectivity is determined by the orientation of the methyl groups of xylenes. *m*-Xylene is preferentially adsorbed if xylenes fit tightly in the intersection of the channels. If the intersection is much larger than the adsorbed molecules, *p*-xylene is preferentially adsorbed. This thesis provides insight on how the zeolite framework can influence the competitive adsorption and selectivity of xylenes at reaction conditions. Different selectivities are observed when molecules are adsorbed from a vapor phase compared to the adsorption from a liquid phase. This suggests that screening studies that consider adsorption only from a vapor phase may have overlooked well-performing candidates for C<sub>8</sub> aromatics processing. This insight has a direct impact on the design criteria for future applications of zeolites in industry. It is observed that MRE-type and AFI-type zeolites exclusively adsorb *p*-xylene and *o*-xylene from a mixture of xylenes in the liquid phase, respectively. These zeolite types show potential to be used as high-performing molecular sieves for xylene separation and catalysis.

# SAMENVATTING

De scheiding van C<sub>8</sub> aromatische koolwaterstoffen zoals xylenen is één van de belangrijkste processen in de petrochemische industrie. Hedendaags onderzoek richt zich op het vinden van materialen die de efficiëntie van dit scheidingsproces verhogen en het energieverbruik verlagen. In de industrie worden C<sub>8</sub>-aromaten gescheiden uit gas- of vloeistofmengsels van aromaten door gebruik te maken van adsorptie in zeolieten. De adsorptie van de aromaten kan gebruikt worden om isomeren te scheiden of deze om te zetten in andere waardevolle producten. Er is echter niet veel bekend over het chemisch (reactie) evenwicht in de geadsorbeerde fase. De meeste onderzoeken (zowel experimenteel als computationeel) naar de adsorptie van aromaten in zeolieten richtten zich op de adsorptie van zuivere componenten in de gasfase. Dichtbij het verzadigde regime is het experimenteel lastig om adsorptie-evenwichten te bepalen en in moleculaire simulaties is het invoegen en verwijderen van moleculen inefficiënt. Nieuwe, geavanceerde simulatiemethoden bieden een oplossing voor dit probleem. Bij simulaties van adsorptie van aromaten in zeolieten wordt vaak aangenomen dat het zeoliet star is. Het is echter bekend dat adsorptie-isothermen van aromaten erg gevoelig zijn voor kleine veranderingen in de posities van de atomen in het zeoliet. In dit proefschrift richten we ons daarom op de volgende vraagstukken: (1) hoe worden de adsorptie en diffusie van C<sub>8</sub>-aromaten beïnvloed door de flexibiliteit van het zeoliet? en (2) welke rol speelt de topologie van de poriën? En voor het scheiden en omzetten van xylenen richten we ons op: (3) hoe wordt de verdeling van de reactieproducten beïnvloed door de structuur van een zeoliet? en (4) zijn er zeolieten die geschikt zijn voor de adsorptie van aromaten die eerder over het hoofd zijn gezien? We bestuderen daarvoor de verschillende factoren die van invloed kunnen zijn op de interacties tussen aromaten en zeolieten.

De intermoleculaire interacties tussen aromaten worden bestudeerd met behulp van simulaties van gas-vloeistofevenwichten van zuivere xylenen en binaire mengsels daarvan. We doen dit voor vier verschillende krachtvelden. De dichtheden van zuiver *p*-xyleen en *m*-xyleen kunnen nauwkeurig worden bepaald met de TRAPPE-UA en AUA krachtvelden. Voor gas-vloeistofevenwichten wordt de grootste afwijking gevonden tussen simulaties en experimenten voor *o*-xyleen. Simulaties van binaire mengsels van *p*-xyleen en *o*-xyleen komen goed overeen met de vloeistofcompositie afkomstig uit experimenten. In de gasfase hangt de nauwkeurigheid af van de nauwkeurigheid van het krachtveld voor de dichtheden van de zuivere stoffen. De compositie van de binaire mengsels wordt sterk beïnvloed door kleine verschillen in de dichtheden van de gasfase en hoe goed het krachtveld deze verschillen beschrijft.

De meeste modellen die framework-framework interacties beschrijven in een flexibel zeoliet gebruiken een combinatie van Lennard-Jones en elektrostatische interacties. Hier bekijken we de invloed van deze modellen op de adsorptie van aro-

maten in zeolieten. Het blijkt dat de framework-framework interacties een kleine, maar belangrijke, invloed hebben op de posities van de atomen in het zeoliet. Dit effect is terug te zien in de adsorptie-isothermen. Wat adsorptie betreft heeft de flexibiliteit van een framework hetzelfde effect als een kleine structuurverandering van een star zeoliet. Simulaties tonen aan dat modellen die flexibiliteit beschrijven niet zo maar toegevoegd kunnen worden aan modellen voor adsorptie en diffusie in zeolieten. Er is daarvoor een andere aanpak nodig. Een systematische studie is uitgevoerd om te onderzoeken hoe adsorptie en diffusie van aromaten in MFI-type zeolieten worden beïnvloed door flexibiliteit. Vooral bij hoge drukken heeft flexibiliteit een effect op de adsorptie van de aromaten in zeolieten. In flexibele zeolieten kan de adsorptie twee keer zo hoog zijn als in een star zeoliet. Door de flexibiliteit van MFI-type zeolieten wordt de diffusiesnelheid van aromaten in het rechte kanaal enkele ordegroottes groter ten opzichte van starre zeolieten. Uit deze simulaties kunnen we concluderen dat flexibiliteit een belangrijke factor is om rekening mee te houden wanneer men kijkt naar diffusie en adsorptie van aromaten in MFI-type zeolieten.

De interacties van aromaten in verschillende zeolieten worden bestudeerd door het bepalen van adsorptie-isothermen van zuivere xylenen en mengsels daarvan bij chemisch evenwicht. Voor zeolieten met één-dimensionale kanalen zien we dat de selectiviteit voor een bepaald xyleen-isomeer bepaald wordt door entropische en enthalpische invloeden. Beide invloeden zijn gerelateerd aan de doorsnede van het kanaal in het zeoliet. In zeolieten met twee kruisende kanalen wordt de selectiviteit bepaald door de oriëntatie van de methylgroepen van het xyleen-isomeer. Als xylenen nauw passen in de kanalen wordt vooral *m*-xyleen geabsorbeerd. Als de kanaaldiameter groter wordt zal vooral *p*-xyleen worden geabsorbeerd. In dit proefschrift gaan we in op hoe de structuur van het zeoliet de adsorptie en selectiviteit van xylenen beïnvloedt wanneer deze een reactie ondergaan. De selectiviteit verschilt wanneer de moleculen worden geabsorbeerd uit de gasfase vergeleken met de vloeistoffase. Voor studies waar alleen gekeken is naar de adsorptie uit de gasfase kan dit betekenen dat sommige zeolieten over het hoofd zijn gezien, terwijl deze wel degelijk geschikt zouden kunnen zijn voor het converteren van C<sub>8</sub>-aromaten. Dit is een belangrijk resultaat voor toekomstige toepassingen van zeolieten in de (petrochemische) industrie. Verder blijkt dat MRE-type zeolieten alleen *p*-xyleen absorbeert uit xyleenmengsels in de vloeistoffase en AFI-type zeolieten alleen *o*-xyleen. Deze typen zeolieten kunnen veelbelovend zijn als moleculaire zeef voor het scheiden én omzetten van xylenen.

# ACKNOWLEDGEMENTS

I would like to thank my promotores Thijs Vlugt and David Dubbeldam for their contributions to this thesis. It has been a pleasure to work with you. You were always available to discuss science and gave me good advice to improve my work and I am grateful for that. Also, I would like to acknowledge the collaboration and insightful discussions with Erik Zuidema and Marcello Rigutto. I thank the committee members for their feedback on this thesis.

I would like to thank friends and coworkers at the Process & Energy department and the Engineering Thermodynamics group. Special thanks to Remco Hens, Julia Boschan, Tim Becker, Metin Çelik, and Dion Koeze for the good laughs and the support throughout these years. I also thank Christos Bardas, Mariëtte de Groen, Máté Erdős, Alper Çelebi, Noura Dawass, Mahinder Ramdin, Seyed Jamali, Meng Wang, Vilborg G., Karsten Baumgarten, Max Döpke, Carlos Infante Ferreira, and Xuan Tao for making the office such a nice place.

I thank Xueqing Zhang, Martijn de Lange, Ariana Torres Knoop, and Jurn Heinen for kindly sharing their expertise in simulations with me. Also, I thank co-authors Desmond Dekker, Ali Poursaeidesfahani, Hirad Salehi, Ahmadreza Rahbari, and Othonas Moultos for the fruitful collaboration.

I am indebted to Anna Hiemstra for her constant support and motivation during the writing of this thesis. Thanks to Maria Dau, an unconditional fan of the watercolors displayed in this thesis. También agradezco a mi familia y amigos. Su apoyo y motivación han sido fundamentales durante esta aventura.

Voorburg, March 2021.



# CURRICULUM VITÆ

## Sebastián Andrés CARO ORTIZ

16-11-1988 Born in Iquique, Chile.

### EDUCATION

2003–2006

Secondary Education

Liceo Academia Iquique, Iquique, Chile

2007–2011

*Licenciado en Ciencias de la Ingeniería Mecánica*

Bachelor of Science in Mechanical Engineering

Universidad Técnica Federico Santa María, Valparaíso, Chile

2007–2015

*Ingeniero Civil Mecánico*

Professional Title of Mechanical Engineer

Universidad Técnica Federico Santa María, Valparaíso, Chile

2012–2015

*Magíster en Ciencias de la Ingeniería Mecánica*

Master of Science in Mechanical Engineering

Universidad Técnica Federico Santa María, Valparaíso, Chile

2016–2021

Doctor

Delft University of Technology, Delft, The Netherlands

*Thesis:* Adsorption and Separation of

C<sub>8</sub> Aromatic Hydrocarbons in Zeolites

*Promotors:* Prof.dr.ir. T.J.H. Vlugt & Dr. D. Dubbeldam



# LIST OF PUBLICATIONS

Publications by the author included in this thesis:

5. **S. Caro-Ortiz**, E. Zuidema, M. Rigutto, D. Dubbeldam, T. J. H. Vlugt, *Competitive adsorption of xylenes at chemical equilibrium in zeolites*, *J. Phys. Chem. C*, (in press) [10.1021/acs.jpcc.0c09411](https://doi.org/10.1021/acs.jpcc.0c09411).
4. **S. Caro-Ortiz**, E. Zuidema, M. Rigutto, D. Dubbeldam, T. J. H. Vlugt, *Effects of framework flexibility on the adsorption and diffusion of aromatics in MFI-type zeolites*, *J. Phys. Chem. C* **124**, 24488 (2020).
3. **S. Caro-Ortiz**, E. Zuidema, D. Dekker, M. Rigutto, D. Dubbeldam, T. J. H. Vlugt, *Adsorption of aromatics in MFI-type zeolites: Experiments and framework flexibility in Monte Carlo simulations*, *J. Phys. Chem. C* **124**, 21782 (2020).
2. **S. Caro-Ortiz**, R. Hens, E. Zuidema, M. Rigutto, D. Dubbeldam, T. J. H. Vlugt, *Corrigendum to “Molecular simulation of the vapor-liquid equilibria of xylene mixtures: Force field performance, and Wolf vs. Ewald for electrostatic Interactions” [Fluid Phase Equilib.] 485 (2019) 239–247, Fluid Phase Equilib.* **506**, 112370 (2020).
1. **S. Caro-Ortiz**, R. Hens, E. Zuidema, M. Rigutto, D. Dubbeldam, T. J. H. Vlugt, *Molecular simulation of the vapor-liquid equilibria of xylene mixtures: Force field performance, and Wolf vs. Ewald for electrostatic interactions*, *Fluid Phase Equilib.* **485**, 239 (2019).

Publications by the author not included in this thesis:

5. R. Hens, A. Rahbari, **S. Caro-Ortiz**, N. Dawass, M. Erdős, A. Poursaeidesfahani, H. S. Salehi, A. T. Celebi, M. Ramdin, O. A. Moulton, D. Dubbeldam, T. J. H. Vlugt, *Brick-CFCMC: Open source software for Monte Carlo simulations of phase and reaction equilibria using the Continuous Fractional Component method*, *J. Chem. Inf. Model.* **60**, 2678 (2020).
4. H. Gonzalez, **S. Caro**, M. Toledo, H. Olguin, *Syngas production from polyethylene and biogas in porous media combustion*, *Int. J. Hydrot. Energy* **43**, 4294 (2018).
3. M. Toledo, C. Rosales, C. Silvestre, **S. Caro**, *Numerical simulation of the hybrid filtration combustion of biomass*, *Int. J. Hydrot. Energy* **41**, 21131 (2016).
2. M. Toledo, F. Gracia, **S. Caro**, J. Gómez, V. Jovicic, *Hydrocarbons conversion to syngas in inert porous media combustion*, *Int. J. Hydrot. Energy* **41**, 5857 (2016).
1. **S. Caro**, D. Torres, M. Toledo, *Syngas production from residual biomass of forestry and cereal plantations using hybrid filtration combustion*, *Int. J. Hydrot. Energy* **40**, 2568 (2015).